Passivation of Advanced Silicon Solar Cells

A Thesis
Submitted in partial fulfillment of
the requirements for the degree of
Doctor of Philosophy
by

Jayshree Bhajipale
(Roll No. 164076018)

Supervisor:
Prof. Anil Kottantharayil

Department of Electrical Engineering
Indian Institute of Technology Bombay
Mumbai 400076 (India)

4 July 2023

Dedicated to my family, teachers, and friends

Approval Sheet

This thesis entitled "Passivation of Advanced Silicon Solar Cells" by Jayshree Bhajipale is approved for the degree of Doctor of Philosophy.

Prof. Vamsi Krishna Komarala
(External Examiner)

Prof. Narendra Shiradkar
(Internal Examiner)

Prof. Anil Kottantharayil
(Supervisor)

Prof. Guruswamy Kumaraswamy
(Chairman)

Date: 04-07-2023

Place: Mumbai

Declaration

I declare that this written submission represents my ideas in my own words and where others' ideas or words have been included, I have adequately cited and referenced the original sources. I declare that I have properly and accurately acknowledged all sources used in the production of this report. I also declare that I have adhered to all principles of academic honesty and integrity and have not misrepresented or fabricated or falsified any idea/data/fact/source in my submission. I understand that any violation of the above will be a cause for disciplinary action by the Institute and can also evoke penal action from the sources which have thus not been properly cited or from whom proper permission has not been taken when needed.

Part of thesis are already published or under review in journals and presented at conferences as listed below:

Chapter 5:

Jayshree Bhajipale and Anil Kottantharayil, "Passivation of n- and p-type silicon surfaces with spray-coated sol-gel silicon oxide thin film," *Transactions of Electron Devices*, vol. 67, no. 11, pp. 5045-5052, 2020.

Jayshree Bhajipale and Anil Kottantharayil, "Effectiveness of UV-Ozone treatment and alneal process for Si surface passivation with sol-gel spray-Coated SiO_2 film," in *proceedings of ECS Meeting Abstracts*, 2021, pp. 643.

Jayshree Bhajipale and Anil Kottantharayil, "Post deposition annealing temperature optimization for sol-gel spray-coated SiO_2 film for p-type Cz Si surface passivation," in *proceedings of 5th IEEE International Conference on Emerging Electronics (ICEE)*, 2020, pp. 1–4.

Chapter 6:

Jayshree Bhajipale, Suchismita Mitra, Hemanta Ghosh, K. P. Sreejith, and Anil Kottantharayil, "Spray-coated SiO_2/PECVD SiN_x stack for the passivation of n^+ emitter of p-type Si solar cell," *Solar Energy*, vol. 246, pp. 113–118, 2022.

Chapter 7:

Jayshree Bhajipale, Anil Kottantharayil, and K. P. Sreejith, "Advantages of TOPCon cell with rear full area hole selective contact on p-type Si with front n^+ emitter over PERC," in *proceedings of 8th World Conference on Photovoltaic Energy Conversion (WCPEC)*, 2022, pp. 184–186.

Chapter 8:

Jayshree Bhajipale, Anil Kottantharayil, and K. P. Sreejith, "TCAD Based numerical exploration of industrially feasible tunnel oxide passivated contact on p-type silicon," *Solar Energy*, vol. 253, pp. 231–239, 2023.

Jayshree Bhajipale
(Roll No. 164076018)

Date: 4 July 2023

Abstract

Bulk and surface recombination loss deteriorate the silicon (Si) solar cell efficiency. However, high bulk lifetime (τ_b) wafers are available in the market due to advancements in Si wafer manufacturing technology. Thereby, surface recombination loss marks the major loss mechanism in Si solar cells. In addition, wafer thinning to cut down the cell cost has set the recombination at the surface as a limiting factor due to the increase in the surface-to-volume ratio of the wafer. Therefore, these demand better Si surface passivation in advanced Si solar cells.

During the early days of Si solar cells, thermally grown silicon dioxide (SiO_2) was extensively used due to its excellent Si surface passivation quality. However, the thermal oxidation process was found unsuitable for the cost effective solar industry. The thermal oxidation performed at high temperatures (> 900°C) deteriorates the bulk lifetime of the Si and needs a long process time increasing its thermal budget making it a costly process for the solar industry. Therefore, alternate low temperature SiO_2 deposition/growth techniques were explored. SiO_2 deposited at low temperatures by Plasma Enhanced Chemical Vapor Deposition (PECVD) was profoundly studied. Later, it was identified that it cannot passivate moderately doped Si wafer at an optimum annealing temperature. Nitric Acid Oxidation of Si (NAOS) and UV-Ozone oxidation were other alternatives. However, these both limit the oxide thickness to < 2 nm. Also, NAOS SiO_2 showed poor interface quality. Therefore, there was a need for an alternative SiO_2 deposition technique.

Wet chemical sol-gel method is an alternative simple and low temperature process, which facilitates oxide deposition at room temperature, tuning of the film composition and properties by sol-gel chemistry, and adaptability towards various substrates. Sol-gel derived oxide can be deposited by various techniques such as spin-, dip- and spray-coating. Spray deposition technique outperforms spin- and dip-coating at an industrial level due to its relative ease to coat industrial scale samples with high throughput. In this thesis, SiO_2 film deposition employing a simple, cost-effective, and industrially viable spray-coating technique is demonstrated, where custom-designed spray-coating tool is

used for its deposition. The solution is sprayed over Si substrate kept in air ambient and further baked to form a film.

Initially, the solution content was optimized by studying the effect of solvent (ethanol, isopropanol, 2-methoxyethanol, and 1-butanol) on the SiO_2 film properties including thickness, density, interface state density (D_{it}), and oxide charge density (Q_f). Continuous film is obtained using ethanol, isopropanol, and 2-methoxyethanol as a solvent on superhydrophilic Si, made by exposing it to UV-Ozone. However, 1-butanol does not give continuous film either on superdyrophilic or weakly hydrophilic Si surfaces. 2-methoxyethanol based SiO_2 films were comparatively dense and uniform followed by isopropanol and then ethanol. Films based on 2-methoxyethanol showed D_{it} of $\sim 10^{11}$ $cm^{-2}eV^{-1}$, an order of magnitude higher than the ethanol and isopropanol based SiO_2 films ($\sim 10^{10}$ $cm^{-2}eV^{-1}$). This suggests that 2-methoxyethanol usage would give inferior passivation of highly doped Si surface. Therefore, isopropanol is chosen as the optimum solvent for spray-SiO_2 film.

Further, the optimized solution was used for a thorough investigation of the SiO_2 film properties on n-type as well as p-type polished Si. The spray-SiO_2 film is amorphous and nearly stoichiometric on both n- and p-type Si. Low values of D_{it} of 1.4×10^{10} $cm^{-2}eV^{-1}$ on n-type and 2.0×10^{10} $cm^{-2}eV^{-1}$ on p-type is achieved. These are the best D_{it} reported for solution based SiO_2 film. Excellent passivation quality was demonstrated on both n- and p-type Si, but more effective on n-type with effective surface recombination velocity (S_{eff}) of 0.97 cm s^{-1} and 8.07 cm s^{-1} on p-type Si. These values are superior to sol-gel based SiO_2 films reported previously and are comparable to or better than those reported for other methods for the growth or deposition of SiO_2 on Si. SiO_2 film exhibits dielectric breakdown field strength of 4.3 $MVcm^{-1}$ and 5.6 $MVcm^{-1}$ and leakage current density of 2.2×10^{-8} Acm^{-2} and 1.1×10^{-8} Acm^{-2} at 1 $MVcm^{-1}$ on n- and p-type Si, respectively. This proves the capability of the spray-SiO_2 to provide exceptional passivation of polished Si with better passivation on n-type than on p-type.

Later, the capability of the spray-SiO_2 to passivate phosphorus diffused textured n^+ emitter is demonstrated. Inefficient passivation of n^+ emitter is one of the limiting factors contributing to lower efficiency in advanced p-type Si solar cells. A stack of SiO_2 and SiN_x with the former as an intermediate layer beneath SiN_x provides better emitter passivation in comparison to SiN_x film alone. Thermal oxide is reported to provide the best passivation, but it is not industrially viable. It has been demonstrated in our work that spray SiO_2/SiN_x is a viable alternative to thermal SiO_2/SiN_x stack. A few nanometer thin ($\sim$ 6.1 nm) conformal spray SiO_2 film deposition is demonstrated for the first time on micrometer sized textured pyramid with full coverage over an entire

deposited area. The passivation of the symmetrical (n^+-p-n^+) structure shows implied open circuit voltage (iV_{oc}) ~ 660 mV and passivation uniformity over the entire wafer area for both stacks. Open circuit voltage (V_{oc}) ~ 630 mV is achieved on Aluminum-Back Surface Field (Al-BSF) cells with spray and thermal SiO_2 as a passivating layer. Similar front passivation is further verified by overlapping Internal Quantum Efficiency (IQE) in the shorter wavelength range. These results ascertain the competence of the spray technique to deposit conformal film over textured Si and of the spray-SiO_2 to provide comparable Si passivation to thermal oxide.

Thereafter, the work is extended to a simulation study in Sentaurus TCAD to compare the advanced solar cells; Passivated Emitter Rear Contact (PERC) and cell with hole passivating contact at the rear with n^+ diffused emitter at the front on p-type Si (p-TOPCon); from a passivation perspective. Prior to this, the TCAD simulation deck is calibrated to simulate the Si solar cells using the experimentally measured data. The calibrated deck is used in all further simulation studies. The simulation study shows that the p-TOPCon has higher V_{oc} and efficiency in comparison to PERC for similar passivation. p-TOPCon has a lower sensitivity to variations in rear surface recombination velocity (S_{rear}) in comparison to PERC. The efficiency of PERC starts decreasing for $S_{rear} \geq 10^2$ cm s^{-1} whereas it drops for $S_{rear} \geq 10^3$ cm s^{-1} in p-TOPCon. Also, in comparison to p-TOPCon, PERC needs stringent condition on S_{rear} to surpass Al-BSF. The sensitivity to front surface recombination velocity (S_{front}) is similar for both PERC and p-TOPCon. This suggests that p-TOPCon outperforms PERC for an identical bulk and rear and front surface passivation.

The highest efficiency reported for TOPCon cell on p-type is for the architecture with rear electron selective passivating contact (n-TOPCon) fabricated with stringent process conditions. Therefore, with confirming the p-TOPCon superiority to PERC, the next immediate task is to compare the performance of p-TOPCon and n-TOPCon with respect to all the industrial design parameters. The TCAD simulation study shows that the p-TOPCon is less sensitive over a wide range of design parameters (τ_b, resistivity, and S_{front}) in comparison to n-TOPCon. The simulation study suggests that p-TOPCon could be the primary successor of PERC. With industrially relevant parameters, p-TOPCon could reach efficiency > 23.8%. However, p-TOPCon needs to be replaced with n-TOPCon to achieve efficiency beyond 24.4%.

Table of Contents

List of Figures

List of Tables

List of Symbols

α	Scale parameter of Weibull distribution
B	Radiative recombination coefficient (cm^{-3} s^{-1})
β	Shape parameter of Weibull distribution
c	Velocity of light (m s^{-1})
C_c	Corrected capacitance (F)
C_{FB}	Flat band capacitance (F)
C_m	Measured capacitance (F)
C_{ma}	Measured capacitance in strong accumulation region (F)
C_{MG}	Mid-gap capacitance (F)
C_{min}	Minimum capacitance (F)
$C_{m,max}$	Capacitance corresponding to maximum conductance (F)
C_n	Auger coefficient for eeh process (cm^6 s^{-1})
C_{ox}	Oxide capacitance in accumulation region of corrected C-V curve (F)
C_p	Auger coefficient for ehh process (cm^6 s^{-1})
C_s	Semiconductor capacitance (F)
$C_{s,FB}$	Semiconductor flat band capacitance (F)
$C_{s,MG}$	Semiconductor mid-gap capacitance (F)
$C_{s,min}$	Minimum semiconductor capacitance (F)
D	Minority diffusion constant (cm^2 s^{-1})

Δn	Excess electron concentration (cm^{-3})
Δp	Excess hole concentration (cm^{-3})
Δn_s	Excess electron concentration at surface (cm^{-3})
Δp_s	Excess hole concentration at surface (cm^{-3})
D_{it}	Interface state density (cm^{-2} eV^{-1})
E_{BD}	Breakdown field (V cm^{-1})
$E_{B.E.}$	Binding energy (eV)
E_c	Conduction band edge (eV)
E_{fc}	Quasi-Fermi levels for electrons in the conductance band (eV)
E_{fv}	Quasi-Fermi levels for holes in the valence band (eV)
$E_{K.E.}$	Kinetic energy of electron (eV)
EOT	Effective oxide thickness (cm)
E_{ox}	Oxide electric field (V cm^{-1})
ε_s	Dielectric permitivity of Si
E_T	Defect energy level (eV)
E_v	Valence band edge (eV)
f	Frequency (Hz)
FF	Fill factor (%)
G_c	Corrected conductance (S)
G_m	Measured conductance (S)
G_{ma}	Measured conductance in strong accumulation region (S)
$G_{m,max}$	Maximum conductance (S)
h	Planck's constant (J s)
iV_{oc}	Implied open circuit voltage (V)

J_{01}	Saturation current density (A cm^{-2})
$J_{0,rear,met}$	Recombination current density at the rear metalized contact (A cm^{-2})
J_{leak}	Leakage current density (A cm^{-2})
J_{MPP}	Current density at maximum power point (A cm^{-2})
$J_{0e,pass}$	Recombination current density at the passivated emitter (A cm^{-2})
J_{sc}	Short circuit current density (A cm^{-2})
k	Boltzmann constant (eV K^{-1})
λ	Wavelength (m)
L_D	Debye length (cm)
n	Non-equilibrium electron concentration (cm^{-3})
n_0	Equilibrium electron concentration (cm^{-3})
N_A	Silicon acceptor doping concentration (cm^{-3})
N_D	Silicon donor doping concentration (cm^{-3})
n_i	Intrinsic carrier concentration (cm^{-3})
N_{it}	Trap density at the surface (cm^{-2})
$N_{Poly-Si}$	Poly-Si doping (cm^{-3})
n_s	Surface electron concentration (cm^{-3})
N_{surf}	Dopant peak concentration at the surface (cm^{-3})
N_t	Trap density in the bulk (cm^{-3})
p	Non-equilibrium hole concentration (cm^{-3})
p_0	Equilibrium hole concentration (cm^{-3})
ϕ_b	Bulk potential (V)
ϕ_{MS}	Metal/semiconductor work function difference (V)
P_{MPP}	Power at maximum power point (W cm^{-2})

p_s	Surface hole concentration (cm^{-3})
ψ_s	Surface potential (V)
q	Electronic charge (Coulomb)
Q_f	Oxide charge density (cm^{-2})
ρ	Bulk resistivity (Ω-cm)
R_s	Series resistance (Ω)
R_{sh}	Shunt resistance (Ω cm^2)
R_{sheet}	Sheet resistance (Ω/sq)
S_{eff}	Surface recombination velocity (cm s^{-1})
S_{front}	Front surface recombination velocity (cm s^{-1})
σ_n	Electron capture cross section (cm^2)
σ_p	Hole capture cross section (cm^2)
S_{n0}	Electron surface recombination velocity parameter (cm s^{-1})
S_{p0}	Electron surface recombination velocity parameter (cm s^{-1})
S_{rear}	Rear surface recombination velocity (cm s^{-1})
T	Temperature (K)
τ_{Auger}	Auger recombination lifetime (s)
τ_b	Bulk lifetime (s)
τ_{eff}	Effective lifetime (s)
τ_n	Electron minority carrier lifetime (s)
τ_{nonrad}	Non-radiative recombination lifetime (s)
τ_p	Hole minority carrier lifetime (s)
τ_{rad}	Radiative recombination lifetime (s)
τ_s	Surface recombination lifetime (s)

T_{BDR}	Indiffusion depth (nm)
$T_{Poly-Si}$	Poly-Si thickness (nm)
U_{Auger}	Auger recombination rate (cm^{-3} s^{-1})
U_{nonrad}	Non-radiative recombination rate (cm^{-3} s^{-1})
U_{rad}	Radiative recombination rate (cm^{-3} s^{-1})
U_s	Surface recombination rate (cm^{-2} s^{-1})
U_{SRH}	SRH recombination rate ($cm^{-3}s^{-1}$)
V_{BD}	Breakdown voltage (V)
V_{FB}	Flat band voltage (V)
$V_{FB,ideal}$	Ideal flat band voltage (V)
V_G	Gate voltage (V)
V_{MG}	Mid-gap voltage (V)
$V_{MG,ideal}$	Ideal mid-gap voltage (V)
V_{MPP}	Voltage at maximum power point (V)
V_{oc}	Open circuit voltage (V)
v_{th}	Thermal velocity (cm s^{-1})
W	Wafer thickness (μm)
W_{finger}	Finger width (μm)

List of Abbreviations

AC	Alternating current
AFM	Atomic Force Microscopy
Ag	Silver
Al	Aluminum
Al_2O_3	Aluminum oxide
Al-BSF	Aluminum Back Surface Field
ALD	Atomic Layer Deposition
ARC	Anti-reflection coating
a-Si	Amorphous silicon
BDR	Back diffusion region
BSF	Back Surface Field
CO_2	Carbon dioxide
C-V	Capacitance-voltage
Cz	Czochralski
DC	Direct current
DI-O_3	Ozonated deionized water
EQE	External Quantum Efficiency
FESEM	Field Emission Scanning Electron Microscopy
FG	Forming Gas

FGA Forming Gas Annealing

FSF Front Surface Field

FZ Float Zone

G-V Conductance-voltage

HNO_3 Nitric acid

IQE Internal Quantum efficiency

ITRPV International Technology Roadmap for Photovoltaic

I-V Current-voltage

J-V Current density-voltage

LeTID Light and elevated Temperature-Induced Degradation

LID Light-Induced Degradation

LPCVD Low Pressure Chemical Vapor Deposition

MOS Metal Oxide Semiconductor

N_2O Nitrous oxide

NaOCl Sodium hypochloride

NAOS Nitric Acid Oxidation of Silicon

O_3 Ozone

PDA Post Deposition Annealing

PECVD Plasma Enhanced Chemical Vapor Deposition

PERC Passivated Emitter and Rear Contact

PERL Passivated Emitter Rear Locally Diffused

PL Photoluminescence

PMA Post Metallization Annealing

$POCl_3$ Phosphorus oxychloride

poly-Si	Polysilicon
PSG	Phosphosilicate glass
PV	Photovoltaic
QE	Quantum efficiency
QSS	Quasi-Steady-State
RCA	Radio Corporation of America
RMS	Root Mean Square
SDE	Sentaurus Structure Editor
Sdevice	Sentaurus Device
SDR	Saw damage removal
SEM	Scanning Electron Microscopy
Si	Silicon
SiH_4	Silane
SiN_x	Silicon nitride
SiO_2	Silicon dioxide
SRH	Shockley–Read–Hall
STC	Standard test condition
Svisual	Sentaurus Visual
TCAD	Technology Computer Aided Design
TEM	Transmission Electron Microscopy
TEOS	Tetraethyl orthosilicate
TFT	Thin-Film Transistor
TiO_2	Titanium oxide
TIR	Total Internal Reflection

TOPCon Tunnel Oxide Passivated Contact

WAR Weighted average reflectance

XPS X-ray Photoelectron Spectroscopy

Chapter 1

Introduction

Renewable energy is a way out to move towards clean and sustainable energy sources from fossil fuels that contribute to greenhouse gas emission. Among renewables, solar photovoltaic (PV) has gained its position in coping with the increasing energy demand. There has been significant growth in the global PV market in 2021. At the end of 2021, the cumulative installed PV capacity in the world reached 942 GW with an increase of around 175 GW compared to 2020 [1]. This has contributed to a saving of as much as 1100 million tons of carbon dioxide (CO_2) emission [1]. Therefore, there is a need to increase PV deployment to reduce CO_2 emission [1].

Of the total PV market, silicon (Si) solar cell technology dominates with a total share of 95% and is expected to remain unchanged in near future according to International Technology Roadmap for Photovoltaic (ITRPV) 2021 [2]. The long-term competitiveness of PV power generation can be ensured by the reduction of PV system costs which will be supported by the combination of reduced manufacturing costs and increased cell and module performance. The overall cost could be reduced by reducing the consumption of materials required for the processing from the wafer to the module level. Also, introducing new technologies and highly productive manufacturing equipment would lead to a reduction in production costs.

With a price share close to 20%, polysilicon (poly-Si), which is consumed for mono-Si wafer manufacturing, is the most expensive material of Si solar cells [2]. Therefore, thinning down the wafer and reducing the kerf loss will yield cost savings by utilizing the ingot efficiently. 165 μm thick p-type mono-Si and 160 μm thick n-type wafers with 158.75 μm x 158.75 μm dimensions are standard in 2021. However, a minimum thickness of 150 μm and 140 μm would be reached for mono-Si p- and n-type wafers within the next 10 years [2]. Also, n-type Czochralski (Cz) Si wafer and its manufacturing is costlier in comparison to p-type Cz Si [3, 4]. In addition, the issue of Light-Induced Degradation

(LID) in boron doped p-type Si has been significantly reduced in gallium doped p-type Si wafers, which are expected to replace the former in the near future [5]. Therefore, sticking to p-type based cell technologies would also add to the cost reduction. In addition, recombination in the bulk and at the surface critically affects the performance of the solar cell. Using high bulk quality wafers and improving the passivation of the Si surface could significantly enhance the cell efficiency, thereby reducing the overall cost. The matured cell concepts of diffused and passivated p-n will be further used and will be the mainstream with different rear side passivation technologies [2]. It has been predicted that among the cell technologies with the passivated diffused emitter at the front and passivated rear side, the concept of passivated contact using the tunnel oxide passivation stack at the rear will gain market share upto 50% within the next 10 years with efficiency reaching upto 25% [2]. Therefore, increasing the cell efficiency by upgrading the cell architecture would also lead to a reduced overall cost.

1.1 Thesis motivation

As discussed, the wafer thickness would be reduced in the near future to cut down the cell cost. This would increase the surface-to-volume ratio of the wafer and set surface recombination as a limiting factor in recent high efficiency advanced Si solar cells demanding better Si surface passivation. Thermally grown oxides are known to give excellent passivation of Si surface with superior Si/silicon dioxide (SiO_2) interface quality [6, 7]. Due to its inbuilt positive charges, it passivates n-type Si better than p-type. For the same reason, it was widely used in the earlier Si solar cells for the passivation of the front textured n^+ emitter [8]. Regardless of the best passivation quality, thermal oxidation is not preferred in the PV industry due to its requirement of high temperature (> 900°C) degrading the Si bulk [9] and long process time adding to the thermal budget and throughput. Alternate low temperature techniques have been explored for SiO_2 growth/deposition. These include Plasma Enhanced Chemical Vapor Deposition (PECVD), Nitric Acid Oxidation of Silicon (NAOS), and UV-Ozone oxidation. PECVD SiO_2 films are reported not to provide as good Si passivation as thermal oxide at optimum annealing conditions for moderate resistivity wafers. NAOS oxide shows poor Si/SiO_2 interface quality. NAOS and UV-Ozone oxidation has limitation of growing $SiO_2 < 2$ nm.

In addition, SiO_2 film alone cannot be used in p-type Si solar cells due to its low refractive index (~ 1.46) making it unsuitable for anti-reflection coating (ARC). Also, it cannot sustain high temperature firing step [10]. Therefore, SiO_2 passivating layer is always capped with the silicon nitride (SiN_x) layer acting as an ARC. Also, SiO_2/SiN_x

stack has been studied to enhance the passivation stability of SiO_2 and the thermal stability of SiN_x [11]. SiO_2/SiN_x stack improves the passivation property of the SiO_2 film [12–14].

Si industry is moving towards rear passivating contact technology for efficiency enhancement due to enhanced rear passivation performance. These cells are mostly fabricated on n-type Si due to its superior bulk properties compared to p-type Si. However, p-type Si is being used in the PV industry since the beginning and the process line is compatible with the same. Also, gallium doped wafers have been proven to give Si wafers with a bulk lifetime in the range of ms, which is comparable to n-type Si [5]. In addition, cells fabricated on gallium doped wafers do not suffer from LID. Therefore, there is high scope to continue with the p-type Si. However, on p-type Si, the best efficiency has been demonstrated for architecture with rear n-type passivating contact (n-TOPCon) [15]. With the current industry being dominated by Passivated Emitter and Rear Contact (PERC) technology, it would be feasible to switch to the architecture with rear p-type passivating contact on p-type Si with front n^+ emitter (p-TOPCon). This would demand only minor upgradation in the current PERC fabrication process line. There has not been extensive work performed on this architecture.

Therefore, there is a requirement for a low temperature and high throughput SiO_2 deposition technique to provide passivation similar to the costlier thermal oxidation process. In this thesis, industrially viable spray-coating has been demonstrated for nanometer SiO_2 film deposition and Si surface passivation. Also, its capability to act as a passivating layer beneath SiN_x ARC coating, passivating the n^+ emitter has been investigated. Further, in this thesis, a thorough study has been performed via Sentaurus Technology Computer Aided Design (TCAD) simulations to investigate the performance of p-TOPCon against PERC and n-TOPCon cells on p-type Si considering industrially relevant design parameters.

1.2 Organization of the thesis

The thesis contents are organized into nine chapters including the introduction. These are organized in the following way.

A review of the literature relevant to the topics discussed in this thesis is presented in chapter 2. Various recombination mechanisms in the semiconductor are discussed. It gives an overview of the Si surface passivation including the critical parameters surface recombination velocity (S_{eff}, cm s^{-1}) and implied open circuit voltage (iV_{oc}, mV) for its characterization and technological methods (chemical and field effect) for its improvement. In depth review of the passivation of Si surface with SiO_2 dielectric

grown/deposited by various techniques and their limitations have been presented, setting up the tone for the development of an alternative industrially viable spray-coating technique for SiO_2 deposition. The importance of SiO_2/SiN_x stack in Si passivation has also been discussed. The chapter ends with a discussion of various surface passivation mechanisms featured in industrial Si solar cells.

Chapter 3 details the theory behind widely used characterization and simulation techniques used in this thesis. It also discusses the methodology used for the extraction of relevant parameters from the respective characterization technique.

Chapter 4 starts with experimental work on the development of SiO_2 film using the sol-gel spray coating technique. It details the effect of different solvents (ethanol, isopropanol, 2-methoxyethanol, and 1-butanol) on the physical and passivation properties of the spray-SiO_2 film. It also discusses the wetting behavior of these solvents on two distinct types of Si surfaces. Considering the experimental data, also pros and cons of the solvents, the chapter concludes by setting isopropanol as the optimum solvent to be used for SiO_2 deposition via the spray-coating technique in this thesis.

Chapter 5 focuses on the detailed study of physical, electrical, and passivation properties of sol-gel spray-coated SiO_2 film on both n- and p-type Si. A demonstration and development of the amorphous and nearly stoichiometric spray-SiO_2 film have been presented. Further, the chapter provides an insight into the interface state density (D_{it}, cm^{-2} eV^{-1}) and oxide charge density (Q_f, cm^{-2}) at the spray-SiO_2/Si interface achieving the lowest D_{it} among sol-gel SiO_2 films at comparatively low annealing temperatures. A comprehensive analysis indicating the superiority of the UV-Ozone and alneal process is presented. The chapter concludes by demonstrating excellent passivation of both n- and p-type polished Si with S_{eff} comparable to other deposition techniques.

Chapter 6 extends the work on the spray-SiO_2 film for its demonstration on textured Si surface, extensively used in Si solar industry. It investigates the conformal coverage of nanometer thin spray-SiO_2 film over micrometer sized pyramidal structure. Further, the capability of the spray SiO_2 capped with PECVD SiN_x to passivate heavily doped textured n^+ emitter surface is investigated. The chapter details an experimental benchmarking of the passivation quality provided by the spray-SiO_2/SiN_x with thermal SiO_2/SiN_x stack. Similar iV_{oc} of symmetrical passivation structure and performance of Aluminum Back Surface Field (Al-BSF) cell is achieved by incorporation of these two individual stacks. Hence, this chapter demonstrates the potential of spray-SiO_2 to replace thermal SiO_2 to passivate n^+ textured emitter of p-type Si solar cell.

Chapter 7 commences the simulation work in Sentaurus Technology Computer Aided Design (TCAD) software. It describes the need and methodology to calibrate the

TCAD simulation deck with the experimental data of the Si solar cells. This calibrated deck is used in all further simulation studies. A comparison of advanced Si solar cell architectures namely PERC and p-TOPCon has been performed via TCAD simulations to study the effect of front and rear surface passivation on them. The chapter concludes with the observation that the p-TOPCon outperforms PERC for identical bulk, front and rear surface passivation.

Chapter 8 investigates a TCAD numerical simulation based comparative study of n-TOPCon, p-TOPCon, and PERC cells on p-type Si considering the industrially relevant cell design parameters. Further, exclusively for p-TOPCon, a detailed roadmap is presented by studying all the design parameters including the bulk lifetime, poly-Si related parameters, front emitter and its passivation, and finger width. The chapter concludes that an efficiency > 23.8% is achieved with p-TOPCon and therefore, it could be an immediate potential successor of PERC.

Chapter 9 summarises the thesis and provides an outlook on the directions for future research in this area.

Chapter 2

Literature Review on Passivation in Silicon Solar Cells

In the last decade, one of the major technological pillars for the huge success of renewable energies is crystalline Si solar cells based PV energy conversion. Increased conversion efficiencies and reduced production costs lead to a rapid reduction of levelized costs of electricity. The PV Si solar cells covert the incident solar illumination into electron-hole pairs and separate these carriers to generate electrical power. High efficiency is realized when all of the free carriers generated are collected by the external circuit. However, the conversion efficiency of the solar cell is limited by the different losses. These include resistive and optical losses and the recombination of photo-generated carriers. Of these, the most detrimental loss channel is the recombination loss in the solar cell.

2.1 Recombination mechanisms in semiconductor

In semiconductors, electron-hole pairs are generated either by light absorption or by energy gained via thermal agitation [16]. In Si solar cells, electron and hole pairs are created when the incident photon energy is greater than the Si bandgap. This process of creation of excess electron-hole pairs is known as generation. Recombination is the opposite of the generation process in which electrons and holes (carriers) are annihilated [16]. Recombination within semiconductors usually takes place through a number of simultaneous processes. The nature of the processes can be classified as intrinsic or extrinsic. Intrinsic processes include radiative recombination [17] and Auger recombination [18]. These are unavoidable properties of the semiconductor material. Extrinsic processes include Shockley–Read–Hall (SRH) bulk [16] and surface recombination [19]. These relate to defects (crystallographic imperfections, impurities, etc.) within the material or at its surface.

2.1.1 Radiative recombination

Radiative recombination, also referred to as band to band or direct recombination, is a process in which an electron in the allowed energy state in the conduction band of a semiconductor falls into the vacant valence band state at an identical crystal momemtum. Direct recombination is radiative, where the energy released due to electron-hole recombination is emitted as a photon with energy equal to the bandgap of the semiconductor. The radiative recombination rate depends on the concentration of electrons in the conduction band and holes in the valence band. The radiative recombination rate (U_{rad}, $cm^{-3}s^{-1}$) is given by [20]

$$U_{rad} = B(np - n_i^2) \tag{2.1}$$

where B is the radiative recombination coefficient ($cm^3\ s^{-1}$), n_i is the intrinsic carrier concentration (cm^{-3}), n and p are the non-equilibrium electron and hole concentration (cm^{-3}), respectively. B represents the probability of direct recombination. The probability of radiative recombination is less in indirect bandgap semiconductors than in direct bandgap [20]. For Si at 300 K, B value is calculated as $4.73 \times 10^{-15}\ cm^3\ s^{-1}$ [17]. In p-type Si, the radiative recombination lifetime (τ_{rad}, s) is given as

$$\tau_{rad} = \frac{\Delta n}{U_{rad}} = \frac{1}{B(p_0 + n_0 + \Delta p)} \tag{2.2}$$

In low level injection condition, where $\Delta n = \Delta p \ll p_0 + n_0$, τ_{rad} is rewritten as

$$\tau_{rad} = \frac{1}{B(p_0 + n_0)} \tag{2.3}$$

and in case of high level injection, where $\Delta n = \Delta p \gg p_0 + n_0$, τ_{rad} transforms to

$$\tau_{rad} = \frac{1}{B\Delta p} \tag{2.4}$$

where p_0 and n_0 are the equilibrium hole and electron concentration (cm^{-3}), respectively and Δn and Δp are the excess electron and hole concentration (cm^{-3}), respectively.

2.1.2 Auger recombination

Auger recombination, also known as three particle recombination, is a process in which an electron from the conduction band recombines with a hole in the valence band. The energy released is transferred to either an electron in the conduction band or a hole in the valence band. The Auger recombination involving two electrons and one hole is called

eeh process. Whereas, recombination involving one electron and two holes is called *ehh* process. The Auger recombination rate (U_{Auger}, $cm^{-3}s^{-1}$) can be represented as [20]

$$U_{Auger} = C_n(n^2p - n_0^2p_0) + C_p(np^2 - n_0p_0^2) \tag{2.5}$$

where C_n and C_p represents Auger coefficients for *eeh* and *ehh* processes ($cm^6\ s^{-1}$), respectively. C_n is 2.8×10^{-31} $cm^6\ s^{-1}$ and C_p is 9.9×10^{-32} $cm^6\ s^{-1}$ for Si with doping concentration (N_A or N_D) $> 5 \times 10^{18}$ cm^{-3} at 300 K [21].

In low level injection condition, where $\Delta n = \Delta p \ll p_0 + n_0$, the Auger recombination lifetime (τ_{Auger}) is

$$\tau_{Auger} = \frac{1}{C_nN_D^2} \quad \text{for n-type Si and} \quad \tau_{Auger} = \frac{1}{C_pN_A^2} \quad \text{for p-type Si} \tag{2.6}$$

In high level injection condition, where $\Delta n = \Delta p \gg p_0 + n_0$, τ_{Auger} is

$$\tau_{Auger} = \frac{1}{(C_n + C_p)\Delta n^2} \quad \text{for both n- and p-type Si} \tag{2.7}$$

The Auger recombination affects carrier lifetime in lowly doped Si under high injection conditions and in highly doped Si under low injection conditions [18, 22].

The traditional Auger theory based on free-particle approximation, as outlined above, is valid for highly doped Si ($N_{A,D} > 5 \times 10^{18}$ cm^{-3}). In contrast, for lower dopant concentrations, the mobile carriers interact with each other by means of Coulombic interaction. Thus, the density of electron increases in the vicinity of the hole, while it decreases in the vicinity of another electron. To account for Coulomb enhanced Auger recombination, the Auger coefficients C_n and C_p are multiplied with the enhancement factors g_{eeh} and g_{ehh}, respectively [23]. Richter et al. proposed general parameterization for intrinsic recombination in crystalline Si at 300 K taking into account the Coulomb-enhanced Auger recombination given as [24]

$$\tau_{intr,adv} = \frac{\Delta n}{(np - n_{i,eff}^2)(2.5 \times 10^{-31}g_{eeh} + 8.5 \times 10^{-32} + 3.0 \times 10^{-29}\Delta n^{0.92} + B_{rel}B_{low})} \tag{2.8}$$

with enhancement factors

$$g_{eeh}(n_0) = 1 + 13\left\{1 - tanh\left[\left(\frac{n_0}{N_{0,eeh}}\right)^{0.66}\right]\right\} \tag{2.9}$$

$$g_{ehh}(p_0) = 1 + 7.5\left\{1 - tanh\left[\left(\frac{p_0}{N_{0,ehh}}\right)^{0.63}\right]\right\} \tag{2.10}$$

and $N_{0,eeh}$ is 3.3×10^{17} cm^{-3}, $N_{0,ehh}$ is 7.0×10^{17} cm^{-3}, $n_{i,eff}$ is the effective intrinsic carrier concentration with a value of 9.65×10^{9} cm^{-3} [25], B_{low} is radiative recombination coefficient for lowly doped and lowly injected Si, 4.73×10^{-15} cm^{3} s^{-1} [17], and B_{rel} is the relative radiative recombination coefficient [26].

2.1.3 Shockley–Read–Hall recombination

Recombination through defect level in the bandgap of the semiconductor is labeled SRH recombination. Physically, these defect levels can be due to crystallographic imperfections or impurity atoms in the semiconductor. SRH recombination is a two step process. An electron from the conduction band and a hole from the valence band is captured at the defect level, resulting in the annihilation of the electron-hole pair. The defect level which annihilates electron-hole pair acts as a recombination center. Alternatively, an electron from the conduction band loses its energy a second time and annihilates a hole in the valence band. Here, the defect level acts as a transition level. SRH recombination, also known as indirect recombination, releases thermal energy or equivalently, produces lattice vibrations. SRH recombination is dominant in indirect bandgap semiconductors like Si. The net recombination rate via single defect level (U_{SRH}, cm^{-3}s^{-1}) can be described by SRH statistics as [20, 27–29]

$$U_{SRH} = \frac{np - n_i^2}{\tau_p(n + n_1) + \tau_n(p + p_1)} \tag{2.11}$$

n_1 and p_1 are related to defect energy level (E_T) by

$$n_1 = n_i exp\Big(\frac{E_T - E_i}{kT}\Big), \quad p_1 = n_i exp\Big(\frac{E_i - E_T}{kT}\Big) \tag{2.12}$$

τ_n and τ_p are electron and hole minority carrier lifetimes (s), respectively given by

$$\tau_p = \frac{1}{\sigma_p v_{th} N_t} \quad \text{for n-type Si and} \quad \tau_n = \frac{1}{\sigma_n v_{th} N_t} \quad \text{for p-type Si} \tag{2.13}$$

where k is the Boltzmann constant (eV K^{-1}), T the temperature (K), σ_n and σ_p are the capture cross sections for electrons and holes (cm^2), respectively, v_{th} is the thermal velocity (cm s^{-1}), and N_t is the defect/trap density in the bulk (cm^{-3}). The net SRH recombination rate is maximum when the defect energy level (E_T, eV) is at the midgap, indicating that the defects at or near the midgap are effective recombination centers.

For mid gap defect energy state, at low injection condition, the net SRH recombination rate becomes [16]

$$U_{SRH} = \frac{\Delta p}{\tau_p} \quad \text{for n-type Si and} \quad U_{SRH} = \frac{\Delta n}{\tau_n} \quad \text{for p-type Si} \tag{2.14}$$

and for high injection case, U_{SRH} becomes [16]

$$U_{SRH} = \frac{\Delta p}{\tau_p + \tau_n} \quad \text{for n-type and p-type Si} \tag{2.15}$$

2.1.4 Surface recombination

The surface of Si shows the largest possible crystal lattice symmetry disturbance compared to the bulk giving rise to unsaturated bonds. These dangling bonds give rise to a large density of surface states within the bandgap at the crystal surface. At the surface, a hole from the valence band recombines with an electron from the conduction band via these surface defect levels/states. Each surface state acts as a recombination center. These surface states result in high recombination probability and therefore surface recombination rate. SRH equation for bulk as in equation 2.11 can be modified to obtain the surface recombination rate (U_s) via a single defect level located at an energy E_T at the surface as [27]

$$U_s = \frac{n_s p_s - n_i^2}{\frac{n_s + n_1}{S_{p0}} + \frac{p_s + p_1}{S_{n0}}} \tag{2.16}$$

where n_s and p_s are surface concentration (cm^{-3}), and S_{n0} and S_{p0} are the surface recombination velocity of the electrons and holes ($cm\ s^{-1}$), respectively. S_{n0} and S_{p0} are related to v_{th}, N_{it} the number of surface states per unit area (cm^{-2}), and σ_n and σ_p by

$$S_{n0} = \sigma_n v_{th} N_{it}, \quad S_{p0} = \sigma_p v_{th} N_{it} \tag{2.17}$$

The recombination rate U_s for a continuum of non interacting surface states over the bandgap can be obtained by equation 2.16 by substituting $dN_{it} = D_{it}(E_T)dE_T$ and integrating over the band gap [30]

$$U_s = (n_s p_s - n_i^2) v_{th} \int_{E_v}^{E_c} \frac{D_{it}(E_T)}{\frac{n_s + n_1}{\sigma_p} + \frac{p_s + p_1}{\sigma_n}} dE_T \tag{2.18}$$

where D_{it} is the energy dependent interface state density ($cm^{-2}\ eV^{-1}$).

2.2 Passivation of silicon surface

Reduction in recombination at the surface is referred to as surface passivation. Reduction in the Si wafer thickness to cut down the cell cost demands better passivation of the Si surface.

2.2.1 Characterization of surface passivation

2.2.1.1 Surface recombination velocity

A quantity that reflects the degree of surface passivation is S_{eff}, which is defined as:

$$S_{eff} = U_s/\Delta n_s \tag{2.19}$$

where Δn_s is the excess carrier density at the surface (cm^{-3}). The smaller the value of S_{eff}, the better the Si surface passivation. Practically, S_{eff} is extracted from the effective lifetime (τ_{eff}, s) measured using photoconductance decay technique with the Sinton lifetime measurement tool. S_{eff} is a very important metric to describe the surface passivation property of dielectric as it is independent of sample thickness and doping concentrations, unlike lifetime [31]. Grivickas et al. showed that for similar surface passivation on both sides, τ_{eff} is described by the expression [32]

$$\frac{1}{\tau_{eff}} = \frac{1}{\tau_b} + \left(\frac{W}{2S_{eff}} + \frac{1}{D}\left(\frac{W}{\pi}\right)^2\right)^{-1} \tag{2.20}$$

where W is the wafer thickness (cm) and D is the minority carrier diffusion constant ($cm^2\ s^{-1}$). D is calculated using PVLighthouse online calculator [33] as 15.15 $cm^2\ s^{-1}$ for n-type and 23.61 $cm^2\ s^{-1}$ for p-type Si at a minority carrier concentration of 10^{15} cm^{-3} for Si substrate with resitivity of 4-7 Ω-cm that would be used in this work for passivation study of polished n- and p-type Si. For sufficiently low S_{eff} values ($S_{eff} < \pi^2 D/2W$), equation (2.20) simplifies to [34]

$$\frac{1}{\tau_{eff}} = \frac{1}{\tau_b} + \frac{2S_{eff}}{W} \tag{2.21}$$

2.2.1.2 Implied open circuit voltage

iV_{oc} is a parameter for the electronic quality of the solar cell test samples. It is used to characterize the passivation quality of different dielectrics at the Si surface. It represents an easily accessible parameter closely related to the external V_{oc}, a device parameter determined as per the standard for solar cells. iV_{oc} is strongly influenced by charge carrier recombination just like the open circuit voltage (V_{oc}, mV) and, thus is a figure of merit for the sample's recombination properties. iV_{oc} is represented as the quasi-fermi level splitting within a noncontacted semiconductor sample under illumination. It differs from V_{oc}, which is defined as the potential difference between the two opposite polarity contacts including potential drops at the two contacts [35, 36]. For steady state generation and uniform distribution of excess carriers, iV_{oc} can be defined as

$$iV_{oc} = \frac{E_{fc} - E_{fv}}{q} \tag{2.22}$$

where E_{fc} is the quasi-Fermi levels for electrons in the conductance band (eV), E_{fv} is quasi-Fermi levels of holes in the valence band (eV), and q is the elementary charge (Coulomb). The splitting in the quasi fermi level cannot be directly measured. iV_{oc} is calculated from the excess charge carrier density. Sinton and Cuevas demonstrated the determination of excess carrier density by contactless measurement using the Sinton lifetime tester [37]. For a p-n junction solar cell, iV_{oc} can be calculated as

$$iV_{oc} = \frac{kT}{q} ln\left(\frac{np}{n_{i,eff}^2}\right) \tag{2.23}$$

For solar cell made on a p-type wafer with dopant density N_A, the above expression can be approximated assuming Boltzmann statistics as [37]

$$iV_{oc} = \frac{k_B T}{q} ln\left(\frac{\Delta n[N_A + \Delta n]}{n_{i,eff}^2}\right) \tag{2.24}$$

Here, the photogenerated electron density has been assumed to be much higher than the equilibrium electron concentration, $\Delta n \gg n_0$.

2.2.2 Technological methods to improve silicon surface passivation

The relation between surface recombination rate and the properties of the surface states, as given by SRH theory (equations 2.16 and 2.18), shows that there are two complementary ways of reducing the surface recombination and therefore, enhancing the surface passivation.

2.2.2.1 Chemical passivation

U_s and S_{eff} are proportional to the defect density at the surface (D_{it}) (equation 2.18). Therefore, the most straightforward strategy to achieve good surface passivation is to reduce D_{it} by saturating the dangling bonds at the Si surface. This is known as chemical passivation.

One of the technological ways to reduce D_{it} is the immersion of the Si wafer into organic liquids like Iodine/Ethanol solution [38] or Quinhydrone/methanol solution [39, 40]. Although this scheme gives the best chemical passivation, it is not applicable to solar cells in the field. However, it is used for characterization purpose to learn the bulk lifetime of the Si used for solar cell fabrication. The other way which is extensively used for chemical passivation of solar cells deployed in the field is the growth or deposition of dielectric film over the Si surface.

2.2.2.2 Field effect passivation

An electron and a hole both are involved in the recombination event. The highest recombination rate is achieved when the product of the concentration and capture cross section of holes equals the corresponding product of the electrons [19, 41]

$$\sigma_p p_s = \sigma_n n_s \tag{2.25}$$

The capture cross section depends on the details of the passivation scheme. Therefore, another way to reduce surface recombination is to significantly reduce the density of one type of charge carrier (n_s or p_s) at the surface by an internal electric field below the semiconductor surface. This is termed field effect passivation [41, 42]. The 'built-in' field could be formed either by implementing a doping profile beneath the semiconductor surface or applying an electrostatic field by virtue of electrical charges in the overlying insulator. The former is achieved by implementing high-low junctions (p^+-p [43] or n^+-n [44] or a p-n junction. The latter is achieved by growing or depositing a dielectric film with Q_f over the Si surface [45].

In practice, both the above mentioned passivation approaches (chemical and field effect) are used simultaneously to minimize surface recombination rates. The best example is thermally grown SiO_2 which reduces D_{it} as well as provides field effect passivation due to positive Q_f [41].

2.3 SiO_2 as a passivation layer

Thermally grown oxide, due to its high quality interface with Si, was the key technology in the microelectronics industry and has been extensively studied [6, 7, 46]. For the same reason, it was adapted very early in the history of Si solar cells and is one of the pioneer passivation schemes for high efficiency Si based solar cells [8].

The most successful passivation with SiO_2 is achieved using alneal process. The term alneal was coined by Deal in 1970 to refer to aluminum (Al) anneals [47–49]. In this process, a layer of Al is deposited over thermal SiO_2 and the system is annealed at 350 °C - 450°C in Forming Gas (FG) ambient [48, 49]. During annealing, Al reacts with the hydroxyl group (OH) at the Al/SiO_2 interface forming aluminum oxide. This reaction releases hydrogen which diffuses to the Si/SiO_2 interface. The hydrogen introduced during the annealing process passivates the electronically active defects such as the prominent P_b-type defect which constitutes a Si dangling bond (≡Si°) [50]. This saturation of dangling bonds leads to the reduction of D_{it}.

Alnealed SiO_2 has been mainly used in laboratory Si solar cells since 1980's. The potential of front and rear passivation due to thermal SiO_2 has already been demonstrated in 1989 in PERC cell (Fig. 2.1(a)) with an efficiency of more than 22%, V_{oc} of 696 mV, short circuit current density (J_{sc}) of 40.3 mA cm^{-2} and fill factor (FF) of 81.4% [51]. Here, the passivating thermal oxide (~ 110 nm) at the front acts as an ARC. At the rear, its function is to combine with the rear reflector forming an efficient light trapping scheme. The Si-SiO_2-metal system acts as a perfect mirror boosting the internal reflection of light at the rear [52]. By incorporating alneal for both the front and rear SiO_2 layer, UNSW demonstrated record-breaking Passivated Emitter Rear Locally Diffused (PERL) cell (Fig. 2.1(b)) on p-type Si with an efficiency ≥ 24.5% [53]. Here, a stack of SiO_2/titanium oxide (TiO_2) was used at the front to improve the optical properties. An intentional alneal step was introduced to enhance the passivation of the front. An additional thin Al layer was deposited and a low temperature anneal step was performed. Thereafter, the Al layer was etched out and TiO_2 was deposited over the front SiO_2. This allowed for high J_{sc} (> 41 mA cm^{-2}) and high V_{oc} (> 700 mV).

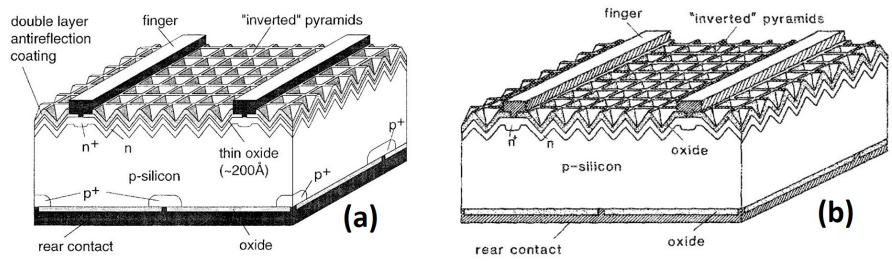

Figure 2.1: Schematic diagram of (a) Passivated Emitter and Rear Contact (PERC) [51] and (b) Passivated Emitter and Rear Locally diffused (PERL) cell structure [53].

Thermal SiO_2 provides the lowest D_{it} in the orders of ~10^9-10^{10} $cm^{-2}eV^{-1}$ [30, 54]. Also, it provides low Q_f, in the range of ~10^{10}-10^{11} cm^{-2} [42, 55]. The Q_f at the Si/SiO_2 interface is generally found to be positive [7,19]. Due to such low defect densities, thermal oxides results in enhanced chemical passivation of both types of Si surfaces.

For alnealed thermal SiO_2 film, Kerr and Cuevas demonstrated a high lifetime of 6 ms in 1.5 Ω-cm n-type and 1.7 ms in 1 Ω-cm p-type Float Zone (FZ) Si, corresponding to a very low S_{eff} of 2.4 cm s^{-1} and 11.8 cm s^{-1}, respectively [56]. In fact, the passivation scheme with alnealed thermal SiO_2 layer was used to characterize the Auger and radiative components of bulk recombination [57]. S_{eff} of both boron doped (p-type) Si substrate and phosphorus doped (n-type) base and emitters for SiO_2 with alneal treatment is shown in Fig. 2.2. The passivation degrades with an increase in surface doping concentration due to the presence of the higher defects introduced at the interface. It has been reported that

at thermally oxidized Si surfaces, the electron capture cross section generally exceeds the hole capture cross section ($\sigma_n/\sigma_p \sim 100$) [19, 55, 58]. SiO_2 has the capability to passivate both n- and p-type Si. However, due to the asymmetry of electron and hole capture crosssection ratios for thermally grown SiO_2, S_{eff} is generally lower on n-type Si than on p-type [19]. Thermal SiO_2 passivates n-type Si better than p-type Si [19].

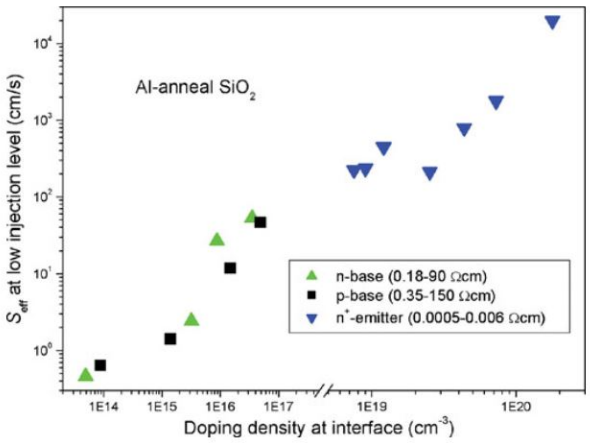

Figure 2.2: Surface recombination velocity (S_{eff}) of boron doped (p-type) Si substrate, phosphorus doped (n-type) Si, and n^+ emitters as a function of doping density at the Si/SiO_2 interface for SiO_2 underwent alneal treatment [59].

Thermal oxides are grown at high temperatures (>900°C) making it an expensive method for the solar industry. In addition, this high processing temperature leads to the degradation of the Si bulk lifetime [9]. Also, thermal oxidation needs a considerably long time which is not desirable from a throughput viewpoint. Therefore, thermal oxidation is not suitable for industrial solar cell mass production. Therefore, there is a need for low temperature deposition techniques. Various other deposition methods have been explored for the development of SiO_2 film at low temperatures.

2.3.1 Low temperature silicon oxidation/deposition methods

2.3.1.1 Plasma Enhanced Chemical Vapor Deposition

PECVD is the most widely used deposition system in the solar industry and was first developed in 1963 [60]. It is capable of depositing amorphous films at low temperatures (200°C - 500°C). A mixture of silane (SiH_4) and nitrous oxide (N_2O) is used for SiO_2 deposition via PECVD.

Batey and Tierney deposited SiO_2 film via remote PECVD over a Si of resistivity 2 Ω-cm at a substrate temperature of 350°C and showed that quite a high $D_{it} \sim 10^{12}$

$cm^{-2}eV^{-1}$ is achieved for as-deposited SiO_2 film [61]. However, the D_{it} was further reduced to mid 10^{10}-10^{11} $cm^{-2}eV^{-1}$ after Post Metallization Annealing (PMA) in FG (10% H_2 in N_2) at 400°C for 30 min [61]. Later, Chen et al. demonstrated high τ_{eff} of > 5 ms and a very low S_{eff} of ≤ 2 cm s^{-1} for remote PECVD deposited thin SiO_2 film at 250°C on a very high resistivity (> 500 Ω-cm) n-type FZ Si subjected to rapid thermal annealing at 350°C in FG ambient [11]. Also, they further performed a detailed study and found that the low recombination velocity is due to low D_{it} ~ 5×10^{10} - 10^{11} $cm^{-2}eV^{-1}$ and moderately high positive oxide charge (~ 5×10^{11} - 10^{12} cm^{-2}) [11]. Mueller et al. also reported low S_{eff} ≤ 2.6 cm s^{-1} on 1Ω-cm n-type FZ Si with PECVD SiO_2 film deposited at a temperature of 155°C but with a significantly longer annealing time of 3 hrs at a temperature of 250°C [62].

Further, it was found that the Si passivation due to PECVD SiO_2 film, when kept unprotected for a long time, degraded with time [11]. Also, it was identified that the PECVD SiO_2 film alone is insufficient in providing excellent Si surface passivation for moderate resistivity wafer at an optimum annealing condition [13].

2.3.1.2 Nitric Acid Oxidation of Silicon

NAOS is a low temperature chemical oxidation method. In the azeotropic NAOS process, the Si wafer is immersed in 68 wt% nitric acid (HNO_3) aqueous solutions at 121°C to grow an ultrathin SiO_2 layer [63, 64]. In this method, high concentration of atomic oxygen is produced by the decomposition of HNO_3. This oxygen is responsible for oxidizing the Si surface growing SiO_2 film. This method grows SiO_2 film ~ 1.4 nm and prolonged oxidation did not increase the SiO_x thickness [64].

Grant et al. reported low S_{eff} of 20 - 35 cm s^{-1} by NAOS technique by simultaneously applying a constant voltage for the SiO_2 film grown on 5 Ω-cm n-type Si subjected to annealing at 400°C in O_2 and then FG [65]. Feldmann et al. used HNO_3 grown ultrathin SiO_2 as tunneling oxide in the fabrication of Tunnel Oxide Passivated Contact (TOPCon) cells demonstrating an efficiency of 24.4% [66]. It has been shown by Stegemann et al. that the NAOS technique led to high D_{it} in the orders of 10^{12} $cm^{-2}eV^{-1}$ giving poor Si surface passivation [67]. Also, thicker oxide cannot be obtained via the NAOS technique.

2.3.1.3 UV-Ozone oxidation

Chen presented the benefits and application of ozonated deionized water (DI-O_3) for the preparation of Si surface in detail, wherein it has been shown superior, or atleast equivalent wafer cleaning and photoresist stripping performance of DI-O_3 technology compared

to the conventional Radio Corporation of America (RCA) process [68]. Since then DI-O_3 research has been undertaken by a number of groups in semiconductor processing [69,70]. Bakhshi et al. demonstrated enhanced p-type Si surface passivation with a stack of aluminum oxide(Al_2O_3)/SiN_x in presence of thin SiO_2 layer formed using DI-O_3 [70]. This resulted in D_{it} of 4.49×10^{11} $cm^{-2}eV^{-1}$ [70].

In addition to the wet DI-O_3 clean technique, an ultraviolet assisted oxidation process, known as UV-Ozone cleaning is simple and an effective technique to remove a wide variety of contaminants from the surface. UV-Ozone technique is also responsible for the removal of organic contaminants as well as for growing oxide [71]. The UV-Ozone system has low pressure mercury vapor UV lamps with simultaneous irradiation of two wavelengths (185 nm and 254 nm). These wavelengths have different roles to play in chemical reactions. Molecular oxygen O_2 is dissociated into free radicals of oxygen ($O^{\cdot}$) by 185 nm UV light. This atomic oxygen combines with molecular oxygen to generate Ozone (O_3). 254 nm is responsible for the dissociation of O_3 which forms molecular oxygen and atomic oxygen. This dissociated oxygen atom has strong oxidation potential. It reacts with the Si surface and oxidizes it. Also, it gently removes the organic residue contaminants from the substrate as volatile byproduct molecules such as CO_2, water (H_2O), and O_2. It was in 1972, that the ability of the UV-Ozone technique to remove organic layers such as photoresist polymer leaving an extremely clean surface, free of carbonaceous material was demonstrated [72]. Moldovan et al. demonstrated that the fingerprints and glue on Si wafers can be removed by UV-Ozone exposure [73]. Also, they have shown high $iV_{oc} > 720$ mV on planar samples and > 710 mV on textured samples symmetrically passivated with UV-Ozone grown ultra-thin SiO_2/poly-Si stack and so this oxide is well suited as tunnel oxide [73]. Bakhshi et al. showed that this relatively simple and inexpensive UV-Ozone technique provides Si surface cleaning efficiency comparable to the RCA cleaning technique [74]. In addition, they also reported D_{it} of 6.2×10^{11} cm^{-2} eV^{-1} for UV-Ozone oxide capped with Al_2O_3 [74]. Srinivasan et al. reported low S_{eff} of 8 cm s^{-1} of p-type Si by incorporating an ultrathin UV-Ozone oxide beneath the spray-coated Al_2O_3 [75]. Like NAOS oxide, UV-Ozone oxide also has a limitation of thickness < 2 nm.

2.3.1.4 Sol-gel method

Solution-processed metal oxides deposited via the sol-gel method have attracted plenty of attention in various semiconductor sectors. Sol-gel metal oxide dielectric films have been used in high-performance electronic devices, mainly in Thin-Film Transistor (TFT) [76] and used as multifunctional coatings for solar panel applications [77]. The sol-gel depo-

sition methods reduce both material and processing costs in comparison to the conventional methods, which rely on either high temperature or vacuum conditions. In contrast, the sol-gel method is a simple, low temperature deposition process, which facilitates the deposition of metal oxides at room temperature. Also, the film properties can be easily tuned by modulating the sol-gel chemistry. Of all the sol-gel dielectrics, silica (SiO_2) film has been extensively studied.

In general, sol-gel processing needs metal alkoxides $M(OR)_n$ as oxide precursor. Here M represents metal and R the alkyl group, C_xH_{2x+1} where typical alkyl groups used are methyl and ethyl [78]. The alkoxides are hydrolyzed and condensed to form M-O-M bonds. For SiO_2 film, the precursor has Si as the metal element. Sol-gel process for SiO_2 is described by three reactions given as

$$\equiv Si - OR + H_2O \quad \leftrightarrow \quad \equiv Si - OH + ROH \quad \text{(hydrolysis)} \tag{2.26}$$

$$\equiv Si - OR + HO - Si \equiv \quad \leftrightarrow \quad \equiv Si - O - Si \equiv +ROH \quad \text{(alcohol condensation)} \tag{2.27}$$

$$\equiv Si - OH + HO - Si \equiv \quad \leftrightarrow \quad \equiv Si - O - Si \equiv +H_2O \quad \text{(water condensation)} \tag{2.28}$$

Si-O-Si (siloxane) complexes form as a product of hydrolysis and condensation reactions. Water is added to the alkoxide solution for its hydrolysis which causes the replacement of the alkoxy group (OR) with the hydroxyl group, OH. This is followed by condensation of hydroxyl containing groups which results in the formation of inorganic polymers containing siloxane complexes. Si precursor is not soluble in H_2O, therefore the precursor is first dissolved in a solvent to produce a homogeneous solution and then H_2O is added [78]. Also, the reaction rate of alkoxides with H_2O is slow. Therefore, to enhance the hydrolysis and condensation reaction rate, a catalyst is added [79]. The final solution is kept for aging to allow siloxane linkages to grow in it.

The influence of various solution and process parameters on the SiO_2 film properties has been critically investigated. It has been demonstrated that the structure and properties of sol-gel silicates can be varied over wide ranges by controlling the process parameters such as type of precursor, H_2O/Si molar ratio (R), nature and the concentration of catalyst, solvent composition, aging and drying condition [80, 152]. Fardad et al. studied the effect of H_2O on spin-coated SiO_2 film thickness, shrinkage, and porosity with varying baking temperature [82]. They concluded that the high water level yielded film with lower thickness and reduced porosity and consequently with higher density (Fig. 2.3) [82]. Also, the film shrinkage with baking temperature is reduced at high water levels (Fig. 2.3) [82]. Due to increasing the hydrolysis rate and therefore lowering the condensation rate with R, the thickness of the as deposited film decreases with R [83]. Abhilash et al.

investigated the role of acid and base catalysts on surface morphology and porosity on dip-coated SiO_2 film and found that acid catalyzed coating exhibits dense and smooth surfaces while base catalyzed coatings shows coarse and rough particle morphology (Fig. 2.4) [84]. They observed that acid catalyzed coating composed of smaller silica particles (< 2 nm) forming highly dense silica particle network structure resulting in denser films. Whereas, base catalyzed coatings are composed of larger particle size with larger inter particle voids resulting in less porous SiO_2 film. Due to the presence of larger particles, the surface packing density decreases and the void space increases between the particles therefore the surface becomes rougher in base catalyzed coatings. In contrast, the surface is comparatively smooth in acid catalyzed coating due to smaller particle size resulting in higher particle density.

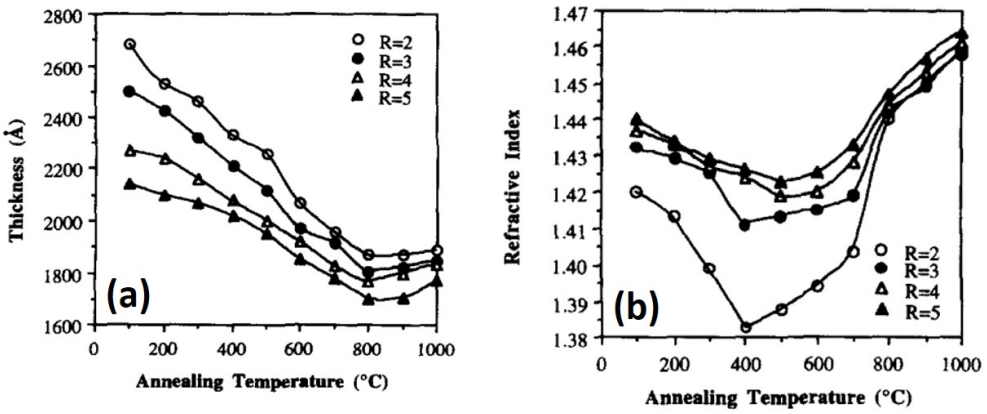

Figure 2.3: Variation of (a) film thickness and (b) refractive index with annealing temperature for different H_2O/Si molar ratio (R) [82].

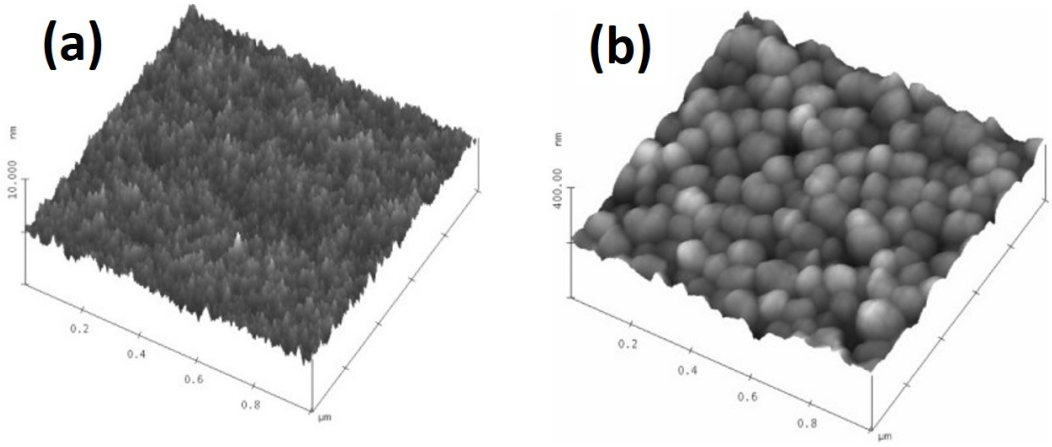

Figure 2.4: AFM images of (a) acid and (b) base catalyzed silica coatings on glass substrate. All the images are taken at 1 μm × 1 μm area [84].

The studies have focussed mainly on the physical properties of the deposited films. Nevertheless, Felix et al. studied the influence of solution processing parameters (molarity and aging time of sol-gel) on physical properties (thickness, refractive index, and porosity) as well as on electrical properties (leakage current density (J_{leak}, A cm^{-2}) and breakdown field (E_{BD}, V cm^{-1})) of spin-coated SiO_2 on a Si substrate [85]. They observed that the film thickness decreases with a decrease in the solution molarity (Fig. 2.5(a)). Also, beyond a certain solution molarity, the leakage current increases and the breakdown field decreases which was attributed to the formation of pinholes in the spin-coated film at low molarity (Fig. 2.5(b)). An increase in HNO_3 molarity led to an increase in leakage current densites and a decrease in refractive index and so increase in porosity of the SiO_2 film (Fig. 2.5(c)). Among electrical properties, D_{it} and Q_f of the dielectric film defines its passivation behavior. Weimer et al. were the first to report D_{it} of $\sim 10^{11}$ $cm^{-2}eV^{-1}$ and E_{BD} of 5 $MVcm^{-1}$ after 1000°C annealing of 200 - 300 nm thick sol-gel spin-coated oxide film [163]. Subsequently, Warren et al. reported an improved D_{it} of 7×10^{10} $cm^{-2}eV^{-1}$ after 900°C annealing of 190 - 210 nm film [159]. Meemongkolkiat et al. realized S_{eff} ~100 cm s^{-1} by spun-on SiO_2 on p-type Si [171].

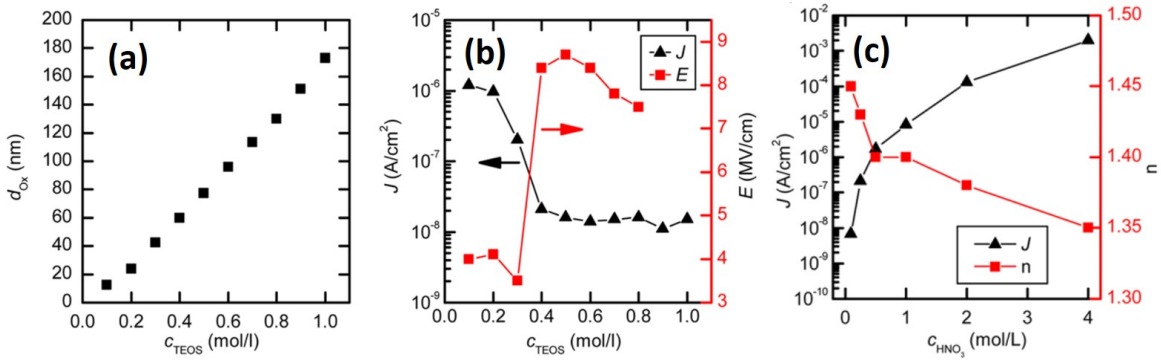

Figure 2.5: (a) Film thickness, (b) leakage current density and breakdown field strength for SiO_2 layers with different solution molarity. (c) Leakage current density at 1 MV/cm and refractive index for different SiO_2 layers with varying HNO_3 concentration between 0.1 and 4 mol l^{-1} [85].

Most of the study was based on spin and dip-coating sol-gel deposition techniques. Both spin- and dip-coating have the disadvantage of being limited to smaller planar substrates [86]. The spray deposition technique surpasses spin- and dip-coating at an industrial level due to its relative ease to coat industrial scale samples with high throughput [87, 88]. Recently, Esro et al. demonstrated solution-processed SiO_2 dielectric over large areas of Si, potassium bromide, and fused glass at 350°C using spray pyrolysis system [89]. They reported J_{leak} in the order of $\sim10^{-7}$ Acm^{-2} at 1 $MVcm^{-1}$ and E_{BD} of 5

$MVcm^{-1}$ for 130 nm thick film and implemented it in TFT. However, spray-deposition of SiO_2 film from a Si surface passivation perspective has not been studied yet.

2.3.2 SiO_2/SiN_x stack for enhanced passivation

SiN_x dielectric synthesized with PECVD is the standard ARC film in the commercial production of industrial Si solar cells [90, 91]. The success of SiN_x film is due to three main advantages it possesses. First, it acts as an excellent ARC as the refractive index can be tuned by tailoring the film composition. Second, a large amount of hydrogen is released during the PECVD deposition of SiN_x. The released hydrogen passivates the bulk as well as the surface defects during film deposition and high temperature firing step which is equivalent to annealing. Third, its passivation behavior is also due to both chemical and field effect, due to the presence of built in positive charge. The optimal antireflection property is obtained for SiN_x film with relatively high nitrogen content (N-rich), exhibiting refractive index ~ 2 when applied on the front of the Si solar cell. Whereas, a higher refractive index and higher extinction coefficient are shown for films with high Si content (Si-rich), leading to some light absorption in the film degrading the antireflection effect. The Si-rich film provides better chemical passivation. The N-rich film provides enhanced field effect passivation with fixed positive charge densities in the orders of 10^{12} cm^{-2} and moderately high D_{it} in the range of 10^{11}-10^{12} cm^{-2} eV^{-1} [92–94]. These interface traps at Si/SiN_x interface may increase the probability of the interface recombination. A low S_{eff} of 33 cm s^{-1} is demonstrated for n-type Si and 68 cm s^{-1} for p-type Si with N-rich SiN_x film with a refractive index of 2.03 [94]. Therefore, this field effect passivation is beneficial for n-type substrates and phosphorus diffused n^+ emitters in comparison to p-type Si surfaces because of positive charges in the SiN_x film.

From a passivation performance viewpoint, SiO_2 and N-rich SiN_x provide complimentary electrical characteristics. SiO_2 film has the lowest D_{it} providing chemical passivation, whereas SiN_x exhibits high positive Q_f providing effective field effect passivation. Therefore, the incorporation of intentional SiO_2 beneath the SiN_x enhances the effective passivation of the Si surface. $S_{eff} < 2.4$ cm s^{-1} was demonstrated on n-type Si passivated with thermal SiO_2/ PECVD SiN_x stack [95]. Chen et al. studied that the passivation of PECVD SiO_2 film degrades over time [11]. Also, the SiN_x film alone is relatively thermally unstable [96]. Therefore, the stack of PECVD SiO_2 and PECVD SiN_x, later used as a capping layer may solve both problems [11]. Also, the study showed that PECVD SiO_2 film alone is insufficient to passivate the Si surface. Dingemans et al. demonstrated relatively poor passivation with $S_{eff} < 500$ cm s^{-1} on as-deposited and moderately improved $S_{eff} < 100$ cm s^{-1} after Forming Gas Annealing (FGA) at 400°C [12]. It was

shown that the passivation could be improved by incorporating a capping layer over SiO_2 film. Dingemans et al. obtained a low $S_{eff} < 6$ cm s^{-1} on n-type and < 11 cm s^{-1} on p-type FZ Si using SiO_2/a-SiN_x stack deposited by PECVD at a substrate temperature of 300°C and further annealing at 400°C in N_2 ambient [13]. For NAOS oxide, Grant et al. revealed that the poor surface passivation of as deposited NAOS SiO_2 film could be improved by depositing a SiN_x capping layer [14]. PECVD SiN_x capping layer enhances the passivation of intermediate SiO_2 film due to the release of hydrogen during deposition and post-annealing [97]. Therefore, a stack of SiO_2/N-rich SiN_x films is often used in high efficiency Si solar cells.

2.4 Industrial silicon solar cells and their passivation

There has been a steady improvement in the bulk lifetime of Si wafers used for manufacturing of Si solar cells. In today's Si solar cells, recombination at the contacts and at the cell surfaces impose major limitations on performance. Every industrial Si solar cell design feature surface passivation technologies, and the same are reviewed in this section.

2.4.1 Aluminum Back Surface Field cell

The conventional industrial Si solar cells were manufactured on p-type Si wafers with screen printed full area Al layer which contacted the rear wafer surface (Fig. 2.6) [98]. Al doping at the rear forms a high-low p^+-p junction forming Back Surface Field (BSF), so the cell is called Al-BSF. Since the 1980s, the Al-BSF cell dominated the Si solar cell market due to its simple and robust production sequence [2].

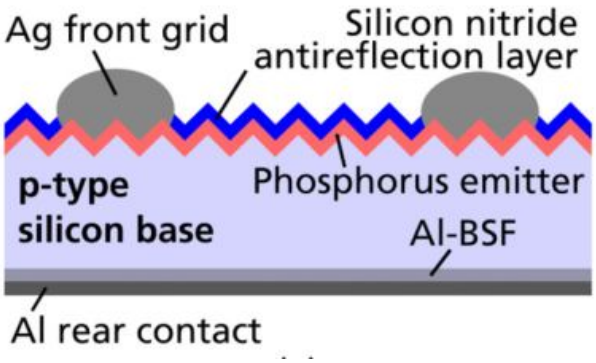

Figure 2.6: Cross-sectional schematic of Al-BSF cell [99].

The front has the heavily doped n^+ emitter formed by phosphorus oxychloride ($POCl_3$) diffusion [2]. The doping profile forming n^+-p junction provides field effect passivation. The passivation at the front surface is a measure of the recombination within

the emitter and at its surface. The S_{eff} at the front is defined by the emitter profile, especially the phosphorus dopant peak concentration at the surface (N_{surf}, cm^{-3}). It is reported that the SiO_2 combined with SiN_x capping has a higher passivation quality than SiN_x for varying emitter surface doping (Fig. 2.7) [99]. Also, it is obvious from Fig. 2.8 that the SiO_2/SiN_x stack provides emitter surface passivation as effective as the alnealed SiO_2 [96]. Here, the recombination current density at the passivated emitter ($J_{0e,pass}$, A cm^{-2}) describes the overall recombination activity of the emitter, and sheet resistance (R_{sheet}, Ω/sq) of the n^+ emitter characterizes the lateral conductivity for the electrons. The front passivation layer is also an optical layer. SiO_2 layer can be incorporated beneath SiN_x. However, the thickness of the SiN_x layer needs to be adjusted so as to keep the optical path $\sim \lambda/4$, a condition to be satisfied for destructive interference to decrease reflection due to optical films [101].

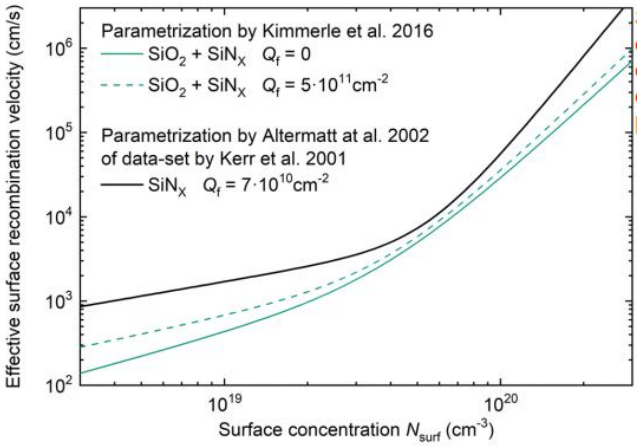

Figure 2.7: Effective surface recombination velocity (S_{eff}) dependency on N_{surf} for different passivation layers [99].

At the rear, p^+-p junction is used to reduce rear surface recombination losses. This high-low junction only marginally suppresses the recombination loss of photogenerated carriers at the Al rear contact [102, 103]. In addition, infrared light is partly absorbed by the full area Al layer reducing the reflection and subsequently absorption of infrared light in the bulk of solar cell [104]. Due to these two major loss mechanisms, industrial Al-BSF cell efficiency is limited to $\sim$ 20%. These losses were overcome in the advanced industrial cell architecture - PERC.

2.4.2 Passivated Emitter Rear Contact cell

PERC cell is an evolutionary adaptation of the conventional Al-BSF cell. BSF in the conventional cell is replaced by a dielectrically passivated rear by incorporating a dielec-

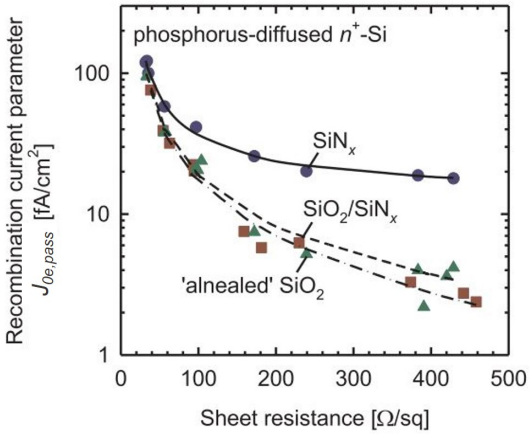

Figure 2.8: Emitter recombination current density $J_{0e,pass}$ as a function of the emitter sheet resistance for planar n^+ emitters passivated by PECVD SiN_x, alnealed thermal SiO_2, and SiO_2/SiN_x stacks [96].

tric layer between Si and metal at the rear, locally opened to provide extraction of charge. This leads to better rear surface performance in comparison with Al-BSF in terms of optical and electrical characteristics. The optical aspect demands higher internal reflection from the rear side. This imposes a condition on the dielectric refractive index to be less than the Si to follow Total Internal Reflection (TIR). It is further improved by depositing Al over the dielectric [52]. Electrical quality requires sophisticated surface passivation compared to full area Al-BSF. Currently, p-type wafer based PERC architecture is dominating the PV market and the average conversion efficiency of industrial PERC is over 22 % (Fig. 2.9) [2, 99].

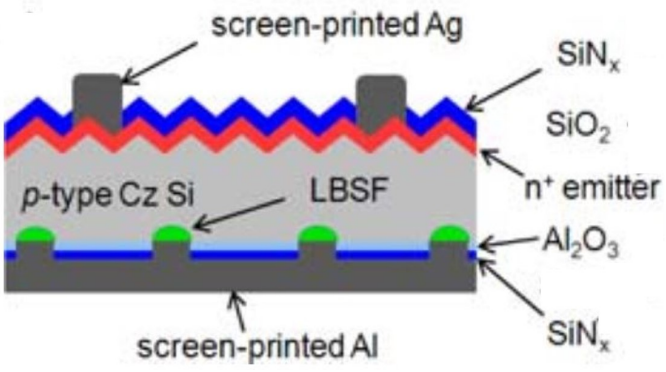

Figure 2.9: Schematic of the PERC solar cell [100].

The front of the PERC solar cell does not differ substantially from Al-BSF cell. SiO_2/SiN_x dielectric stack is used at the front due to its clear advantages as discussed in the previous section. However, the realization of the front side is not trivial in PERC.

The conversion efficiency in PERC is much more sensitive to front surface recombination in comparison to Al-BSF due to better rear passivation in the former. Phosphorus doped emitter region requires low recombination (mainly Auger and surface recombination), high lateral conductivity, and low metal/Si interface contact resistance. Therefore, strong constraints on the emitter doping profile design are imposed due to these requirements. Emitter R_{sheet} in the range of 90 - 100 Ω/sq is typical for industrial PERC cell processing [105–107].

Efforts are being made to further decrease the carrier recombination in the emitter and at the emitter/metal contact as this recombination is mainly limiting the conversion efficiency of the PERC and advanced solar cells. One approach is the reduction in N_{surf}. Fig. 2.10 shows that lower $J_{0e,pass}$, and so more effective emitter passivation can be obtained by reducing N_{surf}. $J_{0e,pass}$ slightly increases with an increasing junction depth due to an increase in Auger recombination within the emitter. However, $J_{0e,pass}$ has a higher dependency on emitter N_{surf} than junction depth. Auger recombination would be reduced substantially for lightly doped emitters, making the surface recombination component dominate the total $J_{0e,pass}$. Therefore, dielectric surface passivation improvement would become important in achieving low $J_{0e,pass}$ in the future. However, N_{surf} reduction negatively affects the metal recombination at the emitter/metal interface as lower N_{surf} would result in reduced shielding of minority carriers at the metal/Si interface. Selective emitter is implemented to overcome the metal/Si recombination issue [108, 109]. Selective emitter consists of two different profiles: one profile beneath the metal contact with higher N_{surf} maintaining low contact resistance by forming ohmic contact and reducing metal/Si recombination by shielding minority carriers from metal/Si interface via field effect passivation. The second profile is between the metal fingers with low N_{surf} decreasing the surface recombination.

PECVD SiN_x seemed to be the promising candidate for rear surface passivation in PERC due to its already successful application as a front n^+ emitter passivation and ARC [111]. However, later it was reported that SiN_x was unsuitable for rear passivation of p-type PERC. Due to high positive charges within SiN_x, an inversion layer induces in the p-type Si beneath the Si/SiN_x interface leading to a significant loss in the J_{sc}. This detrimental effect is identified as parasitic shunting [112]. Subsequently, it was demonstrated that the shunting effect due to SiN_x could be effectively reduced by increasing its refractive index, i.e. using Si-rich SiN_x film, which reduces the oxide charges in the film [113]. However, this high refractive index layer reduces the optical confinement by reducing the internal reflectance at the rear.

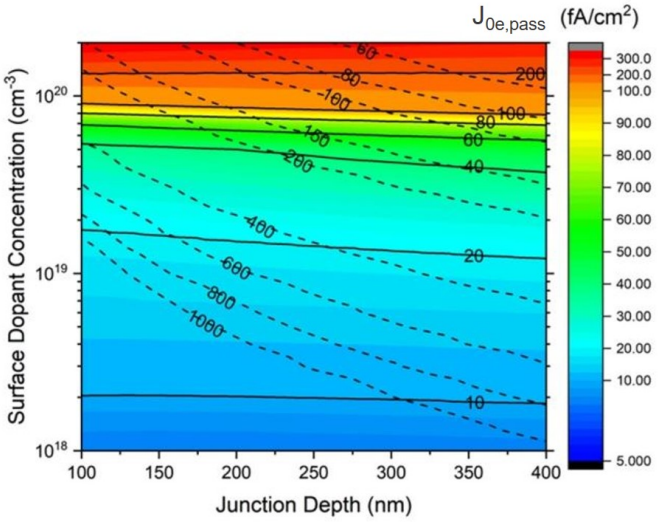

Figure 2.10: $J_{0e,pass}$ of phosphorus diffused textured Si surface with varying surface dopant concentrations and junction depths. The n^+ emitter surface is passivated with SiO_2/SiN_x. Contour lines for $J_{0e,pass}$ is indicated by the solid lines and sheet resistance is marked by the dash lines [110].

The main breakthrough in rear surface passivation was the development of Al_2O_3 film. Jaeger and Hezel were the first to demonstrate a reasonable level of passivation of Si solar cell with Al_2O_3 in 1985 [114]. After two decades, Agostinelli et al. and Hoex et al. demonstrated excellent Si surface passivation with Atomic Layer Deposition (ALD) Al_2O_3 film with S_{eff} below 10 cm s^{-1} on p-type Si [115, 116]. Due to the negative charge in the Al_2O_3 film, it induces an accumulation layer and not leading to parasitic shunting in p-type Si [117, 118]. Therefore, Al_2O_3 dielectric layer is used for passivating the p-type Si surface.

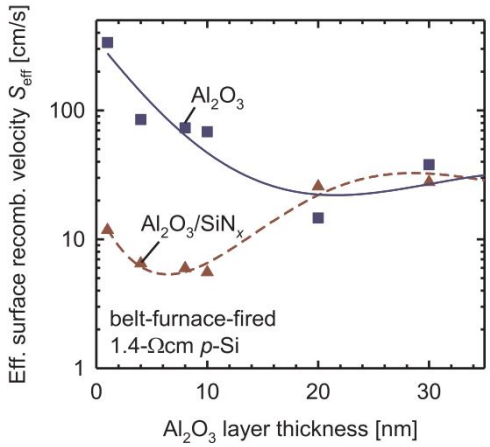

Figure 2.11: Effective surface recombination velocity S_{eff} variation with Al_2O_3 thickness. The Al_2O_3 and Al_2O_3/SiN_x stack is subjected to firing [120].

It is reported that Al_2O_3 film passivation is thermally unstable and degrades at high temperatures (750–850 °C) during the firing step, which is used in the industrial solar cells [119]. However, PECVD SiN_x capping improved the firing stability of the Al_2O_3 [119]. Veith et al. demonstrated that S_{eff} increased after firing an ALD Al_2O_3 single layer thinner than 20 nm, whereas Al_2O_3/SiN_x with 4-10 nm of Al_2O_3 exhibit $S_{eff} \sim 6$ cm s^{-1} after firing (Fig. 2.11) [120]. Similar to SiO_2, Al_2O_3 is unstable against Al paste and cannot withstand liquid Al. During firing, Al_2O_3 gets dissolved in metal destroying the passivation [10]. This chemical attack is survived by a low refractive index SiN_x capping layer protecting the passivation layer from the Al metallization [121]. The low refractive index SiN_x also increases the probability of TIR at the rear. This is possible by optimizing SiN_x thickness allowing constructive interference and maximizing the reflectance at the cell rear side [99]. Hence, Al_2O_3/SiN_x stack is appropriate for the passivation of the rear surface of screen-printed PERC solar cells and is an important discovery that led to the industrialization and mass production of PERC cells.

Although the rear of the PERC is dielectric passivated, there exists recombination at the local Si/metal interface. Industrial PERC cell with an efficiency of 22.20% has a high recombination current density at the rear metalized contact ($J_{0,rear,met}$, A cm^{-2}) of 660 fA cm^{-2} [110]. In addition, locally patterned contact geometry at the rear of PERC architecture results in 3D carrier transport adding to an internal resistance that lowers the FF. These drawbacks are mitigated in the next generation Si solar cell - TOPCon.

2.4.3 Tunnel Oxide Passivated Contact cell

It is demonstrated that TOPCon is the next technology to improve the efficiency of the industrial Si solar cells. TOPCon structure was first proposed by Feldmann et al. [66, 122] (Fig. 2.12). It forms a full area tunneling oxide rear contact, significantly suppressing carrier recombination and internal resistance as compared to PERC. The full area contact provides one directional path for the current flow and low process complexity as compared to PERC (Fig. 2.13).

Most of the TOPCon solar cells are fabricated on n-type Si due to its clear advantage of providing better passivation quality over its p-type counterpart and well established metallization by screen printing of silver (Ag) paste [124–126]. At the laboratory scale, a champion efficiency of 25.60% has been demonstrated on a 4 cm^2 area for TOPCon on n-type Si [127]. At the industrial level, LONGi Solar has reported a conversion efficiency of 25.20% over a larger area of 242.97 cm^2 for TOPCon architecture on n-type wafer [128]. Recently, researchers at Fraunhofer ISE have demonstrated that TOPCon cell fabricated on gallium doped Cz p-type wafers with boron diffused Front Surface Field (FSF) and

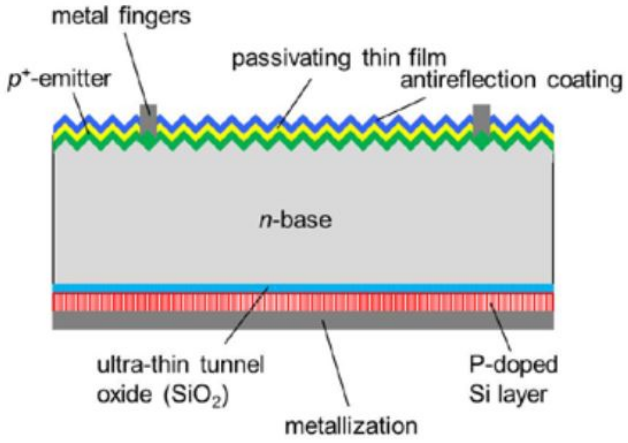

Figure 2.12: Schematic of TOPCon cell on n-type Si with n-type passivated contact at the rear and boron-doped emitter at the front [122].

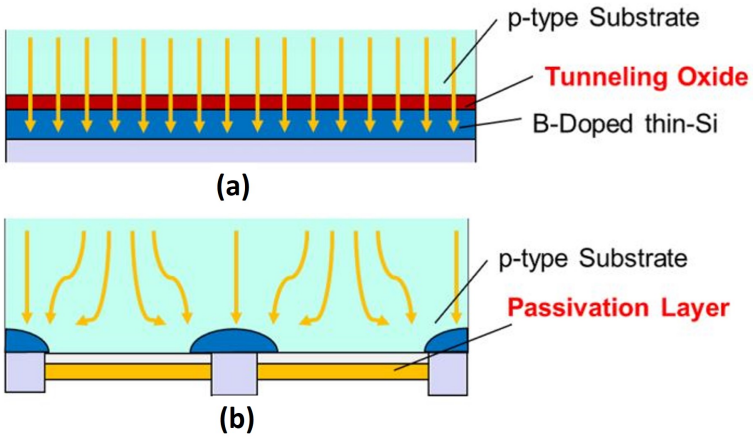

Figure 2.13: Carrier transport inside (a) TOPCon and (b) PERC cell on p-type Si [191].

phosphorus doped poly-Si at the rear (n-TOPCon (Fig. 2.14)) can exhibit 0.2% higher efficiency than the co-processed n-type counterpart without additional LID or Light and elevated Temperature-Induced Degradation (LeTID) [5]. On a similar note, Richter et al. have also demonstrated a record efficiency of 26% with n-TOPCon fabricated on FZ p-type Si over an area of 4.015 cm^2 [15]. They have also used an ultrathin oxide and phosphorus doped poly-Si at the rear with stringent process conditions [15]. These results suggest that TOPCon architecture on p-type wafers can be chosen over n-type wafers for industrial production due to its cost advantage. TOPCon architecture with front phosphorous diffused emitter and full area rear hole selective contact (p-TOPCon (Fig 2.14)) on p-type wafers would be the ideal successor of PERC technology. On this note, Yan et al. implemented the boron doped poly-Si contact over p-type Si wafer demonstrating a low $J_{0,rear,met}$ of 20 fA cm^{-2} and power conversion efficiency of 23% [129].

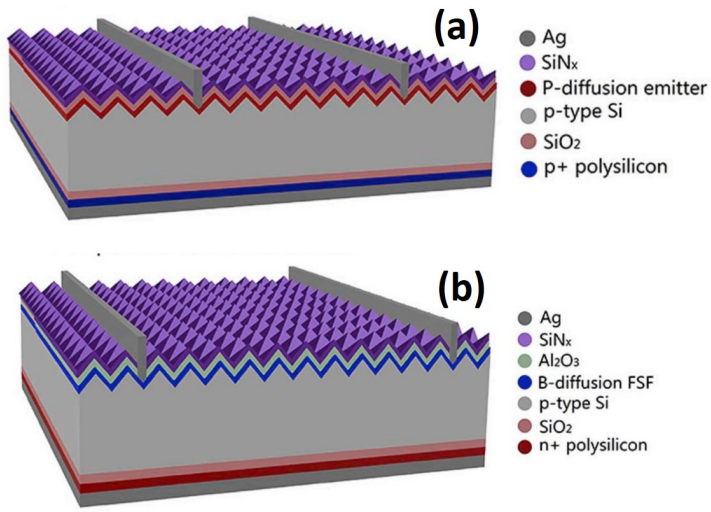

Figure 2.14: Schematic of (a) p-TOPCon and (b) n-TOPCon cells on p-type Si [130].

In n-TOPCon, which is TOPCon structure with rear emitter on p-type Si, front passivation would indicate passivation of p^+ FSF layer. This is achieved by depositing a stack of thin Al_2O_3 and SiN_x over it [131]. In p-TOPCon, which is TOPCon structure with front emitter on p-type Si, the front passivation indicates passivation of n^+ emitter having identical passivation conditions as discussed in section 2.4.2 for PERC.

At the rear of full area carrier selective architecture, ultra-thin oxide is used to passivate the Si interface and a highly doped poly-Si layer is responsible to achieve the carrier selectivity. In n-TOPCon, phosphorus doped poly-Si provides band bending assisting electrons to move toward the rear contact while blocking the holes. Similarly, boron-doped poly-Si in p-TOPCon allows holes to move toward the rear contact while preventing the electrons from reaching towards the rear contact. Therefore, high-quality ultra-thin oxide allows selective carrier transport via quantum tunneling and provides effective chemical passivation and highly doped poly-Si provides field-effect passivation and contact for the transportation of the carriers with a given selectivity [132–134]. Feldmann et al. have demonstrated an iV_{oc} of 720 mV for electron contact and comparatively lower iV_{oc} of 680 mV for hole contact on 1 Ω-cm FZ p-type Si [133].

Of the two TOPCon architectures on p-type Si, p-TOPCon is more industrially feasible as minor modification has to be done to the current PERC fabrication line. Therefore, prior to its industrial implementation and related fabrication challenges, there is a need to study the performance potential of p-TOPCon over PERC. Also, n-TOPCon has been reported to provide comparatively higher efficiency than p-TOPCon but with some stringent process conditions [15, 129]. Therefore, a study is required to learn the maximum achievable performance of p-TOPCon in comparison to n-TOPCOn for industrially rele-

vant parameters. A numerical analysis would be beneficial to provide an insight into the potential of the TOPCon architectures on p-type wafers for current and expected industrial relevant materials and process parameters.

2.5 Summary

This chapter begins with a detailed discussion of the recombination mechanisms in semiconductors. Thereafter, an overview of the Si surface passivation including the parameters for its characterization and technological methods for its improvements have been presented. A detailed review of SiO_2 as a Si passivating layer including techniques for its growth/deposition and the importance of SiN_x capping has been presented. In the end passivation layers used in industrial Si based solar cells have been discussed.

In literature, it has been shown that surface passivation marks the critical mechanism for advanced solar cell efficiency enhancement. Thermal SiO_2 has been found to be the best Si surface passivating material. However, the high thermal budget of the thermal oxidation process makes it unsuitable for the cost-effective Si solar industry. Therefore, low temperature deposition techniques including PECVD, NAOS, and UV-Ozone have been tried. However, these also have a few limitations. Therefore, in this thesis, an industrially viable sol-gel based spray-coating technique for the deposition of SiO_2 film has been explored for passivating Si surface. The passivation study has been extended to study the superiority of the p-TOPCOn over PERC. Further, the study is extended to present an in depth understanding of the performance potential of the TOPCon architectures on p-type Si.

Chapter 3

Experimental and Simulation Techniques Used in this Thesis

The basic principles and theory behind characterization and simulation techniques used in this thesis are discussed in this chapter. In addition, methods to extract different parameters from respective characterization are also discussed.

3.1 Metal oxide semiconductor capacitor measurement and analysis

The electrical properties of the dielectric film can be studied by characterizing the Metal Oxide Semiconductor (MOS) capacitor. Schematic of the MOS capacitor is shown in Fig. 3.1. MOS capacitor gives an insight into the electrical properties of the film and the nature of its interface with the Si. Two main parameters, D_{it} and Q_f, which define the Si surface passivation are calculated from MOS capacitor characterization. D_{it} is extracted from a combination of capacitance-voltage (C-V) and conductance-voltage (G-V) characteristics and Q_f from C-V characteristics. Dielectric breakdown analysis is performed using MOS capacitor current-voltage (I-V) characteristics.

3.1.1 Series resistance correction

The presence of parasitic series resistance which is dependent on the bulk resistivity and the contact resistance affects the high-frequency C-V characteristics [135]. Therefore, the measured capacitance and conductance values are series resistance corrected before proceeding with the parameter extraction from C-V and G-V characteristics. Series resistance (R_s) is calculated using the relation [7].

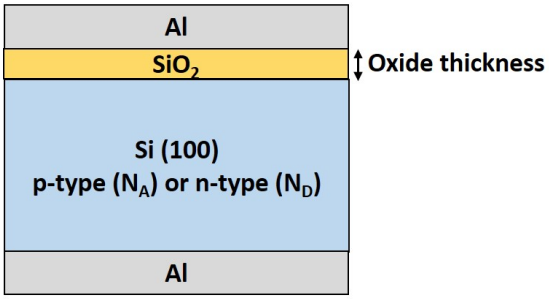

Figure 3.1: Schematic of the MOS capacitor used for analysis in this thesis.

$$R_s = \frac{G_{ma}}{G_{ma}^2 + w^2 C_{ma}^2} \tag{3.1}$$

where G_{ma} (S) and C_{ma} (F) are the measured conductance and capacitance in strong accumulation region. Corrected capacitance C_c (F) and corrected conductance G_c (S) curves are extracted from measured C-V and G-V curves using equations

$$C_c = \frac{(G_m^2 + w^2 C_m^2) C_m}{a^2 + w^2 C_m^2} \tag{3.2}$$

$$G_c = \frac{(G_m^2 + w^2 C_m^2) a}{a^2 + w^2 C_m^2} \tag{3.3}$$

where, a is given by

$$a = G_m - (G_m + w^2 C_m^2) R_s \tag{3.4}$$

C_m (F) and G_m (S) represent the measured capacitance and conductance, respectively. All the MOS capacitor parameters discussed in this thesis will be extracted from series resistance corrected C-V and G-V characteristics. Typical C-V and G-V characteristics of the MOS capacitor are shown in Fig. 3.2.

3.1.2 Interface state density

D_{it} is an important parameter used to monitor how good the semiconductor/insulator interface is. The smaller the D_{it}, the better the interface quality. Several techniques have been employed to determine D_{it}. These include capacitance methods such as Termans high frequency method [136], Berglund's low frequency method [137], Kuhn's quasistatic method [138], High Frequency - Low Frequency C-V technique [139]. However, conductance techniques are a more sensitive method for D_{it} extraction and give accurate and reliable results in comparison to capacitance techniques [20]. This is because of the direct relation of measured conductance to interface states. However, in the capacitance methods, interface-trap capacitance gives the interface state. This interface-trap capacitance is

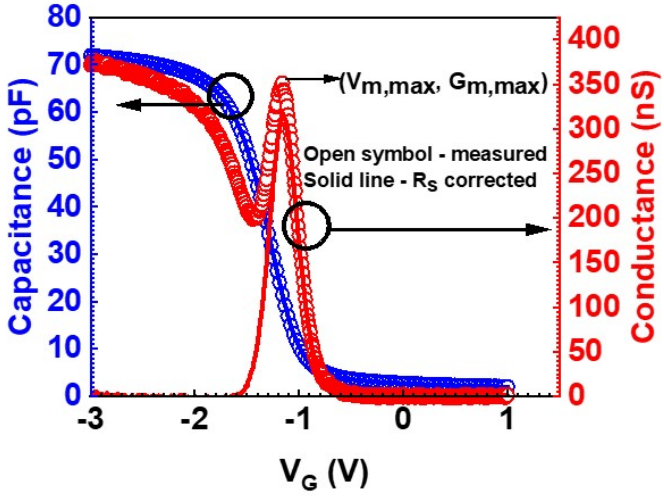

Figure 3.2: Typical C-V and G-V characteristics of the MOS capacitor with and without R_s correction.

to be extracted from the measured capacitance, which also consists of oxide capacitance and depletion-layer capacitance [20].

One of the most sensitive methods for the determination of D_{it} is the conductance method, proposed by Nicollian and Goetzberger in 1967 [140]. This method allows the measurement of D_{it} of 10^9 cm^{-2} eV^{-1} and lower. However, their methods require extensive data acquisition. Hill and Coleman [141] gave an approximation technique that gives results closer to the Nicollian-Goetzberger calculations. The advantage of the approximation is realized from the need for only one C-V and G-V plot. Using this method one needs only three measured values. These are the maximum conductance with its corresponding capacitance and the insulator capacitance. In this thesis, Hill's method is employed to extract D_{it} using the equation [141].

$$D_{it} = \frac{2}{qA} \frac{G_{m,max}/w}{\left(\frac{G_{m,max}}{wC_{ox}}\right)^2 + \left(1 - \frac{C_{m,max}}{C_{ox}}\right)^2} \tag{3.5}$$

where A (cm^2) is the MOS capacitor area, $G_{m,max}$ (S) is the maximum conductance (Fig. 3.2), $C_{m,max}$ (F) is the capacitance corresponding to maximum conductance, C_{ox} (F) is the oxide capacitance in the accumulation region of corrected C-V curve, and $\omega = 2\pi f$ is the measurement angular frequency (rad s^{-1}).

3.1.3 Oxide charge density

Extraction of Q_f from C-V characteristics needs information about substrate doping. Assuming that the Si substrate is uniformly doped, substrate doping concentration i.e.

acceptor doping concentration N_A for p-type Si and donor doping concentration, N_D of n-type Si substrate has been found from the minimum of high frequency Capacitance by iteratively solving the following transcendental equation

$$\frac{1}{C_{s,min}} = \frac{1}{C_{min}} - \frac{1}{C_{ox}} \tag{3.6}$$

where C_{min} (F) is the minimum capacitance of the measured and further series resistance corrected high-frequency C-V characteristics and $C_{s,min}$ (F) is the minimum semiconductor capacitance calculated as

$$C_{s,min} = \frac{\frac{\varepsilon_s}{\sqrt{2}L_D}}{\left(\frac{q(2\phi_b)}{kT} - 1\right)^{1/2}} \tag{3.7}$$

where L_D is the debye length (cm), ε_s is the dielectric permitivity of Si, and ϕ_b is the bulk potential (V) given by

$$L_D = \sqrt{\frac{kT\varepsilon_s}{q^2 N_{A/D}}} \tag{3.8}$$

$$\phi_b = \frac{kT}{q} ln \frac{N_{A/D}}{n_i} \tag{3.9}$$

Flat band voltage (V_{FB}, V) is the voltage where the bands are flat and there exists no semiconductor surface band bending i.e. $\psi_s = 0$ V. V_{FB} is extracted corresponding to the flatband capacitance (C_{FB}, F) calculated as

$$\frac{1}{C_{FB}} = \frac{1}{C_{ox}} + \frac{1}{C_{s,FB}} \tag{3.10}$$

where $C_{s,FB}$ is semiconductor flat band capacitance (F) given by

$$\frac{1}{C_{s,FB}} = \frac{\varepsilon_s}{L_D} \tag{3.11}$$

The ideal flat band voltage ($V_{FB,ideal}$, V) is the flat band voltage in the absence of Q_f and D_{it} (i.e. $D_{it} = Q_f = 0$) and equals metal/semiconductor work function difference (ϕ_{MS}, V). For a known gate metal workfunction and the substrate doping, ϕ_{MS} is calculated as

$$\phi_{MS} = \phi_M - (\chi + \frac{E_g}{2q} \pm \phi_b) \tag{3.12}$$

where '-' sign is for n-type and '+'sign is for p-type Si. ϕ_M for Al is 4.08 eV and E_g of Si is 1.12 eV.

The mid-gap voltage (V_{MG}, V) is the voltage when the semiconductor surface band bending equals the bulk potential i.e. $\psi_s = \phi_b$ and is the voltage corresponding to the mid-gap capacitance C_{MG} (F) calculated as

$$\frac{1}{C_{MG}} = \frac{1}{C_{ox}} + \frac{1}{C_{s,MG}} \tag{3.13}$$

where $C_{s,MG}$ is the semiconductor mid-gap capacitance (F) calculated as

$$\frac{1}{C_{s,MG}} = \frac{\varepsilon_s}{\sqrt{2}L_D} \frac{(1 - e^{\frac{-q\phi_b}{kT}})}{\left(e^{\frac{-q\phi_b}{kT}} + \frac{q\phi_b}{kT} - 1\right)^{\frac{1}{2}}} \tag{3.14}$$

The ideal mid-gap voltage $V_{MG,ideal}$ (V) is the mid-gap voltage when there exists no oxide charge density i.e. $Q_f = 0$ and is calculated as

$$\frac{1}{V_{MG,ideal}} = \phi_{MS} \mp \phi_b \mp \frac{\sqrt{2q\varepsilon_s N_{A/D}\phi_b}}{C_{ox}} \tag{3.15}$$

where '-' sign is for n-type and '+'sign is for p-type Si.

It is the difference between the ideal and actual mid-gap voltage that conveys the Q_f located at the Si/SiO_2 interface. In our work, the difference in the mid-gap voltage is used as a measuring quantity for Q_f instead of the difference in flat band voltage. This is because the latter is affected by the presence of interface states, whereas the former is assumed to be independent of them.

The equation governing the Q_f calculation is

$$Q_f = \frac{C_{ox}\Delta V_{MG}}{q} = \frac{C_{ox}(V_{MG,ideal} - V_{MG})}{q} \tag{3.16}$$

3.1.4 Dielectric breakdown field

Breakdown field and voltage are one of important parameters defining dielectric film. E_{BD} of the film is calculated as

$$E_{BD} = \frac{V_{BD} - V_{FB}}{EOT} \tag{3.17}$$

where V_{BD} is the breakdown voltage (V) at which the gate current increases abruptly when the MOS capacitor is biased in accumulation, EOT is the effective oxide thickness of the film (cm), and V_{FB} is the flatband voltage as calculated above. The EOT of the SiO_2 film equals the oxide optical thickness. In general, Weibull distribution is used for modeling breakdown voltages and fields of insulating systems and is used to estimate the voltage and hence the electric field associated with the probability of breakdown for a particular engineering design. Therefore, in this work, Weibull distribution is used for breakdown analysis. The expression for the cumulative density function for the two-parameter Weibull distribution for electric field breakdown analysis is given as [142].

$$F(E_{BD};\alpha,\beta) = 1 - exp\left\{ -\left(\frac{E_{BD}}{\alpha}\right)^{\beta} \right\} \tag{3.18}$$

where F is the probability of failure at a field $\leq$ to E_{BD}, α and β are scale and shape parameters respectively, and are positive quantities. Both α and β have their own significance. α represents the characteristic breakdown field, where $F = 0.632$ [143]. β provides a measure of how sensitive the specimen (MOS capacitor in this thesis) is to an increase in field. The higher the value of β, the more is the specimen sensitive to the increase in field i.e. the probability of breakdown increases sharply with increasing field [143]. It is also a measure of the range of failure fields [142]. The larger the value of β is, the smaller is the range of breakdown fields. A good, simple, approximation for the most likely probability of failure is found by Ross [144] as

$$F(i,n) = \frac{i - 0.44}{n + 0.25} \tag{3.19}$$

where n is the total number of specimens (measured MOS capacitors) and i is the specimen sequential number ($i = 1$ to n).

The two-parameter Weibull distribution equation can be reduced to a straight line equation

$$ln(-ln(1 - F)) = \beta \frac{log_{10}(E_{BD})}{log_{10}e} - \beta ln(\alpha) \tag{3.20}$$

It is plotted as $ln(-ln(1 - F))$ versus $log(E_{BD})$. The slope of above equation gives the value of β and the intercept gives α as

$$\beta = slope \times log_{10}e \tag{3.21}$$

$$\alpha = exp\left(\frac{intercept}{\beta}\right) \tag{3.22}$$

In this work, more than 20 MOS capacitors at different locations on the sample were characterized to perform breakdown analysis using Weibull distribution so as to investigate the breakdown uniformity of the film under study.

3.1.5 Energy level of interface state density in the silicon band gap

In Hill's technique, the peak of the G-V characteristic is used for D_{it} estimation. Hill's technique does not speculate the position of D_{it} in the bandgap. However, D_{it} position for a particular probed frequency can be located at an energy level corresponding to the gate voltage ($V_{m,max}$) at which the peak of G-V curve occurs ($G_{m,max}$) (Fig. 3.2) [145]. To find the exact E_T of D_{it} in the bandgap, surface potential, ψ_s, was obtained corresponding to $V_{m,max}$ by comparing the theoretical high-frequency C-ψ_s curve with experimental series resistance corrected C-V curve [7]. The analysis would be performed for p-type Si. However, the changes in the equations or in the analysis for n-type Si would be explicitly mentioned. The semiconductor capacitance-ψ_s (C_s-ψ_s) characteristic for p-type

is obtained by using the equation 3.23 for $\psi_s < 0$, i.e. for accumulation condition and equation 3.24 for $\psi_s > 0$, i.e. for depletion and inversion conditions. The total capacitance C_{tot} is obtained from a series combination of oxide capacitance and semiconductor capacitance as

$$C_s = \frac{\varepsilon_s}{\sqrt{2}L_D} \frac{\left(e^{\frac{-q\psi_s}{kT}} - 1\right)}{\left(e^{\frac{-q\psi_s}{kT}} + \frac{q\psi_s}{kT} - 1\right)^{\frac{1}{2}}} \qquad (\psi_s < 0); \tag{3.23}$$

$$C_s = \frac{\varepsilon_s}{\sqrt{2}L_D} \frac{\left(1 - e^{\frac{-q\psi_s}{kT}}\right)}{\left(e^{\frac{-q\psi_s}{kT}} + \frac{q\psi_s}{kT} - 1\right)^{\frac{1}{2}}} \qquad (\psi_s > 0); \tag{3.24}$$

$$\frac{1}{C_{tot}} = \frac{1}{C_{ox}} + \frac{1}{C_s} \tag{3.25}$$

where L_D is the majority carrier debye length (equation. 3.8) dependent on substrate doping, which is calculated iteratively as discussed above in section 3.1.3 and C_{ox} is the oxide capacitance of series resistance corrected experimental C-V characteristics. C_{tot}-ψ_s for n-type Si substrate is obtained by simply inverting the ψ_s axis. Further, ψ_s corresponding to the respective gate voltage (V_G) is obtained by mapping the capacitance of both C-V characteristics with generated C_{tot}-ψ_s characteristics. The energy level E_T corresponding to ψ_s at a particular gate voltage ($V_{m,max}$ in our case) is calculated as in the equation. 3.26 for p-type and equation 3.26 for n-type Si substrate.

$$\left(E_T - E_v\right)_{p-type} = \frac{E_g}{2q} + \phi_s - |\phi_b| \tag{3.26}$$

$$\left(E_c - E_T\right)_{n-type} = \frac{E_g}{2q} - \phi_s - |\phi_b| \tag{3.27}$$

where E_c-E_T is the location of D_{it} from the conduction band edge (E_c) for n-type Si, E_v-E_T is the location of D_{it} from the valence band edge (E_v) for p-type Si.

A detailed analysis incorporating the methodology described above has been performed on one of the MOS capacitors on p-type Si substrate. Fig. 3.3(a) and (b) show the series resistance corrected experimental C-V characteristic and generated C-ψ_s characteristics. Here, C_m represents the measured and series resistance corrected capacitance. ψ_s values mapped for gate voltages are shown in Fig. 3.3(c) and the energy level E_T calculated for each mapped ψ_s is shown Fig. 3.3(d).

In this thesis, Semiconductor Device Analyzer (Keysight, B1500A) is used for MOS capacitor characterization. To obtain C-V and G-V characteristics, the MOS capacitor was probed with an alternating current (AC) voltage signal superimposed over direct current (DC) voltage. To obtain I-V characteristics, DC voltage was applied such that the device

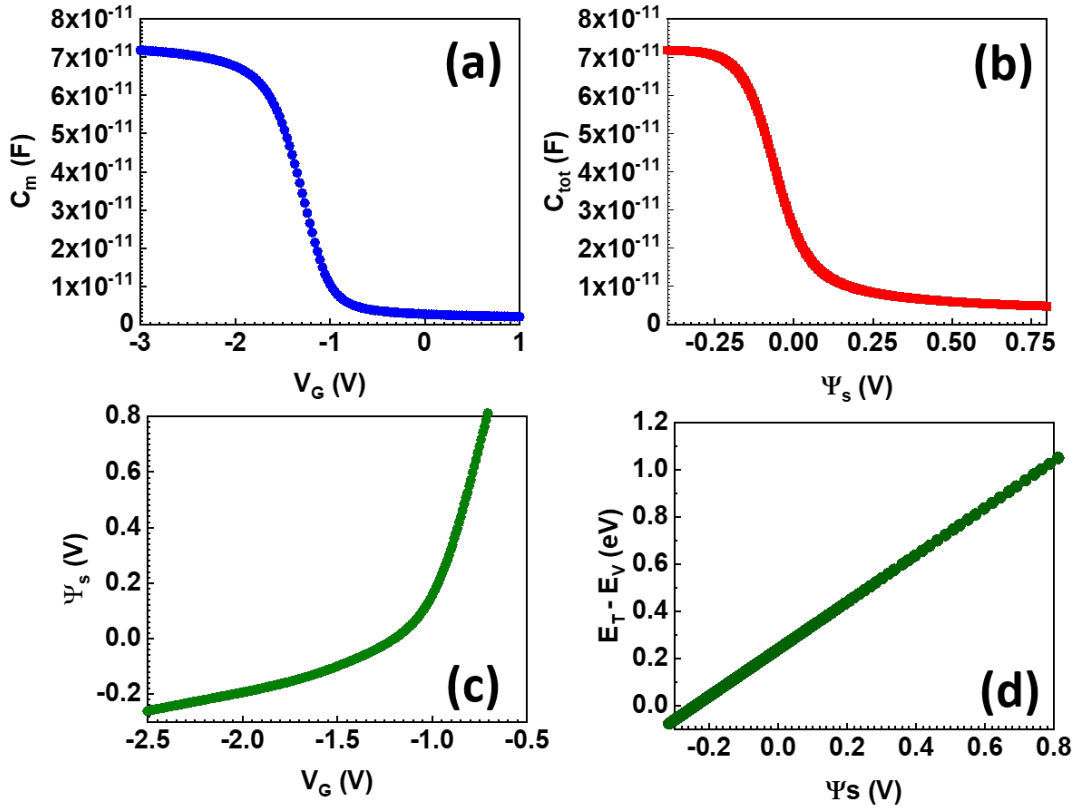

Figure 3.3: (a) Measured and R_s corrected C-V, (b) calculated C_{tot}-ψ_s, (c) ψ_s-V, and (d) (E_T-E_v)-ψ_s for a MOS capacitor on a p-type Si substrate.

works in accumulation depending on the substrate type i.e. positive for p-type and negative for n-type Si. The DC voltage was continuously increased till the point where the current increases abruptly so as to get the breakdown voltage.

3.2 Effective lifetime measurement

Lifetime measurement is used to investigate the passivation quality of the dielectric layer over the Si wafer. In this technique, the test sample is illuminated with light for a time instance leading to the generation of excess carriers, whose concentration decreases on turning off the light. This change in minority carrier concentration changes the conductance of the test sample. The conductance change is used to measure the effective lifetime. For $\tau_{eff} < 200\,\mu$s, measurement is performed in Quasi-Steady-State (QSS) mode, whereas transient mode is used for higher τ_{eff} values.

The S_{eff} of symmetrically passivated non-diffused Si wafer is extracted from the measured effective lifetime value at a specific excess minority carrier density using the equation 2.21 as discussed in section 2.2.1.1 given as

$$\frac{1}{\tau_{eff}} = \frac{1}{\tau_{bulk}} + \frac{2S_{eff}}{W} \tag{3.28}$$

In this thesis, lifetime tester from Sinton Instruments (WCT-120) is used to measure the τ_{eff} at a specific minority carrier density and 1 Sun iV_{oc} of the symmetrically passivated non-diffused polished Si and diffused textured Si wafers, respectively. The τ_b of the Si wafer is evaluated by immersing RCA and 2% HF treated Si wafer in a sealed plastic bag containg passivating solution, which is prepared by adding 1.5 gm of quinhydrone (Sigma-Aldrich, 97% HPLC grade) to 100 ml of methanol (MeOH; Merk).

3.3 Transmission Electron Microscopy

In general, optical microscope and electron microscope have a similar design, light and glass lenses are substituted by electrons and electromagnetic lenses, respectively in the latter case. Electron microscope has high resolving power in comparison with optical microscopes due to the small de Broglie electron wavelength. Transmission Electron Microscopy (TEM) is a technique in which an electron beam transmits through and interacts with the ultra-thin sample, forming an image that is focused and magnified on an imaging device. The electrons in the TEM instrument are generated by thermionic or field electron emission at the tip of the filament in the electron gun section. These emitted low energy electrons are accelerated by applying a high voltage (80 - 300 kV) between the cathode and anode. These high energies enable the electrons to penetrate through the specimen. The higher the voltage applied, the faster the electrons travel, and the smaller will be their wavelength, the better will be the resolution, and therefore, will obtain a detailed high resolution image of the specimen. These high energy electrons pass through a column consisting of a series of electromagnetic lenses, lens apertures, and specimens. TEM instrument generally has three stages of lens. The condenser lens is responsible for focussing the electrons into a beam of controlled convergence and diameter. The beam after transmitting through the sample encounters the objective lens which focuses the beam to form a primary image. The objective lens is followed by projector lens, which magnify and demagnify the image and projects it onto the imaging system. The image is monitored on a phosphorescent screen or a specially designed CCD camera. The apertures in these lens systems help in adjusting the beam intensity by removing the scattered electrons. These unscattered electrons form the bright-field image. TEM instrument is always maintained in a high vacuum. The high-vacuum of $\sim 10^{-7}$-10^{-10} mbar in the electron source prevents oxidation/burning of the heated filament and $\sim 10^{-5}$-10^{-7} mbar in the column reduces collision with the residual gas particles which might lead to resolution

degradation due to electron scattering. Therefore, it consists of a series of low and high vacuum pumps to maintain the desired vacuum in the specific areas of the instrument. The sample is mounted onto the sample holder which is inserted into the system. TEM sample stage design consists of airlocks that allow sample holder insertion into the vacuum with minimal pressure increase in other regions of the microscope.

In this work cross-sectional imaging has been carried out to study the thickness and nature of the thin film. The cross-sectional sample preparation is a time consuming task and involves a sequence of processes to finally give a thin electron transparent sample. These processes include ultrasonic disc cutting creating $\sim$ 3 mm diameter disk, dimpling, and ion-milling. Imaging of the film was carried out with JEOL JEM 2100F FEG-TEM operating at 200 kV.

3.4 X-ray Photoelectron Spectroscopy

X-ray Photoelectron Spectroscopy (XPS) is a surface analysis technique used for elemental and chemical state identification of the material surface. XPS works on the principle of the photoelectric effect. In this technique, the sample surface is excited with monoenergetic X-rays (1-2 KeV) causing the emission of photoelectrons from the surface. By measuring the kinetic energy ($E_{K.E.}$, eV) of the emitted electrons, binding energy ($E_{B.E.}$) is determined as

$$E_{B.E.} = h\nu - (E_{K.E.} - \phi_{sp}) \tag{3.29}$$

where $h\nu$ is the energy of incident X-rays, ϕ_{sp} is the spectrometer's work function (eV). The $E_{B.E.}$ (eV) of the emitted electron is influenced by its chemical state allowing chemical and elemental identification of the material. The photoelectrons mainly emit from 0.5 - 5 nm depth from the surface [135]. The photoelectrons excited deep into the sample do not exit the surface due to low mean free path of these electrons [135]. Depth profiling is used to reveal subsurface information wherein an ion beam is used to etch the layers of the surface. Layer thickness as well as respective quantified information can be obtained by combining the sequence of ion gun etch cycles with XPS analysis. A spectrum or set of spectra is recorded from the surface of the sample prior to removing material from the sample. Etching of the surface is performed by raster scanning the ion beam over a square or rectangular sample area. The ion beam is blanked after each etch cycle and another set of spectra is recorded. The sequence of etching the sample surface and acquisition of spectrum at respective depth is repeated until profiling is completed to the desired depth.

In this thesis, XPS has been used to examine the chemical composition and stoichiometry of the spray-coated SiO_2 film. The data in this thesis has been acquired from XPS (PHI 5000 Versa Probe-II) with Al Kα X-ray monochromatic source.

3.5 Current - voltage measurements of solar cells

Solar cell performance is assessed by the performance parameters extracted from the measured illuminated I-V characteristics. The I-V measurement is performed under standard test condition (STC), which includes (i) illumination spectra of the lamp matching with AM 1.5G spectra (ii) measurement temperature at 25°C, and (iii) illumination intensity of 1000 W-m^{-2} [146].

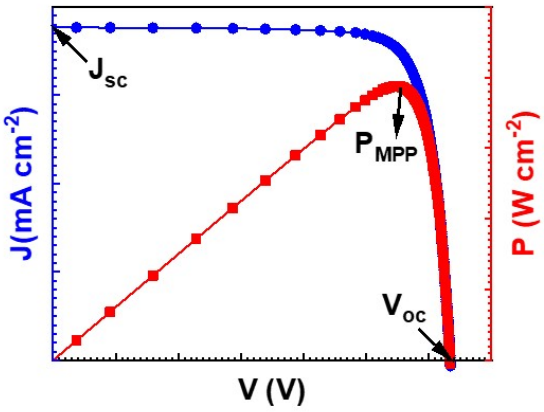

Figure 3.4: J-V and P-V characteristics of Si solar cell fabricated at NCPRE and measured using Abet Technologies AAA solar simulator.

The illuminated current density-voltage (J-V) and power-voltage (P-V) characteristics of a cell fabricated at NCPRE is shown in Fig. 3.4. Power at maximum power point (P_{MPP}, W cm^{-2}) is extracted along with the corresponding current density (J_{MPP}, A cm^{-2}) and voltage (V_{MPP}, mV). These parameters are used to calculate the FF and efficiency of the solar cell using the following equations:

$$FF = \frac{P_{MPP}}{J_{SC} \times V_{OC}} = \frac{J_{MPP} \times V_{MPP}}{J_{SC} \times V_{OC}} \tag{3.30}$$

$$Efficiency = \frac{P_{MPP}}{P_{in}} = \frac{J_{MPP} \times V_{MPP}}{P_{in}} \tag{3.31}$$

where P_{in} is the incident power on the solar cell under STC, which is equal to 1000 W-m^{-2}.

In this thesis, a class AAA solar simulator from Abet Technologies is used for dark and illuminated I-V characterization of the fabricated solar cells. In addition to the extraction of solar cell performance parameters (V_{oc}, J_{sc}, FF, and efficiency), R_s is determined using the Bowden method [147] and shunt resistance (R_{sh}) is calculated by considering the inverse slope of dark I-V in -50 mV to 50 mV range.

3.6 Quantum Efficiency measurements

Quantum Efficiency (QE) measurement is crucial to analyze the wavelength dependent behavior of solar cells because it gives an insight into their optical and recombination losses. QE is the ratio of the number of electrons collected from the solar cell to the number of photons incident on the solar cell. QE is classified as External QE (EQE) and Internal QE (IQE) depending on the consideration of optical losses for its calculation. All the photons incident on the solar cell are considered in EQE and therefore include the effect of optical losses such as transmission and reflection. Whereas only the photons entering the solar cell are considered in IQE, and therefore it excludes the optical losses. IQE and EQE are related as

$$IQE = \frac{EQE}{(1 - R - T)} \tag{3.32}$$

where R and T represent the reflection and transmission loss. The transmission loss is zero for the solar cell considered in this work as the rear is full area metal printed. Therefore, the eq. 3.32 reduces to

$$IQE = \frac{EQE}{(1 - R)} \tag{3.33}$$

In QE measurement, xenon/halogen dual light source combined with a monochromator is used for spot illumination in a range of wavelengths over the solar cell contacted in short circuit condition. The measured wavelength dependent short circuit current (I_{sc}) is used to determine the corresponding EQE governed by the equation:

$$EQE = \frac{I_{sc} \times hc/\lambda}{P \times q} \tag{3.34}$$

where h is the Planck's constant (J s), c is the velocity of light (m s^{-1}), λ is the wavelength of incident laser light (m), and P is the incident laser power (W).

In this thesis, QE measurement is performed with PVE-300 tool from Bentham instruments over an illumination spot of 1 mm × 5 mm in the wavelength range from 300 nm to 1200 nm. IQE of an ideal Si solar cell is unity over 300 nm - 1200 nm range. Representative QE characteristics including IQE and reflectance of Si solar cell fabricated at

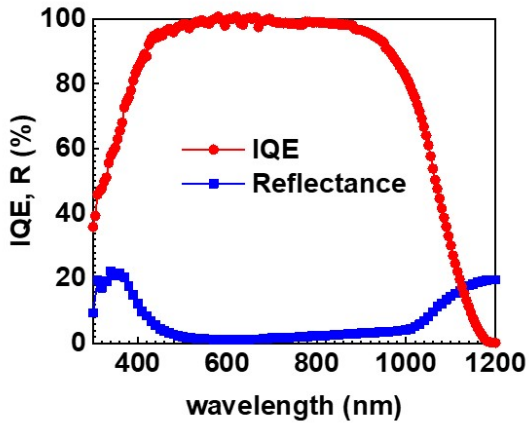

Figure 3.5: IQE and reflectance curve as a function of wavelength of a Si solar cell fabricated at NCPRE and measured using PVE-300 tool from Bentham instrument.

NCPRE are shown in Fig. 3.5. Decrease in IQE at lower wavelengths (300 nm - 500 nm) and longer wavelengths (900 nm - 1200 nm) is due to recombination at the front and rear side of the solar cell, respectively. The bulk quality of the cell is represented by IQE in the mid wavelength range. Therefore, passivation quality along the cell top to the bottom surface can be analyzed with wavelength dependent IQE characteristics. IQE and reflectance together is a representative of the recombination and optical properties of the solar cell.

3.7 Photoluminescence imaging

Photoluminescence (PL) imaging is a fast, contactless, and spatially resolved technique for the characterization of large area Si wafers and solar cells. In Si solar cells, the optical absorption into the Si leads to the generation of excess electron and hole pairs. These generated carriers undergo radiative or non-radiative recombination. Radiative recombination results in photon emission and the photon energy is equal to the bandgap of Si. This phenomenon is known as photoluminescence. Radiative recombination is less in comparison to non-radiative recombination in Si due to its indirect bandgap. This minimal amount of photoluminescence is detected and is further used for material analysis. The luminescence efficiency is given by:

$$\eta = \frac{U_{rad}}{U_{rad} + U_{nonrad}} \tag{3.35}$$

$$U_{rad} = \frac{\Delta n}{\tau_{rad}} \tag{3.36}$$

$$U_{nonrad} = \frac{\Delta n}{\tau_{nonrad}} \tag{3.37}$$

$$\frac{1}{\tau_{eff}} = \frac{1}{\tau_{rad}} + \frac{1}{\tau_{nonrad}} \tag{3.38}$$

where U_{rad} and U_{nonrad} represent radiative and non-radiative recombination rates ($cm^{-3}s^{-1}$), respectively, Δn is the excess carrier concentration (cm^{-3}), τ_{eff}, τ_{rad}, τ_{nonrad} are the effective, radiative, and non-radiative carrier lifetime (s), respectively. PL imaging gives an insight into the spatial variation of τ_{eff}. The PL image comprises of bright and dark pixels. The brighter pixels are indicative of less non-radiative recombination loss showing higher PL intensity/counts whereas dark pixels are indicative of higher non-radiative recombination showing lower PL intensity/counts.

In this thesis, Lumisolar system from Greateyes is used to capture PL images. The system has two arrays of 660 nm wavelength LEDs as an illumination source. The luminescence signal from the illuminated sample is filtered by 960 nm high pass filter to receive the emission signal near the Si bandgap.

3.8 Scanning Electron Microscopy

Unlike TEM, in which the electrons that transmit through ultra-thin sample are detected, Scanning Electron Microscopy (SEM) makes use of the electrons that are knocked or reflected from the near surface region of the sample for creating an image. In SEM, a focussed beam of electrons is used to produce a detailed and magnified image of an object by scanning its surface.

The electrons are generated at the top of the microscope's column by the electron source/gun. The electron beam is accelerated towards the sample by an anode placed inside the column close to the electron source with a potential of 0.2- 30 kV. SEM systems are broadly classified into two categories based on the principle of electron emission (thermionic heating and field emission) from the gun: Thermal and Field Emission. Of these two, Field Emission Scanning Electron Microscopy (FESEM) offers a higher resolution and would be used in this work. During the electron beam travel, it passes through a series of electromagnetic lenses, that control the path of electrons i.e. condenses and focusses the electrons using Lorentz force. These lenses consist of coils of wires inside the metal pole pieces. The current passing through the coils generates the magnetic field. The electron path is controlled by the electromagnetic lenses by adjusting the applied current to them as electrons are sensitive to the magnetic fields. There are two types of lenses: Condensor and Objective lenses. Condensor lens is the first lens electrons meet

while traveling toward the sample. It converges the beam prior to reopening the electron beam cone and is further converged again by the objective lens before striking the sample. The size of the beam which describes the resolution is defined by the condensor lens. Objective lens plays a role in focusing the electron beam onto the sample. The lens system of the SEM also has scanning coils which allow the beam to raster scan onto the sample. The interaction of the sample with the electron beam generates different types of electrons or irradiations. In SEM, two types of electrons namely backscattered (BSE) and secondary electrons (SE) are used. BSEs are the primary electron beam that is reflected back after elastic interaction between the sample and the beam. These are high energy electrons that are scattered out of the sample by losing a small amount of energy. These interact strongly with the sample and originate from a few microns deep below the sample. These usually provide compositional contrast information. SE are the result of inelastic interaction between the sample and the electron beam and originates from the sample atoms. These arise from within a few nanometers of the sample surface and have comparatively less energy than the BSE. SE are highly sensitive to the surface structure of the sample and provides topographic information. Therefore, BSE originates from deeper regions of the sample, whereas SE from the surface regions. Hence, both BSE and SE carry different sets of information. BSE images are highly sensitive to atomic numbers: the higher the atomic number, the larger the incident electron beam scattering, and the brighter the material looks in the SEM image. Whereas, SE imaging provides detailed surface information and image resolution independent of the material. There are separate detectors to detect BSEs and SEs. To maximize the BSE collection, BSE detectors are placed above the sample to maximize the collection of BSE. Whereas, SE detectors are placed at an angle in the vicinity of the sample.

In this work, FESEM (Zeiss Ultra 55) is used to study the spray-coated SiO_2 film coverage over the pyramidal structure.

3.9 Spectroscopic Ellipsometry

Ellipsometry is a non-contact and non-destructive optical method for determining the thickness and complex refractive index of a thin film. This method is based on the principle of polarization state change of incident polarized electromagnetic radiation interacting with the material surfaces. There exists a change in the polarization state of the reflected light from the interface or surface of the samples with respect to the incident light. This change in polarization is characteristic of the sample or material under investigation. This state change of light upon reflection is detected and interpreted. This measured data is

expressed as two ellipsometric parameters Ψ and Δ. Ψ describes the change in the relative amplitude ratio and phase difference of the parallel and perpendicular components of the electronic field vector of the light with respect to the incidence plane. Information related to the sample's optical properties is contained in these two parameters. Ψ and Δ are measured as a function of wavelength in the case of spectroscopic ellipsometry.

Being an indirect measurement technique, the desired output quantities (thickness and refractive index) are not calculated directly from the measured quantities (Ψ and Δ). Therefore, evaluation is performed by assuming properties (film layers, layer thickness, and optical functions of layer) of the investigated sample to determine theoretical ellipsometric Ψ and Δ values using layer specific models. The theoretical (modeled) and measured results are fitted. The agreement between the two data sets is measured in terms of mean square error for a particular set of model parameters. These model parameter variables of the models are adjusted by applying the regression algorithm to minimize the error.

In this work, Ψ and Δ plots at an incidence angle of 75° were measured using spectroscopic ellipsometer (Semilab, SE-2000). The Cauchy dispersion model was used to fit the measured and calculated plots to extract the thickness and refractive index of the film.

3.10 Atomic Force Microscopy

In Atomic Force Microscopy (AFM), force acting between the fine tip and the sample is measured to obtain the topography image of the surface of the sample [148]. A tip fixed to the free end of the cantilever is brought near the sample surface. The interaction of the tip and the sample results in the force depending on the distance between them. The force is repulsive at close contact and is attractive at larger separation causing positive and negative bending of the cantilever. This bending is detected by a laser that reflects from the cantilever back. The force (F) on the cantilever is related to its tip deflection (Δ) by Hook's law as $F = k\Delta x$, where k indicates the spring constant of the cantilever. AFM has two modes of operation depending on the interaction forces namely, contact and non-contact. In contact mode, the cantilever deflection is maintained constant. In non-contact mode, the cantilever is oscillated near or at its resonance frequency maintaining a constant cantilever oscillation amplitude.

In this work, Asylum/ Oxford Instruments, MFP3D was used in non contact mode to study the morphology and surface roughness of the films/structures over the Si surface.

3.11 Contact angle measurement

The contact angle established by a liquid on a solid surface quantifies the wettability of a solid by that liquid. Geometrically, it is defined as the angle formed by a liquid at the three-phase boundary where a liquid and gas meet a solid surface. Contact angles can be static and dynamic. The contact angle measured when the three phase boundary condition is stable and not moving is the static contact angle. The contact angle measured when the three phase boundary condition is not stable and is moving is the dynamic contact angle. The static angle provides a quantitative and quick wettability measurement. In this work, a static contact angle is used for the analysis. Static angle is measured using optical tensiometers. A dispenser is used to dispense the liquid over the solid surface. The image of the droplet sitting over the solid surface is captured and further analyzed with the software. The baseline i.e. the contact between the solid and droplet and droplet outline is detected by evaluating the grey scale values of the captured image. The left and right contact angles are determined by applying tangents at the intersection of the baseline and the outline of the droplet.

In this work, contact angle system (Data Physics, OCA 15) is used to measure the static contact angle using 2 μl of the test liquid.

3.12 Simulation of silicon solar sells

In this thesis, TCAD is used for the simulation study of Si solar cells. TCAD is an Electronic Design Automation (EDA) tool. It solves different fundamental physics equations and models to simulate a semiconductor device. TCAD simulation has better predictive accuracy due to its deep physical approach. This makes it possible to substitute TCAD simulations for the time consuming and costly test wafer runs during the initial stage of semiconductor device or technology development. TCAD is used by the semiconductor industry to optimize and analyze yield, study the impact of process and related parameter variations, and further optimize the device process flow. This assists the semiconductor industry to cut down the time and cost in the research and development phase. TCAD simulations play a crucial role in providing insights into semiconductor device behavior. This could assist in the modeling of the physical phenomenon or could lead to new device concepts.

Sentaurus TCAD is widely used in Si solar cell simulation. Initially, a unit structure of the solar cell is created in Sentaurus Structure Editor (SDE). The unit cell geometry and dimensions, doping profiles of the emitter, selective emitter, and BSF doping profiles, substrate doping, dielectric ARC and passivation layers, and the contact materials

are specified while creating the structure for simulation under investigation. The unit cell is further divided into meshes, i.e. the cell domain is discretized into non-overlapping subregions or elements connected by nodes within the domain. The electrical or opto-electrical behavior of the cell is simulated using Sentaurus Device (Sdevice) tool. Based on the physical device equation governing the carrier distribution and conduction mechanisms, the terminal voltages, currents, and charges are computed [149, 150]. The Poisson equation is used to solve electric potential in all the meshes. The electron quasi-fermi level is calculated by plugging this electric potential into the electron continuity equation. The hole quasi fermi level is found by plugging the calculated electron quasi fermi level and electric potential together into the hole continuity equation. This process is continued till the desired level of convergence is achieved. Further, Sentaurus Visual (Svisual) is used to visualize the device geometry, a particular region, field, and doping profile. In addition, it is used to view the output characteristics of the Sdevice simulations.

In our work, Sentaurus TCAD is used to simulate Al-BSF, PERC, TOPCon Si solar cell architecture. The codes used in the simulations are included in Appendix 9.

Chapter 4

Effect of Solvent on Sol-gel Spray-coated SiO_2 Thin Film Properties

4.1 Motivation

As discussed in chapter 2, thermally grown SiO_2 is known for its superior passivation over the Si surface. However, these thermal oxides are grown at high temperatures (> 900°C) which increases the thermal budget and deteriorates the minority carrier bulk lifetime [9]. Therefore, there arises a need for alternate low temperature SiO_2 deposition techniques to cater to various applications where the presently used techniques are not viable or expensive. In this regard, alternative low-temperature deposition techniques such as PECVD and NAOS were explored to replace thermal oxides [65, 151]. However, inefficiency of the SiO_2 to provide excellent passivation for moderate resistivity Si at an optimum annealing condition in case of PECVD [13], and oxide thickness limitation to ~1.5 nm and very high D_{it} in case of NAOS [67] demands an alternative low-temperature SiO_2 deposition technique.

This chapter reports experimental work on the development of SiO_2 film using industrially feasible solution based spray-coating technique. The sol-gel SiO_2 film properties have a heavy dependence on the solution content (precursor, H_2O, and catalyst) as discussed in section 2.3.1.4. The effect of solution parameters like precursor, molarity, H_2O, and catalyst on SiO_2 film properties have been studied by numerous groups [79, 80, 82, 84, 152, 154], as discussed in section 2.3.1.4. Unlike these parameters, the impact of solvent on the film properties has not been studied rigorously. Vorotilov et al. gave some details about the influence of solvents on the thickness and refractive index of the SiO_2 film deposited on the Si substrate by spin-coating [153]. However, the effect

of the solvents on the physical as well as passivation (D_{it} and Q_f) properties of the SiO_2 films deposited via sol-gel spray-coating technique has not been studied.

In this chapter, we report the behavior of Si surfaces due to different surface modification treatments and studied the wetting behavior of different solvents on varying Si surface conditions. The SiO_2 film is then deposited via spray-coating deposition method. Further, we investigated the effect of solvent on the film properties including thickness, density, roughness, D_{it}, and Q_f.

4.2 Experimental details

In this work, experiments were performed on Si wafers ((100), 4-7 Ωcm). Both n- and p-type wafers were used. n-type Si wafers were used for MOS capacitor fabrication and p-type Si wafers for all other set of experiments. All Si wafers were subjected to RCA cleaning [155]. Four different solvents: ethanol (absolute alcohol, 99.5%), isopropanol (J.T. Baker CMOS grade), 2-methoxyethanol (Sigma Aldrich, for HPLC, ≥99.9%), and 1-butanol (Sigma Aldrich, 99.9%), were used for a comparative study.

4.2.1 Contact angle measurement

Water contact angle was measured on three different sets of Si wafers: RCA cleaned with 2% HF dip (Set-A), RCA cleaned without 2% HF dip (Set-B), and RCA cleaned with 2% HF dip and UV-Ozone treatment (Set-C). 2% HF dip after RCA was performed for 30 sec. UV-Ozone treatment was carried out in a UV-Ozone chamber (Holmarc Mechatronics Pvt. Ltd, HO-TH-UV02) in O_2 ambient for 10 min. Contact angle measurements with solvents as test liquids were also performed on Set-A and Set-C. The contact angle was measured using 2 μl of the test liquid on a contact angle system (Data Physics, OCA 15). The contact angles reported in this work are the averages of values measured at three different locations on the sample.

4.2.2 Sol-gel solution preparation

The sol-gel solution was prepared with tetraethyl orthosilicate (TEOS) (Sigma-Aldrich, 99.999% trace metal basis) as a precursor, DI H_2O, HNO_3 (J.T. Baker, CMOS grade) as a catalyst, and each of ethanol (absolute alcohol, 99.5%), isopropanol (J.T. Baker, CMOS grade), 2-methoxyethanol (Sigma Aldrich, for HPLC, ≥ 99.9%), and 1-butanol (Sigma Aldrich, 99.9%) as a solvent. TEOS was dissolved in each of the solvents and the mixture was sonicated for 30 min using magnetic stirrer (Torrey Pines Scientific.inc, HS50) at a frequency of 150 Hz. Solution with different molarity was prepared

by varying the TEOS concentration. DI H_2O and HNO_3 were gently added to the mixture and the solution was further sonicated for 1.5 hours. The H_2O:TEOS molar ratio and HNO_3 molarity were fixed at 6:1 and 0.1 mol l^{-1}, respectively. The sonicated solution was kept for aging at room temperature for approximately 10 hours. In this work, the solution was prepared with 18 ml of each solvent. 0.02 mol l^{-1} of solution contains 80 μl of TEOS, 39 μl of DI H_2O, and 113 μl of HNO_3. For varying solution molarity TEOS quantity and subsequently, DI H_2O quantity was varied so as to have a constant H_2O:TEOS molar ratio of 6, however solvent and HNO_3 volume were kept fixed so as to have constant HNO_3 molarity of 0.1 mol l^{-1}. For 0.06 mol l^{-1} and 0.08 mol l^{-1} solution, TEOS of 2410 μl and 3215 μl and DI H_2O of 1555 μl, respectively were used.

4.2.3 Solution spraying, film formation and characterization

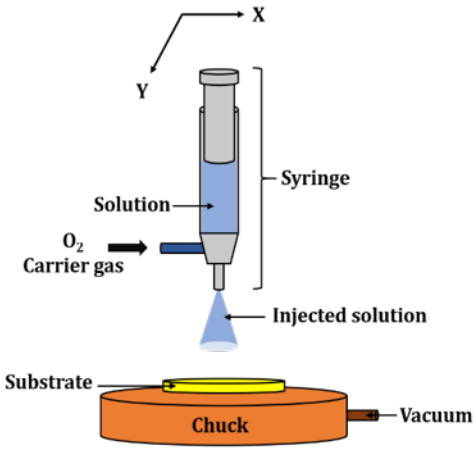

Figure 4.1: Schematic of the spray-coater tool used in this thesis work.

The behavior of the solution prepared with these four solvents was analyzed by spraying the final solution over Set-A and Set-C Si substrates. A custom-designed spray-coater tool (Holmarc Mechatronics Pvt. Ltd) was used to spray the solution over the Si substrate. The schematic of the spray-coater tool is shown in Fig. 4.1. It consists of a glass syringe of 20 ml capacity coupled to a moving-head held above a vacuum connected chuck over which the wafer is placed. The syringe was raster scanned over the wafer with a speed of 250 mm s^{-1} in the x-direction and 3 mm s^{-1} in the y-direction. The spray process parameters including solution flow rate, carrier gas flow rate, and substrate to nozzle distance affect the film thickness and uniformity. It was observed that the film thickness and roughness increase with increasing solution flow rate, decreasing carrier gas flow rate, and decreasing the syringe to nozzle distance. Therefore these parameters were optimized to obtain a uniform film. The solution with a flow rate of 300 μl min^{-1}

was sprayed with O_2 as a carrier gas with a flow rate of 0.8 bar onto the substrate placed on the chuck at room temperature. The syringe nozzle was fixed at a distance of 8 cm from the substrate. These solution sprayed wafers were subsequently dried at 150°C in air ambient. After drying, the morphology of the films/structures over the Si surface was analyzed using AFM (Asylum/ Oxford Instruments, MFP3D) in non-contact mode. The thickness and refractive index of the films were measured at an incident angle of 75° using a spectroscopic ellipsometer (Semilab, SE-2000). The refractive index was extracted at a wavelength of 632.8 nm.

4.2.4 MOS capacitor fabrication and characterization

MOS capacitors were fabricated for the Set-C on n-type Si wafers. The solution prepared using a specific solvent was sprayed on UV-Ozone treated Si wafers and then dried at 150°C. These samples were subjected to Post Deposition Annealing (PDA) at 650°C for 30 min in O_2 ambient in a quartz furnace. Subsequently, front metal contact was created over the film by thermally evaporating Al dots using a metal shadow mask in 4-Target E-Beam Evaporator System (HHV 15F6T). Rear contact was formed by blanket Al deposition. These samples were subjected to PMA in FG ambient (FG; 4% H_2 and 96% N_2) at 450°C for 30 min in a quartz furnace. After PMA, MOS capacitors were characterized using Semiconductor Device Analyzer (Keysight, B1500A) to obtain C-V and G-V characteristics.

4.3 Results and discussions

4.3.1 Nature of silicon surface with varying surface conditioning

Before proceeding with the film deposition and its study, the nature of the Si surface (hydrophilic or hydrophobic) was confirmed by water contact angle measurement on Set-A, Set-B, and Set-C. Among the three surface treatments, Set-A gives a weakly hydrophobic surface [156] with a contact angle of 86.1°. Set-B and Set-C give superhydrophilic Si surface [156] with a contact angle of 0°. For Si subjected to RCA without further 2% HF treatment, i.e. for Set-B, native oxide grows over it as a result of RCA-2 process [155]. For Set-C, the 2% HF treated wafers were kept in a UV-Ozone chamber that features UV lamps emitting photons at 185 nm and 254 nm wavelengths. UV-Ozone exposure removes residual organic contamination from the Si surface and improves its wettability [157], and results in the growth of an ultrathin SiO_x on the surface [75]. This suggests that the presence of native oxide after RCA cleaning or organic free surface with

few nm of oxide grown after UV-Ozone exposure makes the Si surface superhydrophilic. In this work, UV-Ozone exposure will be used to make the Si surface superhydrophilic due to its capability to give a better Si surface passivation [74]. In this report, hydrophobic and hydrophilic Si surface would imply Set-A and Set-C Si, respectively.

4.3.2 Wettability of hydrophobic and hydrophilic silicon by solvents

After studying the nature of the Si surface for various treatments, we investigated the wetting behavior of solvents on hydrophobic and hydrophilic Si surfaces. The contact angles on Set-A and Set-C were determined using the four solvents as test liquids. The contact angle values are tabulated in Table 4.1. Ethanol, isopropanol, and 2-methoxyethanol spreads on the hydrophilic surface giving 0° contact angle. These solvents show the best wetting behaviors on the superhydrophilic Si surface, suggesting that they should give a film on superhydrophilic Si surface. However, they show finite contact angles on the hydrophobic surface. 1-butanol shows contrasting behavior in comparison to other solvents. It gives a finite contact angle for both superhydrophilic and weakly hydrophobic Si surfaces. Because of these contrasting contact angles, the film forming quality during spray-coating had to be confirmed. For this purpose, precursor solutions prepared using each of these four solvents were spray-coated over both types of Si surfaces.

Table 4.1: Contact angle of ethanol, isopropanol, 2-methoxyethanol, and 1-butanol on weakly hydrophobic (Set-A) and superhydrophilic (Set-C) Si surface.

Solvent	Hydrophobic (Set-A)	Superhydroplilic (Set-C)
ethanol	20.6°	0°
isopropanol	6.7°	0°
2-methoxyethanol	19.1°	0°
1-butanol	4.9°	5.3°

4.3.3 Film formation on hydrophobic and hydrophilic silicon

0.02 mol l^{-1} solution was sprayed over Set-A and Set-C Si wafers, which were subsequently baked at 150°C. AFM images of the Si surface after spray-coating and baking are shown in Fig. 4.2. Solution with ethanol, isopropanol, and 2-methoxyethanol as solvents give continuous films on superhydrophilic Si surface, which agrees with contact angle measurement results (Fig. 4.2(a), (c), and (g)). However, no film formation is observed on weakly hydrophobic surfaces; instead, blisters are visible (Fig. 4.2 (b), (d), and (h)). Solution with 1-butanol as solvent shows unexpected behavior. In spite of having a finite contact angle on both surface types, continuous film formation was observed on

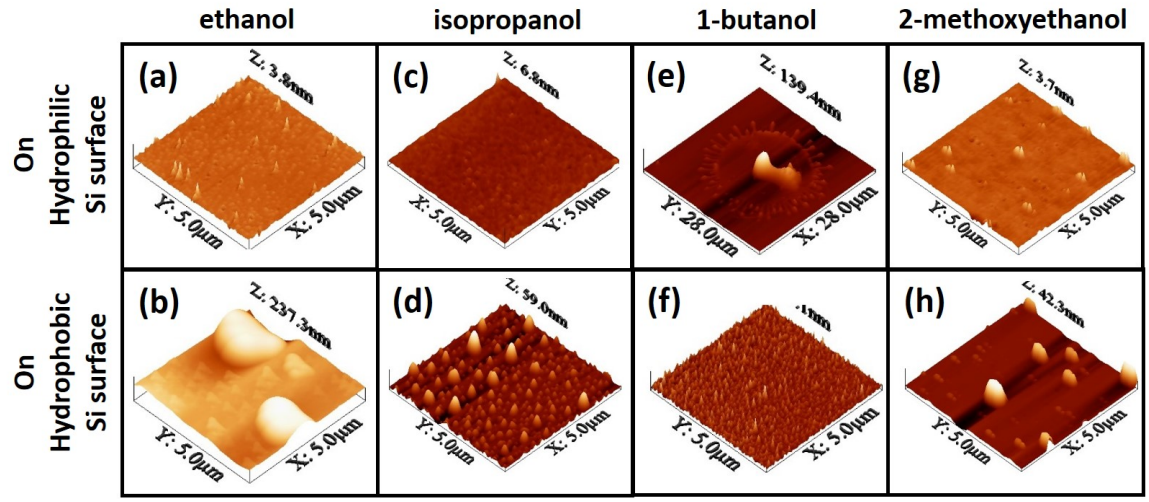

Figure 4.2: AFM images of film/structures over superhydrophilic and weakly hydrophobic Si surface for solution with ethanol, isopropanol, 2-methoxyethanol, and 1-butanol as solvent.

a weakly hydrophobic surface, but, not on superhydrophilic surface. Root Mean Square (RMS) roughness values for the surface conditions on which the solvent gives a continuous film are tabulated in Table 4.2. All the solvents show films with roughness values < 1 nm. The film with 1-butanol as the solvent has the highest roughness of ~0.7 nm in comparison to ethanol, isopropanol, and 2-methoxyethanol, which have RMS roughness values < 0.5 nm. Additionally, a solution with increased molarity of 0.06 mol l^{-1} was also sprayed over Si wafers to confirm the solvent behavior during spray-coating. Spray-coating parameters were similar to those used for 0.02 mol l^{-1} solution. The films become rough with an increase in molarity for ethanol and isopropanol based solutions. Interestingly, 1-butanol based solution with 0.06 mol l^{-1} molarity did not form a film (therefore, roughness and thickness data are not listed). Hence, 1-butanol solvent was not used for further analysis.

Table 4.2: RMS roughness values of the film obtained using solution with solvent as ethanol, isopropanol, and 2-methoxyethanol on superhydrophilic and 1-butanol on weakly hydrophobic Si.

Solvent	0.02 mol l^{-1}		0.06 mol l^{-1}	
	Thickness (nm)	Roughness (nm)	Thickness (nm)	Roughness (nm)
ethanol	4.8	0.21	9.65	1.19
isopropanol	5.4	0.26	19.72	1.63
2-methoxyethanol	4.48	0.15	21.36	0.19
1-butanol	6.66	0.71	-	-

4.3.4 Effect of molarity

Upon the confirmation of the film formation, the effect of solution concentration on the physical properties of the film was studied for ethanol, isopropanol, and 2-methoxyethanol. Physical properties were studied in terms of thickness and refractive index, measured using an ellipsometer. Corresponding porosity was calculated from the measured refractive index values using the Lorentz-Lorentz relation given by equation 4.1 [158]

$$\frac{n^2-1}{n^2+2} = (1 - Porosity)\frac{n_o^2-1}{n_o^2+2} \tag{4.1}$$

where n and n_o represents the refractive index value for the spray-coated film and for reference dense silica (n_o=1.46), respectively. Variation in thickness, refractive index, and porosity with molarity are shown in Fig. 4.3.

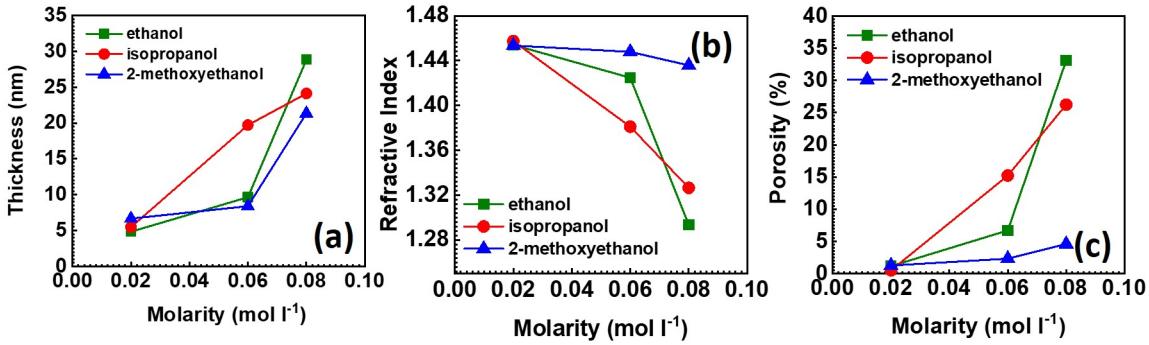

Figure 4.3: Variation in (a) thickness (b) refractive index, and (c) porosity of the spray-SiO_2 films with molarity of the solution prepared with ethanol, isopropanol, and 2-methoxyethanol as solvent.

With an increase in solution molarity, the thickness of the film increases. This might be due to an increase in both the rate of hydrolysis and condensation with molarity resulting in thickness increment [83]. However, the refractive index decreases with molarity. Therefore, corresponding film porosity increases with molarity (equation 4.1). This might be due to the larger size of silica particles in the film, increasing the interparticle voids making the film more porous with an increase in hydrolysis and condensation rate with molarity. Also, the solvent is playing a role in defining the thickness and porosity of the film for variable molarity. This might be due to the different densities of the solvent; 2-methoxyethanol being highly dense among all and ethanol being the least. We anticipate that the higher the density of the solvent, the more dense is the solution, and therefore, the thicker and denser the film is obtained. For 2-methoxyethanol, thickness increases

from 6.7 nm to 21.4 nm and refractive index decreases from 1.453 to 1.435 for molarity increment from 0.02 mol $^{-1}$ to 0.08 mol l^{-1}. Although the film thickness is increasing appreciably with molarity, the corresponding decrease in refractive index is lower in 2-methoxyethanol based films in comparison to the other two solvents. Therefore, a denser film with varying thicknesses is obtained using 2-methoxyethanol as a solvent and less dense film is obtained with increasing molarity when the solution is prepared with ethanol and isopropanol. Also, for a molarity of 0.08 mol l^{-1}, ethanol gives more porous films in comparison to isopropanol.

4.3.5 Interface state and fixed oxide charge density

A comparison of D_{it} and Q_f for ethanol, isopropanol, and 2-methoxyethanol solvents was performed for a gate dielectric SiO_2 of ~10 nm, measured after PDA at 650°C. Solution molarity and spray parameters were varied to obtain ~10 nm film. However, identical H_2O:TEOS and HNO_3 molarity ratio, as before, were used. D_{it} was extracted using Hill's single frequency method and Q_f from the difference in midgap voltage [7, 141]. The typical C-V and G-V characteristics are shown in Fig. 4.4.

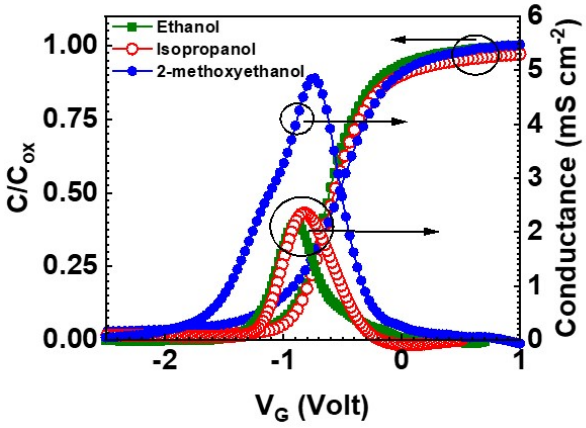

Figure 4.4: Series resistance corrected C-V and G-V characteristics for the SiO_2 films based on ethanol, isopropanol, and 2-methoxyethanol as solvents deposited on n-type Si and subjected to PDA at 650°C in O_2 ambient and PMA at 450°C in FGA.

D_{it} is in the range of 2.7-5.2×10^{10} $cm^{-2}eV^{-1}$ and 2.9-4.1×10^{10} $cm^{-2}eV^{-1}$ for ethanol and isopropanol, respectively. However, 2-methoxyethanol based film shows an order of magnitude higher D_{it} in the range of 1.0-2.0 ×10^{11} $cm^{-2}eV^{-1}$ for similar process conditions providing comparatively inferior chemical passivation (Fig. 4.5(a)). Warren et al. reported D_{it} of 7×10^{10} $cm^{-2}eV^{-1}$ for sol-gel SiO_2 film at a higher annealing temperature of 900°C [159]. The interface quality of Si and SiO_2 film formed with 2-methoxyethanol

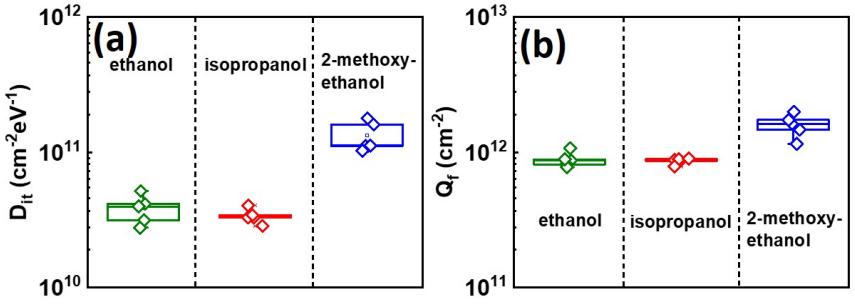

Figure 4.5: (a) D_{it} and (b) Q_f for ~10 nm SiO_2 films based on ethanol, isopropanol, and 2-methoxyethanol as solvents deposited on n-type Si. The films were subjected to PDA at 650°C in O_2 ambient and PMA at 450°C in FGA.

solvent is inferior to the films based on ethanol and isopropanol as solvents. Q_f in the range of 7.7×10^{11}-1.1×10^{12} cm^{-2}, 7.8×10^{11}-9×10^{11} cm^{-2}, and 1.1×10^{12}-2×10^{12} cm^{-2} is obtained for ethanol, isopropanol, and 2-methoxyethanol based SiO_2 film, respectively (Fig. 4.5(b)). Films based on 2-methoxyethanol solvent gave double the Q_f in comparison to other two solvents, and therefore would give better field effect passivation. However, it has been reported that for highly doped Si surfaces (e.g. emitters), Q_f has smaller influence on the surface band bending [42, 103, 160]. Therefore, additional field effect passivation due to overlying dielectric field has a little role to play. Chemical passivation obtained by reducing the surface defect states would be the dominating mechanism defining the overall passivation in case of highly doped Si surfaces [42, 103, 160].

4.3.6 Choice of solvent for spray-SiO_2 film

Although films based on 2-methoxyethanol as a solvent shows comparatively uniform and dense film for varying film thicknesses, it provides an order of magnitude higher D_{it} compared to ethanol and isopropanol. Therefore, providing inferior passivation of highly doped Si surfaces. In this thesis, we would also be studying the passivation of phosphorus diffued emitter with spray-SiO_2 film (Chapter 6). Therefore, 2-methoxyethanol would not be the chosen solvent considering the passivation aspect. Also, it was observed that with increasing molarity to obtain thicker films, ethanol based films were non-uniform and less dense in comparison to isopropanol based films. Most of the studies on sol-gel silica films have been performed using ethanol as solvent [79, 82, 154], however, the availability of the high purity electronic grade ethanol is regulated by the Federal government. Therefore, procuring electronic grade ethanol has become a tedious task. In contrast, isopropanol is already being used in the semiconductor industry for

cleaning purposes. In the solar industry, it is used in combination with the alkaline solution for the chemical texturization of mono-Si to reduce the optical reflectance [161, 162]. Besides, the cost of isopropanol (CMOS grade) is about half that of 2-methoxyethanol (HPLC grade). Therefore, considering the pros and cons of the solvents as well as their properties, we have chosen isopropanol for sol-gel spray-coated SiO_2 film for further investigations.

4.4 Conclusions

We demonstrated the effect of solvents on sol-gel spray-coated SiO_2 film properties including, thickness, refractive index, porosity, D_{it}, and Q_f. It was shown that the presence of native oxide after RCA, as well as oxide grown after UV-Ozone exposure makes the Si surface superhydrophilic and the removal of native oxide after RCA makes the Si surface weakly hydrophobic. Continuous films could not be obtained on either type of Si substrate using 1-butanol solvent, but, could be obtained on superhydrophilic Si with ethanol, isopropanol, and 2-methoxyethanol solvent. UV-Ozone exposure assisted in improving the wettability of these solvents and thus, of the respective sol-gel solutions. 2-methoxyethanol showed uniform and dense films in comparison to ethanol and isopropanol solvent. $D_{it} \sim 10^{10}$ $cm^{-2}eV^{-1}$ was achieved for both ethanol and isopropanol based solutions. However, 2-methoxyethanol based films provided an order of magnitude higher D_{it} ($\sim 10^{11}$ $cm^{-2}eV^{-1}$). Therefore, 2-methoxyethanol based films would provide inferior passivation of highly doped Si surface in comparison to other ethanol and isopropanol. Hence, isopropanol would be used in the work reported in subsequent chapters.

Chapter 5

Passivation of n- and p-type Silicon with Spray-SiO_2 Film

5.1 Motivation

After selecting the solvent, the immediate next task was the development and in-depth investigation of the spray-SiO_2 film. As discussed in section 2.3.1.4, the majority of the sol-gel SiO_2 work has been focused on studying the physical properties of the film. There are few studies on the electrical properties of the sol-gel SiO_2 film. Jaehnike et al. investigated the E_{BD} and J_{leak} of spin-coated SiO_2 film on Si substrate [85]. Weimer et al. [163] and Warren et al. [159] studied the D_{it} of the spin-coated SiO_2 film. Esro et al. studied the J_{leak} and E_{BD} of the SiO_2 film deposited with a spray pyrolysis system [89].

In this chapter, we demonstrate sol-gel SiO_2 film deposition employing a simple, cost-effective, and industrially viable spray-coating technique. In this technique, sol-gel is sprayed over the substrate at room temperature and dried subsequently using thermal treatment, unlike spray-pyrolysis as used by Esro et al. [89], where the sol-gel is sprayed over a substrate maintained at a certain high temperature. A detailed comparison of sol-gel spray-coated SiO_2 film on both n- and p-type polished Si is presented. Physical properties including thickness, refractive index, nature, elemental composition, and morphology are studied. Electrical properties like J_{leak} and E_{BD} are reported. Also, the passivation behavior of the film is investigated with D_{it}, Q_f, and S_{eff}. Enhanced film properties in comparison to sol-gel SiO_2 films reported in the literature are demonstrated.

5.2 Experimental details

5.2.1 Solution preparation

Sol-gel solution of molarity 0.06 mol l^{-1} was synthesized using TEOS (Sigma-Aldrich, 99.999% trace metal basis), isopropanol (J.T. Baker, CMOS grade), DI H_2O, and HNO_3 (J.T. Baker, CMOS grade). DI water with H_2O:TEOS molar ratio of 2.22 and HNO_3 (J.T. Baker, CMOS grade) with a molarity of 0.039 mol l^{-1} was used. The same methodology as discussed in section 4.2.2 was used for the solution preparation.

5.2.2 Film deposition and characterization

Both p-type (boron-doped) and n-type (phosphorus-doped) Cz Si wafers ((100), 4-7 Ωcm, 280 μm) were used. These wafers were RCA cleaned [155] and later dipped in 2% HF solution to remove native oxide formed during RCA-2 cleaning stage, prior to further processing. These were exposed to UV radiations in O_2 ambient in an UV-Ozone chamber (Holmarc Mechatronics Pvt. Ltd, HO-TH-UV02) for 5 min. This improves wettability and grows an ultrathin oxide over the Si wafer [75, 157], as discussed in chapter 2 and 3. The aged solution was immediately spray-coated on UV-Ozone exposed Si surface using custom-designed spray-coating equipment (Holmarc Mechatronics Pvt. Ltd). The solution sprayed Si wafers were immediately kept on a hot plate preheated at 150°C for 10 minutes and were further subjected to PDA at 650°C in O_2 ambient.

Spectroscopic ellipsometer (Semilab, SE-2000) was used to measure psi-delta plots at an incidence angle of 75°. The plots were fitted using a Cauchy dispersion model to extract the film thickness. Thickness was measured at five different points on the wafer and the average was considered for analysis. Cross sectional TEM imaging of the film was carried out with high resolution TEM operating at 200 kV (JEOL, JEM 2100F). For cross-sectional TEM sample preparation, Al was deposited over the spray-SiO_2 film. The Si/SiO_2/Al stack underwent disc cutting, dimpling, and ion-milling to make the sample electron transparent prior to TEM imaging. The elemental composition of the film was analyzed using XPS (PHI 5000 Versa Probe-II) with Al Kα monochromatic source of excitation energy 2 keV.

5.2.3 MOS capacitor fabrication and characterization

MOS capacitors were fabricated to study the electrical properties of the deposited film on both n- and p-type single side polished (SSP) Si wafers ((100), 4-7 Ωcm, 280 μm). RCA cleaned, 2% HF treated and UV-Ozone exposed Si wafers were spray-coated

and baked at 150°C and were subjected to PDA at 650°C in O_2 ambient. Al dots of 0.125 mm^2 area were thermally evaporated using Al shadow mask in 4-Target E-Beam Evaporator System (HHV 15F6T) on the annealed film to create front contact. Native oxide at the back was etched off using 5:1 buffered hydrofluoric acid (BHF; J.T Baker, CMOS grade) solution. Back metal contact was created by blanket deposition of Al. The final structure was subjected to PMA in FG (4% H_2 and 96% N_2) ambient at 450°C for 30 min.

MOS capacitors were also fabricated on p-type Si substrate where the SiO_2 was spray-coated on Si wafers after the RCA-2 process, without UV exposure. All other processes for MOS capacitor fabrication were identical to those described above.

Semiconductor Device Analyzer (Keysight, B1500A) was used for the characterization of the MOS capacitors. D_{it} and Q_f were extracted from C-V and G-V characteristics measured at 200 kHz frequency and J_{leak} and E_{BD} were extracted from I-V characteristics measured in accumulation.

5.2.4 Lifetime structure fabrication and characterization

Symmetric lifetime structures were fabricated on both n- and p-type Cz double side polished (DSP) Si wafers ((100), 4-7 Ωcm, 280 μm) to measure effective minority carrier lifetime, τ_{eff}. One side of the wafer (RCA cleaned and 2% HF dipped) was UV-Ozone treated for 5 min followed by immediate spraying. The sprayed wafer was subjected to 5 min baking at 150°C. The other side of the wafer was subsequently UV-Ozone treated and spray-coated. This structure was hot plate annealed at 150°C for 10 min and was subjected to PDA in O_2 ambient at 650°C for 30 min. Al (150 nm) was thermally evaporated over deposited film on either surface followed by PMA at 450°C for 30 min in FG (4% H_2 and 96% N_2) ambient. Al was etched off in Al etchant (phosphoric acid 80%, acetic acid 5%, nitric acid 5% and DI water 10% by volume) after PMA. To measure the bulk lifetime, τ_b, identical DSP wafers (same as used for τ_{eff} measurement) were chemically passivated by immersing in a solution of quinhydrone (Sigma-Aldrich, 97% HPLC grade) and methanol (MeOH; Merk) in a sealed plastic bag immediately after RCA and 2% HF treatment.

Lifetime tester (Sinton Instruments, WCT-120) was used for the measurement of the contactless injection dependent τ_{eff} of symmetric lifetime structures and τ_b of chemically passivated Si wafers either in QSS or transient photoconductance mode. All the lifetime values are quoted at an excess minority carrier density of 10^{15} cm^{-3}.

5.3 Results and discussion

5.3.1 Physical characterization

Physical characterizations were performed on spray-coated SiO_2 film deposited on both n- and p-type Si after PDA at 650°C in O_2 ambient for 30 min. SiO_2 film thickness and refractive index were measured as 18.83 nm and 1.43 on n-type and 21.64 nm and 1.42 on p-type Si, respectively using spectroscopic ellipsometer. The film was also characterized before PDA to obtain thickness and refractive index of 24.86 nm and 1.38, respectively on n-type wafer. The film has become thinner and the refractive index has increased after PDA. It is concluded that the film has become denser after PDA. A similar trend was observed for the film on p-type substrate.

Cross-sectional TEM micrograph shows the amorphous nature of the film (Fig. 5.1). The TEM sample was prepared for the p-type wafer, on which the thickness was measured as 22 nm using ellipsometry. The deviation from the mean for the film after PDA is measured as $\sim \pm 1.6$ nm. Thickness measured from the TEM image is $\sim$ 24 nm, which can be correlated to the ellipsometer thickness for p-type wafer.

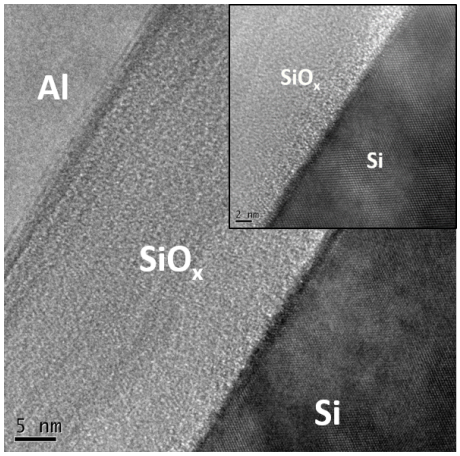

Figure 5.1: Bright field cross-sectional TEM micrograph of spray-coated SiO_2 film on p-type Si after PDA in O_2 ambient at 650°C. The inset image shows a higher resolution image near Si-SiO_2 interface demonstrating the crystalline and amorphous nature of Si and SiO_2, respectively.

Elemental composition in terms of atomic percentage obtained from XPS analysis is plotted as a function of sputter time in Fig. 5.2. Two distinct profiles of Si oxidation states are shown. Si^{4+}_{2p} corresponds to fully oxidized SiO_2 and Si^{0}_{2p} to metallic Si. The atomic percentage of Si^{0}_{2p} decreases and Si^{4+}_{2p} increases from the Si substrate towards the film surface. This implies the formation of SiO_2 in the film. The stoichiometry of the

film is defined by the atomic percent ratio (O:Si) of O_{1s} and Si_{2p}^{4+} oxidation state. O:Si ranges from 1.97 to 2.25 on n-type and from 1.95 to 2.28 on p-type in a region between the surface and Si substrate. This indicates nearly stoichiometric film on either type of substrates. There exists negligible carbon content in the film in comparison to Si and oxygen, which can be concluded from near to zero atomic concentration of C_{1s} oxidation state. This indicates negligible traces of residual organics due to solvent residues present in the film after annealing.

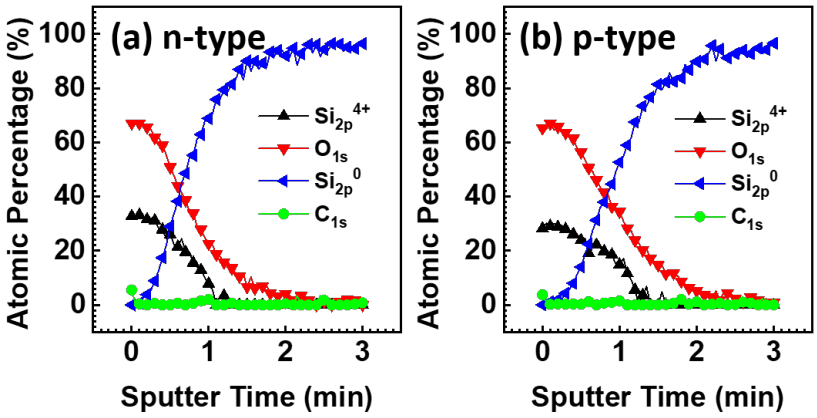

Figure 5.2: XPS depth profiles of various chemical species of interest in spray-coated SiO_2 film on (a) n-type and (b) p-type Si after PDA in O_2 ambient at 650°C.

A detailed XPS analysis has been performed on the SiO_2 film deposited on n-type Si surface. XPS analysis would be the same for the film on p-type Si due to similar depth profile of the films on both the substrates. Fig. 5.2(a) shows the depth profile of the SiO_2 film on n-type Si surface showing atomic percentage of different elements as a function of sputter time, t. From Fig. 5.2(a) below, it can be concluded that the Si_{2p}^{4} atomic percentage goes to zero for sputter time $\geqslant$ 1.36 min. However, there exist O_{1s} after t = 1.36 min and it goes to zero at t = 2 min. Si_{2p}^{0} peak also saturates to 100% after t = 2 min. This suggests that there may exist different oxidation states of Si in the region from 1.36 min to 2 min (region highlighted in yellow Fig. 5.3(a)). Therefore, we deconvoluted the Si_{2p} peak at points in the sputter time span 1.36 < t < 2 min, i.e. at time t = 1.4 min and 1.7 min and at a point beyond t = 2.2 min. The deconvoluted peaks of Si_{2p} spectra are shown in Fig. 5.3(b)-(d) and corresponding percentage area of respective oxidation states are tabulated in Table 5.3. The peaks at binding energy ~99 eV, ~100 eV, ~101 eV, ~102 eV, and ~103 eV corresponds to Si_{2p}^{0}, Si_{2p}^{1+}, Si_{2p}^{2+}, Si_{2p}^{3+}, and Si_{2p}^{4+} oxidation states, respectively [164].

From Fig. 5.3(b)-(d) and Table 5.1, it can be observed that there exist peaks at ~100 eV and ~102 eV at time t = 1.4 min and 1.7 min, which corresponds to Si_{2p}^{1+} and Si_{2p}^{3+}

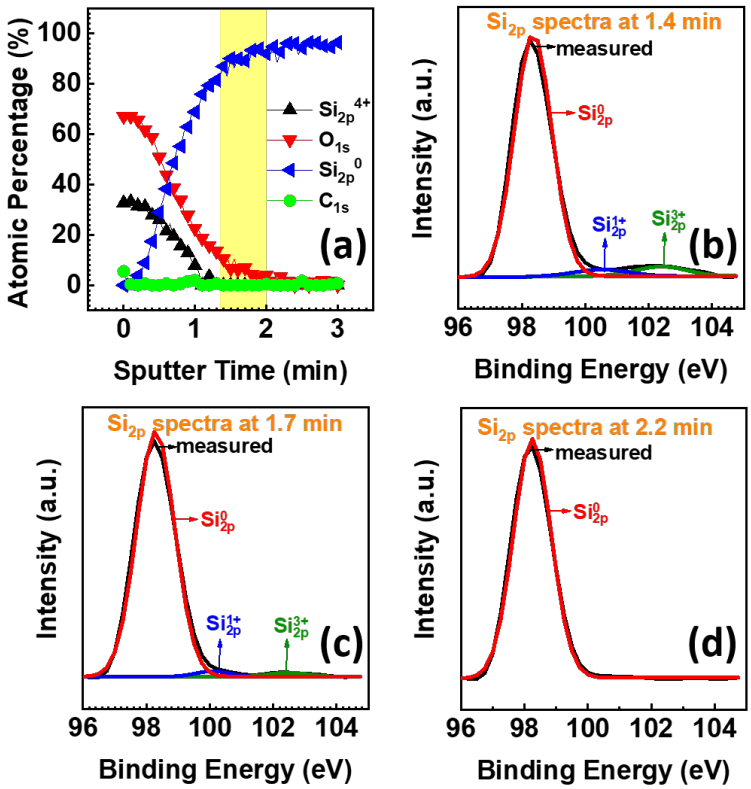

Figure 5.3: (a) XPS depth profiles of various chemical species of interest in spray-coated SiOx film on n-type Si after PDA in O_2 ambient at 650°C with the transition layer at the interface highlighted in yellow. Deconvolution of Si_{2p} spectra at (b) t = 1.4 min, immediately after Si_{2p}^{4} state goes to zero, (c) t = 1.7 min, and (d) t = 2.2 min, where O_{1s} XPS depth spectra goes to zero.

oxidation states, whose concentration decreases moving towards the Si. However, the Si_{2p}^{0} peak concentration increases as we approach the Si surface and reaches 100% after 2 min (Fig. 5.3 and Table 5.3). Therefore, it can be concluded that there exist intermediate oxidation states of Si at and near the Si/SiO_2 interface in the region highlighted by yellow in the XPS depth profile in Fig. 5.3(a). Young-Bae Park et al. deconvoluted the Si_{2p} peak at the interface of Si/SiO_2 where SiO_2 was deposited by PECVD [165]. They have shown that the transition layer at Si/SiO_2 interface consisted of intermediate oxidation states in addition to Si_{2p}^{4+}. However, there only exits intermediate oxidation states of Si_{2p} in the transition region from the sputter time at which Si_{2p}^{4+} goes to zero and upto the sputter time at which O_{1s} goes to zero in our work. Therefore, it can be concluded that there exist intermediate oxidation states of Si at and near the Si/SiO_2 interface in the region highlighted by yellow in the XPS depth profile in Fig. 5.3. This suggests that the sol-gel spray-coated SiO_2 film is not stoichiometric in the highlighted transition region.

Table 5.1: Percentage area of oxidation states after deconvolution of Si_{2p} spectra in the transition region at the interface of Si and spray-coated SiO_2.

Sputter time (t)	~99 eV (Si^{0}_{2p})	~100 eV (Si^{1+}_{2p})	~101 eV (Si^{2+}_{2p})	~102 eV (Si^{3+}_{2p})	~103 eV (Si^{4+}_{2p})
1.4 min	91.52	3.54	-	4.9	-
1.7 min	96.4	1.92	-	1.68	-
2.2 min	100	-	-	-	-

The presence of sub-stoichiometric oxide with unsatisfied Si atomic bonds at and in the vicinity of Si/SiO_2 interface is the likely origin of the oxide charges.

TEM and XPS results conclude that the physical behavior (nature, composition, and morphology) of the spray-coated SiO_2 film is independent of the Si dopant type as anticipated.

5.3.2 Electrical characterization

5.3.2.1 Interface state density and oxide charge density

Dielectric passivation is correlated to the minority carrier recombination rate at the surface. Better passivation results in smaller S_{eff}, which can be minimized by reducing D_{it} at the Si/dielectric interface (chemical passivation) and by varying the surface carrier densities by means of the electric field (field effect passivation) achieved by Q_f present in the overlying dielectric film [19]. Therefore, a study of both D_{it}, as well as Q_f, is helpful to understand the passivation mechanism. These two parameters were extracted from C-V and G-V characteristics of fabricated MOS capacitors after being subjected to PMA in FG (4% H_2 and 96% N_2) ambient at 450°C for 30 min. Spray-coated SiO_2 film subjected to PDA acts as a dielectric and its thickness was measured as 17.6 nm on n-type and 17.1 nm on p-type Si substrate using ellipsometer. C-V and G-V curves were series resistance corrected prior to D_{it} and Q_f extraction using the methodology mentioned in section 3.1.1 of chapter 3. D_{it} (cm^{-2} eV^{-1}) was evaluated from the combination of single-frequency C-V and G-V characteristics using Hill's method [141] as discussed in section 3.1.2.

Fig. 5.4 shows series resistance corrected C-V and G-V characteristics of MOS capacitor at 200 kHz with best D_{it} of 1.4×10^{10} cm^{-2} eV^{-1} on n-type and 2.0×10^{10} cm^{-2} eV^{-1} on p-type. V_{FB} which is contributed by Q_f and ϕ_{MS} was calculated as -0.87 V and -1.20 V for n-type and p-type, respectively. V_{FB} shift of only -0.20 V on n-type and -0.85 V on p-type is due to ϕ_{MS}. The remaining shift is entirely due to Q_f. This implies that the Q_f tend to shift C-V towards negative V_G indicating that the oxide charges present in the deposited SiO_2 film are positive. These were determined to be $+9.2\times10^{11}$ cm^{-2} on n-type

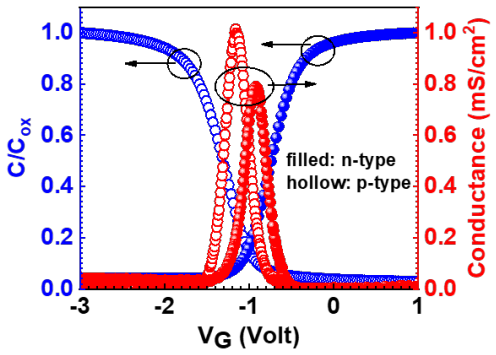

Figure 5.4: Series resistance corrected C-V and G-V characteristics at 200 kHz for the MOS capacitors with best D_{it} value obtained on both n- and p-type Si substrates subjected to PDA at 650°C in O_2 ambient and PMA at 450°C in FG ambient. The capacitance is normalized to the accumulation capacitance.

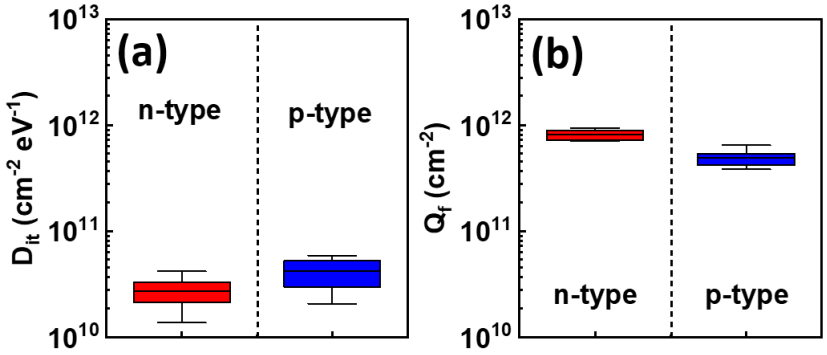

Figure 5.5: Range of (a) interface state density (D_{it}) and (b) fixed oxide charges (Q_f) on n-type and p-type Si substrate for PDA in O_2 ambient at 650^{o}C and PMA in FG ambient at 450^{o}C. D_{it} and Q_f values were extracted from series resistance corrected C-V and G-V curves measured at 200 kHz for five different MOS capacitors.

and +6.1×10^{11} cm^{-2} on p-type substrate. Ranges of D_{it} and Q_f were obtained by characterizing five different MOS capacitors. D_{it} in the range of 1.4 - 4.2×10^{10} cm^{-2} eV^{-1} on n-type and 2.0 - 6.0×10^{10} cm^{-2} eV^{-1} on p-type was achieved (Fig. 5.5(a)). This indicates that the deposited SiO_2 film should provide similar chemical passivation irrespective of Si substrate doping type. Positive Q_f in the range of 7.1 - 9.4×10^{11} cm^{-2} on n-type and 3.9 - 6.5×10^{11} cm^{-2} on p-type was obtained (Fig. 5.5(b)). The higher positive Q_f should result in better field effect passivation on n-type Si. Effective passivation of p-type surface in solar cells would require -ve Q_f.

D_{it} and Q_f values were also extracted for the film without PDA and with PMA. D_{it} is in the range of 2.4 - 2.8 ×10^{12} cm^{-2} eV^{-1} and 0.83 - 1.4 ×10^{12} cm^{-2} eV^{-1} on n- and p-type

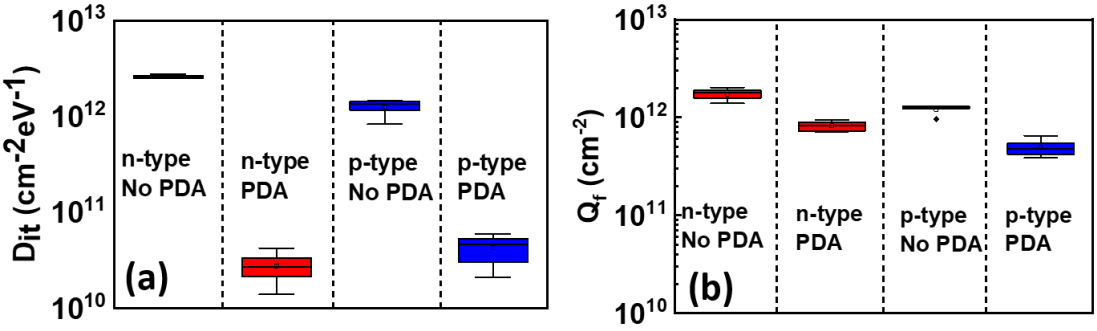

Figure 5.6: Range of (a) interface state density (D_{it}) and (b) fixed oxide charges (Q_f) on n- and p-type Si substrate for without and with PDA in O_2 ambient at 650°C. All samples were subjected to PMA in FG ambient at 450°C. D_{it} and Q_f values were extracted from series resistance corrected C-V and G-V curves measured at 200 kHz for five different MOS capacitors.

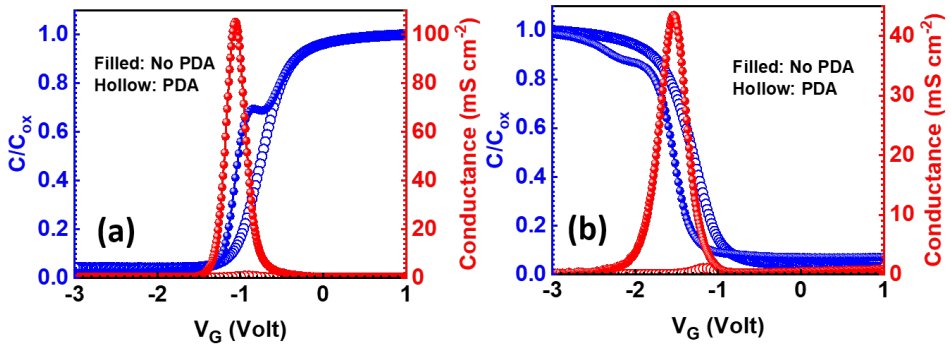

Figure 5.7: Series resistance corrected C-V and G-V characteristics at 200 kHz for the MOS capacitor on (a) n-type and (b) p-type Si substrate without and with PDA in O_2 ambient at 650°C. All samples were subjected to PMA in FG ambient at 450°C. D_{it} and Q_f values were extracted from series resistance corrected C-V and G-V curves measured at 200 kHz for five different MOS capacitors.

Si, respectively without PDA (Fig. 5.6(a)). This shows that the PDA step has reduced the D_{it} by two orders of magnitude enhancing the chemical passivation. Also, Q_f has reduced after PDA from 1.4 - 2 $\times 10^{12}$ cm^{-2} and 0.96 - 1.3 $\times 10^{12}$ cm^{-2} to 7.1 - 9.4 $\times 10^{11}$ cm^{-2} and 3.9 - 6.5 $\times 10^{11}$ cm^{-2} on n- and p-type Si, respectively (Fig. 5.6(b)). Typical C-V and G-V curves for the alnealed films before and after PDA are shown in Fig. 5.7. The C-V characteristics with no PDA step show a hump, which indicates large D_{it} values [48].

Low D_{it} value in our experiment can be partly attributed to alneal process which was carried out in FG ambient at 450°C for 30 min. Alneal reduces D_{it} and hence enhancing

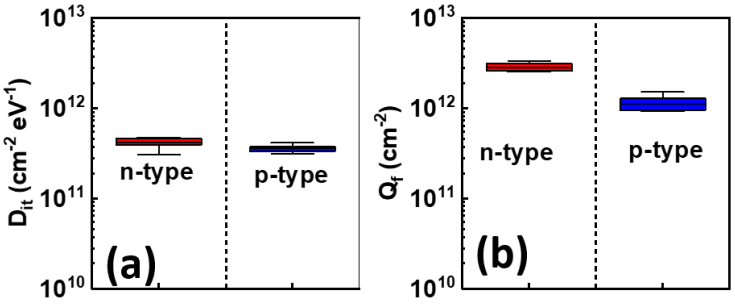

Figure 5.8: Range of (a) D_{it} and (b) Q_f for the film deposited on n- and p-type Si substrate before alneal (i.e. PMA in FG ambient at 450°C for 30 min). The film was subjected only to PDA in O_2 ambient at 650°C for 30 min. D_{it} and Q_f values were extracted from series resistance corrected C-V and G-V curves measured at 200 kHz for five different MOS capacitors.

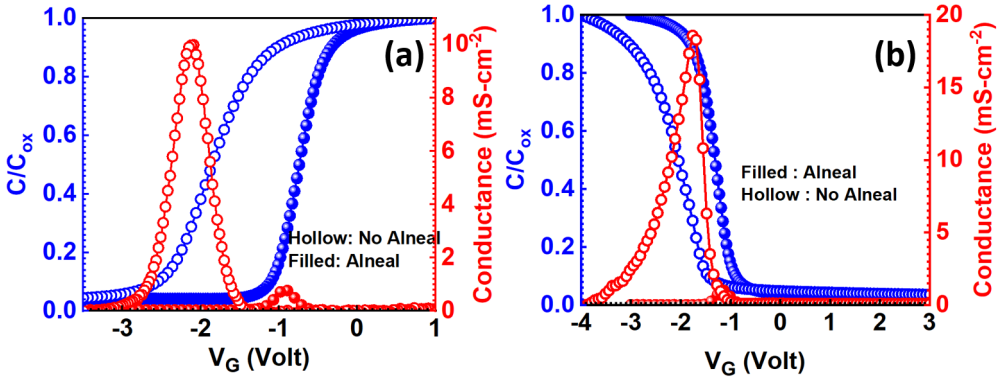

Figure 5.9: Typical C-V and G-V characteristics for the film on (a) n-type and (b) p-type Si substrate subjected to PDA in O_2 ambient at 650°C. Samples were not subjected to PMA in FG ambient at 450°C. D_{it} and Q_f values were extracted from series resistance corrected C-V and G-V curves measured at 200 kHz for five different MOS capacitors.

chemical passivation (section 2.3). In our experiment, the alneal process is seen to be effective by comparing D_{it} values before and after FGA. D_{it} ranges between 3.1 - 5.7×10^{11} cm^{-2} eV^{-1} on n-type and 3.0 - 4.1×10^{11} cm^{-2} eV^{-1} on p-type Si before alneal (Fig. 5.8(a)). D_{it} was reduced by an order of magnitude after alneal. Q_f was also reduced after alneal. It was in the range of 2.5 - 3.4×10^{12} cm^{-2} on n-type and 9.2 - 12.8×10^{11} cm^{-2} on p-type Si before alneal (Fig. 5.8(b)). Typical C-V and G-V characteristics for the films subjected to PDA and no PMA are shown in Fig. 5.9.

We experimentally confirmed the effect of UV-Ozone oxide by replacing it with RCA-2 oxide, which is the native oxide grown during RCA-2 process. It had a thickness

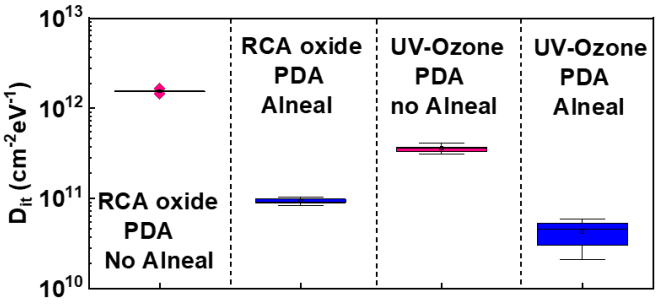

Figure 5.10: D_{it} for RCA-2 oxide/SiO_2 and UV-Ozone oxide/SiO_2 stack on p-type Si substrate after PDA and before and after alneal process. D_{it} and Q_f values were extracted from series resistance corrected C-V and G-V curves measured at 200 kHz for five different MOS capacitors.

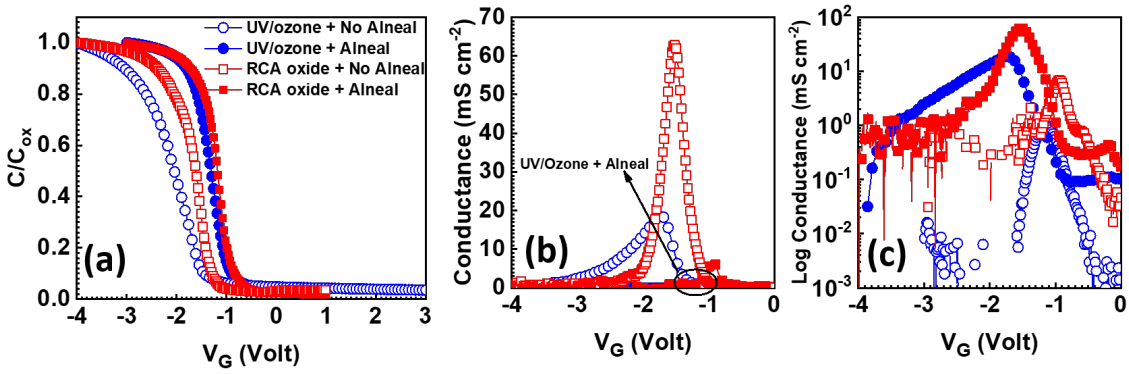

Figure 5.11: Series resistance corrected (a) C-V and (b) G-V (c) G-V with conductance in logarithmic scale for RCA-2 oxide/SiO_2 and UV-Ozone oxide/SiO_2 stack on p-type Si substrate subjected to PDA at 650°C for 30 min, before and after alneal process.

~1.5 nm, similar to UV-Ozone oxide, as confirmed by ellipsometry. The solution was sprayed on the Si wafers after RCA-2 process. The experiments were performed on p-type Si. We anticipate similar D_{it} values and its trend on n- and p-type Si from our experimental results as presented above. D_{it} in the range of 1.4 - 1.6×10^{12} $cm^{-2}eV^{-1}$ was obtained for RCA-2 oxide after PDA 650°C for 30 min in O_2 ambient without alneal process. However, D_{it} reduced by an order of magnitude after alneal process. D_{it} values for spray-coated film on RCA-2 oxide is in the range of 0.84 - 1.1×10^{11} $cm^{-2}eV^{-1}$ after PDA and alneal process. Fig. 5.10 shows the comparison of D_{it} for RCA-2 and UV-Ozone oxide without and with alneal process. D_{it} values are an order of magnitude less for UV-Ozone oxide in comparison to the RCA-2 oxide for similar process conditions. Therefore, it can be concluded that the inclusion of UV-Ozone oxide has effectively reduced the D_{it} value

by an order of magnitude. Fig. 5.11 shows the typical C-V and G-V curves for RCA-2 oxide/SiO_2 and UV-Ozone oxide/SiO_2 stack subjected to PDA at 650°C for 30 min in O_2 ambient and without and with incorporating PMA at 450°C for 30 min in FG ambient, i.e. the alneal process. The G-V peak for UV-Ozone oxide/SiO_2 stack after alneal is not prominent in Fig. 5.11(b) as its peak value is 1 mS-cm^{-2}, which is significantly less than the maximum G-V peak value observed for the RCA-2 oxide without alneal. Therefore, conductance is shown on a logarithmic scale for all the four cases in Fig. 5.11(c).

Table 5.2: Comparison of D_{it} and Q_f reported for alnealed SiO_2 film on Si by various deposition techniques

Method	Process details	Thickness (nm)	Substrate <100>	D_{it} ($cm^{-2}eV^{-1}$)	Q_f (cm^{-2})	Reference
Thermal (Dry)	1200°C/30 min; alneal (475°C)	129.5	n-type (5.25×10^{15} cm^{-3})	1.9×10^{9}	2.8×10^{10}	[54]
		135	p-type (1.61×10^{15} cm^{-3})	$2\text{-}3\times10^{9}$	7×10^{10}	
PECVD	250°C; alneal (300°C/20 min/FG)	50	p-type (10 Ωcm)	1.1×10^{10}	$> 10^{11}$	[151]
Sol-gel (Dip)	900°C/5 min/air; alneal (400°C/30 min/FG)	190-210	n-type (10 Ωcm)	7×10^{10}	-	[159]
Sol-gel (Spray)	**650°C/30 min/O_2; alneal (450°C/30 min/FG)**	**~17**	**n-type (4-7 Ωcm)** **p-type (4-7 Ωcm)**	**1.39×10^{10}** **2.05×10^{10}**	**$7.1\text{-}9.4\times10^{11}$** **$3.9\text{-}6.5\times10^{11}$**	**This work**

Table 5.2 presents D_{it} values reported for various deposition techniques for alnealed SiO_2 film. We achieved D_{it} less than the value previously reported for sol-gel SiO_2 films [159]. This might be due to the difference in surface preparation prior to the deposition of the film. Warren et al. dipped the wafers in a solution consisting of isopropanol and a wetting agent after cleaning [159], whereas wafers were exposed to UV-Ozone in O_2 ambient in our experiments. It has been reported in the literature that in addition to the Si surface modification, UV-Ozone treatment results in the growth of a chemical oxide of ~1.5 nm [166] over the Si surface which assists in enhancing the Si surface passivation [74, 75]. Our experiments show that UV-Ozone oxide is better than RCA-2 oxide as a surface preparation process prior to spray coating. Therefore, it can be concluded that the low D_{it} value in this work might be due to the UV-Ozone treatment carried out immediately before spray-coating in addition to the alneal process.

5.3.2.2 Distribution of interface state density in the bandgap

D_{it} is evaluated using Hill's single frequency conductance technique, where the peak of G-V characteristic is used for D_{it} estimation [141]. However, the peak value of conductance and the corresponding bias point might change with frequency [7]. Therefore, to confirm the frequency effect on the MOS capacitor C-V characteristics and to analyze the energy level of D_{it}, we characterized the MOS capacitor at probing frequencies of 20 kHz, 50 kHz, 100 kHz, and 200 kHz. MOS capacitors used for analysis are the same devices for which best D_{it} values have been reported for both n- and p-type Si. In our work, D_{it} values have been extracted at a probing frequency of 200 kHz.

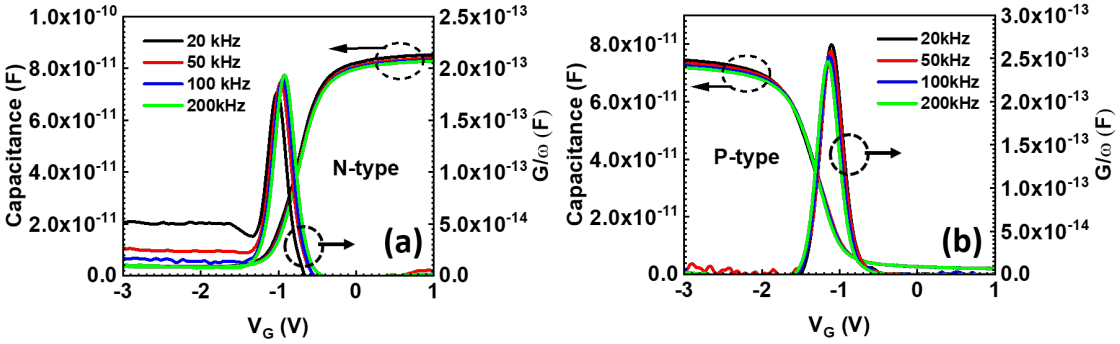

Figure 5.12: Series resistance corrected C-V and G/ω-V characteristics of the MOS capacitors subjected to PDA at 650°C in O_2 ambient and PMA at 450°C in FG ambient measured at 20 kHz, 50 kHz, 100 kHz, and 200 kHz on (a) n-type and (b) p-type Si substrate. Here, ω=2πf is the angular frequency, where f is the probing frequency.

For the best D_{it} values reported in this work, the peak or the maximum conductance, $G_{m,max}$, is situated at a voltage, $V_{m,max}$, of -0.92 V and -1.15 V for n- and p-type Si, respectively. C-V and G/ω-V characteristics of the MOS capacitors on n- and p-type Si for the probing frequencies of 20 kHz, 50 kHz, 100 kHz, and 200 kHz are shown in Fig. 5.12(a) and (b), respectively. Here, ω=2πf (rad s^{-1}) is the angular frequency with f being the frequency at which measurements were performed. A very slight variation in C-V characteristics with frequency is observed in Fig. 5.12. In addition, the conductance peak and corresponding bias point also varies slightly with frequency. Therefore, it can be concluded that frequency dispersion is not that significant in the frequency range considered for analysis.

Distribution of D_{it} as a function of E_T in the bandgap for $V_{m,max}$ corresponding to 20 kHz, 50 kHz, 100 kHz, and 200 kHz frequency is shown in Fig. 5.13(a) below for both n- and p-type Si. D_{it} position for a particular probed frequency is located at an energy level corresponding to the gate voltage, $V_{m,max}$, where the peak of G-V curve occurs (as

discussed in section 3.1.5 of chapter 3) [7]. It can be observed from Fig. 5.13(a) that D_{it} as well as the energy level E_T cannot be differentiated in the considered frequency range for respective substrate dopant type, as there exist a very slight variation in these values with frequency. Therefore, the distribution is plotted separately for n-type Si in Fig. 5.13(b) and for p-type Si in Fig. 5.13(c). D_{it} is in the range of 1.1-1.4×10^{10} $cm^{-2}eV^{-1}$ and 1.9-2.0×10^{10} $cm^{-2}eV^{-1}$ in the frequency range 20 kHz - 200 kHz on n- and p-type Si, respectively (Fig. 5.13(b) and (c)). The energy level E_T corresponding to D_{it} varies from 0.304 eV to 0.27 eV from E_c on n-type Si and from 0.844 eV to 0.857 eV from E_c (i.e. from 0.276 eV to 0.263 eV from E_v) on p-type Si in the frequency range from 20 kHz to 200 kHz (Fig. 5.13(b) and (c)). This shows that with increasing probing frequency, there exists slight shift in E_T away from the mid-gap position i.e. towards the majority carrier band edge.

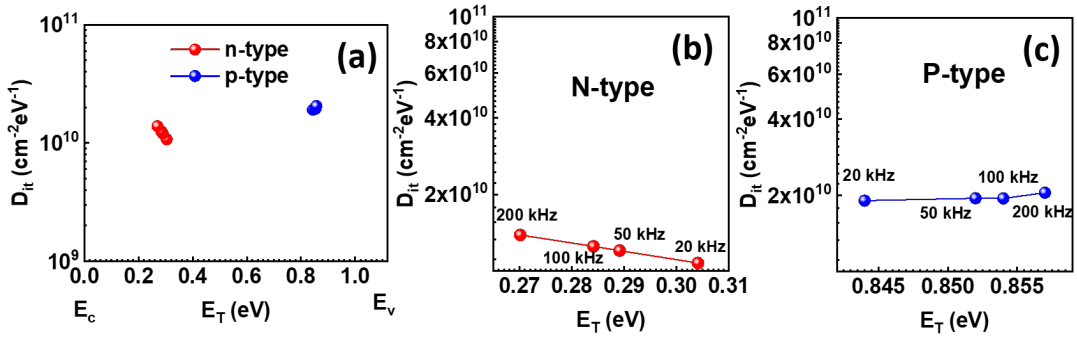

Figure 5.13: (a) Distribution of interface state density (D_{it}) within the bandgap for n- and p-type Si substrate. Magnified D_{it} spectrum for (b) n-type and (c) p-type Si. D_{it} is plotted at an energy level corresponding to $V_{m,max}$ for 20 kHz, 50 kHz, 100 kHz, and 200 kHz frequency.

5.3.2.3 Dielectric leakage current density and breakdown field

Breakdown analysis is mandatory to ensure the sustainability of the dielectric to large voltages. Solar cells in the field undergo reverse biasing due to partial module shadowing [167]. This reverse bias may cause a significant voltage drop across the dielectric which might lead to its breakdown [168]. When biased with high voltage, the film might lose its dielectric property and become conducting and hence leaky. J_{leak} and E_{BD} were determined with reference to an oxide electric field E_{ox} (V cm^{-1}) calculated using equation (5.1) and were extracted from I-V characteristics of alnealed MOS capacitors biased in accumulation region by applying positive and negative gate voltage for n-type and p-type Si substrates, respectively.

$$E_{ox} = \frac{V_G - V_{FB}}{EOT} \tag{5.1}$$

where V_{FB} and EOT are the flat band voltage (V) and effective oxide thickness (cm), respectively, extracted from the measured and series resistance corrected C-V curve. The quoted J_{leak} values are extracted at E_{ox} of 1 MV cm^{-1} for consistency and comparison with the data from the literature. E_{BD} was calculated from equation (5.1) by substituting V_G with the breakdown voltage (V_{BD}).

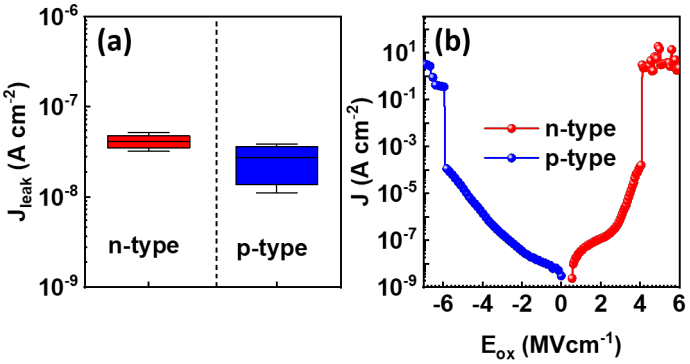

Figure 5.14: (a) Range of leakage current density (J_{leak}) extracted at E_{ox} = 1 MV cm^{-1} considering five different MOS capacitors. (b) Typical J_{leak} versus E_{ox} for MOS capacitor each on n-type and p-type substrates in accumulation mode. All samples were subjected to PDA at 650°C in O_2 ambient and PMA at 450°C in FG ambient.

J_{leak} in the range of 2.2 - 5.17×10^{-8} Acm^{-2} on n-type and 1.12 - 3.96×10^{-8} Acm^{-2} on p-type substrate for ~17 nm film was obtained (Fig. 5.14(a)). This implies that the oxide deposited on p-type substrate is less leaky. Typical J-V characteristics for a MOS capacitor on Si of either of the dopant type is shown in Fig. 5.14(b).

Breakdown statistics was analyzed using Weibull distribution as it can model the breakdown field of the insulating system and hence can be used to estimate the electric field associated with the probability of breakdown. The details of the Weibull distribution plot and analysis have been presented in section 3.1.4. Weibull distribution plot of E_{BD} of deposited SiO_2 film on n-type and p-type substrate is shown in Fig. 5.15. The characteristic oxide breakdown field for ~17 nm film on n-type substrates was calculated as 4.3 MVcm^{-1} and 5.6 MV cm^{-1} on p-type substrate. β was calculated as 4.2 and 5.0 for the film on n- and p-type substrates, respectively. Leakage and breakdown analysis concludes that the SiO_2 dielectric film on p-type Si substrate has higher breakdown field strength, smaller breakdown field range, and is less leaky in comparison to the film on n-type substrate. This might be due to smaller oxide charges in the film deposited on the p-type, which is consistent with the Q_f analysis in the last section. J_{leak} and E_{BD} values in

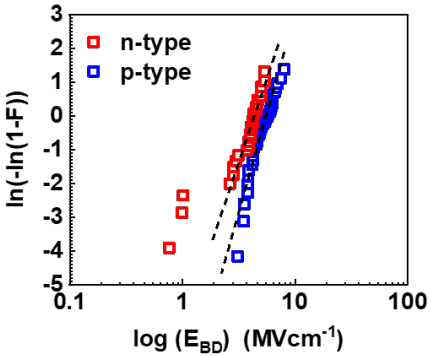

Figure 5.15: Weibull distribution of oxide breakdown field strength of spray-coated SiO_2 film annealed in O_2 at 650°C and alnealed in FG at 450°C on n- and p-type Si substrates. 28 and 36 MOS capacitors on n-type and p-type Si, respectively were characterized for Weibull analysis. Outliers were not considered for a straight-line fit of the distribution data.

our experiment are better than the sol-gel spin-coated film realized by Jaehnike et al. for approximately the same oxide thickness (~20 nm) [85].

5.3.3 Silicon surface passivation

S_{eff} is a parameter that characterizes the recombination at the Si surface and its effectiveness as a recombination site. We used equation 2.21 from chapter 3 for S_{eff} calculation as the samples investigated in our study satisfy both the constraints of symmetric surface passivation and low S_{eff}.

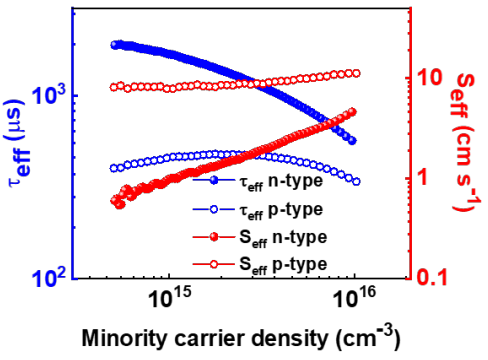

Figure 5.16: Injection level dependent effective lifetime and corresponding calculated S_{eff} of lifetime structures for SiO_2 film on both n-type and p-type Cz Si annealed in O_2 ambient at 650°C and alnealed at 450°C in FG ambient.

Measured τ_{eff} and corresponding S_{eff} of symmetric lifetime structures with alnealed SiO_2 film on either sides of the wafer are plotted as a function of excess minority carrier

Table 5.3: S_{eff} realized with the passivating layer(s) deposited by various techniques on double side polished n- and p-type Si surface.

Passivating layer(s)	Process details	Substrate	S_{eff} (cm s^{-1})	D_{it} ($cm^{-2}eV^{-1}$)	Q_f (cm^{-2})	Reference
Thermal SiO_2	1050°C/120 min/ TCA[a]/O_2; alneal (400°C /30 min/FG)	n-type, FZ, 1.5 Ωcm	2.4	-	-	[56]
		p-type, FZ, 1 Ωcm	11.8	-	-	
Thermal SiO_2 (100 nm)	1050°C/DCE[b]/O_2; enhanced alneal	n-type, FZ, 1 Ωcm	0.4	3×10^{11}	1.7×10^{12}	[169]
Thermal SiO_2 (100 nm)	1050°C/DCE; anneal (425°C); corona discharge	n-type, FZ, 1 Ωcm	<0.6	-	4.5×10^{12}	[170]
PECVD a-SiO_x:H (250 nm)	150°C; anneal (250°C/FG/3 hrs)	n-type, FZ, 1 Ωcm	2.6	-	-	[62]
PECVD SiO_2/SiN_y (50nm/70nm)	SiO_2-300°C/ SiN_y-350°C; anneal (400°C/N_2/10 min)	n-type, FZ, 3.5 Ωcm	<6	-	$> 6\times10^{11}$	[13]
		p-type, FZ, 2.2 Ωcm	<11			
NAOS SiO_2	400°C/O_2/30 min;	n-type, FZ, 5 Ωcm	20-35	$< 3\times10^{12}$	$\sim2\times10^{12}$	[65]
Spin SiO_2 (260 nm)	875°C/10 min/O_2/N_2; FGA	p-type, 2.5 Ωcm	120	-	-	[171]
Spray SiO_2 (~16 nm)[c]	**PDA (650°C/30 min/O_2); alneal (450°C/FG/30 min)**	**n-type, Cz, 4-7 Ωcm**	**0.97**	**1.39×10^{10}**	**$7.1\text{-}9.4\times10^{11}$**	**This work**
		p-type, Cz, 4-7 Ωcm	**8.07**	**2.05×10^{10}**	**$3.9\text{-}6.5\times10^{11}$**	

[a] Trichloroethane; [b] Dichloroethelyne; [c] Film thickness was measured as 15.62 nm on n-type and 16.31 nm on p-type for lifetime samples using ellipsometer

density in Fig. 5.16. τ_{eff} of 1.67 ms and 459.52 μs were measured on n-type and p-type Si substrate, respectively at an injection level of 10^{15} cm^{-3}. The superior lifetime on n-type is due to its high bulk lifetime of 1.90 ms in comparison to p-type which was measured as 625.25 μs. S_{eff} of 0.97 cm s^{-1} and 8.07 cm s^{-1} was calculated from τ_{eff} and τ_b for n-type and p-type wafers, respectively at an injection level of 10^{15} cm^{-3}. This shows that spray-coated SiO_2 dielectric film provides superior passivation on n-type Si than on p-type. This can be attributed to the difference in the field effect component of passivation as there exists similar chemical passivation. The field effect component arises from the charges present in the dielectric, which was found out to be positive from C-V analysis, and of higher density on n-type Si than on p-type Si. Aberle et al. [19] demonstrated that

the better passivation of n-type by thermally grown SiO_2 can be attributed to the positive fixed charges and to the high electron to hole capture cross section ratio (σ_n/σ_p) at the Si-SiO_2 interface.

Table 5.3 lists S_{eff} data reported in the literature for SiO_2 film synthesized by various methods. All previous works listed in the table demonstrated passivation related properties on FZ Si wafers. In our work, we have used Cz Si, which is much more widely used for the fabrication of mono crystalline Si solar cells. S_{eff} realized in our experiment is less than alnealed thermal oxide, spin-coated oxide, NAOS film and PECVD films with and without incorporating SiN_x capping layer. S_{eff} demonstrated on n-type Si by Collett et al. [169] and Bonilla et al. [170] are slightly less. These reduced S_{eff} may be due to higher Q_f values ($> 10^{12}$ cm^{-2}) giving better field effect passivation in comparison to our work ($Q_f < 10^{12}$ cm^{-2}). Collett et al. introduced Na^+ ions into the film during processing and Bonilla et al. used corona discharge method to increase positive charges in the film. These results demonstrate the passivation capability of the spray-coated SiO_2 film both on n-type and p-type Cz Si substrates.

5.4 Conclusions

In this chapter, we demonstrated sol-gel based SiO_2 dielectric film deposition via spray-coating technique and investigated the film behavior on Si substrates with two different dopant types. Film properties were studied with various characterization techniques that confirmed analogous nature and composition with amorphous, nearly stoichiometric and ~1 nm roughness on either substrate type. Similar D_{it} (~10^{10} cm^{-2}eV^{-1}) was realized on both n- and p-type Si for ~17 nm film. This is the lowest reported value for sol-gel SiO_2 film, and is attributed to the UV-Ozone oxidation step prior to the spray-coating of the SiO_2 film and the alneal process. Fixed oxide charges in the order of ~10^{11} cm^{-2}, with higher magnitude on n-type than on p-type Si were obtained. Best D_{it} of 1.4×10^{10} cm^{-2}eV^{-1} on n-type and 2.0×10^{10} cm^{-2}eV^{-1} on p-type at 200 kHz lies at an energy level 0.27 eV from the conduction band edge on n-type Si and 0.263 eV from the valence band edge on p-type Si substrate. There is insignificant frequency dispersion in the range of frequencies (20 kHz to 200 kHz) considered for analysis. J_{leak} (~10^{-8} Acm^{-2}) and E_{BD} (~5 MVcm^{-1}) better than previously reported sol-gel SiO_2 films were achieved. Good passivation quality was demonstrated on both n-type and p-type Si, but more effective on n-type with S_{eff} of 0.97 cm s^{-1} and 8.07 cm s^{-1} on p-type Si. These S_{eff} values are the best reported so far for sol-gel and are comparable to other deposition techniques. Low D_{it} and S_{eff} for sol-gel SiO_2 film with industrial feasible spray-coating technique substantiate

its potential for the passivation of both n-type and p-type Si surfaces in advanced Si solar cell applications.

Chapter 6

Demonstration of Spray-SiO_2/PECVD SiN_x as Front Passivation Stack in Silicon Solar Cell

6.1 Motivation

Currently, industrial cells are fabricated on p-type Si wafers, where the heavily doped n^+ emitter is formed by $POCl_3$ diffusion ([2]). Therefore, the front surface passivation indicates the passivation of the n^+ emitter formed over a textured Si wafer. SiO_2/SiN_x stack is used at the front of p-type Si as it offers enhanced Si surface passivation [96, 172]. Interfacial SiO_2 can be obtained through various methods, including thermal oxidation [169], PECVD [13], UV-Ozone treatment [74] and other chemical processes [65]. It has been demonstrated that of all the oxides, thermally grown oxide capped with SiN_x gives the best passivation on n^+ emitter [166]. Oxide obtained via other methods provide similar passivation, yet inferior to the thermal oxide [166]. We have already demonstrated excellent passivation of n-type polished Si surface with SiO_2 film using industrially viable spray-coating technique in chapter 5.

It is challenging to deposit thin film throughout the surface of micrometer sized random pyramids using solution based techniques [173, 174]. Hou et al. reported perovskite Si tandem devices where perovskite was deposited using solution based technique on textured Si surface in such a way that the perovskite top surface is nearly flat [173]. This implies that the solution-processed perovskite film thickness varies along the textured surface. Thick film filling up the texture compromises the primary objective of effective light trapping provided by surface textures. A nanometer-thin SiO_2 passivating film

on micrometer-sized pyramids using the spray-coating deposition technique has not been demonstrated yet.

In this chapter, we report the passivation of n^+ textured Si surface with SiO_2/SiN_x stack, where the nanometer thin SiO_2 film is obtained by spray-coating deposition technique. The film coverage of the spray SiO_2 film over a textured surface is investigated. Further, the passivation provided by the spray SiO_2 capped with PECVD SiN_x over a heavily doped n^+ emitter surface is studied. The passivation quality is benchmarked with respect to the SiN_x film and thermal SiO_2/SiN_x stack. Finally, the performance comparison of Si Al-BSF solar cell fabricated with front spray SiO_2/SiN_x and thermal SiO_2/SiN_x stack is presented.

6.2 Experimental details

The experimental process flow for the fabrication of Al-BSF solar cell and corresponding passivation test structures on textured Si is shown in Fig. 6.1.

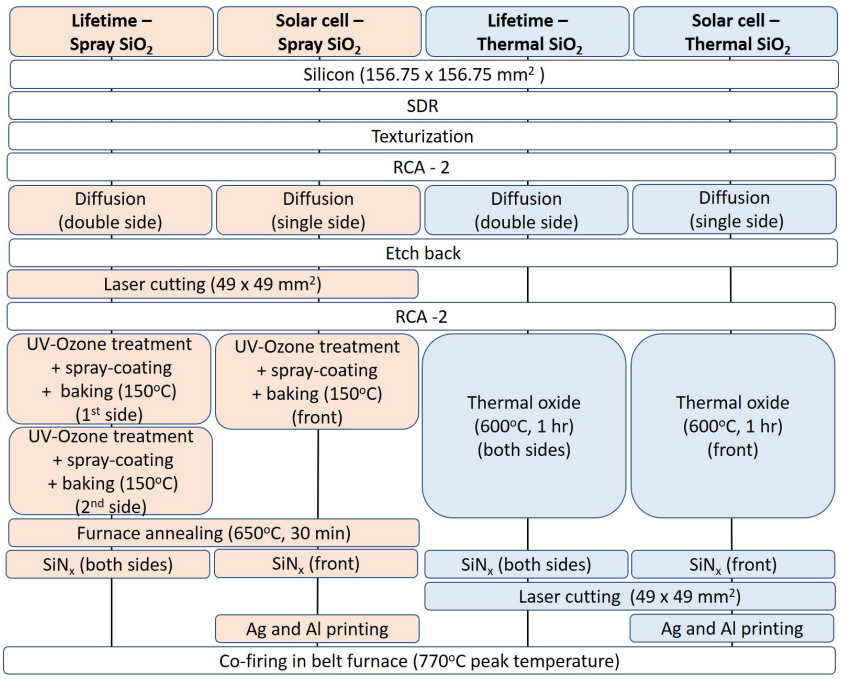

Figure 6.1: Process flow for the fabrication of Al-BSF cell and corresponding symmetrically diffused test structures passivated with spray and thermal SiO_2/SiN_x stack. Lifetime structures were also prepared with only SiN_x passivation.

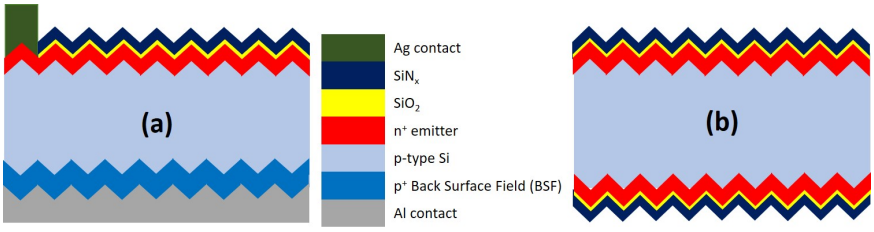

Figure 6.2: 2D schematic cross-section of (a) Al-BSF unit cell and (b) passivation test structure.

6.2.1 Solar cell fabrication

In this work, p-type (boron-doped), industrial grade monocrystalline Cz Si wafers (156.75 mm x 156.75 mm, <100>, 0.5-1.5 Ω-cm, ~180 μm) were used. The wafers underwent saw damage removal (SDR) in sodium hypochloride (NaOCl) followed by isopropanol and potassium hydroxide (KOH) alkaline solution based texturization process to generate random pyramids [175, 176]. After standard cleaning, the wafers were subjected to phosphorus diffusion using $POCl_3$ as a dopant source in a tube furnace (Protemp USA, Sirius PRO 200) at a peak diffusion temperature of 830°C. This was followed by phosphosilicate glass (PSG) removal in 2% HF solution. The wafers subsequently underwent etch back process in NaOCl solution at 80°C for 6 min [175] to obtain emitter with R_{sheet} of 65.62 Ω/sq. The R_{sheet} contour plot over the complete diffused Si wafer is shown in Fig. 6.3. Thereafter, the experiment was bifurcated into two sets. One set underwent spray-coating and the other thermal oxidation.

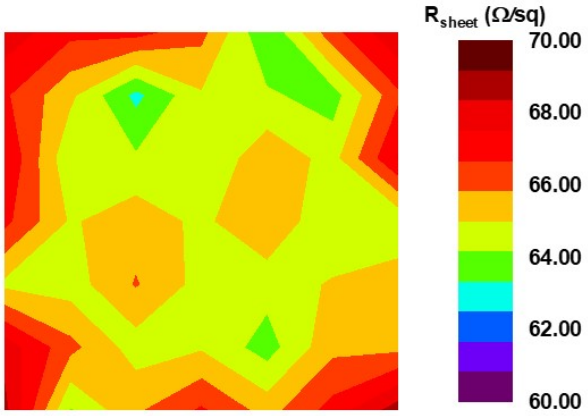

Figure 6.3: Sheet resistance (R_{sheet}) contour plot of the complete phosphorus diffused emitter wafer surface. R_{sheet} was measured using four point probe (4PP) tester (Jandel, MHP-12 & Multi-PT8) over a wafer area of 156.75 mm x 156.75 mm in a 7 x 7 matrix.

For spray-coating, 156.75 mm × 156.75 mm Si wafer was cut into 49 × 49 mm^2 sized squares. The cut wafers went through RCA-2 cleaning [155]. The emitter was exposed to Ultraviolet radiations in presence of O_2 ambient in a UV-Ozone chamber (Holmarc Mechatronics Pvt. Ltd, HO-TH-UV02). Solution with a molarity of 0.02 mol l^{-1} prepared with TEOS (Sigma-Aldrich, 99.999% trace metal basis) precursor, isopropanol (J.T. Baker, CMOS grade) solvent, DI H_2O, and HNO_3 (J.T. Baker, CMOS grade) was immediately sprayed on the UV-Ozone treated wafers and a custom-designed spray-coater equipment (Holmarc Mechatronics Pvt. Ltd) was used for spraying the solution over a vacuum-connected Si wafer. The details of the solution content quantities, preparation methodology, and spray-coating process are given in section 4.2.2. These sprayed wafers were subsequently baked at 150°C and further subjected to PDA at 650°C for 30 min in O_2 ambient. SiN_x was deposited on the top of the oxide at 380°C in a capacitively coupled PECVD system (Oxford Instruments, Plasmalab System 100). For the other set, processing was performed on the 156.75 mm x 156.75 mm Si wafer after etch back. Subsequently, RCA-2 was performed. Further, the wafer was subjected to thermal oxidation at 600°C for 1 hour. PECVD SiN_x was deposited over the thermally grown SiO_2. Thereafter, the wafer was cut into 49 x 49 mm^2 size squares for further processing.

Metal contacts were printed on a 49 x 49 mm^2 Si wafer processed upto SiN_x deposition of both the sets using a screen printer (Micro-tec) with Al paste (ALSOLAR, TLCO-07A33) for rear and Ag paste (Dupont, PV20A) for front metal contacts. The front metal pattern has a single busbar of 0.8 mm width and 24 fingers of 60 μm width each. The printed wafers were co-fired in a belt furnace (BTU, SinTerra) at a peak temperature of 770°C. The schematic cross-section of the Al-BSF unit cell is shown Fig. 6.2(a).

6.2.2 Lifetime structure fabrication

Symmetrically diffused (n^+-p-n^+) and passivated test structures (Fig. 6.2(b)) are used in this study to investigate the passivation potential of the spray SiO_2/SiN_x stack in comparison to SiN_x film and thermal SiO_2/SiN_x stack. All the process parameters including diffusion, spray-coating, PDA, thermal oxidation, SiN_x deposition, and belt furnace firing are identical to the cell fabrication process.

6.2.3 Characterization

The SiO_2 film coverage over textured Si was studied using a field emission scanning electron microscope (FESEM; Zeiss Ultra 55). The thickness of the dielectric thin films was measured using a spectroscopic ellipsometer (Sentech, SE800). Ellipsometry was conducted on four different points on the films deposited/grown on polished Si wafers

and a mean of those values was considered. Lifetime tester (Sinton Instruments, WCT-120) was used for the measurement of the iV_{oc} of the symmetrical diffused and passivated samples. PL images of the symmetrical test structures were obtained using a PL imaging setup (LumiSolarCell System, Greateyes) consisting of a bank of red LEDs of 660 nm wavelength as an excitation source. The dark and active area illuminated J-V characteristics of the cells were extracted with class AAA solar simulator (Abet Technologies, Sun 3000) under standard test conditions of AM1.5G spectrum, 1000 W m^{-2} intensity, and 25°C cell temperature. The spectral response and the reflectance of the cells were measured in the wavelength range of 300–1200 nm range using quantum efficiency measurement system (Bentham, PVE 300). The weighted average reflectance (WAR) of the dielectric layer over the textured surface was computed by weighing the simulated and measured reflectance against AM1.5G spectra.

6.3 Results and discussion

6.3.1 Optical simulations

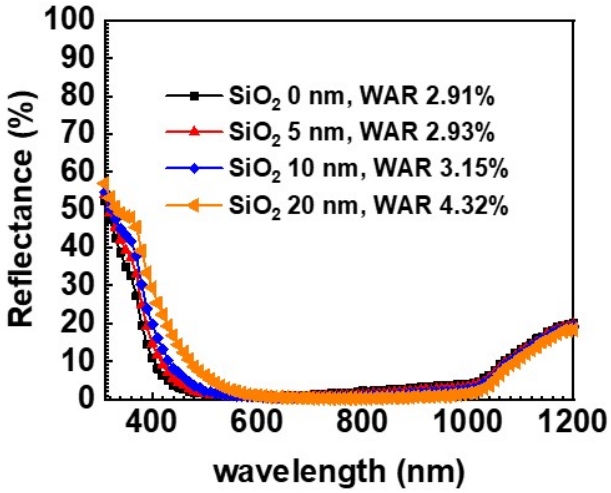

Figure 6.4: Sentaurus TCAD simulated reflectance curves computed for varying intermediate SiO_2 film thickness and fixed SiN_x of 63 nm. WAR is calculated for each of the reflectance characteristics.

The front dielectric layer or stack over the n^+ emitter of p-type Si solar cell acts both as an optical as well as a passivation layer. The optical properties of the front dielectric layer should ensure minimum reflectance from and maximum absorption into the Si absorber. SiN_x is the state of art ARC in Si photovoltaics as its refractive index can be

tuned to achieve minimal front optical reflection. Incorporating a SiO_2 film, which has low refractive index than SiN_x, as a passivating layer beneath SiN_x should not have an adverse effect on the optics (reflectance) of the solar cell [177]. To reduce the experiment time, we investigated the range of SiO_2 thickness over which the WAR of the SiO_2/SiN_x stack on textured Si would not change significantly through a simulation study performed in Sentaurus TCAD using the approach given in [178] (Fig. 6.4). The TCAD simulation deck was calibrated with the reflectance measured for Al-BSF cell fabricated at NCPRE lab. The details of the TCAD simulations are presented in chapter 7. SiN_x film alone gives a WAR of 2.9%. Incorporating a thicker (>10 nm) intermediate SiO_2 film leads to optical loss with a significant increase in WAR. However, SiO_2/SiN_x stack at the front with fixed SiN_x thickness and SiO_2 ≤10 nm has a WAR in the range of 2.9% to 3.2% on textured Si surface. In our work, the thickness of the spray SiO_2 film is 6.1 nm and thermal SiO_2 is 2.2 nm. Therefore, the simulation suggests that spray and thermal SiO_2 films would not add significantly to the optical losses in the solar cell.

6.3.2 Film morphology over textured silicon

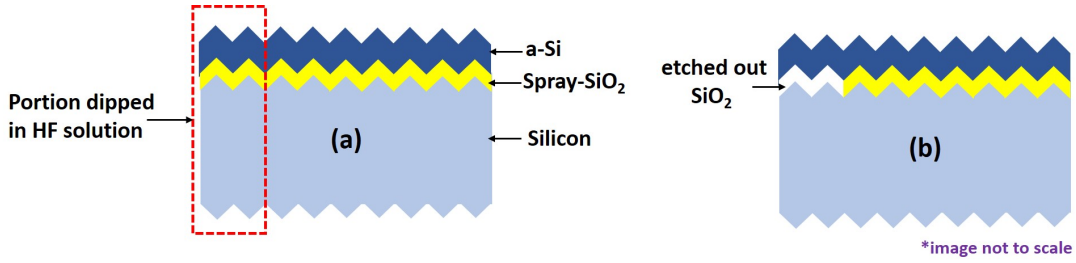

Figure 6.5: Schematic of the cross section of amorphous Si (a-Si)/spray-SiO_2/textured Si (a) before and (b) after sectional HF dip. A section of a-Si/spray-SiO_2/Si sample was dipped in 2% HF solution for 5 min to etch out a certain depth of spray SiO_2.

The surface morphology and the nature of the nanometer thin spray-coated SiO_2 film over textured Si is not yet reported elsewhere. To obtain a detailed insight into the conformal coverage of the deposited SiO_2 film over textured Si, a cross-sectional SEM imaging was performed. However, the thin spray SiO_2 film (~ 6 nm) could not be imaged due to the limitation of the SEM imaging technique. Therefore, an alternate way based on contrast imaging was used. An amorphous silicon (a-Si) film of thickness ~ 100 nm was deposited using PECVD (Oxford, Pro100) over the SiO_2 film on textured Si surface. Further, a section of the a-Si/spray SiO_2/Si was dipped in HF solution to sufficiently etch out the SiO_2 film for contrast imaging. The details and the schematic of the cross-sectional SEM sample preparation is summarized in Fig. 6.5. The cross-sectional image

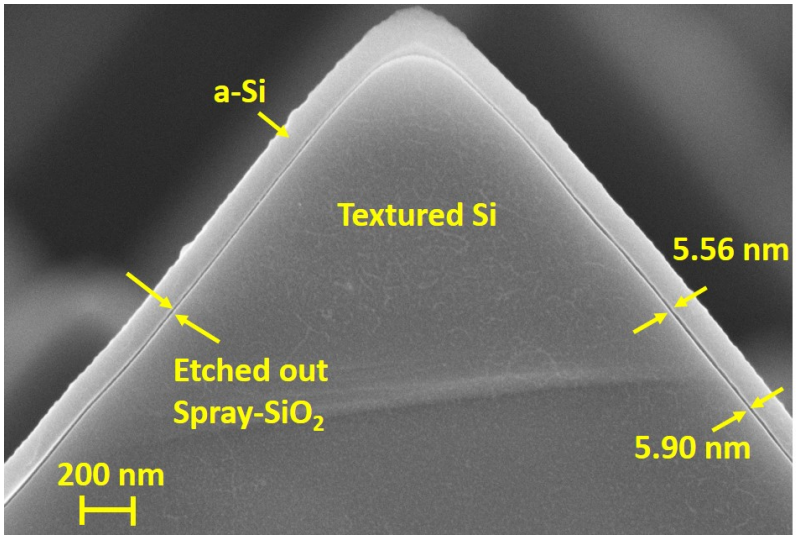

Figure 6.6: (a) Cross section SEM image of pyramid showing etched out spray SiO_2 beneath the supporting a-Si film.

of the resultant sample is shown in Fig. 6.6. The dark region between a-Si and textured Si which corresponds to the etched out SiO_2 layer is present over the entire pyramidal structure. From the cross-sectional SEM image it can be inferred that the spray-SiO_2 film covers the complete pyramid and therefore, is conformally deposited over the textured Si surface.

6.3.3 Passivation of n^+ emitter with SiO_2/SiN_x stack

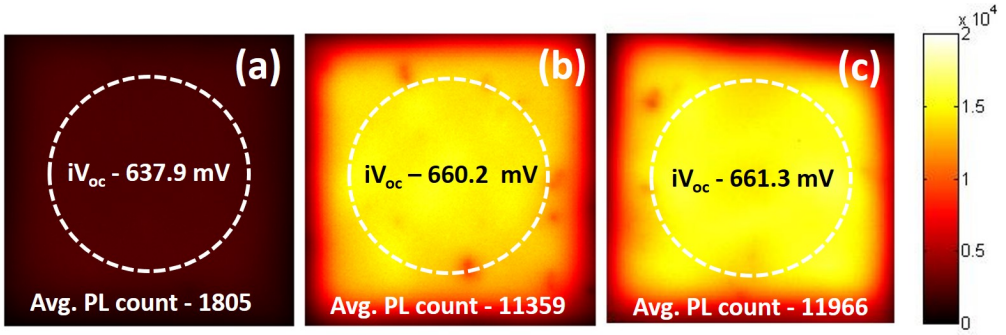

Figure 6.7: PL images of symmetrical emitter structure (n^+-p-n^+) passivated with (a) SiN_x, (b) spray SiO_2/SiN_x, and (c) thermal SiO_2/SiN_x stack.

The passivation of n^+ emitter was evaluated by measuring iV_{oc} of passivated symmetrical emitter structures. The enclosed area of the dotted circle shown in Fig. 6.7 corresponds to the 40 mm diameter sensor area of the lifetime tester used for iV_{oc} measurement. The upper limit of V_{oc} of the solar cell is represented by iV_{oc} as it does not take into ac-

count the recombination losses at the Si/metal interface. iV_{oc} of 637.9 mV is achieved for symmetric emitter structure passivated with SiN_x film. iV_{oc} increases significantly after incorporating a thin SiO_2 intermediate layer indicating enhanced Si surface passivation, attributed to the enhanced chemical passivation with an interfacial SiO_2 layer. iV_{oc} for spray SiO_2/SiN_x stack was measured as 660.2 mV and for thermal SiO_2/SiN_x stack the value was 661.3 mV. Nearly similar iV_{oc} values indicate that the passivation of the highly doped n^+ emitter provided by both spray SiO_2/SiN_x and thermal SiO_2/SiN_x stacks are comparable.

Further, the large area passivation uniformity of the spray SiO_2/SiN_x stack was investigated with PL imaging. Fig. 6.7 shows PL image of symmetrical diffused structures. SiN_x, spray SiO_2/SiN_x, and thermal SiO_2/SiN_x shows uniform passivation across the wafer area. Enhanced passivation due to SiO_2 film is apparent from the PL images. Spray SiO_2/SiN_x stack shows identical PL intensity distribution similar to the thermal SiO_2/SiN_x stack. From the passivation study, including iV_{oc} and PL imaging, it is evident that the spray and thermal SiO_2/SiN_x stack provides similar n^+ emitter passivation surpassing the passivation provided by the SiN_x alone. Due to inferior passivation with only SiN_x film, further study was performed on cells with emitter passivated only with spray and thermal SiO_2 capped with SiN_x film.

6.3.4 Solar cell performance

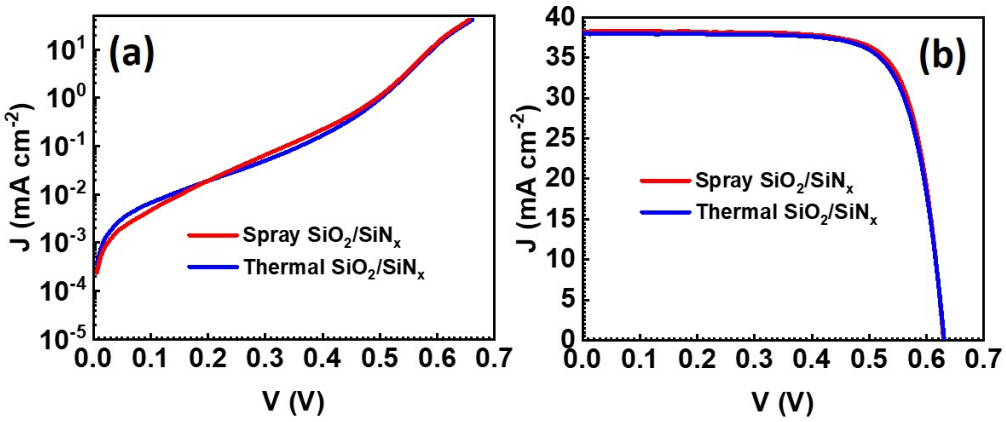

Figure 6.8: (a) Dark and (b) illuminated current density-voltage (J-V) characteristics of the cell with front spray SiO_2/SiN_x and thermal SiO_2/SiN_x stack.

Dark and illuminated J-V characteristics of the cells are shown in Fig. 6.8 and corresponding parameters are tabulated in Table 6.1. Saturation current densities (J_{01}), extracted from dark J-V characteristic is a representative of the recombination in the

Table 6.1: Comparison of illuminated I-V parameters for cell with front spray SiO_2/SiN_x and thermal SiO_2/SiN_x stack. The parameters are extracted by considering the active cell area.

Front dielectric stack	J_{sc} (mA cm^{-2})	V_{oc} (mV)	FF (%)	Efficiency (%)
Spray SiO_2/SiN_x	38.3	629.12	76.7	18.48
Thermal SiO_2/SiN_x	38.02	630.21	75.8	18.16

quasineutral bulk region and at the two surfaces. Therefore, in our case, J_{01} is also an indicator of the quality of the Si surface passivation provided by the overlying dielectric layer. The 2/3-diode model tool from the nanohub was used to extract the J_{01} value corresponding to an ideality factor of 1 [179]. The dark J-V fitting for this condition is at voltages beyond 0.5 V where the J-V curve for the samples with thermal and spray oxide coincides, giving similar J_{01} values. J_{01} is 9.7×10^{-13} A cm^{-2} for spray SiO_2/SiN_x and 1.0×10^{-12} A cm^{-2} for thermal SiO_2/SiN_x based cells. Similar J_{01} ($\sim1.0\times10^{-12}$ A cm^{-2}) for both the cells with spray and thermal SiO_2 confirm similar surface passivation. V_{oc} achieved for spray SiO_2 based cells, 629.12 mV is comparable to thermal SiO_2/SiN_x passivated cells, 630.21 mV.

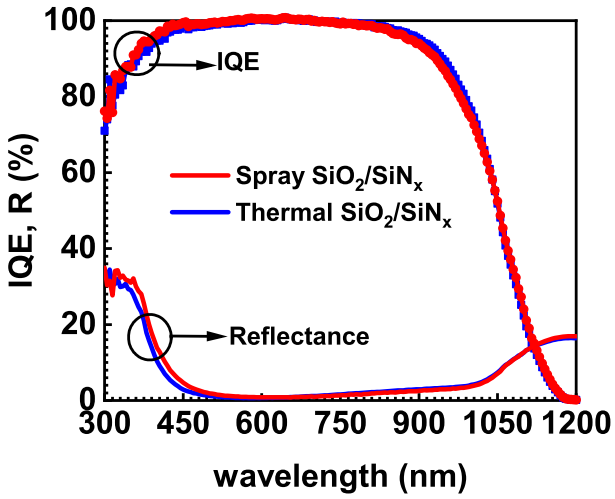

Figure 6.9: Internal Quantum Efficiency (IQE), and reflectance for the cell with front spray SiO_2/SiN_x and thermal SiO_2/SiN_x stack.

Fig. 6.9 shows the reflectance and IQE of the representative cells with spray SiO_2 and thermal SiO_2 as the passivating layers. In agreement with the simulation results presented in section 6.3.1, variation in surface reflectance is marginal for the cell with relatively thicker spray SiO_2 film as compared to thermal oxide. WAR of the textured Si with

spray SiO_2/SiN_x stack is 3.01% and 2.77 % for thermal SiO_2/SiN_x stack. Nearly comparable IQE values, especially in the blue region confirm that spray SiO_2 can be used as an effective replacement of the thermal oxide for passivating the n^+ diffused emitters. Conclusively, optical as well as passivation provided by the nanometer thin spray SiO_2/SiN_x stack is comparable to the thermal SiO_2/SiN_x stack at the front of the p-type Si solar cell.

6.4 Conclusions

We have successfully demonstrated nanometer thin SiO_2 film deposition over micrometer sized pyramids using an industrially viable spray-coating technique. SEM imaging confirmed the full coverage of the spray SiO_2 film over the pyramidal structure. Further, the passivation of the heavily doped n^+ emitter was accomplished by incorporating the spray SiO_2 passivating layer beneath the front SiN_x ARC layer. The passivation and the cell performance of the spray SiO_2/SiN_x stack were benchmarked against the thermal SiO_2/SiN_x stack. Similar iV_{oc} of ~ 660 mV indicates that the passivation provided by both the stacks was comparable. In addition, incorporating the spray SiO_2 as an intermediate layer provided uniform passivation of n^+ emitter across the wafer similar to the thermal SiO_2. The overall performance of the cell with spray SiO_2/SiN_x stack was comparable to the cell with thermal SiO_2/SiN_x stack. Therefore, SiO_2 deposited via an industrially feasible spray-coating technique demonstrates its potential to replace the thermal oxide to be used as the front passivating layer over heavily doped n^+ emitter of p-type Si solar cell.

Chapter 7

TCAD Simulation Study Comparing Advanced Cell Architecture (PERC and p-TOPCon) from a Passivation Perspective

7.1 Motivation

As discussed, the PV industries have adopted the PERC architecture over the conventional Al-BSF for solar cell production due to its superior rear surface performance [2]. However, the performance of PERC solar cells is still limited by the recombination at the localized metal/Si interface and higher series resistance due to the patterned contacts at the rear side. The TOPCon structures completely mitigate the above drawbacks as it uses a combination of ultrathin oxide and doped poly-Si layer, which offers an excellent full area rear side passivation and low contact resistance [66, 122].

TOPCon architecture on p-type Si is not widely implemented due to its inferior bulk quality and non-availability of efficient metallization schemes over its counterpart [124, 126]. However, recent reports suggest the manufacturability of gallium doped Si wafers with high bulk lifetime and do not show LID [5]. In addition, it has also been demonstrated that the bulk lifetime of the boron doped Si wafers could be enhanced after deactivation of boron-oxygen complex [180]. Further, Mack et al. identified commercially available Ag paste that allows low contact resistivity of 4-5 mΩ cm^2 [181]. These open up the window for the fabrication of TOPCon architecture over p-type Si. Switching from PERC to p-TOPCon will be more feasible as most of the existing PERC line processes can be used without major alterations. Implementation of p-TOPCon would pro-

vide hole selectivity and improved passivation at the rear compared to PERC. Therefore, the influence of carrier selective structure on the cell performance in terms of passivation needs to be evaluated against the rear dielectric passivated PERC. Numerical simulations of p-TOPCon and PERC would provide insight into the performance potential of the device prior to its industrial fabrication challenges.

In this work, numerical simulations are realized in Sentaurus TCAD to compare the performance of PERC and p-TOPCon test structures with respect to surface passivation. Both front and rear surface passivation effects are studied by considering surface recombination velocity. Before proceeding with the simulation study, the simulation environment of the solar cell needs to be calibrated with the environment of the real device.

7.2 TCAD calibration

7.2.1 Need for TCAD calibration

TCAD simulations mimic the devices which are actually fabricated using the same process flow. These simulations are carried out on the basis of a number of physical models and parameters present in the background. Appropriate physical models and parameters need to be selected and further tuned to suit the application. The selection and tuning are performed to minimize the error between the simulation output and the experimental data. This process of selecting appropriate model and tuning the parameters to achieve high accuracy with real world observations is known as TCAD calibration. To expect the electrical behavior of the fabricated device under test similar to the simulated one, it becomes mandatory to calibrate the TCAD environment with the device's behavior.

7.2.2 Calibration of Al-BSF silicon solar cell

The methodology followed is that the generation profile obtained from 3D optical simulation is used in 2D electrical simulations. Due to the different length scales of the symmetric unit element simulation domain, optical and electrical simulations are performed separately. The results of optical analysis performed on a smaller simulation domain (~μm) are linked to the electrical analysis performed on larger simulation domain (~mm). A 1D optical carrier generation rate profile is imported from 3D optical simulations and is given as an input to the 2D electrical simulations.

The optical, as well as the electrical model for general Si solar cell, was initially calibrated with the actual experimental data of Al-BSF cell fabricated at NCPRE lab with

19.4% efficiency. The 2D schematic of the Al-BSF unit cell is shown in Fig. 7.1(a). Al-BSF cell has a substrate thickness of 160 μm, bulk resistivity (ρ) of 2 Ω-cm, finger width (W_{finger}) of 45 μm, and finger pitch of 1775 μm. The emitter profile with R_{sheet} of 65 Ω/sq and the rear BSF profile are shown in Fig. 7.1(a) and (b).

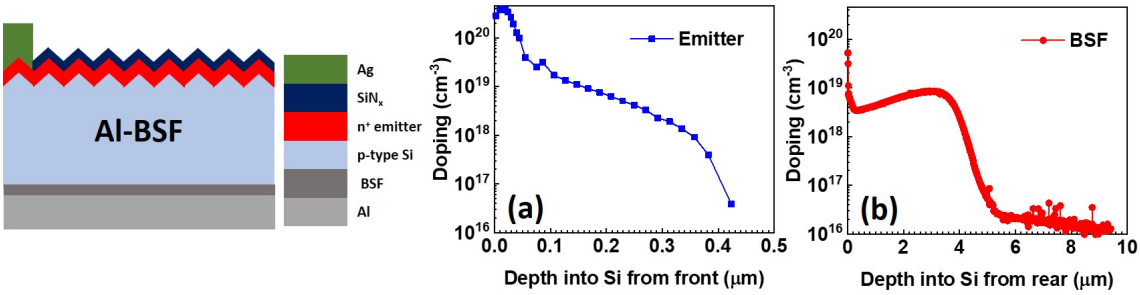

Figure 7.1: (a) 2D schematic of Al-BSF unit cell, (b) phosphorus emitter profile with R_{sheet} of 65 Ω/sq with active phosphorus doping concentration at varying depth into the Si from the front, and (c) BSF profile with active Al concentration varying along the depth of the Si from the rear end. These profiles are used in the simulations for Si solar cell calibration.

7.2.2.1 Reflectance calibration

The optical simulations were performed using an approach similar to that given in [178]. 3D structure on a p-type Si substrate of an area of 5 μm × 5 μm with a single pyramid at the front and planar rear surface is used for optical simulations as a symmetric unit. ARC of SiN_x thin film or SiO_2/SiN_x stack is included at the top of the pyramid. The ARC is modeled using the transfer matrix method. At the rear surface, Al layer is included. Front n^+ emitter and rear BSF doping profiles (Fig. 7.1(a) and (b)), obtained from ECV measurements were incorporated into the structure. The doping reduces the Si band gap and subsequently, affects the carrier generation due to the infrared light via the free carrier absorption (FCA) effect. Therefore, the FCA is included in the analysis. Here, Monte Carlo raytracing is used to achieve good simulation accuracy and efficiency. The reflectance data is obtained from the optical simulations. The analysis is performed to calibrate the simulated reflectance with the measured data. The 1D optical generation profile obtained at these optimized parameters is used in the subsequent electrical simulations.

The reflectance at wavelengths < 1000 nm was calibrated by tuning the optical properties including the refractive index, extinction coefficient, and thickness of the SiN_x ARC layer. The refractive index and extinction coefficient of SiN_x over textured Si of the test sample were measured using ellipsometry as shown in Fig. 7.2. Therefore, the reflectance

was calibrated by varying the SiN_x thickness (Fig. 7.3). The simulated reflectance for wavelength < 1000 nm was matched with measured reflectance at a SiN_x thickness of 63 nm.

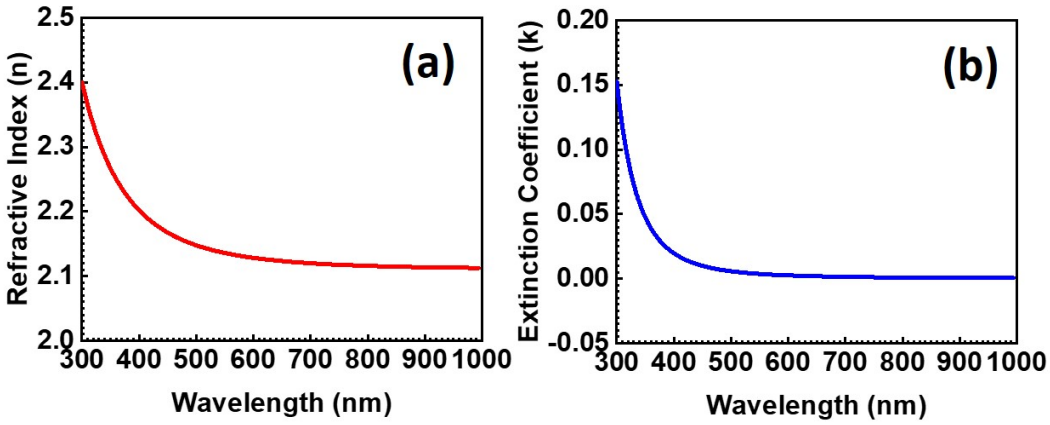

Figure 7.2: Measured wavelength dependent (a) refractive index and (b) extinction coefficient curve for PECVD SiN_x layer over textured Si test sample.

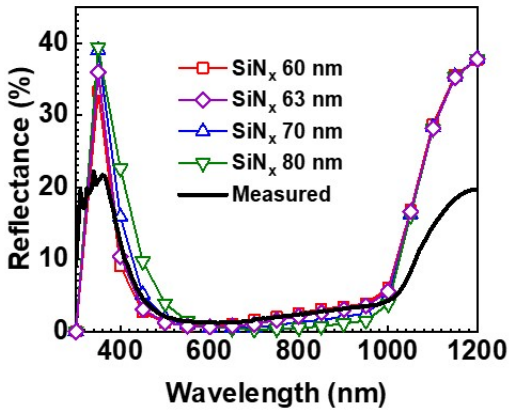

Figure 7.3: Simulated reflectance versus wavelength curve for varying SiN_x thickness with fixed measured refractive index and extinction coefficient.

At wavelengths greater than 1000 nm, internal light trapping becomes significant due to the rough surface at the rear of the cell [182, 183]. The roughness of the rear surface was modeled using Phong's scattering model [184]. It takes into account both the diffused and specular reflection of light at the rear textured Si/Al interface. The diffused component is modeled as [185]

$$R(\theta) = R_0(cos\theta)^{\omega} \tag{7.1}$$

Here, R_0 denotes the specular reflection, θ the angle between the specular and diffused light, and ω the Phong exponent. ω represents the level of diffuse reflection which depends on the roughness of the rear surface. Both R_0 and ω were taken into account for reflectance calibration at the longer wavelengths (Fig. 7.4). The measured reflectance for wavelength > 1000 nm was matched at R_0 of 0.88 and ω of 4.

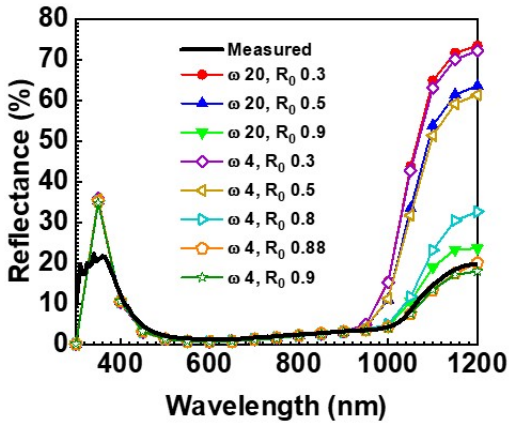

Figure 7.4: Simulated reflectance versus wavelength variation with Phong scattering parameters R_0 and ω for fixed SiN_x thickness and measured refractive index and extinction coefficient.

Therefore, the simulated reflectance was calibrated with the measured reflectance for SiN_x of 63 nm and Phong components R_0 of 0.88, and ω of 4 as shown in Fig. 7.5(a). The 1D generation rate profile corresponding to the calibrated reflectance is shown in Fig. 7.5(b).

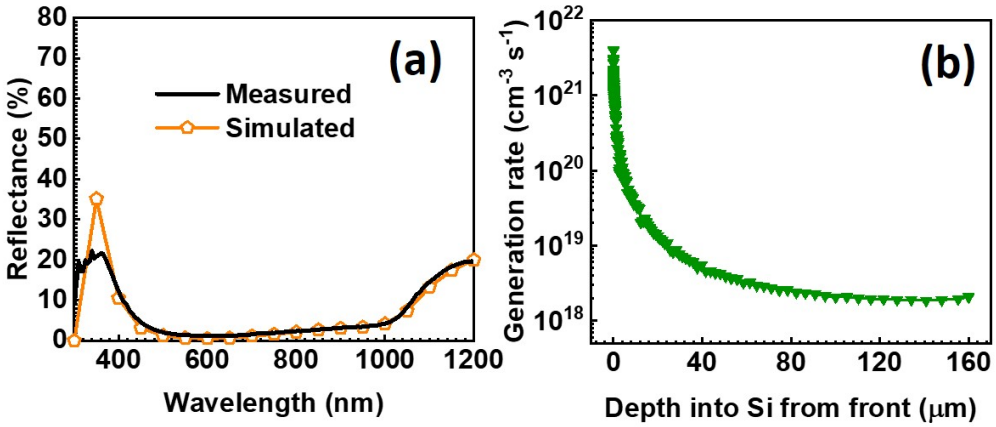

Figure 7.5: (a) Calibrated reflectance versus wavelength curve and (b) corresponding 1D generation rate profile obtained from 3D optical simulations for optimized SiN_x thickness of 63 nm and Phong scattering parameters R_0 of 0.88 and ω of 4.

7.2.2.2 Internal Quantum Efficiency calibration

IQE calibration was performed to get an insight into the recombination behavior within different regions of the actual cell. For QE simulations, wavelength dependent 1D optical generation profiles obtained from calibrated optical simulations were used. The recombination at the Si interface is studied in terms of surface recombination velocity. It is fixed to 10^7 cm s^{-1} at the Si/metal interface. Surface recombination velocity at the front Si/dielectric interface (S_{front}) is varied to correlate the IQE at the lower wavelengths. IQE increases with a decrease in S_{front}. The simulated IQE matches with the experimental IQE at S_{front} of 5×10^5 cm s^{-1} (Fig. 7.6(a)). The effect of bulk recombination was taken into account by τ_b. The IQE decreases with a decrease in τ_b in the longer wavelength range (> 500 nm) (Fig. 7.6(b)). The simulated IQE matches measured one at the longer wavelengths for τ_b of 70 μs. The measured and calibrated reflectance and IQE characteristics are shown in Fig. 7.7.

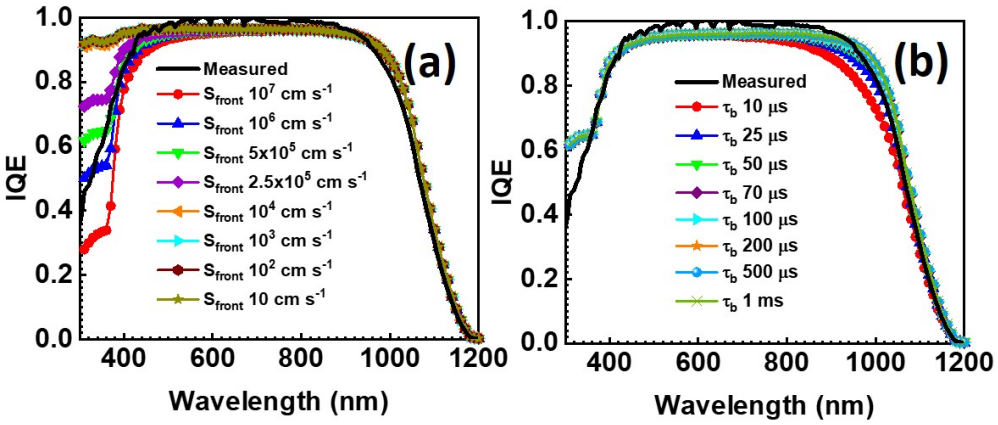

Figure 7.6: Simulated IQE versus wavelength variation with (a) S_{front} for fixed τ_b of 150 μs and (b) τ_b for fixed S_{front} of 5×10^5 cm s^{-1}.

7.2.2.3 Current - voltage calibration

I-V simulations were performed to confirm the accuracy of models and optimized parameters used in the earlier set of simulations. 1D optical generation profile as shown in Fig. 7.5(b) was given as an input for the I-V simulations. R_s of 160 mΩ-cm^{-2} is added to include the contact resistance. The calibrated I-V characteristics and the corresponding I-V parameters are shown in Fig. 7.8. With this calibration, the TCAD deck is ready for simulation of Si solar cell. The physical models used in simulations are tabulated in Table 7.1. Identical models as in Al-BSF architecture are used for PERC simulations.

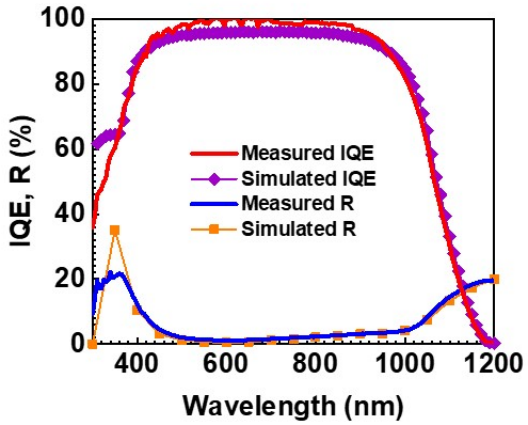

Figure 7.7: Measured and simulation calibrated reflectance and IQE versus wavelength characteristics of NCPRE Al-BSF cell.

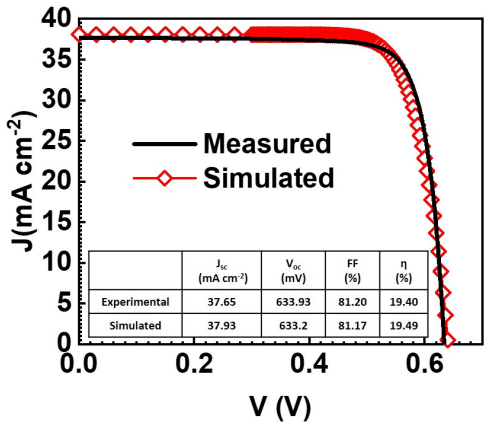

Figure 7.8: Measured and simulation calibrated J-V characteristics and performance parameters of NCPRE Al-BSF cell.

7.2.3 Calibration of TOPCon architecture

TOPCon with full area rear passivating contact architecture incorporates an ultrathin SiO_2 film (< 2 nm), which acts as tunneling oxide allowing carriers to tunnel through it. A 2 nm is the minimum oxide thickness at which tunneling becomes ineffective for metal-insulator-semiconductor solar cells [189]. Therefore, in addition to the general models used in Si solar cells as tabulated in Table 7.1, the nonlocal tunneling model was included to model the carrier transport through the ultra-thin interfacial oxide. The validation of the simulation setup was performed by fitting the experimental solar cell characteristics for TOPCon on n-type Si using the same input parameters as reported by Steinkemper et al. [134]. The experimental and simulated IV characteristics and corresponding output

Table 7.1: Physical modeling parameters used for simulations of Si solar cell.

Model/Parameter	Value
General	
Temperature	300 K
Intrinsic carrier density	$n_i = 9.65 \times 10^9$ cm^{-3} [25]
Free carrier statistics	Fermi-Dirac
Band gap narrowing model	Schenk [186]
Mobility	Klaassen [187]
Auger recombination	Richter [24]
Radiative recombination	$B_{rad} = 4.73 \times 10^{-15}$ cm^3 s^{-1} [17]
Metal/Si recombination velocity	10^7 cm s^{-1}
TOPCon	
Carrier tunneling	Nonlocal tunneling model [150]
Effective tunneling mass	$m_{te} = 0.40m_o$, $m_{th} = 0.32m_o$ [188]

parameters are shown in Fig. 7.9. This calibrated setup is used for the simulation study of the TOPCon architectures on p-type Si.

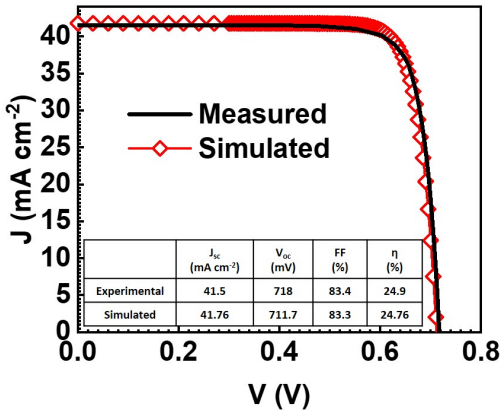

Figure 7.9: Experimental and simulation calibrated J-V characteristics and output parameters for TOPCon architecture on n-type Si [134].

The TCAD scripts for structure creation and Sdevice simulation of Al-BSF, PERC, and TOPCon are included in Appendix 9.

7.3 Results and discussions

The 2D schematics of the PERC and p-TOPCon unit cells used for the simulation study are shown in Fig. 7.10.

In this simulation work, the p-type Si substrate with a ρ of 2 Ω-cm, the thickness of 160 μm, and a τ_b of 900 μs is considered [110]. An emitter with R_{sheet} of 95 Ω/sq

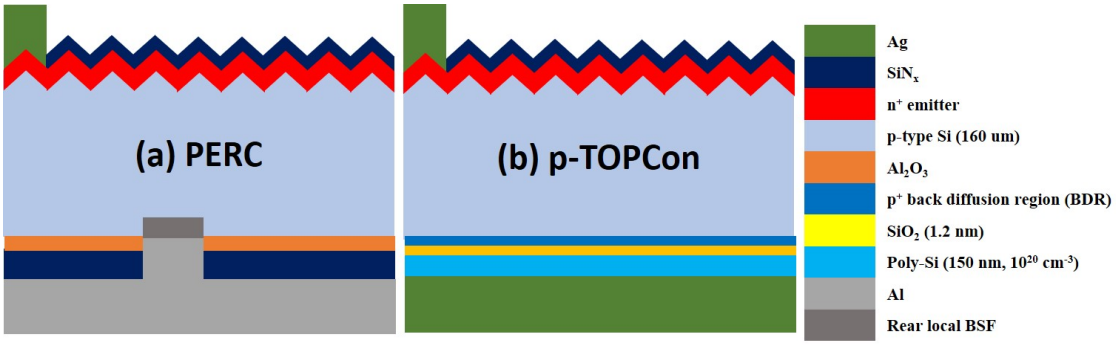

Figure 7.10: 2D schematic of PERC and p-TOPCon unit cells under study.

is considered [107]. These values closely match the current process parameters used for PERC solar cell production in the industry. A negative oxide charge of 10^{12} cm^{-2} is considered at the rear side Al_2O_3 dielectric layer and Si interface.

The surface recombination and therefore the surface passivation characteristics of the cell are evaluated in terms of V_{oc}. In all the simulations, passivation at the non-metalized interfaces is studied.

7.3.1 Rear side passivation

In Fig. 7.11(a), V_{oc} is plotted against the rear surface recombination velocity (S_{rear}). A similar trend is observed for both cells. However, the PERC cell is more sensitive to the rear surface passivation in comparison to p-TOPCon. The latter has a higher V_{oc} of 680.6 mV, constant for low S_{rear} ($\leq 10^3$ cm s^{-1}) and starts to decrease for $S_{rear} > 10^3$ cm s^{-1}. In PERC cell, V_{oc} is constant at 675 mV and decreases for $S_{rear} > 10^2$ cm s^{-1}. Therefore, p-TOPCon has an order of magnitude broader range of S_{rear} before the rear surface recombination starts dominating over the bulk.

For identical cell parameters, a V_{oc} of 653.1 mV is achieved for the Al-BSF cell. Therefore, $S_{rear} \leq 10^4$ cm s^{-1} and $S_{rear} \leq 10^5$ cm s^{-1} for PERC and p-TOPCon, respectively is required to ensure these cells outperform conventional Al-BSF from the passivation aspect. Therefore, PERC solar cell need comparatively stringent conditions on S_{rear} to surpass the V_{oc} obtained with Al-BSF cell. This is in contrast with the p-TOPCon cell where a broader range of S_{rear} could suffice for it to outperform both Al-BSF and PERC cells. Further, it can be observed from Fig. 7.11(b) that the efficiency follows the V_{oc} trend implying that the V_{oc} dominates the overall cell performance.

V_{oc} trend can be verified from the minority carrier electron concentration (n_s) at the rear passivating interface; Si/Al_2O_3 for PERC and Si/SiO_2 for p-TOPCon, at open circuit condition. For the identical base doping and front and rear surface passivation, n_s is lower

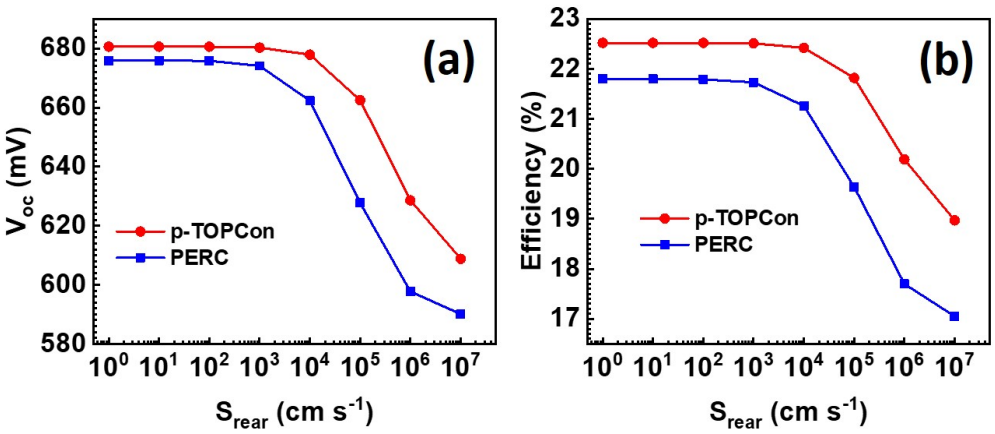

Figure 7.11: (a) V_{oc} and (b) efficiency variation with S_{rear} for p-TOPCon and PERC architecture.

in p-TOPCon leading to low surface recombination and therefore higher V_{oc} in comparison to PERC (Fig. 7.12(a)). The low n_s at low S_{rear} is clear from the energy band diagram at the rear interface of both the cells considered at open circuit condition (Fig. 7.12(b)). Larger band bending at Si/SiO_2 interface in p-TOPCon ensures a higher electric field repelling minority carriers (electrons) away from the rear surface. This minority carrier repulsion leads to reduced rear surface recombination in p-TOPCon in comparison to PERC.

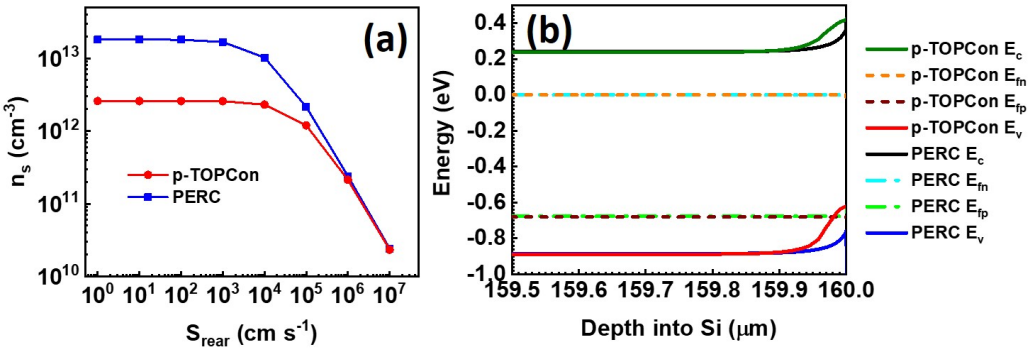

Figure 7.12: (a) Surface minority carrier concentration (n_s) and (b) band diagram at Si/SiO_2 interface for p-TOPCon and at Si/Al_2O_3 interface for PERC for S_{rear} of 1 cm s^{-1} at open circuit condition.

7.3.2 Front side passivation

With excellent rear surface passivation, the front surface limits the overall performance of advanced Si solar cells. In this work, a low emitter $J_{0e,pass}$ ~ 56 fA cm^{-2},

which corresponds to the S_{front} of 37000 cm s^{-1} was considered for an emitter R_{sheet} of 95 Ω/sq [107]. Passivation potential is studied by varying the S_{front} for different S_{rear} (10-1000 cm s^{-1}).

A similar V_{oc} and efficiency trend with S_{front} variation is observed for both PERC and p-TOPCon. Due to better rear passivation, PERC and p-TOPCon cell shows significant improvement in V_{oc} in comparison to Al-BSF (653.1 mV). At this S_{front}, PERC and TOPCon have V_{oc} of 680.6 mV and 675 mV, respectively considering S_{rear} of 10 cm s^{-1}. The sensitivity of PERC to S_{rear} can be verified from Fig. 7.13. Increasing S_{rear} from 10^2 to 10^3 cm s^{-1}, there exists no change in V_{oc} and efficiency of p-TOPCon, however, their values decrease in the case of PERC. There is a scope to increase the V_{oc} and efficiency of both the cells by improving the front emitter passivation. The results clearly indicate that p-TOPCon outperforms PERC for identical S_{rear}.

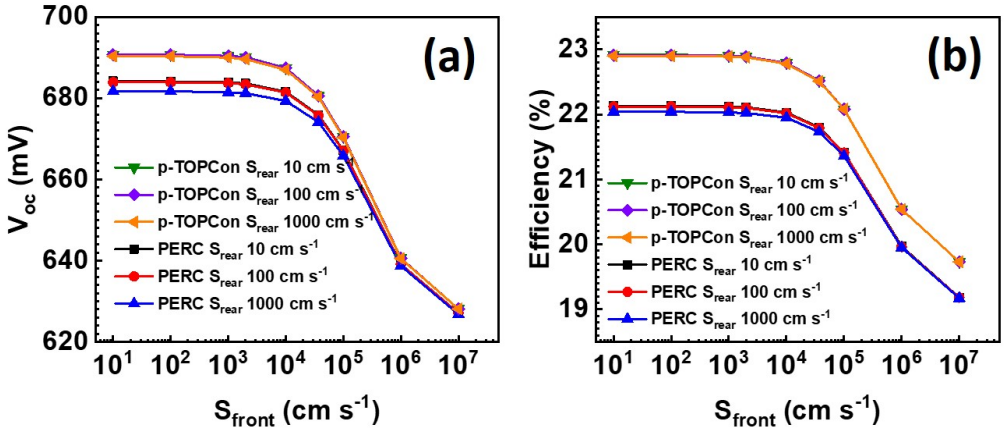

Figure 7.13: (a) V_{oc} and (b) efficiency variation with S_{front} for S_{rear} of 10, 10^2, 10^3 cm s^{-1} for p-TOPCon and PERC architecture.

7.4 Conclusions

In this chapter, initially, Sentaurus TCAD simulation deck was calibrated to simulate the Si solar cell. Thereafter, TCAD simulations were successfully performed to study the effect of front and rear surface passivation on PERC and p-TOPCon architecture with front n^+ emitter on p-type Si. The performance of p-TOPCon is less sensitive and has a broader range of operation to rear surface passivation than PERC. The V_{oc} and further, the efficiency decrement is at an order of magnitude higher S_{rear} in p-TOPCon than in PERC. Whereas, the V_{oc} and efficiency trend for S_{front} variation is similar for both cells. However, it is observed that p-TOPCon outperforms PERC for identical bulk lifetime, front emitter recombination, and rear and front surface recombination velocity.

Chapter 8

TCAD Based Numerical Exploration of Industrially Feasible Tunnel Oxide Passivated Contact on p-type Silicon

8.1 Motivation

Due to the better bulk quality of n-type Si and well established metallization of Ag paste by screen printing, the majority of TOPCon cells are being fabricated on n-type Si [124–126], as discussed in chapter 2. However, implementation of TOPCon architecture on p-type wafers would be more industrially feasible as a majority of the production lines use p-type wafers for solar cell fabrication. In chapter 7, we have also shown the superiority of the p-TOPCon architecture over PERC via TCAD simulations (chapter 7). Yan et al. demonstrated p-TOPCon architecture with an efficiency of 23% [129]. However, it has a 3% lower efficiency in comparison to Richter et al., who reported an efficiency of 26% for TOPCon cell on p-type Si [15]. This might be due to the implementation of n-TOPCon architecture over p-TOPCon and by adopting stringent fabrication processes in the former. Therefore, there exists a need to study this process window so that the maximum achievable performance of TOPCon cell on p-type Si with the industrially viable process and related parameters can be known. Numerical simulations of both p-TOPCon and n-TOPCon would provide insight into it.

In recent years, few simulation studies have been reported focussing on the p-TOPCon with SiO_2/poly-Si passivating contacts at the rear. Procel et al. studied the impact of the doping indiffussion in the Si wafer at the Si/SiO_2 interface on the transport and passivation with SiO_2/poly-Si(p) junctions by means of TCAD simulations [190]. Sigiura et al. evaluated TOPCon cell parameters by varying the tunneling oxide thickness

and bulk properties for p-type wafer using TCAD simulations [191]. Gao et al. have performed a Quokka based simulation study of p-TOPCon architecture with industrial grade process parameters reporting an efficiency of 22.40% [130]. Zeng et al. investigated cell parameters including τ_b and ρ, and carrier selectivity of poly-Si passivated contact on p-TOPCon cell through Quokka simulations [192]. However, none of these studies have considered front related parameters including the emitter and its passivation, which marks the bottleneck for advanced Si solar cell performance [192]. Therefore, a complete numerical study to have a better understanding of all design parameters including the bulk, rear, and front of p-TOPCon cell with industrial compatible values has not been reported. In addition, none of the above literature provides an in-depth comparison of the performance of p-TOPCon with PERC and n-TOPCon for the current and expected industrially relevant materials and process parameters. Such a study would be beneficial to identify the potential of TOPCon architecture on p-type wafers and evaluate its potential future developments for industrial production.

In this work, a comparative study of n-TOPCon, p-TOPCon, and PERC is performed by means of Sentaurus TCAD numerical simulations. The TCAD simulation model is calibrated against the published experimental results. Further, a detailed roadmap exclusively for p-TOPCon is presented where all the design parameters including the bulk (τ_b and ρ), rear (poly-Si related parameters), and front (emitter, passivation, W_{finger}) are studied. A roadmap to achieve efficiency > 23.50% with industrially viable p-TOPCon is discussed. The TCAD simulations suggest that further improvement in performance beyond 24% can only be achieved by replacing p-TOPCon with n-TOPCon architecture.

8.2 Results and discussion

The 2D schematic of the n-TOPCon, PERC, and p-TOPCon unit cell under investigation is shown in Fig. 8.1(a), (b), and (c) respectively. The geometrical and doping parameters used in the simulation of n-TOPCon, PERC, and p-TOPCon cells are tabulated in Table 8.1 and corresponding output parameters are presented in Table 8.2. Identical simulation approach as presented in chapter 7 is used in this chapter as well.

8.2.1 n-TOPCon solar cell

Simulations for advanced and industrial n-TOPCon cells were performed and the results were compared with Quokka simulations reported by Gao et al. [130]. Gao et al. considered an external R_s of 200 mΩ-cm^2 in their simulation work. However, recent studies suggest that R_s associated with TOPCon solar cells is <100 mΩ-cm^2 [181]. Therefore,

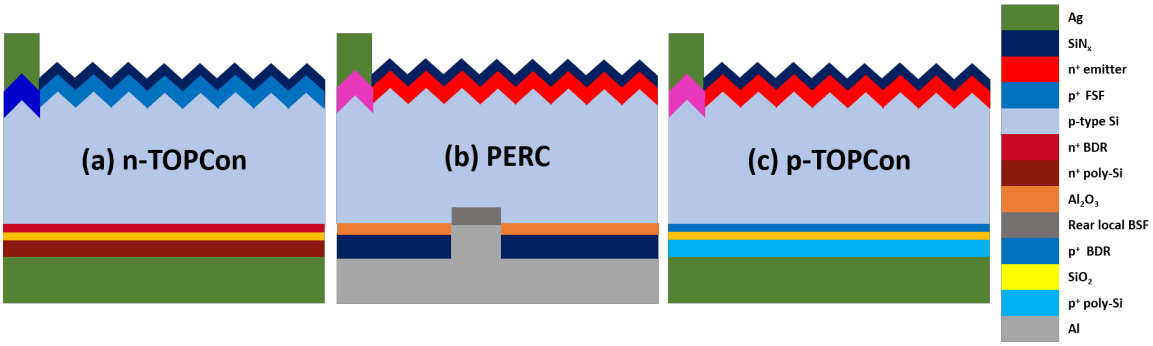

Figure 8.1: 2D schematic of (a) n-TOPCon (b) PERC and (c) p-TOPCon unit cells.

Table 8.1: Geometrical and doping parameters used in simulation of advanced and industrial n-TOPCon, PERC, and p-TOPCon cell on p-type Si.

Parameter	n-TOPCon (advanced)	n-TOPCon (industrial)	PERC	p-TOPCon
Substrate thickness (μm)	160	160	160	160
Finger pitch (μm)	700 [130]	1775	1775	1775
Finger width (μm)	10	45	45	45
Bulk resisitivity (Ω-cm)	1	1	1	1
Bulk SRH lifetime (ms)	100	1	1	1
Diffused emitter R_{sheet} (Ω/sq)	-	-	95 [107]	95 [107]
Front passivated $J_{o,pass}$ (fA cm^{-2})	10	50	56 [107]	56 [107]
Front surface field depth (nm)	400 [130]	400 [130]	-	-
Selective emitter R_{sheet} (Ω/sq)	30 [130]	30 [130]	75 [193]	75 [193]
Poly-Si thickness (nm)	150	150	-	100
Tunneling SiO_x thickness (nm)	1.2 ([190, 194])	1.2 ([190, 194])	-	1.2 ([190, 194])
Poly-Si doping (cm^{-3})	10^{20} [130]	10^{20} [130]	-	5×10^{19} [181]
BDR junction depth (nm)	50 [130]	50 [130]	-	100 [181]
S_{rear} (cm s^{-1})	10	10	10	10
Rear contact opening (μm)	-	-	40	-

the effect of external R_s is not included in our simulation study. The performance parameters; J_{sc} and V_{oc}, of TCAD simulated n-TOPCon structures are comparable to the values reported by Gao et al. [130]. Marginally higher FF in our case is due to an assumption of neglecting the R_s. An efficiency of 25.07% is achieved for advanced n-TOPCon cell for an extremely high τ_b of 100 ms and aggresively reduced W_{finger} of 10 μm. It has been demonstrated that the performance of the back emitter solar cells are highly prone to recombination in the bulk and high bulk quality is mandatory [195]. In addition, such a low value of W_{finger} is not achievable with the current industrially viable screen printing technique. Industrially relevant parameters with a τ_b of 1 ms and W_{finger} of 45 μm bring down the efficiency to 22.94%. Interestingly, p-PERC with the industrial design parameters as

Table 8.2: Output parameters of advanced and industrial n-TOPCon, PERC, and p-TOPCon Si solar cell.

	J_{sc} (mA cm^{-2})	V_{oc} (mV)	FF (%)	η (%)
Advanced n-TOPCon [130]	40.91	725.2	83.92	24.9
Industrial n-TOPCon [130]	39.63	697.1	82.42	22.8
This work				
Advanced n-TOPCon	40.63	725	85.11	25.07
Industrial n-TOPCon	39.33	698.8	83.46	22.94
PERC	39.34	679	82.44	22.02
p-TOPCon	40.08	683.8	82.77	22.69

given in Table 8.1 results in an efficiency of 22.02%. Higher efficiency in n-TOPCon is due to a 19.80 mV gain in V_{oc} and 1.02% gain in FF (Table 8.2). J_{sc} for n-TOPCon has similar values as that of PERC (Table 8.2). For n-TOPCon to replace PERC, a reversal of all the processes at the front and rear is needed. However, for p-TOPCon only the rear of the PERC has to be modified.

8.2.2 p-TOPCon solar cell

The results for industrial p-TOPCon show that its efficiency is only 0.25% lower than n-TOPCon (Table 8.2). Although V_{oc} and FF are lower, there is a gain in J_{sc} in comparison to n-TOPCon. p-TOPCon is an extension of p-PERC and there is already a roadmap available for the current industrial processes and design parameter upgradation [2]. In this work, all the industrial relevant cell design parameters related to the bulk, rear, and front of the p-TOPCon cell are considered for predicting its maximum possible conversion efficiency.

8.2.2.1 Bulk: lifetime and resistivity

The bulk property of the Si substrate is defined by its lifetime as well as its doping (resistivity). Therefore, the effect of these two parameters on cell performance is investigated. In Si solar cells, the bulk minority carrier lifetime should be adequately high to guarantee the collection of the generated carriers by the metal contacts prior to their recombination in the bulk itself. Bulk recombination is one of the major contributors to the recombination losses, limiting the efficiency of the cell. Currently, industrial-grade Si wafers have a τ_b in the range of 250 μs - 1.5 ms [110, 196, 197] and it has been demonstrated that the lifetime can be improved to nearly 4 ms after boron–oxygen complex deactivation [180]. Recently, Horzel et al. has shown that an impressive lifetime in the range of 3 ms - 17 ms

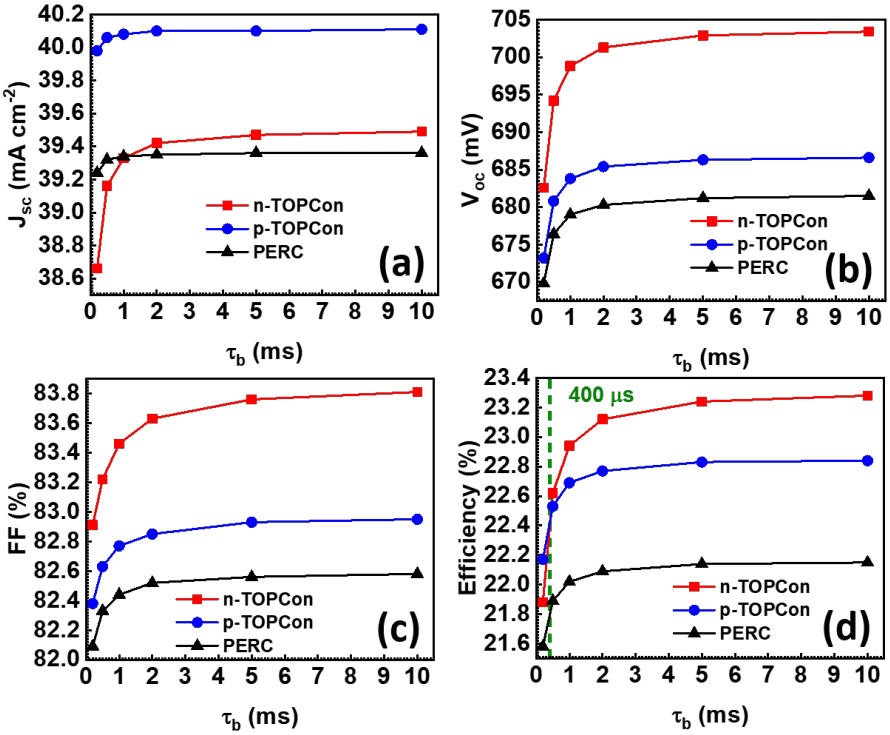

Figure 8.2: (a) J_{sc}, (b) V_{oc}, (c) FF, and (d) efficiency variation with bulk lifetime (τ_b) for industrial n-TOPCon, p-TOPCon, and PERC cell with 1 Ω-cm bulk resistivity.

can be achieved for gallium doped Cz grown p-type wafers [5]. Hence, in this work, τ_b is varied from 200 μs to 10 ms. The n-TOPCon, p-TOPCon, and PERC cell performance variation with τ_b is shown in Fig. 8.2. n-TOPCon has better performance when τ_b > 400 μs. Thereafter, the performance gap between n-TOPCon and p-TOPCon increases consistently with an increase in τ_b. n-TOPCon has better V_{oc} and FF in comparison to the other two for the entire range of τ_b. However, n-TOPCon performance is limited by low J_{sc} values (Fig. 8.2). n-TOPCon shows a large variation in the J_{sc} and V_{oc} for the industrial grade wafers with the lifetime range of 250 μs - 1.5 ms. Whereas, p-TOPCon shows lower variation in J_{sc} and V_{oc} values in the identical range of τ_b. Hence, the adoption of n-TOPCon would be appropriate for higher bulk lifetime (τ_b > 5 ms) as it may lead to significant variation in J_{sc} and V_{oc} for the current industrial grade wafers.

Further, the effect of ρ is evaluated on n-TOPCon, p-TOPCon, and PERC cells for τ_b of 1 ms, 5 ms, and 10 ms, and the results are shown in Fig. 8.3. n-TOPCon has a significant dependency of efficiency on ρ; especially for τ_b of 1 ms and efficiency reduces drastically for ρ < 1 Ω-cm. There exist a tradeoff in V_{oc} and FF with ρ for all three architectures; V_{oc} increases and FF decreases with increase in ρ. However, the tradeoff is more prominent in n-TOPCon. An order of magnitude decrease in J_{sc} is observed in n-TOPCon as compared to p-TOPCon for a change in ρ from 1 Ω-cm to < 0.5 Ω-cm. This

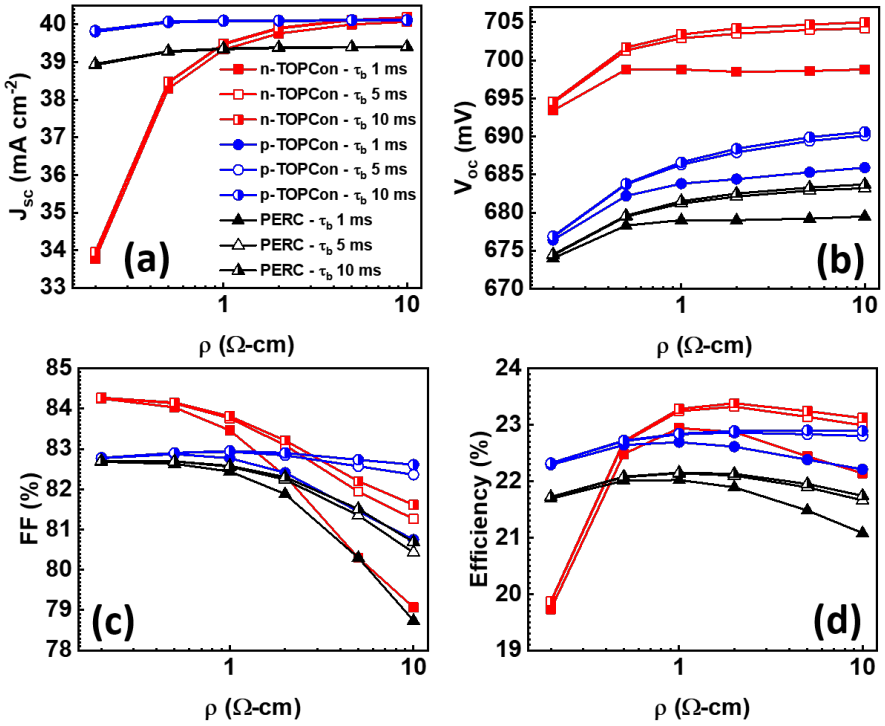

Figure 8.3: Bulk resistivity (ρ) effect on (a) J_{sc}, (b) V_{oc}, (c) FF, and (d) efficiency for industrial n-TOPCon, p-TOPCon, and PERC cell parameters with bulk lifetime (τ_b) of 1 ms and 5 ms.

pulls down the efficiency of n-TOPCon to a comparatively lower value to < 21% for $\rho <$ 0.50 Ω-cm. Therefore, n-TOPCon has inferior performance for low resistivity wafers. J_{sc} and V_{oc} increase proportionally with resistivity values. However, drastic decrease in FF limits the overall performance of n-TOPCon at higher resistivity regime. These trends are in agreement with the report of Richter et al. [15]. A similar increase in V_{oc} is observed in p-TOPCon. However, the decrease in FF is marginally lower than n-TOPCon for high resistivity range. Importantly, the simulations suggest that the performance of p-TOPCon and n-TOPCon is similar for high $\rho \sim 10$ Ω-cm. p-TOPCon outperforms PERC for all resistivity range under evaluation. In summary, both TOPCon architecture enables the use of high resistivity wafers with nearly identical efficiency values. Interestingly, maximum efficiency values were obtained for the resistivity range of 1-2 Ω-cm for all three types of solar architecture. In further simulations, current industry relevant τ_b of 1 ms and ρ of 1 Ω-cm are considered.

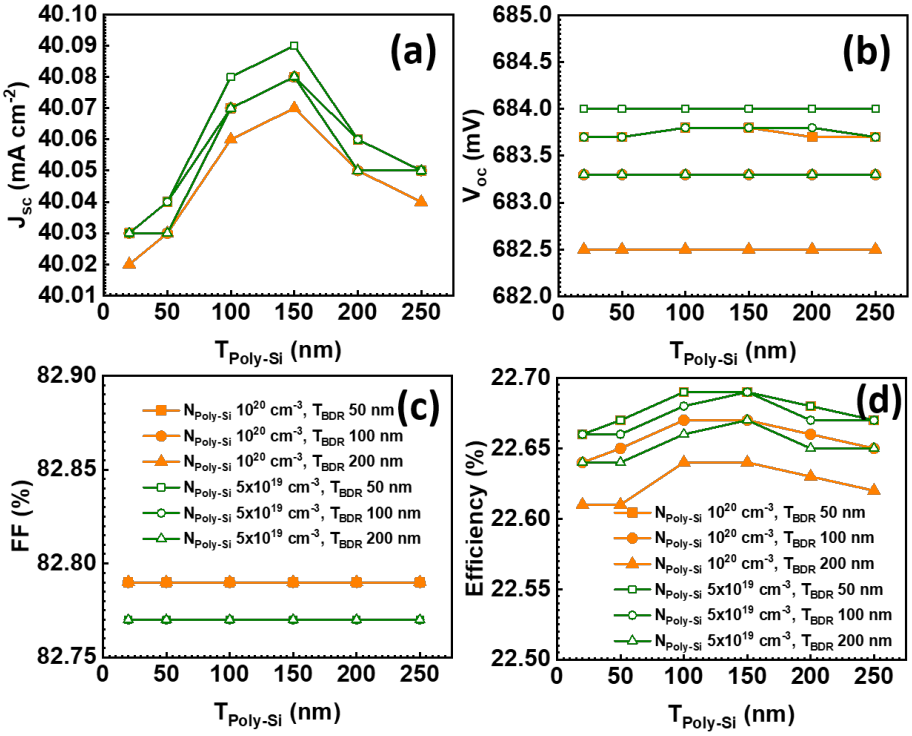

Figure 8.4: Effect of poly-Si thickness ($T_{Poly-Si}$), poly-Si doping ($N_{Poly-Si}$),and BDR depth (T_{BDR}) on (a) J_{sc}, (b) V_{oc}, (c) FF, and (d) efficiency for p-TOPCon cell.

8.2.2.2 Poly-Si: thickness, doping, and indiffusion depth

Along with the bulk, the rear side plays a crucial role in deciding the overall performance of the TOPCon cell. The rear of p-TOPCon comprises an ultra-thin SiO_2 and boron-doped poly-Si, which is generally deposited by Low Pressure Chemical Vapor Deposition (LPCVD) [198] or PECVD [199] followed by a high temperature annealing process. This annealing leads to the diffusion of boron from the poly-Si layer, acting as a dopant source, into Si forming a boron profile underneath the interfacial oxide. This indiffusion would be called the back diffusion region (BDR). Hence, three parameters have been considered for analysis; poly-Si thickness ($T_{Poly-Si}$), its doping ($N_{Poly-Si}$), and indiffusion depth (T_{BDR}) (Fig. 8.4). $N_{Poly-Si}$ is set to a constant value. BDR region is modeled as a gaussian profile with its peak the same as the $N_{Poly-Si}$ [190]. Typically, the $N_{Poly-Si}$ lies between 5×10^{19} cm^{-3} and 10^{20} cm^{-3} [181, 198, 200]. Hence, two different $N_{Poly-Si}$ of 5×10^{19} cm^{-3} and 10^{20} cm^{-3} were considered. T_{BDR} is the depth of BDR region from Si/SiO_2 interface into the Si bulk. T_{BDR} was varied from 50 nm to 200 nm [181, 200]. The $T_{Poly-Si}$ was varied from 20 nm to 250 nm [201].

No significant variation in performance is observed for all sets of poly-Si related parameters (Fig. 8.4). J_{sc} has a slight dependency on $T_{Poly-Si}$ where the maximum is at 150

nm. This dependency is translated to efficiency. There exist no V_{oc} and FF dependency on $T_{Poly-Si}$. This suggests that even 20 nm of poly-Si film is capable of giving the desired performance. The T_{BDR} has an adverse effect on V_{oc}. Its value decreases with an increase in T_{BDR}. However, the variation of V_{oc} with T_{BDR} is not significant. Similarly, the dependency of the $N_{Poly-Si}$ of 5×10^{19} cm^{-3} and 10^{20} cm^{-3} is also minimal. This suggests that the p-type poly-Si has a broader process window for all the poly-Si related parameters with efficiency values in the range of 22.60% to 22.70%. In further simulations, we have considered $T_{Poly-Si}$ of 150 nm, $N_{Poly-Si}$ of 10^{20} cm^{-3}, and T_{BDR} of 50 nm.

8.2.2.3 Front: Emitter sheet resistance, surface recombination velocity, and finger width

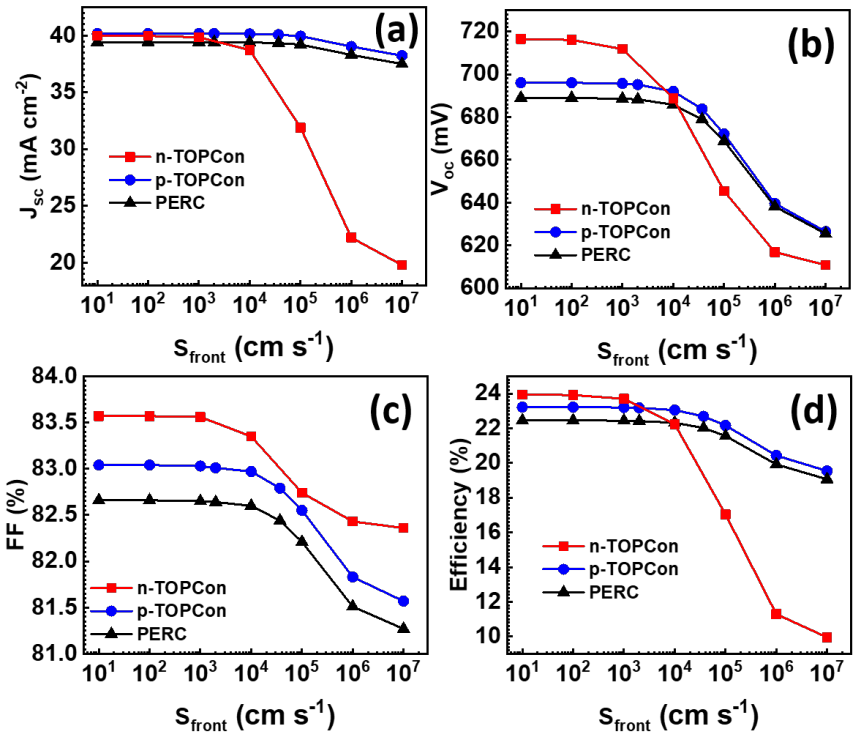

Figure 8.5: Impact of front surface recombination velocity (S_{front}) on (a) J_{sc}, (b) V_{oc}, (c) FF, and (d) efficiency of industrial n-TOPCon, p-TOPCon, and PERC cell for fixed rear surface recombination velocity (S_{rear}) of 10 cm s^{-1}.

With bulk and rear optimized, the front emitter would define the overall performance of the advanced cells. The front of n-TOPCon is different from p-TOPCon and PERC. n-TOPCon has a heavily boron diffused surface forming a FSF whereas p-TOPCon and PERC have heavily phosphorus diffused surface forming an n$^+$p junction. S_{front} is determined by the front diffused region and its passivation with an overlying dielectric

layer. The dependency of S_{front} on performance parameters of n-TOPCon, p-TOPCon, and PERC is shown in Fig. 8.5. n-TOPCon performance is highly sensitive to S_{front}. Its efficiency reduces drastically from 23.70% to 17.03% for a change in S_{front} from 10^3 cm s^{-1} to 10^5 cm s^{-1}. In n-TOPCon, V_{oc}, J_{sc}, and so efficiency starts decreasing significantly for S_{front} of 100 cm s^{-1}, whereas these degrades gradually for $S_{front} > 10^3$ cm s^{-1} in p-TOPCon, making the former highly sensitive to S_{front}. This sensitivity is attributed to a higher rate of loss of surface minority carriers (electrons in n-TOPCon and holes in p-TOPCon) with increasing S_{front} in n-TOPCon than in p-TOPCon. $S_{front} < 10^3$ cm s^{-1} is required for n-TOPCon to outperform p-TOPCon. Therefore, adopting n-TOPCon at the industrial level is not merely related to switching to new processes but also getting a stringent condition on the front passivation. In contrast to n-TOPCon, p-TOPCon and PERC is less sensitive to S_{front}. p-TOPCon has an order of magnitude higher range of S_{front} before the front surface recombination starts dominating over the bulk in comparison to n-TOPCon. However, p-TOPCon has superior performance than PERC.

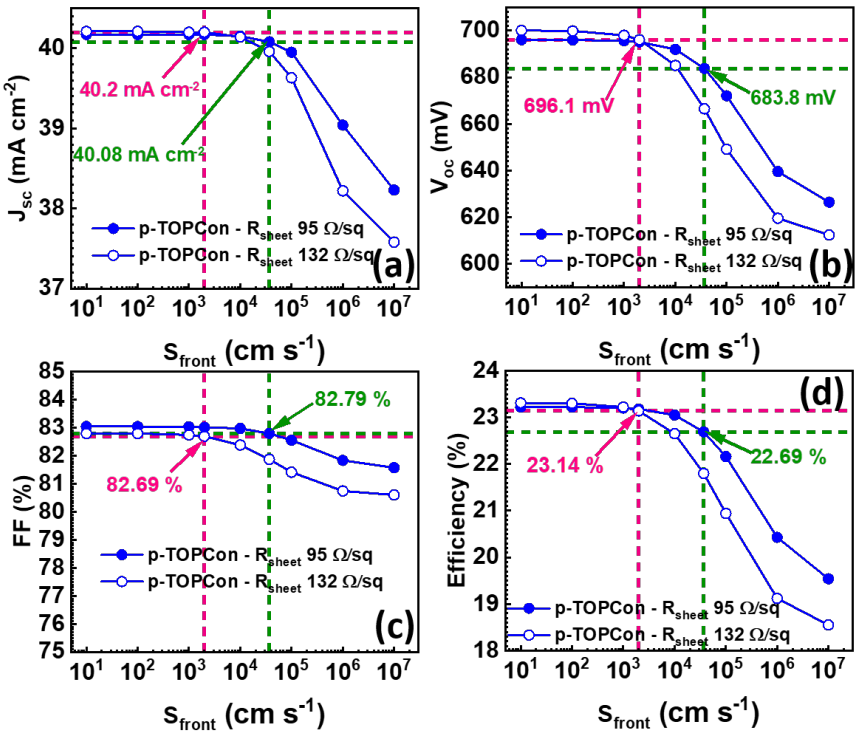

Figure 8.6: A comparison of (a) J_{sc}, (b) V_{oc}, (c) FF, and (d) efficiency of the p-TOPCon cell with two different emitter sheet resistance (R_{sheet}) of 95 Ω/sq and 132 Ω/sq.

Currently, emitter R_{sheet} of 90-100 Ω/sq is used in PERC technology [106, 107]. Hence, R_{sheet} of 95 Ω/sq having emitter $J_{0e,pass} \sim 56$ fA cm^{-2} (corresponding S_{front} of 37000 cm s^{-1}) [107] is used so far in all the PERC and p-TOPCon simulations in this work. Front surface passivation quality can be improved by reducing the surface peak

concentration of the emitter profile. Also, ITRPV predicts that the R_{sheet} of the phosphorus diffused emitter would go beyond 130 Ω/sq in five years down the line [2]. Profile with R_{sheet} of 132 Ω/sq allows for low $J_{0e,pass}$ of ~ 30 fA cm^{-2} (corresponding to S_{front} of 2000 cm s^{-1}) [202]. The p-TOPCon shows improved cell performance after incorporating R_{sheet} of 132 Ω/sq with J_{sc} of 40.20 mA cm^{-2}, V_{oc} of 696.10 mV, FF of 82.69%, and efficiency of 23.14% (Fig. 8.6). A clear enhancement in V_{oc} by 12.30 mV and efficiency of 0.41% is achieved over R_{sheet} of 95 Ω/sq.

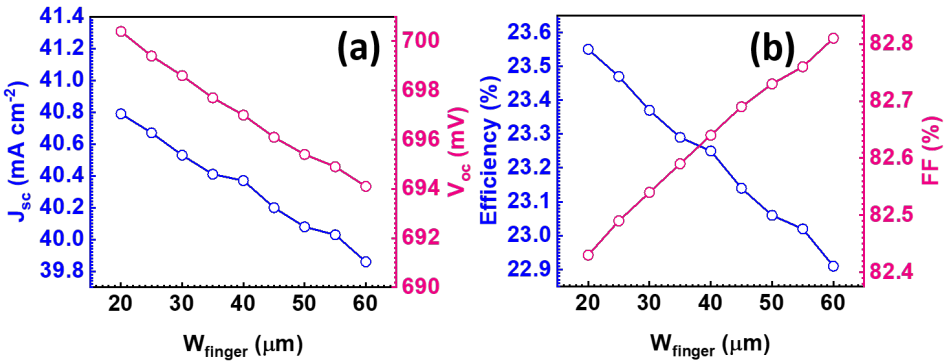

Figure 8.7: Influence of finger width (W_{finger}) on (a) J_{sc}, (b) V_{oc}, (c) FF, and (d) efficiency of p-TOPCon with emitter R_{sheet} of 132 Ω/sq.

Screen printing is the choice for electrical contact formation in industrial mass production. One of the major drivers of continuous increase in efficiency and reduction in cost of solar cells is the optimization of the screen printing process. It plays a critical role in W_{finger} reduction diminishing the optical shadowing loss. Finger width reduction to 20 μm appears possible over a decade [2]. Therefore, the W_{finger} has been varied down to 20 μm in the simulation (Fig. 8.7). FF increases whereas J_{sc}, V_{oc}, and efficiency decreases with increase in W_{finger}. Reducing W_{finger} from 45 μm to 20 μm significantly increases the efficiency from 23.14% to 23.55% for R_{sheet} of 132 Ω/sq.

8.2.2.4 Achievable efficiency with p-TOPCon and n-TOPCon

We have shown via simulations that an efficiency > 23% is achievable for p-TOPCon with industrially feasible cell design parameters. Fig. 8.8 consolidates the step by step performance variation with different cell parameters considered in this work. J_{sc} of 40.08 mA cm^{-2}, V_{oc} of 683.80 mV, FF of 82.77%, and efficiency of 22.69% is obtained with τ_b of 1 ms, ρ of 1 Ω-cm, R_{sheet} of 95 Ω/sq, and W_{finger} of 45 μm. By incorporating a higher R_{sheet} of 132 Ω/sq improves the J_{sc} by 0.12 mA cm^{-2}, V_{oc} by 12.30 mV, and enhances the overall efficiency by 0.45%. Further, the W_{finger} reduction to 20 μm also adds to an efficiency improvement by 0.41% with increment in J_{sc} by 0.59 mA cm^{-2} and V_{oc} by 4.30 mV. Both,

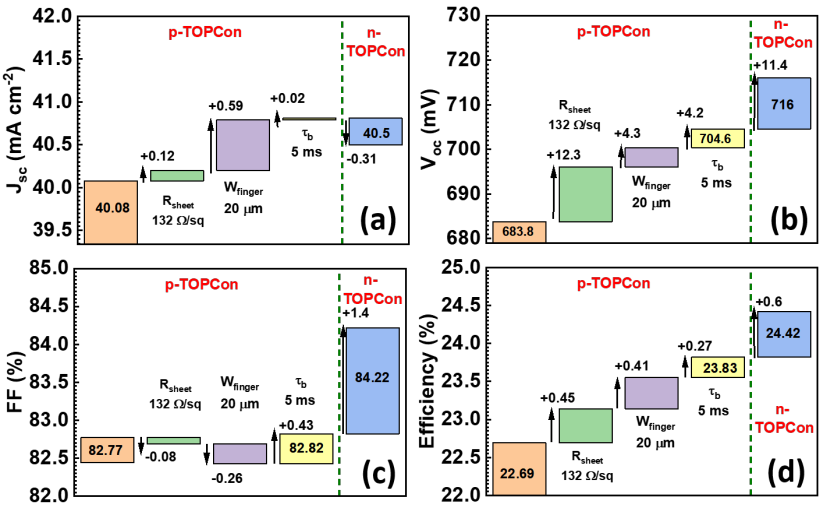

Figure 8.8: Variation in performance parameters for the projected upgradation in cell design parameters required for achieving efficiency beyond 23.8% for p-TOPCon and 24.4% for n-TOPCon solar cells.

high R_{sheet} and finger width reduction lead to an overall decrement in FF by 0.31%. In addition, by improving the bulk quality of the p-type Si wafer to atleast 5 ms, efficiency of 23.83% is achieved with J_{sc} of 40.81 mA cm^{-2}, V_{oc} of 704.6 mV, and FF of 82.82%. From our simulation study, it can be concluded that an efficiency > 24% is not attainable with p-TOPCon architecture with current industrial process parameters. However, the efficiency can be improved to 24.42% by implementing n-TOPCon with identical set of design parameters (τ_b = 1 ms, ρ = 1 Ω-cm, and W_{finger} = 20 μm). Switching from p-TOPCon to n-TOPCon does not change the J_{sc} values significantly. The comparable J_{sc} is obtained only after applying the designed roadmap in this simulation work. Remarkable improvement in V_{oc} by 11.40 mV and FF by 1.40% is obtained with n-TOPCon which enables overall efficiency gain of ~ 0.60%. Therefore, p-TOPCon can be an immediate replacement for industrial PERC with slight process modification targeting efficiency > 23.8%. In addition, simulation results indicate that p-TOPCon architecture has less sensitivity to τ_b, ρ, and S_{front} than n-TOPCon, ensuring better performance consistency suitable for batch processing (preferred for mass production) for an identical range of industrial relevant parameters. Further efficiency beyond 24.4% at industrial level on p-type Si can be targeted with n-TOPCon architecture discussed in this work.

8.3 Conclusion

The potential performance of p-TOPCon has been explored in Sentaurus TCAD considering the industrially relevant cell design parameters. Further, the results are compared with well established p-PERC and n-TOPCon solar cells. The variation in performance parameters with respect to τ_b, ρ, and S_{front} indicate that p-TOPCon is less sensitive over a wide range of these design parameters in comparison to n-TOPCon. Incorporation of high R_{sheet} of 132 Ω/sq and reduced W_{finger} of 20 μm with τ_b of 5 ms, and ρ of 1 Ω-cm can ensure conversion efficiency beyond 23.8% for p-TOPCon. Our simulation results suggest that p-TOPCon can be an immediate potential successor of PERC. However, improvement in efficiency beyond 24.4% can only be achieved for industrially relevant parameters by replacing the p-TOPCon with n-TOPCon architecture.

Chapter 9

Conclusions and Future Directions

This thesis revolves broadly around the passivation aspect of Si solar cells. In the first part, experimental work focusing on the development of nanometer thin SiO_2 film on both polished and textured Si surface as a passivating layer deposited via industrially viable spray-coating technique was presented. In the second part, a simulation work aiming at comparing the performances of advanced industrial Si solar cell architectures was presented.

Spray-coating being a solution-based technique, the properties of the film deposited via the same depend profoundly on the solution contents. For SiO_2 film, the effect of solvent on SiO_2 film, especially deposited via spray technique was not studied. Therefore, we started the study with four different solvents namely ethanol, isopropanol, 2-methoxyethanol, and 1-butanol. It was found that ethanol, isopropanol, and 2-methoxyethanol perfectly wets the superhydrophobic Si surface and therefore gives a continuous film on the same substrate, which is not the case with weakly hydrophobic Si surface. 1-butanol did not give film on both surface types via the spray-coating technique. Further, from thickness, refractive index, and porosity analysis, it was confirmed that 2-methoxyethanol gives comparatively uniform and dense film followed by isopropanol-based film. MOS capacitor analysis showed that 2-methoxyethanol based films gave an order of magnitude higher D_{it} ($\sim 10^{11}$ $cm^{-2}eV^{-1}$) in comparison to the other two solvents indicating its inferiority of passivating highly doped Si surface. In addition, ethanol purchase has been limited by the Federal government and isopropanol is extensively used in the semiconductor industry. Therefore, considering all the pros and cons, isopropanol seemed to be the perfect choice of solvent and was used in our further study.

Further being confirmed with the solution content, we proceeded with the in-depth analysis of the spray deposited SiO_2 film. Film properties were studied on Si wafers with two different dopant types. It was confirmed that the spray-SiO_2 film was amorphous

and nearly stoichiometric in nature on n- and p-type Si. The spray-SiO_2 film showed similar D_{it} ($\sim 10^{10}$ $cm^{-2}eV^{-1}$) with the best values of 1.4×10^{10} $cm^{-2}eV^{-1}$ on n-type and 2.0×10^{10} $cm^{-2}eV^{-1}$ on p-type. This is the lowest D_{it} reported for sol-gel films at a low annealing temperature of 650°C. Detailed MOS capacitor analysis for varying process conditions confirmed that this low D_{it} is due to UV-Ozone treatment and alneal process. It was found that these D_{it} values lie at an energy level of 0.27 eV from the E_c on n-type Si and 0.263 eV from the E_v on p-type Si substrate. Spray-SiO_2 film exhibits dielectric E_{BD} of 4.3 $MVcm^{-1}$ and 5.6 $MVcm^{-1}$ and J_{leak} of 2.2×10^{-8} Acm^{-2} and 1.1×10^{-8} Acm^{-2} at 1 $MVcm^{-1}$ on n- and p-type Si, respectively. These values are superior to sol-gel based SiO_2 films reported previously. Excellent passivation resulted in S_{eff} of 0.97 cm s^{-1} and 8.07 cm s^{-1} on n- and p-type Cz Si, respectively without the use of a capping layer. This indicates spray-SiO_2 passivates n-type better than p-type Si. S_{eff} values reported in this thesis are comparable to other deposition techniques for SiO_2 films. With these results, it could be said that the spray-SiO_2 film substantiates its potential to be used for Si surface passivation in solar cell applications.

The passivation potential of the spray-SiO_2 was successfully demonstrated on polished Si with comparatively better passivation on n-type Si. However, textured Si is used in Si solar cells. Therefore, the next target was to demonstrate the passivation potential of the film on phosphorus diffused n^+ emitter. Thermal SiO_2/SiN_x gives the best passivation of n^+ emitter. However, thermal SiO_2 is not industrially viable. We investigated spray-SiO_2 as a viable alternative to it. We successfully demonstrated full coverage over the deposited area with conformal deposition of a nanometer ($\sim$ 6.1 nm) spray-SiO_2 film over micrometer sized pyramid. Spray-SiO_2/SiN_x and thermal SiO_2/SiN_x showed iV_{oc} $\sim$ 660 mV with uniform passivation over the entire deposited area. Al-BSF cells fabricated with front spray-SiO_2 and thermal oxide as passivating layer showed similar V_{oc} $\sim$ 630 mV. Overlapping IQE in the shorter wavelength range confirmed the similar front passivation with both stacks. Conclusively, SiO_2 deposited using an industrially feasible spray-coating technique is a viable alternative to costlier thermal oxide as a front passivating layer over a textured n^+ emitter.

With limited resources in fabricating advanced Si solar cells in the NCPRE lab, we continued the study via simulations comparing PERC and TOPCon architectures from a passivation perspective. p-TOPCon would be the ideal successor for currently dominating PERC. Hence, an effort to predict the performance gain of p-TOPCon over the PERC architecture is needed. Sentaurus TCAD based simulation study was performed to investigate the advantages of p-TOPCon cell over PERC with respect to surface passivation. Prior to the study, the TCAD simulation deck was calibrated with the experimental data.

From the simulations, it was found that p-TOPCon and PERC outperform Al-BSF for identical cell parameters. Also, p-TOPCon performance is comparatively less sensitive and has a broader range of operation to S_{rear} than PERC. V_{oc} and efficiency of p-TOPCon decreases for an order of magnitude higher S_{rear} (> 10^3 cm s^{-1}) compared to PERC (> 10^2 cm s^{-1}). V_{oc} and efficiency trends are identical for p-TOPCon and PERC with S_{front} variation for fixed R_{sheet}. PERC and TOPCon have V_{oc} of 680.6 mV and 675 mV, respectively considering S_{rear} of 10 cm s^{-1}. However, there is a scope for performance improvement with enhanced front surface passivation. Conclusively, p-TOPCon consistently showed better performance compared to PERC for an identical bulk lifetime and front and rear passivation conditions.

p-TOPCon would be an incremental upgrade from PERC. However, limited studies are present on p-type Si and most of them are on n-TOPCon. We explored the potential of p-TOPCon by incorporating industry relevant material and process parameters in Sentaurus TCAD simulations including τ_b, ρ, poly-Si related rear parameters, R_{sheet}, S_{front}, and W_{finger}. Simulation results were benchmarked against PERC and n-TOPCon. p-TOPCon outperforms PERC and has lower sensitivity to a wider range of τ_b, ρ, and S_{front} in comparison to n-TOPCon. Simulation suggests that an efficiency of 23.83% can be achieved for industrially feasible τ_b of 5 ms, ρ of 1 Ω-cm, emitter R_{sheet} of 132 Ω/sq, and W_{finger} of 20 μm for p-TOPCon. Replacement of diffused emitter with n-TOPCon would be ideal after accomplishing above anticipated advancements and in such a scenario, efficiency > 24.4% can be achieved on p-type Si.

Although, detailed analysis and concrete results were presented in the thesis, we understand that there is a scope to extend both the experimental and simulation work to explore a wide area in the Si solar cell applications.

- **Scaling the spray-coating technique to larger industrial size silicon wafer**

  We have demonstrated the deposition as well as passivation uniformity of the SiO_2 film deposited with a spray-coating technique on textured Si. The spray-SiO_2 was deposited over a wafer size of 49 mm × 49 mm in our work. However, at the industrial level, wafer size of more than 156 mm × 156 mm is used for Si solar cell fabrication. Therefore, the immediate next task would be to scale the process to these larger wafers and further demonstrate the Al-BSF solar cell incorporating spray-SiO_2 as front passivating layer. Thereafter, comparing the passivation cell performance with thermal SiO_2/SiN_x stack can be undertaken.

- **Application of developed spray-SiO_2 as a passivating layer at the front of PERC and p-TOPCon solar cell**

Spray-SiO_2 potential to passivate n^+ emitter has been demonstrated on Al-BSF cell. However, its effectiveness as a passivating layer could be worked and tested on advanced Si solar cells, PERC and p-TOPCon, where the front surface passivation has a critical role to play in defining cell performance in comparison to the conventional Al-BSF cell.

- **Development of spray-Al_2O_3 as a passivating layer over SDR or polished textured p-type Si for PERC application**

  We have successfully demonstrated the potential of the spray-coater tool to deposit nanometer thin SiO_2 film over textured Si. Industrial PERC cell uses ALD Al_2O_3 at the rear as a passivating layer due to its in-built negative charges. The rear of the PERC cell is either SDR treated or polished textured Si. Al_2O_3 film could be developed with industrially viable spray-coater to deposit over SDR or polished textured Si surface. Initially, the detailed MOS capacitor analysis could be performed to analyze the D_{it} and magnitude and polarity of Q_f for the spray-Al_2O_3/SiN_x stack on p-type Si. Further, the same spray-Al_2O_3 could be incorporated in the PERC cell at the rear as a passivating layer beneath the SiN_x capping layer.

- **Integration of spray-SiO_2 and spray-Al_2O_3 passivating layers into PERC cell**

  After the successful demonstration of the passivation capability of spray-SiO_2/SiN_x stack at the front of Al-BSF cell and spray-Al_2O_3/SiN_x at the rear of PERC cell, both the stacks could be applied to the PERC cell. This indicates spray-SiO_2/SiN_x at the front and spray-Al_2O_3/SiN_x at the rear of the PERC cell. The integration of spray-SiO_2 and spray-Al_2O_3 would demand optimization of the PDA temperature and time so as to incorporate one single annealing step in the cell fabrication process flow.

- **TCAD simulations of the perovskite silicon tandem solar cell**

  Perovskite Si tandem solar cells, which take advantage of both Si based and perovskite based solar cells, are predicted to be the future technology at the industrial level for achieving efficiency beyond Si solar cell Shockley Queisser limit. We have already set up the Sentaurus TCAD simulation deck for Si based solar cells. The same deck could be upgraded for the TCAD simulation study of the perovskite Si tandem solar cell.

Appendices

This comprises the Sentaurus TCAD codes used for simulations in the thesis work. The simulations were performed using Sentaurus Workbench by including the required tools (SDE, Sprocess, and Sdevice). The variables used in each of the tools are mentioned in the script written in between two @ symbols. The values of these variables are set in the workbench itself.

A.1 TCAD scripts for optical simulation

A.1.1 SDE and Sprocess scripts for 3D structure creation

The below codes are used to form a single pyramidal 3D structure for the optical simulation of Al-BSF. The same codes are used for optical simulation of PERC and TOP-Con structure creation with appropriate modification.

A.1.1.1 SDE script

```
; - - - - -(BEGIN) SDE script for 3D structure creation for optical simulation - - - - -
; - - - - - - - - - - - - - - - - - - - - Variables definition - - - - - - - - - - - - - - - - - - - -
(define type "@surfaceType@") ; regular (single -pyramid)
(define CellW @cellW@)
(define SubstrateThickness (- @substrateThickness@))
(define CellL @cellL@)
(define tAL @AL_thickness@)
(define Pyramid_angle @Theta@)
(define substratedoping 7.17e15)
(define dair 1)
( define emitter_dop_file "./emitter_doping_file.plx")
( define BSF_dop_file "./BSF_doping_file_1.plx")
; - - - - - - - - - - - - - - - - - - - - Geometry creation - - - - - - - - - - - - - - - - - - - -
(sdegeo:set-default-boolean "AB")
```

```
;- - - - - - - Pyramid - - - - - - -
(define pWidth CellW)
(define pHeight (/ (/ pWidth 2) (tan (* (/ 3.14152654 180) Pyramid_angle)))); max height of the pyramid (define pMR (* (/ pWidth 2) (sqrt 2)))
(define reg_pyramid (sdegeo:create-pyramid (position (/ CellW 2) (/ CellL 2) (/ pHeight 2)) pHeight pMR pMR 4 0 "Silicon" "Pyramid"))
; - - - - - - - Substrate - - - - - - -
(sdegeo:set-default-boolean "ABA") ; substractes overlapping regions from the existing regions
(define reg_si (sdegeo:create-cuboid (position 0 0 0) (position CellW CellL SubstrateThickness) "Silicon" "substrate"))
; - - - - - - - Rear Aluminum - - - - - - -
(sdegeo:set-default-boolean "BAB") ; substractes existing regions from the newly created regions
(define reg_aluminium (sdegeo:create-cuboid (position 0 0 SubstrateThickness)
(position CellW CellL (- SubstrateThickness tAL)) "Aluminum" "AL_layer"))
;- - - - - - - Top Gas layer above the pyramid - - - - - - -
(define reg_air (sdegeo:create-cuboid (position 0 0 0)
(position CellW CellL (+ pHeight dair)) "Gas" "topair"))
(sdegeo:create-cuboid (position 0 0 (+ pHeight dair))
(position CellW CellL (+ pHeight (* 2 dair))) "Gas" "topair2")
; - - - - - - -
(sdegeo:chop-domain (list 0.0 0.0 CellW 0.0 CellW CellL 0.0 CellL))
(define zRecWin (+ pHeight (* 1.5 dair)))
(display (string-append (string-append "DOE: zRecWin " (number->string zRecWin)) "\n")) (newline)
(display (string-append (string-append "DOE: max_pHeight " (number->string pHeight)) "\n")) (newline)
(define CellTop (+ pHeight (* 2 dair)))
(define CellBot (- SubstrateThickness tAL))
(display (string-append (string-append "DOE: cellTop " (number->string CellTop)) "\n")) (newline)
(display (string-append (string-append "DOE: cellBot " (number->string CellBot)) "\n")) (newline)
; - - - - - - - - - - - - - - - - - - - Doping placement - - - - - - - - - - - - - - - - - - -
; - - - - - - - Substrate - - - - - - -
```

```
(sdedr:define-constant-profile "default" "BoronActiveConcentration" substratedoping)
(sdedr:define-constant-profile-material "SubDop" "default" "Silicon")
;- - - - - - - Front emitter - - - - - - -
(extract-interface-normal-offset-refwindow reg_pyramid reg_air 0.01
"refine_window_top")
(sdedr:define-1d-external-profile "emitter_dop_define" emitter_dop_file "Scale" 1
"Range" 0.0029 0.4235 "Gauss" "Factor" 1)
(sdedr:define-analytical-profile-placement "emitter_dop_place" "emitter_dop_define"
"refine_window_top" "Positive" "NoReplace" "Eval")
;- - - - - - - Rear BSF - - - - - - -
(sdedr:define-body-interface-refwin (list reg_si reg_aluminium)
"refine_window_bottom")
(sdedr:define-1d-external-profile "Gauss_BSF" BSF_dop_file "Scale" 1 "Range" 0.0
9.4142 "Gauss" "Factor" 1)
(sdedr:define-analytical-profile-placement "Placement_BSF" "Gauss_BSF"
"refine_window_bottom" "Negative" "NoReplace" "Eval")
;- - - - - - - - - - - - - - - - - - - - Meshing - - - - - - - - - - - - - - - - - - - -
;- - - - - - -Emitter and BSF - - - - - - -
(sdedr:define-refinement-window "dop_ref_window" "Cuboid" (position 0 0 CellTop)
(position CellW CellL (- SubstrateThickness tAL)))
(sdedr:define-refinement-size "dop_def_refsize" 2 2 2 0.02 0.02 0.02)
(sdedr:define-refinement-function "dop_def_refsize" "DopingConcentration"
"MaxTransDiff" 1)
(sdedr:define-refinement-material "dop_ref_place" "dop_def_refsize" "Silicon")
;- - - - - - - Above substrate - - - - - - -
(sdedr:define-refinement-window "toppy_win" "Cuboid" (position 0 0 -0.5)
(position CellW CellL pHeight))
(sdedr:define-multibox-size "toppy_refsize" 0.2 0.2 0.4 0.2 0.2 0.01 1 1 -1.1)
(sdedr:define-multibox-placement "toppy_refplace" "toppy_refsize" "toppy_win")
;- - - - - - - Substrate - - - - - - -
(sdedr:define-refinement-window "sub_win" "Cuboid" (position 0 0 -0.5)
(position CellW CellL SubstrateThickness))
(sdedr:define-multibox-size "sub_refsize" 2 2 4 2 2 0.2 1 1 -1.4)
(sdedr:define-multibox-placement "sub_refplace" "sub_refsize" "sub_win")
(sdedr:offset-global "hlocal" 0.00 "factor" 1.2 "maxlevel" 20 )
(sdedr:offset-block "material" "Silicon" "maxlevel" 15)
```

```
(sdedr:offset-interface "region" "Pyramid" "topair" "hlocal" 0.01 "factor" 1.25 )
;- - - - - - - - - - - - - - - - - - - - Mesh building - - - - - - - - - - - - - - - - - - -
(sde:build-mesh " -offset -m 1000000 " "n@node@_msh")
; - - - - - - -(END) SDE script for 3D structure creation for optical simulations - - - - - -
```

A.1.1.2 Sprocess script

Sprocess is used to create six virtual contacts. These contacts are used to define the ray-tracer boundary conditions in the optical analysis. These contacts are: four side contacts surrounding the sides of the simulation structure, one top contact, and one bottom contact. The Sprocess code for the same is given below.

```
; - - - - - - -(BEGIN) Sprocess script for virtual contact formation - - - - - - -
#setdep @node|sde@
sde off
init tdr=n@node|sde@_msh
# Create virtual contacts
contact bottom name=BotContact
contact box Gas name=topContact zlo=0.0 zhi=@cellW@ ylo=0 yhi=@cellL@
xlo=-@cellTop@ xhi=-@cellTop@
contact box sidewall Silicon name= "sideContact1" \
zlo=0 zhi=@cellW@ ylo=0 yhi=0 xlo=-@cellTop@ xhi=@substrateThickness@
contact add box sidewall Gas name= "sideContact1" \
zlo=0 zhi=@cellW@ ylo=0 yhi=0 xlo=-@cellTop@ xhi=0
contact add box sidewall Aluminum name= "sideContact1" \
zlo=0 zhi=@cellW@ ylo=0 yhi=0 xlo=@substrateThickness@ xhi=-@cellBot@
contact box sidewall Silicon name= "sideContact2" \
zlo=0 zhi=@cellW@ ylo=@cellL@ yhi=@cellL@ xlo=-@cellTop@ xhi=-@cellBot@
contact add box sidewall Gas name= "sideContact2" \
zlo=0 zhi=@cellW@ ylo=@cellL@ yhi=@cellL@ xlo=-@cellTop@ xhi=0
contact add box sidewall Aluminum name= "sideContact2" \
zlo=0 zhi=@cellW@ ylo=@cellL@ yhi=@cellL@ xlo=@substrateThickness@
xhi=@cellTop@
contact box sidewall Silicon name= "sideContact3" \
zlo=0 zhi=0 ylo=0 yhi=@cellL@ xlo=0 xhi=@substrateThickness@
contact add box sidewall Gas name= "sideContact3" \
zlo=0 zhi=0 ylo=0 yhi=@cellL@ xlo=-@cellTop@ xhi=0
contact add box sidewall Aluminum name= "sideContact3" \
```

```
zlo=0 zhi=0 ylo=0 yhi=@cellL@ xlo=@substrateThickness@ xhi=-@cellBot@
contact box sidewall Silicon name= "sideContact4" \
zlo=@cellW@ zhi=@cellW@ ylo=0 yhi=@cellL@ xlo=0 xhi=@substrateThickness@
contact add box sidewall Gas name= "sideContact4" \
zlo=@cellW@ zhi=@cellW@ ylo=0 yhi=@cellL@ xlo=-@cellTop@ xhi=0
contact add box sidewall Aluminum name= "sideContact4" \
zlo=@cellW@ zhi=@cellW@ ylo=0 yhi=@cellL@ xlo=@substrateThickness@
xhi=-@cellBot@
struct smesh=n@node@ Gas
; - - - - - - -(END) Sprocess script for virtual contact formation - - - - -
```

A.1.2 Sdevice script

Following is the Sdevice script used in the optical simulations.

```
; - - - - - - -(BEGIN) Sdevice script for optical simulation - - - - - - -
#setdep @previous@
*- - - - - - -
File { grid = "@tdr@"
current = "@plot@"
output = "@log@"
plot = "@tdrdat@"
parameter= "@parameter@"
IlluminationSpectrum= "am15g_1.2um_equi-10nm_19pt.txt"
PMIPATH= "./pmi/"
}
*- - - - - - -
Electrode {
{ name="BotContact" voltage=0.0 }
}
*- - - - - - -
Physics {
EffectiveIntrinsicDensity(TableBGN NoFermi)
} *- - - - - - -
RayTraceBC {
* Constant Reflectivity boundary condition
{ Name= "sideContact1" reflectivity= 1.0 }
{ Name= "sideContact2" reflectivity= 1.0 }
```

```
{ Name= "sideContact3" reflectivity= 1.0 }
{ Name= "sideContact4" reflectivity= 1.0 }
{ Name= "topContact" reflectivity= 0 transmittivity= 0 } * total absorbing BC
{ Name= "BotContact" reflectivity= 0 transmittivity= 0 } * total absorbing BC
}
#if @nitride_thickness@ != 0
#if "@surfaceType@" == "flat"
Physics(RegionInterface="substrate/topair") {
RayTraceBC (
TMM (
ReferenceMaterial = "Gas"
LayerStructure { @nitride_thickness@ "Nitride"; }
)
)
}
#else
Physics(RegionInterface="Pyramid/topair") {
RayTraceBC (
TMM (
ReferenceMaterial = "Gas"
LayerStructure { @nitride_thickness@ "Nitride"; }
)
)
}
#endif
#endif
Physics(RegionInterface="topair/topair2") { RayTraceBC (Fresnel) }
* Raytrace BC at rear side
Physics(MaterialInterface="Aluminum/Silicon") {
RayTraceBC (
pmiModel=pmi_rtDiffuseBC( * diffusive phong reflection at bottom contact
roughsurfacemodel = 0 # 0=Phong or 1=Lambert, 2=Random, 3=Gaussian
phong_w = @phong_w@
surfacereflectivity = @backR@
surfacetransmittivity = -1
set_randomseed = -1   -1:don't set
```

```
)
)
}
*- - - - - - -
Plot {
AbsorbedPhotonDensity
OpticalGeneration
DopingConcentration
ComplexRefractiveIndex
QuantumYield
Doping TotalConcentration
DonorConcentration AcceptorConcentration
eEquilibriumDensity hEquilibriumDensity
EffectiveIntrinsicDensity IntrinsicDensity
BandGap
EffectiveBandGap
BuiltinPotential
BandGapNarrowing
ConductionBand ValenceBand
eDensity hDensity
TotalCurrent/Vector eCurrent/Vector hCurrent/Vector
Current
eMobility hMobility
eVelocity hVelocity
eQuasiFermi hQuasiFermi
eLifetime hLifetime
eDriftVelocity
ElectricField/Vector eEffectiveField
Potential SpaceCharge
}
* - - - - - - -
CurrentPlot {
OpticalGeneration(Integrate(Material="Silicon"))
AbsorbedPhotonDensity(Integrate(EveryWhere))
AbsorbedPhotonDensity(Integrate(Material="Silicon"))
pmi_currentplot
```

```
}
*- - - - - - -
Physics {
Temperature = 300
Optics(
ComplexRefractiveIndex(
WavelengthDep(real imag)
CarrierDep(Imag)
)
OpticalGeneration (
ComputeFromSpectrum
QuantumYield(EffectiveAbsorption)
)
OpticalSolver (
RayTracing (
PlotInterfaceFlux
CompactMemoryOption
MonteCarlo
PolarizationVector= (1,1,0)
DepthLimit= 100000
MinIntensity= 1e-6
RectangularWindow (
RectangleV1= (0, 0, @zRecWin@) * vertex 1 of rectangular window [um]
RectangleV2= (@cellW@, 0, @zRecWin@) * vertex 2 of rectangular window [um]
RectangleV3= (@cellW@, @cellL@, @zRecWin@) * vertex 3 of rectangular window
[um]
LengthDiscretization= 200
WidthDiscretization= 200
RayDirection= (0,0,-1) * Normal Incidence
) * end RectangularWindow
) * end RayTracing
) * end of OpticalSolver
) * end of Optics
}
*- - - - - - -
Math{
```

CurrentPlot (IntegrationUnit = cm)
Number_of_Threads = 4
Stacksize= 200000000
}
*- - - - - - -
Solve {
Poisson
}
; - - - - - - -(END) Sdevice script for optical simulation - - - - - - -

A.2 SDE TCAD scripts for 2D structure creation for opto-electrical simulations

A.2.1 SDE script for QE and I-V simulations of Al-BSF cell

The code for the generation of 2D Al-BSF unit cell for QE and I-V simulations is given below. For I-V simulations, the only difference is that the 1D optical generation profile is included during 2D structure creation (commented in the code). Whereas the wavelength dependent generation profiles are used in Sdevice simulation in the case of QE simulations.

; - (BEGIN) SDE script for 2D Al-BSF structure creation for QE and I-V simulations -
; - - - - - - - - - - - - - - Geometry variables definition - - - - - - - - - - - - - -
(define SubstrateThickness @dsub@); Thickness of the substrate (um)
(define SiNThickness @dSiN@) ; Thickness of front SiNx (um)
(define Width @wtot@); Total horizontal width of the unit cell (um)
(define FrontContactThickness @dfrontAg@); Height of the front Ag contact (um)
(define FrontContactWidth @wfinger@); Horizontal width of the front Ag finger (um)
(define BackContactThickness @drearAl@); Height of the back Al contact (um)
(define BackContactWidth Width); Horizontal width of the back Al contact (um)
; - - - - - - - - - - - - - -Doping definition - - - - - - - - - – - - -
(define SubstrateDoping @NA@); constant substrate doping (cm^{-3})
(define FrontEmitterProfile “./pardb/profiles/emitter_doping_file.plx"); path to measured emitter profile
(define BackSurfaceProfile "./pardb/profiles/BSF_doping_file.plx"); path to measured BSF profile

```
 ; - - - - - - - Optical generation profile (ONLY FOR I-V SIMULATION) - - - - - - -
(define opt_gen_profile "./pardb/profiles/@generation@" )
; path to optical generation profile
 ; - - - - - - - Mesh refinement variables definition - - - - - - -
(define RefOptScale 1.1)
(define RefOptYmin 0.001)
(define RefOptDepth 10)
(define RefGlobalX 50)
(define RefGlobalY 15)
(define RefFrontContactOffset 1)
(define RefFrontContactX 5)
 ; - - - - - - - Node definition - - - - - - -
(define Node "@node@")
 ; - - - - - - - - - - - - - - -2D geomtery creation - - - - - - - - - - - - - -
; - - - - - - - Substrate - - - - - - - -
(sdegeo:create-rectangle (position 0 0 0) (position Width SubstrateThickness 0) "Silicon"
"substrate")
; - - - - - - -SiNx top layer - - - - - - -
(sdegeo:create-rectangle (position FrontContactWidth (- SiNThickness ) 0)
(position Width 0 0) "Nitride" "frontSiNx")
; - - - - - - -Front metal contact- - - - - - - -
(sdegeo:create-rectangle (position 0 (- FrontContactThickness) 0)
(position FrontContactWidth 0 0) "Silver" "frontMetalAg")
; - - - - - - -Back metal contact - - - - - - - -
(sdegeo:create-rectangle (position (- Width BackContactWidth) SubstrateThickness 0)
(position Width (+ SubstrateThickness BackContactThickness) 0) "Aluminum"
"backMetalAl")
 ; - - - - - - - - - - - - - - Doping placement - - - - - - - - - - - - - -
; - - - - - - -Substrate - - - - - - -
(sdedr:define-constant-profile "substrateDop" "BoronActiveConcentration"
SubstrateDoping)
(sdedr:define-constant-profile-region "substrateDop" "substrateDop" "substrate")
; - - - - - - - Front emitter - - - - - - -
(sdedr:define-refeval-window "frontEmitterDop" "Line" (position 0 0 0)
(position Width 0 0))
```

```
(sdedr:define-1d-external-profile "frontEmitterDop" FrontEmitterProfile "Scale" 1
"Range" 0.0029 0.4235 "Gauss" "Factor" 1)
(sdedr:define-analytical-profile-placement "frontEmitterDop" "frontEmitterDop"
"frontEmitterDop" "Positive" "NoReplace" "Eval")
; - - - - - - -BSF - - - - - - -
(sdedr:define-refeval-window "backSurfaceDop" "Line" (position 0 SubstrateThickness
0) (position Width SubstrateThickness 0))
(sdedr:define-1d-external-profile "backSurfaceDop" BackSurfaceProfile "Scale" 1
"Range" 0.0 9.4142 "Gauss" "Factor" 1)
(sdedr:define-analytical-profile-placement "backSurfaceDop" "backSurfaceDop"
"backSurfaceDop" "Negative" "NoReplace" "Eval")
;- - - - - - - - Optical generation placement (ONLY FOR I-V SIMULATIONS) - - - - - - -
(sdedr:define-refinement-window "Win.opticalGen" "Line"
(position FrontContactWidth 0 0) (position Width 0 0))
(sdedr:define-1d-external-profile "Profile.opticalGen" opt_gen_profile "Scale" 1.0 "Erf"
"Factor" 0.0)
(sdedr:define-analytical-profile-placement "Place.opticalGen" "Profile.opticalGen"
"Win.opticalGen" "Positive" "NoReplace" "Eval")
 ; - - - - - - - - - - - - - - Contact definition - - - - - - - - - - - - - -
(sdegeo:define-contact-set "cathode" 4 (color:rgb 1 0 0 ) "##" )
(sdegeo:define-contact-set "anode" 4 (color:rgb 0 0 1 ) "##" )
(sdegeo:define-2d-contact (find-edge-id (position (/ FrontContactWidth 2) 0 0)) "cath-
ode")
(sdegeo:define-2d-contact (find-edge-id (position (- Width (/ BackContactWidth 2))
SubstrateThickness 0)) "anode")
 ; - - - - - - - - - - - - - - Mesh refinement placement - - - - - - - - - - - - - -
; - - - - - - - Global mesh- - - - - - - -
(sdedr:define-refinement-size "ref.global" RefGlobalX RefGlobalY 0 RefGlobalX
RefGlobalY 0 )
(sdedr:define-refeval-window "win.global" "Rectangle" (position 0 0 0)
(position Width SubstrateThickness 0) )
(sdedr:define-refinement-placement "ref.global" "ref.global" "win.global" )
; - - - - - - - Doping profile - - - - - - -
(sdedr:define-refinement-size "AlPdoping" 1000 100 0 1000 0.01 0 )
(sdedr:define-refinement-function "AlPdoping" "DopingConcentration"
"MaxTransDiff" 1)
```

```
(sdedr:define-refinement-region "AlPdoping" "AlPdoping" "substrate" )
; - - - - - - - Front contact - - - - - - -
(sdedr:define-refeval-window "frontContact" "Rectangle" (position 0 0 0)
(position (+ FrontContactWidth RefFrontContactOffset) 2 0) )
(sdedr:define-refinement-size "frontContact" (/ FrontContactWidth RefFrontContactX) 1
0 (/ FrontContactWidth (* 2 RefFrontContactX)) 1 0 )
; - - - - - - - Back contact - - - - - - - -
(sdedr:define-refinement-size "ref.back" 25 0.2 0 20 0.01 0)
(sdedr:define-refeval-window "win.back" "Rectangle"
(position 0 (- SubstrateThickness 3.0) 0) (position Width SubstrateThickness 0) )
(sdedr:define-refinement-placement "ref.back" "ref.back" "win.back" )
; - - - - - - -Optical generation profile ( ONLY FOR IV SIMULATIONS) - - - - - - -
(sdedr:define-refeval-window "optics" "Rectangle" (position 0 0 0)
(position Width RefOptDepth 0) )
(sdedr:define-multibox-size "optics" 1000 100 1000 RefOptYmin 0 RefOptScale )
(sdedr:define-multibox-placement "optics" "optics" "optics" )
 ; - - - - - - - - - - - - - - Saving the structure - - - - - - - - - - - - - -
(sde:save-model (string-append "n" Node "_msh"))
 ;- - - - - - - - - - - - - - Mesh building - - - - - - - - - - - - - -
(sde:build-mesh "-y 1e5" (string-append "n" Node "_msh") ) ;-y sets the max aspect ratio
of the elements
 ; - -(END) SDE scripts for 2D Al-BSF structure creation for QE and I-V simulations - -
```

A.2.2 SDE script for PERC cell

Following is the code used for the generation of 2D unit cell of PERC for I-V simulations.

```
; - - -(BEGIN) SDE script for 2D PERC structure creation for I-V simulation - - -
; - - - - - - - - - - - - - - Geometry variables definition - - - - - - - - - - - - - -
(define SubstrateThickness @dsub@); um
(define SiNThickness @dSiN@ ) ; um
(define Width @wtot@); um
(define FrontContactThickness @dfrontAg@ ); um
(define FrontContactWidth @wfinger@); um
(define BackContactThickness @drearAl@ ); um
(define BackContactWidth Width ); Horizontal width of the back contact (um)
```

```
(define Offset @backOffset@); Distance between the back contact from left edge of unit cell (um)
(define WidthBackContact @wbackcontact@);
(define ThicknessAl2O3 @Al2O3_thickness@ ); Thickness of rear Al2O3
(define ThicknessBackSiNx @Back_SiNx_thickness@ ); Thickness of rear SiNx
 ; - - - - - - - - - - - - - - Doping definition - - - - - - - - - - - - - -
(define SubstrateDoping @NA@); cm^-3
(define FrontEmitterProfile "./pardb/profiles/preu_emitter_Rsheet_95_ohm_sq_updated.plx" )
(define SelectEmitterProfile "./pardb/profiles/Zhang_selective_emitter_profile.plx" ); Selective emitter
(define BackSurfaceProfile "./pardb/profiles/Zhang_AlBSF_profile.plx" )
 ; - - - - - - - Optical generation profile definition- - - - - - - -
(define opt_gen_profile "./pardb/profiles/@generation@" )
 ; - - - - - - - - - - - - - - Mesh refinement variables definition - - - - - - - - - - - - - -
(define RefOptScale 1.1)
(define RefOptYmin 0.001)
(define RefOptDepth 10)
(define RefGlobalX 50)
(define RefGlobalY 15)
;(define RefDopDiff 1)
(define RefFrontContactOffset 1)
(define RefFrontContactX 5)
 ; - - - - - - - Node definition - - - - - - -
(define Node "@node@")
; - - - - - - - - - - - - - - 2D geomtery creation - - - - - - - - - - - - - -
; - - - - - - - Substrate - - - - - - -
(sdegeo:create-rectangle (position 0 0 0) (position Width SubstrateThickness 0) "Silicon" "substrate")
; - - - - - - - SiN top layer - - - - - - -
(sdegeo:create-rectangle (position FrontContactWidth (- SiNThickness ) 0)
(position Width 0 0) "Nitride" "frontSiNx")
 ; - - - - - - - front contact metal - - - - - - -
(sdegeo:create-rectangle (position 0 (- FrontContactThickness) 0)
(position FrontContactWidth 0 0) "Silver" "frontMetalAg")
```

```
; - - - - - - - back contact metal - - - - - - -
(sdegeo:create-rectangle (position (- Width BackContactWidth) SubstrateThickness 0)
(position Width (+ SubstrateThickness BackContactThickness) 0) "Aluminum"
"backMetalAl")
(sdegeo:set-default-boolean "ABA")
; - - - - - - - back Al2O3 - - - - - - -
(sdegeo:create-rectangle (position 0 SubstrateThickness 0)
(position Offset (+ SubstrateThickness ThicknessAl2O3) 0) "Al2O3" "backAl2O3_1")
(sdegeo:create-rectangle (position (+ Offset WidthBackContact) SubstrateThickness 0)
(position Width (+ SubstrateThickness ThicknessAl2O3) 0) "Al2O3" "backAl2O3_2")
; - - - - - - - back SiNx - - - - - - - -
(sdegeo:create-rectangle (position 0 (+ SubstrateThickness ThicknessAl2O3) 0)
(position Offset (+ (+ SubstrateThickness ThicknessAl2O3) ThicknessBackSiNx) 0)
"Nitride" "backNitride_1")
(sdegeo:create-rectangle (position (+ Offset WidthBackContact) (+ SubstrateThickness
ThicknessAl2O3) 0) (position Width (+ (+ SubstrateThickness ThicknessAl2O3)
ThicknessBackSiNx) 0) "Nitride" "backNitride_2")
 ; - - - - - - - - - - - - - -Doping placement - - - - - - - - - - - - - -
; - - - - - - -Substrate - - - - - - -
(sdedr:define-constant-profile "substrateDop" "BoronActiveConcentration"
SubstrateDoping)
(sdedr:define-constant-profile-region "substrateDop" "substrateDop" "substrate")
; - - - - - - - Front emitter - - - - - - -
(sdedr:define-refeval-window "frontEmitterDop" "Line" (position 0 0 0)
(position Width 0 0))
(sdedr:define-1d-external-profile "frontEmitterDop" FrontEmitterProfile "Scale" 1
"Range" 0.00137 0.4141 "Gauss" "Factor" 1)
(sdedr:define-analytical-profile-placement "frontEmitterDop" "frontEmitterDop"
"frontEmitterDop" "Positive" "NoReplace" "Eval")
; - - - - - - - Front selective emitter - - - - - - -
(sdedr:define-refeval-window "SelectEmitterDop" "Line" (position 0 0 0)
(position FrontContactWidth 0 0))
(sdedr:define-1d-external-profile "SelectEmitterDop" SelectEmitterProfile "Scale" 1
"Range" 0.00406 0.71087 "Gauss" "Factor" 1)
(sdedr:define-analytical-profile-placement "SelectEmitterDop" "SelectEmitterDop"
"SelectEmitterDop" "Positive" "NoReplace" "Eval")
```

```
; - - - - - - - Local BSF - - - - - - -
(sdedr:define-refeval-window "backSurfaceDop" "Line" (position Offset
SubstrateThickness 0) (position (+ Offset WidthBackContact) SubstrateThickness 0))
(sdedr:define-1d-external-profile "backSurfaceDop" BackSurfaceProfile "Scale" 1
"Range" 0.00752 7.76199 "Gauss" "Factor" 1)
(sdedr:define-analytical-profile-placement "backSurfaceDop" "backSurfaceDop"
"backSurfaceDop" "Negative" "NoReplace" "Eval")
; - - - - - - - Optical generation placement - - - - - - -
(sdedr:define-refinement-window "Win.opticalGen" "Line"  (position FrontContactWidth
0 0) (position Width 0 0))
(sdedr:define-1d-external-profile "Profile.opticalGen" opt_gen_profile "Scale" 1.0 "Erf"
"Factor" 0.0)
(sdedr:define-analytical-profile-placement "Place.opticalGen" "Profile.opticalGen"
"Win.opticalGen" "Positive" "NoReplace" "Eval")
 ; - - - - - - - - - - - - - Contact definition - - - - - - - - - - - - -
(sdegeo:define-contact-set "cathode" 4 (color:rgb 1 0 0 ) "##" )
(sdegeo:define-contact-set "anode" 4 (color:rgb 0 0 1 ) "##" )
(sdegeo:define-2d-contact (find-edge-id (position (/ FrontContactWidth 2) 0 0)) "cath-
ode")
(sdegeo:define-2d-contact (find-edge-id (position (+ Offset (/ WidthBackContact 2))
SubstrateThickness 0)) "anode")
 ; - - - - - - - - - - - - - Mesh refinement placement - - - - - - - - - - - - -
; - - - - - - - Global mesh - - - - - - -
(sdedr:define-refinement-size "ref.global" (/ RefGlobalX 5) RefGlobalY 0
(/ RefGlobalX 5) RefGlobalY 0 )
(sdedr:define-refeval-window "win.global" "Rectangle" (position 0 0 0)
(position Width SubstrateThickness 0) )
(sdedr:define-refinement-placement "ref.global" "ref.global" "win.global" )
; - - - - - - -Phosphorus doping profile - - - - - - -
(sdedr:define-refinement-size "Pdoping" 1000 100 0 1000 0.1 0 )
(sdedr:define-refinement-function "Pdoping" "PhosphorusActiveConcentration"
"MaxTransDiff" 1)
(sdedr:define-refinement-region "Pdoping" "Pdoping" "substrate" )
; - - - - - - -Local BSF doping profile - - - - - - -
(sdedr:define-refinement-size "Aldoping" 1000 100 0 1000 0.1 0 )
(sdedr:define-refinement-function "Aldoping" "AluminumActiveConcentration"
```

```
"MaxTransDiff" 1)
(sedr:define-refinement-region "Aldoping" "Aldoping" "substrate" )
; - - - - - - -Front contact - - - - - - -
(sedr:define-refeval-window "frontContact" "Rectangle" (position 0 0 0)
(position (+ FrontContactWidth RefFrontContactOffset) 2 0) )
(sedr:define-refinement-size "frontContact" (/ FrontContactWidth RefFrontContactX) 1
0 (/ FrontContactWidth (* 2 RefFrontContactX)) 1 0 )
(sedr:define-refinement-placement "frontContact" "frontContact" "frontContact" )
; - - - - - - -Rear interfaces - - - - - - - -
(sedr:define-refinement-window "RefEvalWin.Channel" "Rectangle"
(position 0 (- SubstrateThickness 1) 0)
(position Width (+ (+ SubstrateThickness ThicknessAl2O3) ThicknessBackSiNx) 0))
(sedr:define-refinement-size "RefDef.Channel" 25 5e-2 20 1e-2)
(sedr:define-refinement-function "RefDef.Channel" "MaxLenInt" "Silicon"
"Al2O3" 1e-2 1.2)
(sedr:define-refinement-function "RefDef.Channel" "MaxLenInt" "Al2O3"
"Nitride" 1e-2 1.2)
(sedr:define-refinement-placement "RefPlace.Channel" "RefDef.Channel"
"RefEvalWin.Channel")
 ; - - - - - - – Back contact - - - - - - -
(sedr:define-refinement-size "ref.back" 1000 1 0 1000 1 0)
(sedr:define-refeval-window "win.back" "Rectangle"
(position 0 (- SubstrateThickness 2) 0) (position Width (+ SubstrateThickness 1) 0) )
(sedr:define-refinement-placement "ref.back" "ref.back" "win.back" )
; - - - - - - - Optical generation profile - - - - - - - -
(sedr:define-refeval-window "optics" "Rectangle" (position 0 0 0)
(position Width RefOptDepth 0) )
(sedr:define-multibox-size "optics" 1000 100 1000 RefOptYmin 0 RefOptScale )
(sedr:define-multibox-placement "optics" "optics" "optics" )
 ; - - - - - - - - - - - - - - Saving the structure - - - - - - - - - - - - - -
(sde:save-model (string-append "n" Node "_msh"))
 ; - - - - - - - - - - - - - - Mesh building - - - - - - - - - - - - - -
(sde:build-mesh "-y 1e5" (string-append "n" Node "_msh") ) ;-y sets the max aspect ratio
of the elements
; - - (END) SDE script for 2D PERC structure creation for I-V simulation - -
```

A.2.3 SDE script for p-TOPCon cell

Following is the code used for the generation of 2D unit cell of p-TOPCon for I-V simulations. 2D structure for n-TOPCon can be easily created using the same code by inverting the doping type.

```
; - - (BEGIN) SDE script for 2D p-TOPCon structure creation for I-V simulation - -
; - - - - - - - - - - - - - - Geometry variables definition - - - - - - - - - - - - - -
(define SubstrateThickness @dsub@); um
(define SiNThickness @dSiN@ ) ; um
(define Width @wtot@); um
(define FrontContactThickness @dfrontAg@ ); um
(define FrontContactWidth @wfinger@); um
(define BackSiO2Thickness @dRSiO2@ ) ; Thickness of utrathin SiO2 (um)
(define BackPolySiThickness @dRPolySi@ ) ; Thickness of rear poly-Si (um)
(define BackContactThickness @drearAg@ ); um
(define BackContactWidth Width ); um
 ; - - - - - - - - - - - - - - Doping definition - - - - - - - - - - - - - -
(define SubstrateDoping @NA@); cm^-3
(define FrontEmitterProfile "./pardb/profiles/preu_emitter_Rsheet_95_ohm_sq_updated.plx"
)
(define SelectEmitterProfile "./pardb/profiles/Zhang_selective_emitter_profile.plx" )
(define PolySiDoping @DopPoly@); Poly-Si doping (cm^-3)
(define BackDiffusionPeak @DiffPeak@); cm^-3
(define BackDiffusionDepth @DiffDepth@); BDR depth (cm^-3)
 (define opt_gen_profile "./pardb/profiles/@generation@" )
 ; - - - - - - - - - - - – Mesh refinement variables definition - - - - - - - - - - - - -
(define RefOptScale 1.1)
(define RefOptYmin 0.001)
(define RefOptDepth 10)
(define RefGlobalX 50)
(define RefGlobalY 15)
;(define RefDopDiff 1)
(define RefFrontContactOffset 1)
(define RefFrontContactX 5)
 ; - - - - - -Node definition - - - - - -
(define Node "@node@")
```

```
; - - - - - - - - - - - - - - 2D geomtery creation - - - - - - - - - - - - - -
; - - - - - - -Substrate - - - - - - -
(sdegeo:create-rectangle (position 0 0 0) (position Width SubstrateThickness 0)
"Silicon" "substrate")
; - - - - - - - SiNx top layer - - - - - - -
(sdegeo:create-rectangle (position FrontContactWidth (- SiNThickness ) 0)
(position Width 0 0) "Nitride" "frontSiNx")
; ———- Front contact metal - - - - - - -
(sdegeo:create-rectangle (position 0 (- FrontContactThickness) 0)
(position FrontContactWidth 0 0) "Silver" "frontMetalAg")
; - - - - - - - Back SiO2 ————-
(sdegeo:create-rectangle (position (- Width BackContactWidth) SubstrateThickness 0)
(position Width (+ SubstrateThickness BackSiO2Thickness) 0) "Oxide" "backSiO2")
; - - - - - - - back Poly-Si - - - - - - -
(sdegeo:create-rectangle
(position (- Width BackContactWidth) (+ SubstrateThickness BackSiO2Thickness) 0)
(position Width (+ (+ SubstrateThickness BackSiO2Thickness) BackPolySiThickness)
0) "PolySi" "backPolySi")
; - - - - - - - back contact metal - - - - - - -
(sdegeo:create-rectangle (position (- Width BackContactWidth) (+ (+ SubstrateThickness
BackSiO2Thickness) BackPolySiThickness) 0)
(position Width (+ (+ (+ SubstrateThickness BackSiO2Thickness) BackPolySiThick-
ness) BackContactThickness) 0) "Silver" "backMetalAg")
; - - - - - - - - - - - - - - Doping placement - - - - - - - - - - - - - -
; - - - - - - - Substrate - - - - - - -
(sdedr:define-constant-profile "substrateDop" "BoronActiveConcentration"
SubstrateDoping)
(sdedr:define-constant-profile-region "substrateDop" "substrateDop" "substrate")
; - - - - - - -Front emitter - - - - - - -
(sdedr:define-refeval-window "frontEmitterDop" "Line" (position 0 0 0)
(position Width 0 0))
(sdedr:define-1d-external-profile "frontEmitterDop" FrontEmitterProfile "Scale" 1
"Range" 0.00137 0.4141 "Gauss" "Factor" 1)
(sdedr:define-analytical-profile-placement "frontEmitterDop" "frontEmitterDop"
"frontEmitterDop" "Positive" "NoReplace" "Eval")
; - - - - - - - Selective front emitter - - - - - - -
```

```
(sdedr:define-refeval-window "SelectEmitterDop" "Line" (position 0 0 0)
(position FrontContactWidth 0 0))
(sdedr:define-1d-external-profile "SelectEmitterDop" SelectEmitterProfile "Scale" 1
"Range" 0.00406 0.71087 "Gauss" "Factor" 1)
(sdedr:define-analytical-profile-placement "SelectEmitterDop" "SelectEmitterDop"
"SelectEmitterDop" "Positive" "NoReplace" "Eval")
; - - - - - - - BDR - - - - - - -
(sdedr:define-refeval-window "backSurfaceDop" "Line" (position 0 SubstrateThickness
0) (position Width SubstrateThickness 0))
(sdedr:define-gaussian-profile "backSurfaceDop" "BoronActiveConcentration"
"PeakPos" 0 "PeakVal" BackDiffusionPeak "ValueAtDepth" SubstrateDoping "Depth"
BackDiffusionDepth "Gauss" "Factor" 1.0)
(sdedr:define-analytical-profile-placement "backSurfaceDop" "backSurfaceDop"
"backSurfaceDop" "Negative" "NoReplace" "Eval")
; - - - - - - - Poly-Si - - - - - - -
(sdedr:define-constant-profile "PolySiDop" "BoronActiveConcentration" PolySiDoping)
(sdedr:define-constant-profile-region "PolySiDop" "PolySiDop" "backPolySi")
; - - - - - - - Optical generation placement - - - - - - -
(sdedr:define-refinement-window "Win.opticalGen" "Line"
(position FrontContactWidth 0 0) (position Width 0 0))
(sdedr:define-1d-external-profile "Profile.opticalGen" opt_gen_profile "Scale" 1.0 "Erf"
"Factor" 0.0)
(sdedr:define-analytical-profile-placement "Place.opticalGen" "Profile.opticalGen"
"Win.opticalGen" "Positive" "NoReplace" "Eval")
; - - - - - - - - - - - - - - Contact definition - - - - - - - - - - - - - -
(sdegeo:define-contact-set "cathode" 4 (color:rgb 1 0 0 ) "##" )
(sdegeo:define-contact-set "anode" 4 (color:rgb 0 0 1 ) "##" )
(sdegeo:define-2d-contact (find-edge-id (position (/ FrontContactWidth 2) 0 0)) "cath-
ode")
(sdegeo:define-2d-contact (find-edge-id (position (- Width (/ BackContactWidth 2))
(+ (+ SubstrateThickness BackSiO2Thickness) BackPolySiThickness) 0)) "anode")
; - - - - - - - - - - - - - -Mesh refinement placement - - - - - - - - - - - - - -
; - - - - - - -Global mesh - - - - - - -
(sdedr:define-refinement-size "ref.global" (/ RefGlobalX 5) RefGlobalY 0
(/ RefGlobalX 5) RefGlobalY 0 )
(sdedr:define-refeval-window "win.global" "Rectangle" (position 0 0 0)
```

```
(position Width SubstrateThickness 0) )
(sdedr:define-refinement-placement "ref.global" "ref.global" "win.global" )
; - - - - - - - Emitter doping - - - - - - -
(sdedr:define-refinement-size "Pdoping" 1000 100 0 1000 0.01 0 )
(sdedr:define-refinement-function "Pdoping" "PhosphorusActiveConcentration"
"MaxTransDiff" 1)
(sdedr:define-refinement-region "Pdoping" "Pdoping" "substrate" )
; - - - - - - – BDR doping - - - - - - -
(sdedr:define-refinement-size "Bdoping" 1000 100 0 1000 0.01 0 )
(sdedr:define-refinement-function "Bdoping" "BoronActiveConcentration"
"MaxTransDiff" 1)
(sdedr:define-refinement-region "Bdoping" "Bdoping" "substrate" )
; - - - - - - - Front contact - - - - - - -
(sdedr:define-refeval-window "frontContact" "Rectangle" (position 0 0 0)
(position (+ FrontContactWidth RefFrontContactOffset) 2 0) )
(sdedr:define-refinement-size "frontContact" (/ FrontContactWidth RefFrontContactX) 1
0 (/ FrontContactWidth (* 2 RefFrontContactX)) 1 0 )
(sdedr:define-refinement-placement "frontContact" "frontContact" "frontContact" )
; - - - - - - - Rear interfaces - - - - - - -
(sdedr:define-refinement-window "RefEvalWin.Channel" "Rectangle"
(position 0 (- SubstrateThickness 1) 0)
(position Width (+ (+ SubstrateThickness BackSiO2Thickness) BackPolySiThickness)
0))
(sdedr:define-refinement-size "RefDef.Channel" 25 5e-2 20 1e-2)
(sdedr:define-refinement-function "RefDef.Channel" "MaxLenInt" "Silicon"
"Oxide" 1e-2 1.2)
(sdedr:define-refinement-function "RefDef.Channel" "MaxLenInt" "PolySi"
"Oxide" 1e-2 1.2)
(sdedr:define-refinement-placement "RefPlace.Channel" "RefDef.Channel"
"RefEvalWin.Channel")
; - - - - - - - - - - - - - - Optical generation - - - - - - - - - - - - - -
(sdedr:define-refeval-window "optics" "Rectangle" (position 0 0 0)
(position Width RefOptDepth 0) )
(sdedr:define-multibox-size "optics" 1000 100 1000 RefOptYmin 0 RefOptScale )
(sdedr:define-multibox-placement "optics" "optics" "optics" )
 ; - - - - - - - - - - - - - - Saving the structure - - - - - - - - - - - - - -
```

```
(sde:save-model (string-append "n" Node "_msh"))
 ; - - - - - - - - - - - - - - Mesh building - - - - - - - - - - - - - -
(sde:build-mesh "-y 1e5" (string-append "n" Node "_msh") ) ;;-y sets the max aspect ratio
of the elements
 ; - - - (END) SDE script for 2D p-TOPCon structure creation for I-V simulation - - -
```

A.3 Sdevice TCAD scripts for QE and I-V simulations

A.3.1 QE simulation of Al-BSF

Below is the Sdevice code used for QE simulation of the Al-BSF unit cell.

```
; - - - - - - (BEGIN) Sdevice script for QE simulation of Al-BSF - - - - - - - -
!(
set gfile_input "@pwd@/pardb/gspec/@gfile@"
# read in wavelengths of spectrum file
set specfile "@pwd@/pardb/spectra/@spectrum@"
set spectrumstart 0 ;# start of spectrum
set spectrumend 1.2 ;# end of spectrum in um
# extract wavelength list from spectrum file
set wavelengthlist {}
set fid [open "$specfile" r]
while { [gets $fid LINE] >= 0 } {
set LINE [string trim $LINE]
if { [string range $LINE 0 0] == "#" || [string length $LINE] == 0} {continue}
if {![regexp {^[0-9\.eE\-\+]+} [lindex $LINE 0]]} {continue}
set w [lindex $LINE 0]
# limit wavelength range to wend and wstart
if {$spectrumstart <= $w && $w <= $spectrumend} {lappend wavelengthlist $w}
}
close $fid
set wavelengthlist [lsort -real $wavelengthlist]
set wstart [lindex $wavelengthlist 0]
set wend [lindex $wavelengthlist end]
set wsteps [llength $wavelengthlist]
puts "* wavelength range: \[$wstart, $wend\] entries: $wsteps"
# puts "* wavelengthlist: $wavelengthlist"
```

```
# transform wavelength list to time list [0..1]
set timelist {}
foreach w $wavelengthlist {
lappend timelist [expr 1.*($w-$wstart)/($wend-$wstart)]
}
# puts "* timelist: $timelist"
)!
 * - - - - - - -
File {
* input
grid = "@tdr@"
parameter = "@parameter@"
OpticalSolverInput = "!(puts -nonewline $gfile_input)!"
IlluminationSpectrum = "!(puts -nonewline $specfile)!"
PMIUserFields = "@tdr@"
* output
plot = "@tdrdat@"
current = "@plot@"
output = "@log@"
OpticsOutput = "n@node@_optics_des.log"
}
 * - - - - - - -
Electrode {
{ name="anode"
voltage=0.0
eRecVelocity=@Srear_contact@
hRecVelocity=@Srear_contact@
}
{ name="cathode"
voltage=0.0
eRecVelocity=@Sfront_contact@
hRecVelocity=@Sfront_contact@
}
}
 * - - - - - - -
Plot {
```

```
DonorConcentration AcceptorConcentration Doping
BoronActiveConcentration
PhosphorusActiveConcentration
ElectronAffinity
ConductionBandEnergy ValenceBandEnergy
BandGap EffectiveBandGap
eDensity hDensity
eMobility hMobility
eCurrent/vector hCurrent/vector TotalCurrent/vector CurrentPotential
eQuasiFermi hQuasiFermi
ElectricField/vector
Potential SpaceCharge
eLifeTime hLifeTime
SRH Auger
SurfaceRecombination
TotalRecombination
OpticalGeneration
AbsorbedPhotonDensity QuantumYield ComplexRefractiveIndex
}
 *- - - - - - -
CurrentPlot {
ModelParameter = "Optics/Excitation/Wavelength"
OpticalGeneration(Integrate(Semiconductor) )
OpticalGeneration(Integrate(material="Silicon") )
SRH(Integrate(Semiconductor))
Auger(Integrate(Semiconductor))
SRH(Average(Semiconductor))
Auger(Average(Semiconductor))
}
 * - - - - - - -
Physics
Area = @<1e11/wtot>@
Temperature=300
Fermi(-WithJoyceDixon)
Recombination (
SRH(DopingDependence)
```

```
intrinsicRichter
)
Mobility ( PhuMob (Klaassen) )
EffectiveIntrinsicDensity(TableBGN NoFermi)
Optics(
OpticalGeneration(
ComputeFromSpectrum(
Select(
Condition="!(puts -nonewline $spectrumstart)!  <= $wavelength && $wavelength <=
!(puts -nonewline $spectrumend)!"
)
)
ComputeFromMonochromaticSource(scaling=0)
)
Excitation(
Wavelength = !(puts -nonewline $wstart)!
Intensity = @signalIntensity@
Window(
Line(x1=@wfinger@ x2=@wtot@)
)
)
OpticalSolver(
fromFile(
ProfileIndex = 0
IdentifyingParameter = ("Wavelength")
propagationDirection = perpendicular
datasetName = OpticalGeneration
)
)
)
}
 Physics (MaterialInterface = "Nitride/Silicon")
Recombination(surfaceSRH)
}
 * - - - - - - -
Math {
```

```
NumberOfThreads = 4
DirectCurrentComputation
Extrapolate
Derivatives
RelErrControl
ErReff(electron)=1.e3
ErReff(hole)=1.e3
Digits=5
Iterations=50
Notdamped=20
Method=pardiso
AutoCNPMinStepFactor=0
AutoNPMinStepFactor=0
}
 * - - - - - - -
Solve {
NewCurrentPrefix = "tmp_"
Coupled (Iterations=100) {Poisson}
 NewCurrentPrefix = "bias_"
Coupled (Iterations=100) {Poisson Electron Hole }
 NewCurrentPrefix = "tmp_"
Quasistationary (
InitialStep=1
Goal { ModelParameter="Optics/OpticalGeneration/ComputeFromMonochromaticSource/Scaling"
value=1 }) {
coupled {Poisson Electron Hole }
}
 NewCurrentPrefix = ""
Quasistationary (
InitialStep=1 MaxStep=1 MinStep=1
Goal { modelParameter="Optics/Excitation/Wavelength" value=!(puts -nonewline
$wend)! } ) {
coupled { Poisson Electron Hole }
CurrentPlot(Time=(!(puts -nonewline "[join $timelist "\;"]")!))
}
```

```
System("rm -f tmp*") *remove the "tmp" plot
}
 ;; - - - - - - - - - - - (END) Sdevice script for QE simulation of Al-BSF - - - - - - - - -
```

A.3.2 I-V simulations

Following is the Sdevice code used for I-V simulations. The overall script for all three cell structures is the same with a few additions for PERC, p-TOPCon, and n-TOPCon that are specifically mentioned in the code.

```
    ;; - - - - - - - - - (BEGIN) Sdevice script for I-V simulations - - - - - - - - -
* - - - - - - -
File{
* input
grid = "@tdr@"
parameter = "@parameter@"
OpticalGenerationInput= "@tdr@"
PMIUserFields = "@tdr@"
* output
plot = "@tdrdat@"
current = "@plot@"
output = "@log@"
}
* - - - - - - -
Electrode {

    { name="anode" # For p-TOPCon
{name="cathode" # For n-TOPCon
voltage=0.0
eRecVelocity=@Srear_contact@
hRecVelocity=@Srear_contact@
}
{ name="cathode" # For p-TOPCon
{name="anode" # For n-TOPCon
Resist=@<Rseries*1e8/wtot>@
voltage=0.0
eRecVelocity=@Sfront_contact@
hRecVelocity=@Sfront_contact@
```

```
}
}
* - - - - - - -
Physics {
Area = @<1e11/wtot>@
Temperature=300
Recombination (
SRH(DopingDependence)
intrinsicRichter
)
Mobility ( PhuMob (Klaassen) )
EffectiveIntrinsicDensity( TableBGN NoFermi)
Fermi(-WithJoyceDixon)
Optics(
OpticalGeneration(
ReadFromFile(
TimeDependence(
WaveTime= (1, 2)
WaveTSlope= 0.05
)
)
)
)
eBarrierTunneling "Substrate_backSiO2" # For TOPCon
hBarrierTunneling "Substrate_backSiO2" # For TOPCon
}
Physics (MaterialInterface = "Nitride/Silicon") {
Recombination(surfaceSRH)
}
* - - - - - - -FOR PERC - - - - - - - -
Physics (RegionInterface = "substrate/backAl2O3_1") {
Recombination(surfaceSRH)
Traps(
(FixedCharge Conc=-@AlOx_Qf@)
)
}
```

```
Physics (RegionInterface = "substrate/backAl2O3_2") {
Recombination(surfaceSRH)
Traps(
(FixedCharge Conc=-@AlOx_Qf@)
)
}
* - - - - - - - FOR TOPCon - - - - - - -
Physics (RegionInterface = "substrate/backSiO2") {
Recombination(surfaceSRH)
}
Math {
NonLocal "Substrate_backSiO2" (
RegionInterface="substrate/backSiO2"
Length= 1.5e-7
Digits= 4
EnergyResolution= 1e-4
)
}
* - - –
Plot{
DonorConcentration AcceptorConcentration Doping
BoronActiveConcentration
PhosphorusActiveConcentration
ElectronAffinity
ConductionBandEnergy ValenceBandEnergy
BandGap EffectiveBandGap
eDensity hDensity
eMobility hMobility
eCurrent/vector hCurrent/vector TotalCurrent/vector CurrentPotential
eQuasiFermi hQuasiFermi
ElectricField/vector
Potential SpaceCharge
eLifeTime hLifeTime
SRH Auger
SurfaceRecombination
TotalRecombination
```

```
OpticalGeneration
AbsorbedPhotonDensity QuantumYield ComplexRefractiveIndex
}
* - - - -
CurrentPlot {
OpticalGeneration(Integrate(Semiconductor) )
OpticalGeneration(Integrate(material="Silicon") )
SRH(Integrate(Semiconductor))
Auger(Integrate(Semiconductor))
}
* - - -
Math{
NumberOfThreads = 4
DirectCurrentComputation
Extrapolate
Derivatives
RelErrControl
ErReff(electron)=1.e3
ErReff(hole)=1.e3
Digits=5
Iterations=50
Notdamped=20
Method=pardiso
}
* - - -
Solve{
Coupled(Iterations=100){ Poisson }
Coupled(Iterations=100){ Poisson Electron Hole }
 Quasistationary(
InitialStep=0.1 Increment=1.35
MinStep=1e-5 MaxStep=0.1
Goal{ name=anode Voltage= 0.3 } # For Al-BSF, PERC, p-TOPCon
Goal{ name=cathode Voltage= 0.3 } # For n-TOPCon
){ Coupled Poisson Electron Hole
}
 Quasistationary(
```

```
InitialStep=0.01 Increment=1.35
MinStep=1e-6 MaxStep=0.01
Goal{ name=anode Voltage= 0.8 } # For Al-BSF, PERC, p-TOPCon
Goal{ name=cathode Voltage= 0.8 } # For n-TOPCon
){ Coupled Poisson Electron Hole }
}
System("rm -f tmp_*")
}
; - - - - - - - - - - - - - - (END) Sdevice script for I-V simulations - - - - - - - - - - - -
```

A.3.3 Parameter file

The parameter file is used to define model parameters or coefficients for the region, material, and interfaces. The .par file is called during Sdevice simulation. Below is the parameter file content used in the I-V simulations.

```
# - - - - - - - - – - - - - (BEGIN) Parameter file - - - - - - - - – - - - -
Material = "Silicon" {
Bandgap {
Eg0 = +1.1752165e+00
alpha = +4.73e-04
beta = +6.36e+02
}
 eDOSMass {
Formula = 1
a = +1.905e-01
ml = +9.163e-01
}
hDOSMass {
Formula = 1
a = 0.4435870
b = 0.3609528e-2
c = 0.1173515e-3
d = 0.1263218e-5
e = 0.3025581e-8
f = 0.4683382e-2
g = 0.2286895e-3
h = 0.7469271e-6
```

```
i = 0.1727481e-8
mm = 0.0
}
ConstantMobility
{
mumax = 1.4170e+03 ,4.7050e+02
Exponent = 2.5 ,2.2
}
 Scharfetter {
taumin = @tau_bulk@ , @tau_bulk@
taumax = @tau_bulk@ , @tau_bulk@
Etrap = 0
}
TableBGN {
Acceptor +1.0000000e+10 +000000000e+00
Acceptor +1.0000000e+15 +1.4051583e-03
Acceptor +1.1748976e+15 +1.5206727e-03
Acceptor +1.3803843e+15 +1.6454732e-03
Acceptor +1.6218101e+15 +1.7802713e-03
Acceptor +1.9054607e+15 +1.9258276e-03
Acceptor +2.2387211e+15 +2.0829536e-03
Acceptor +2.6302680e+15 +2.2525147e-03
Acceptor +3.0902954e+15 +2.4354322e-03
Acceptor +3.6307805e+15 +2.6326857e-03
Acceptor +4.2657952e+15 +2.8453154e-03
Acceptor +5.0118723e+15 +3.0744238e-03
Acceptor +5.8884366e+15 +3.3211775e-03
Acceptor +6.9183097e+15 +3.5868093e-03
Acceptor +8.1283052e+15 +3.8726185e-03
Acceptor +9.5499259e+15 +4.1799729e-03
Acceptor +1.1220185e+16 +4.5103084e-03
Acceptor +1.3182567e+16 +4.8651296e-03
Acceptor +1.5488166e+16 +5.2460092e-03
Acceptor +1.8197009e+16 +5.6545873e-03
Acceptor +2.1379621e+16 +6.0925695e-03
Acceptor +2.5118864e+16 +6.5617248e-03
```

Acceptor +2.9512092e+16 +7.0638822e-03
Acceptor +3.4673685e+16 +7.6009265e-03
Acceptor +4.0738028e+16 +8.1747919e-03
Acceptor +4.7863009e+16 +8.7874538e-03
Acceptor +5.6234133e+16 +9.4409168e-03
Acceptor +6.6069345e+16 +1.0137196e-02
Acceptor +7.7624712e+16 +1.0878292e-02
Acceptor +9.1201084e+16 +1.1666151e-02
Acceptor +1.0715193e+17 +1.2502602e-02
Acceptor +1.2589254e+17 +1.3389274e-02
Acceptor +1.4791084e+17 +1.4327467e-02
Acceptor +1.7378008e+17 +1.5317973e-02
Acceptor +2.0417379e+17 +1.6360844e-02
Acceptor +2.3988329e+17 +1.7455116e-02
Acceptor +2.8183829e+17 +1.8598517e-02
Acceptor +3.3113112e+17 +1.9787260e-02
Acceptor +3.8904514e+17 +2.1016072e-02
Acceptor +4.5708819e+17 +2.2278648e-02
Acceptor +5.3703180e+17 +2.3568704e-02
Acceptor +6.3095734e+17 +2.4881569e-02
Acceptor +7.4131024e+17 +2.6215946e-02
Acceptor +8.7096359e+17 +2.7575083e-02
Acceptor +1.0232930e+18 +2.8966616e-02
Acceptor +1.2022644e+18 +3.0400895e-02
Acceptor +1.4125375e+18 +3.1888388e-02
Acceptor +1.6595869e+18 +3.3437288e-02
Acceptor +1.9498446e+18 +3.5052217e-02
Acceptor +2.2908677e+18 +3.6734250e-02
Acceptor +2.6915348e+18 +3.8481835e-02
Acceptor +3.1622777e+18 +4.0292000e-02
Acceptor +3.7153523e+18 +4.2161341e-02
Acceptor +4.3651583e+18 +4.4086607e-02
Acceptor +5.1286138e+18 +4.6064873e-02
Acceptor +6.0255959e+18 +4.8093417e-02
Acceptor +7.0794578e+18 +5.0169411e-02
Acceptor +8.3176377e+18 +5.2289550e-02

Acceptor +9.7723722e+18 +5.4449713e-02
Acceptor +1.1481536e+19 +5.6644789e-02
Acceptor +1.3489629e+19 +5.8868845e-02
Acceptor +1.5848932e+19 +6.1115840e-02
Acceptor +1.8620871e+19 +6.3381069e-02
Acceptor +2.1877616e+19 +6.5663281e-02
Acceptor +2.5703958e+19 +6.7967054e-02
Acceptor +3.0199517e+19 +7.0304467e-02
Acceptor +3.5481339e+19 +7.2695032e-02
Acceptor +4.1686938e+19 +7.5163362e-02
Acceptor +4.8977882e+19 +7.7735212e-02
Acceptor +5.7543994e+19 +8.0433422e-02
Acceptor +6.7608298e+19 +8.3275258e-02
Acceptor +7.9432823e+19 +8.6271728e-02
Acceptor +9.3325430e+19 +8.9428500e-02
Acceptor +1.0964782e+20 +9.2747564e-02
Acceptor +1.2882496e+20 +9.6228912e-02
Acceptor +1.5135612e+20 +9.9871838e-02
Acceptor +1.7782794e+20 +1.0367577e-01
Acceptor +2.0892961e+20 +1.0764072e-01
Acceptor +2.4547089e+20 +1.1176740e-01
Acceptor +2.8840315e+20 +1.1605729e-01
Acceptor +3.3884416e+20 +1.2051250e-01
Acceptor +3.9810717e+20 +1.2513568e-01
Acceptor +4.6773514e+20 +1.2992990e-01
Acceptor +5.4954087e+20 +1.3489856e-01
Acceptor +6.4565423e+20 +1.4004528e-01
Acceptor +7.5857758e+20 +1.4537385e-01
Acceptor +8.9125094e+20 +1.5088819e-01
Acceptor +1.0471285e+21 +1.5659232e-01
Acceptor +1.2302688e+21 +1.6249042e-01
Acceptor +1.4454398e+21 +1.6858680e-01
Acceptor +1.6982437e+21 +1.7488602e-01
Acceptor +1.9952623e+21 +1.8139296e-01
Acceptor +2.3442288e+21 +1.8811299e-01
Acceptor +2.7542287e+21 +1.9505213e-01

Acceptor +3.2359366e+21 +2.0221722e-01
Acceptor +3.8018940e+21 +2.0961622e-01
Acceptor +4.4668359e+21 +2.1725839e-01
Acceptor +5.2480746e+21 +2.2515463e-01
Acceptor +6.1659500e+21 +2.3331769e-01
Acceptor +7.2443596e+21 +2.4176248e-01
Acceptor +8.5113804e+21 +2.5050626e-01
Acceptor +1.0000000e+22 +2.5956885e-01
Donor +1.0000000e+10 +000000000e+00
Donor +1.0000000e+15 +1.4062347e-03
Donor +1.1748976e+15 +1.5219386e-03
Donor +1.3803843e+15 +1.6469623e-03
Donor +1.6218101e+15 +1.7820231e-03
Donor +1.9054607e+15 +1.9278886e-03
Donor +2.2387211e+15 +2.0853788e-03
Donor +2.6302680e+15 +2.2553687e-03
Donor +3.0902954e+15 +2.4387915e-03
Donor +3.6307805e+15 +2.6366404e-03
Donor +4.2657952e+15 +2.8499720e-03
Donor +5.0118723e+15 +3.0799081e-03
Donor +5.8884366e+15 +3.3276384e-03
Donor +6.9183097e+15 +3.5944230e-03
Donor +8.1283052e+15 +3.8815942e-03
Donor +9.5499259e+15 +4.1905585e-03
Donor +1.1220185e+16 +4.5227991e-03
Donor +1.3182567e+16 +4.8798772e-03
Donor +1.5488166e+16 +5.2634341e-03
Donor +1.8197009e+16 +5.6751936e-03
Donor +2.1379621e+16 +6.1169637e-03
Donor +2.5118864e+16 +6.5906400e-03
Donor +2.9512092e+16 +7.0982093e-03
Donor +3.4673685e+16 +7.6417546e-03
Donor +4.0738028e+16 +8.2234619e-03
Donor +4.7863009e+16 +8.8456296e-03
Donor +5.6234133e+16 +9.5106804e-03
Donor +6.6069345e+16 +1.0221177e-02

Donor +7.7624712e+16 +1.0979842e-02
Donor +9.1201084e+16 +1.1789578e-02
Donor +1.0715193e+17 +1.2653491e-02
Donor +1.2589254e+17 +1.3574911e-02
Donor +1.4791084e+17 +1.4557386e-02
Donor +1.7378008e+17 +1.5604661e-02
Donor +2.0417379e+17 +1.6720575e-02
Donor +2.3988329e+17 +1.7908875e-02
Donor +2.8183829e+17 +1.9172870e-02
Donor +3.3113112e+17 +2.0514899e-02
Donor +3.8904514e+17 +2.1935611e-02
Donor +4.5708819e+17 +2.3433144e-02
Donor +5.3703180e+17 +2.5002439e-02
Donor +6.3095734e+17 +2.6635059e-02
Donor +7.4131024e+17 +2.8319882e-02
Donor +8.7096359e+17 +3.0044811e-02
Donor +1.0232930e+18 +3.1799142e-02
Donor +1.2022644e+18 +3.3575801e-02
Donor +1.4125375e+18 +3.5372605e-02
Donor +1.6595869e+18 +3.7192170e-02
Donor +1.9498446e+18 +3.9040695e-02
Donor +2.2908677e+18 +4.0926272e-02
Donor +2.6915348e+18 +4.2857330e-02
Donor +3.1622777e+18 +4.4841561e-02
Donor +3.7153523e+18 +4.6885363e-02
Donor +4.3651583e+18 +4.8993682e-02
Donor +5.1286138e+18 +5.1170056e-02
Donor +6.0255959e+18 +5.3416736e-02
Donor +7.0794578e+18 +5.5734777e-02
Donor +8.3176377e+18 +5.8124085e-02
Donor +9.7723722e+18 +6.0583432e-02
Donor +1.1481536e+19 +6.3110525e-02
Donor +1.3489629e+19 +6.5702249e-02
Donor +1.5848932e+19 +6.8355268e-02
Donor +1.8620871e+19 +7.1067129e-02
Donor +2.1877616e+19 +7.3837903e-02

Donor +2.5703958e+19 +7.6672069e-02
Donor +3.0199517e+19 +7.9579985e-02
Donor +3.5481339e+19 +8.2578090e-02
Donor +4.1686938e+19 +8.5687344e-02
Donor +4.8977882e+19 +8.8930252e-02
Donor +5.7543994e+19 +9.2327600e-02
Donor +6.7608298e+19 +9.5896151e-02
Donor +7.9432823e+19 +9.9647875e-02
Donor +9.3325430e+19 +1.0359053e-01
Donor +1.0964782e+20 +1.0772892e-01
Donor +1.2882496e+20 +1.1206626e-01
Donor +1.5135612e+20 +1.1660522e-01
Donor +1.7782794e+20 +1.2134866e-01
Donor +2.0892961e+20 +1.2630001e-01
Donor +2.4547089e+20 +1.3146340e-01
Donor +2.8840315e+20 +1.3684371e-01
Donor +3.3884416e+20 +1.4244647e-01
Donor +3.9810717e+20 +1.4827781e-01
Donor +4.6773514e+20 +1.5434434e-01
Donor +5.4954087e+20 +1.6065310e-01
Donor +6.4565423e+20 +1.6721147e-01
Donor +7.5857758e+20 +1.7402714e-01
Donor +8.9125094e+20 +1.8110807e-01
Donor +1.0471285e+21 +1.8846250e-01
Donor +1.2302688e+21 +1.9609897e-01
Donor +1.4454398e+21 +2.0402636e-01
Donor +1.6982437e+21 +2.1225397e-01
Donor +1.9952623e+21 +2.2079164e-01
Donor +2.3442288e+21 +2.2964992e-01
Donor +2.7542287e+21 +2.3884018e-01
Donor +3.2359366e+21 +2.4837493e-01
Donor +3.8018940e+21 +2.5826799e-01
Donor +4.4668359e+21 +2.6853482e-01
Donor +5.2480746e+21 +2.7919283e-01
Donor +6.1659500e+21 +2.9026166e-01
Donor +7.2443596e+21 +3.0176349e-01

```
Donor +8.5113804e+21 +3.1372335e-01
Donor +1.0000000e+22 +3.2616938e-01
}
}
MaterialInterface = "Nitride/Silicon" {
SurfaceRecombination {
S0 = @Sfront_SiNx@, @Sfront_SiNx@
Sref = 0
}
}
# - - - - - - -To be added for TOPCon - - - - - - -
Material = "PolySi" {
Bandgap {
Eg0 = +1.1752165e+00
alpha = +4.73e-04
beta = +6.36e+02
}
BarrierTunneling {
mt = 0.36,0.38
}
}
Material = "Oxide" {
BarrierTunneling {
mt = 0.4 , 0.32
}
}
RegionInterface = "substrate/backSiO2"{
SurfaceRecombination {
S0 = @Srear_Si_SiO2@, @Srear_Si_SiO2@
Sref = 0
}
}
# - - - - - - - To be added for PERC - - - - - - -
RegionInterface = "substrate/backAl2O3_1" {
SurfaceRecombination {
S0 = @Srear_dielectric@, @Srear_dielectric@
```

```
Sref = 0
}
}
RegionInterface = "substrate/backAl2O3_2" {
SurfaceRecombination {
S0 = @Srear_dielectric@, @Srear_dielectric@
Sref = 0
}
}
# - - - - - - - - - - - - - - (END) Parameter file - - - - - - - - - - - - - -
```

References

[1] The International Energy Agency, “Snapshot of Global PV Markets 2022," https://iea-pvps.org/snapshot-reports/snapshot-2022/ (accessed January 21, 2022).

[2] ITRPV, 2021. “International Technology Roadmap for Photovoltaic (ITRPV) 2020 results," https://itrpv.vdma.org (accessed March 11, 2022).

[3] Weekly Snapshots and Price, http://www.pvinsights.com (accessed February 15, 2022).

[4] M. Woodhouse, B. Smith, A. Ramdas, and R. Margolis, “Crystalline silicon photovoltaic module manufacturing costs and sustainable pricing: 1H 2018 benchmark and cost reduction roadmap," *National Renewable Energy Laboratory*, Technical Report NREL/TP-6A20-72134, 2019, https://www.nrel.gov/docs/fy19osti/72134.pdf.

[5] J. Horzel, S. Mack, I. V. Vulanean, K. Zimmermann, S. Pingel, W. Kwapil, F. Maischner, H. Höffler, S. Bashardoust, D. Wagenmann, J. Greulich, J. Seif, A. Steinmetz, and J. Rentsch, “High lifetime Ga-doped Cz-Si for carrier selective junction solar cells," *Solar RRL*, pp. 2200613, 2022, doi:10.1002/solr.202200613.

[6] M. L. Green, E. P. Gusev, R. Degraeve, and E. L. Garfunkel, “Ultrathin (< 4 nm) SiO_2 and Si–O–N gate dielectric layers for silicon microelectronics: understanding the processing, structure, and physical and electrical limits," *Journal of Applied Physics*, vol. 90, no. 5, pp. 2057–2121, 2001, doi:10.1063/1.1385803.

[7] E. H. Nicollian and J. R. Brews, *Metal Oxide Semiconductor (MOS) Physics and Technology*, New York, Wiley, 1982, ISBN:978-0-471-43079-7.

[8] J. Zhao, A. Wang, P. Altermatt, and M. A. Green, “Twenty-four percent efficient silicon solar cells with double layer antireflection coatings and reduced resistance

loss," *Applied Physics Letters*, vol. 66, no. 26, pp. 3636–3638, 1995, doi:10.1063/1.114124.

[9] D. McDonald and A. Cuevas, "The trade-off between phosphorus gettering and thermal degradation in multicrystalline silicon," in *proceedings of 16th European Photovoltaic Solar Energy Conference (EU PVSEC)*, 2000, http://hdl.handle.net/1885/40855.

[10] P. Saint-Cast, J. Haunschild, C. Schwab, E. Billot, M. Hofmann, J. Rentsch, and R. Preu, "Metal pinning through rear passivation layers: characterization and effects on solar cells," *Energy Procedia*, vol. 8, pp. 324–330, 2011, doi:10.1016/j.egypro.2011.06.144.

[11] Z. Chen, S. K. Pang, K. Yasutake, and A. Rohatgi, "Plasma-enhanced chemicalvapor-deposited oxide for low surface recombination velocity and high effective lifetime in silicon," *Journal of Applied Physics*, vol. 74, no. 4, pp. 2856–2859, 1993, doi:10.1063/1.354638.

[12] G. Dingemans, M. C. M. Van De Sanden, and W. M. M. Kessels, "Excellent Si surface passivation by low temperature SiO_2 using an ultrathin Al_2O_3 capping film," *Physica Status Solidi (RRL)–Rapid Research Letters*, vol. 5, no. 1, pp. 22–24, 2011, doi:10.1002/pssr.201004378.

[13] G. Dingemans, M. Mandoc, S. Bordihn, M. Van de Sanden, and W. Kessels, "Effective passivation of Si surfaces by plasma deposited SiO_x/a-SiN_x:H stacks," *Applied Physics Letters*, vol. 98, no. 22, pp. 222102, 2011, doi:10.1063/1.3595940.

[14] N. E. Grant, T. C. Kho, and K. Weber, "High-level silicon surface passivation by anodically grown silicon dioxide and silicon nitride stacks," *IEEE Journal of Photovoltaics*, vol. 5, no. 4, pp. 1047–1052, 2015, doi:10.1109/JPHOTOV.2015.2422577.

[15] A. Richter, R. Müller, J. Benick, F. Feldmann, B. Steinhauser, C. Reichel, A. Fell, M. Bivour, M. Hermle, and S. W. Glunz, "Design rules for high-efficiency bothsides-contacted silicon solar cells with balanced charge carrier transport and recombination losses," *Nature Energy*, vol. 6, no. 4, pp. 429–438, 2021, doi:10.1038/s41560-021-00805-w.

[16] R. F. Pierret and G. W. Neudeck, *Advanced semiconductor fundamentals*, Addison-Wesley Reading, MA, 1987.

[17] T. Trupke, M. A. Green, P. Würfel, P. P. Altermatt, A. Wang, Z. Zhao, and R. Corkish, “Temperature dependence of the radiative recombination coefficient of intrinsic crystalline silicon," *Journal of Applied Physics*, vol. 94, no. 8, pp. 4930–4937, 2003, doi:10.1063/1.1610231.

[18] P. P. Altermatt, J. Schmidt, G. Heiser, and A. G. Aberle, “Assessment and parameterisation of Coulomb-enhanced Auger recombination coefficients in lowly injected crystalline silicon," *Journal of Applied Physics*, vol. 82, no. 10, pp. 4938–4944, 1997, doi:10.1063/1.366360.

[19] A. G. Aberle, S. Glunz,and W. Warta, “Impact of illumination level and oxide parameters on Shockley–Read–Hall recombination at the Si-SiO_2 interface," *Journal of Applied Physics*, vol. 71, no. 9, pp. 4422–4431, 1992, doi:10.1063/1.350782.

[20] S. M. Sze and K. K. Ng, *Physics of semiconductor devices*, John Wiley & Sons, 2006, ISBN:9780471143239.

[21] J. Dziewior and W. Schmid, “Auger coefficients for highly doped and highly excited silicon," *Applied Physics Letters*, vol. 31, no. 5, pp. 346–348, 1977, doi:10.1063/1.89694.

[22] E. Yablonovitch and T. Gmitter, “Auger recombination in silicon at low carrier densities," *Applied Physics Letters*, vol. 49, no. 10, pp. 587–589, 1986, doi:10.1063/1.97049.

[23] A. Hangleiter and R. Häcker, “Enhancement of band-to-band Auger recombination by electron-hole correlations," *Physical Review Letters*, vol. 65, no. 2, pp. 215, 1990, doi:10.1103/PhysRevLett.65.215.

[24] A. Richter, S. W. Glunz, F. Werner, J. Schmidt, and A. Cuevas, “Improved quantitative description of Auger recombination in crystalline silicon," *Physical Review B*, vol. 86, no. 16, pp. 165202, 2012, doi:10.1103/PhysRevB.86.165202.

[25] P. P Altermatt, A. Schenk, F. Geelhaar, and G. Heiser, “Reassessment of the intrinsic carrier density in crystalline silicon in view of band-gap narrowing," *Journal of Applied Physics*, vol. 93, no. 3, pp. 1598–1604, 2003, doi:10.1063/1.1529297.

[26] P. P. Altermatt, F. Geelhaar, T. Trupke, X. Dai, A. Neisser, and E. Daub, “Injection dependence of spontaneous radiative recombination in c-Si: experiment, theoretical analysis, and simulation," in *proceedings of 5th International Conference*

on Numerical Simulation of Optoelectronic Devices (NUSOD), 2005, pp. 47–48, doi:10.1109/NUSOD.2005.1518128.

[27] W. Shockley and W. Read Jr, “Statistics of the recombinations of holes and electrons," *Physical Review*, vol. 87, no. 5, p. 835, 1952, doi:10.1103/PhysRev.87.835.

[28] R. E. Hall, “Electron-hole recombination in germanium," *Physical Review*, vol. 87, no. 2, pp. 387, 1952, doi:10.1103/PhysRev.87.387.

[29] C. Sah, R. N. Noyce, and W. Shockley, “Carrier generation and recombination in pn junctions and pn junction characteristics," in *proceedings of the IRE*, 1957, pp. 1228–1243, doi:10.1109/JRPROC.1957.278528.

[30] W. D. Eades and R. M. Swanson, “Calculation of surface generation and recombination velocities at the Si-SiO_2 interface," *Journal of Applied Physics*, vol. 58, no. 11, pp. 4267–4276, 1985, doi:10.1063/1.335562.

[31] K. R. McIntosh and L. E. Black, “On effective surface recombination parameters," *Journal of Applied Physics*, vol. 116, no. 1, pp. 014503, 2014, doi:110.1063/1.4886595.

[32] V. Grivickas, D. Noreika, and J. Tellefsen, “Surface and auger recombinations in silicon wafers of high carrier density," *Lithunian Physics Journal*, vol. 29, no. 5, pp. 591–8, 1989.

[33] PV Lighthouse Mobility Calculator. https://www2.pvlighthouse.com.au/calculators/mobility%20calculator/mobility%20calculator.aspx (accessed Aug.10, 2019).

[34] A. W. Stephens, A. G. Aberle, and M. A. Green, “Surface recombination velocity measurements at the silicon–silicon dioxide interface by microwave-detected photoconductance decay," *Journal of Applied Physics*, vol. 76, no. 1, pp. 363–370, 1994, doi:10.1063/1.357082.

[35] W. Shockley, “The Theory of p-n Junctions in Semiconductors and p-n Junction Transistors," *Bell System Technical Journal*, vol. 28, no. 3, pp. 435–489, 1949, doi:10.1002/j.1538-7305.1949.tb03645.x.

[36] A. Onno, C. Chen, P. Koswatta, M. Boccard, and Z. C. Holman, “Passivation, conductivity, and selectivity in solar cell contacts: Concepts and simulations based on a

unified partial-resistances framework," *Journal of Applied Physics*, vol. 126, no. 18, pp. 183103, 2019, doi:10.1063/1.5117201.

[37] A. Cuevas and R. A. Sinton, "Prediction of the open-circuit voltage of solar cells from the steady-state photoconductance," *Progress in Photovoltaics: Research and Applications*, vol. 5, no. 2, pp. 79–90, 1997, doi:10.1002/(SICI)1099-159X(199703/04)5:2<79::AID-PIP155>3.0.CO;2-J.

[38] A. W. Stephens and M. A. Green, "Effectiveness of 0.08 molar iodine in ethanol solution as a means of chemical surface passivation for photoconductance decay measurements," *Solar Energy Materials and Solar Cells*, vol. 45, no. 3, pp. 255–265, 1997, doi:10.1016/S0927-0248(96)00061-X.

[39] B. Chhabra, S. Bowden, R. L. Opila, and C. B. Honsberg, "High effective minority carrier lifetime on silicon substrates using quinhydrone-methanol passivation," *Applied Physics Letters*, vol. 96, no. 6, pp. 063502, 2010, doi:10.1063/1.3309595.

[40] H. Takato, I. Sakata, and R. Shimokawa, "Quinhydrone/methanol treatment for the measurement of carrier lifetime in silicon substrates," *Japanese Journal of Applied Physics*, vol. 41, no. 8A, pp. L870, 2002, doi:10.1143/JJAP.41.L870.

[41] A. G. Aberle, S. Glunz, and W. Warta, "Field effect passivation of high efficiency silicon solar cells," *Solar Energy Materials and Solar Cells*, vol. 29, no. 2, pp. 175–182, 1993, doi:10.1016/0927-0248(93)90075-E.

[42] S. W. Glunz, D. Biroand, S. Rein, and W. Warta, "Field-effect passivation of the SiO_2-Si interface," *Journal of Applied Physics*, vol. 86, no. 1, pp. 683–691, 1999, doi:10.1063/1.370784.

[43] J. Mandelkorn and J. H. Lamneck Jr, "Simplified fabrication of back surface electric field silicon cells and novel characteristics of such cells," *Solar Cells*, vol. 29, no. 2-3, pp. 121–130, 1990, doi:10.1016/0379-6787(90)90021-V.

[44] R. R. King, R. A. Sinton, and R. M. Swanson, "Front and back surface fields for point-contact solar cells," in *proceedings 20th IEEE Photovoltaic Specialists Conference (PVSC)*, 1998, pp. 538–544, doi:10.1109/PVSC.1988.105760.

[45] R. S. Bonilla, B. Hoex, P. Hamer, and P. .R. Wilshaw, "Dielectric surface passivation for silicon solar cells: A review," *Physica Status Solidi (A)*, vol. 214, no. 7, pp. 1700293, 2017, doi:10.1002/pssa.201700293.

[46] B. E. Deal, ans A. S. Grove, “General relationship for the thermal oxidation of silicon," *Journal of Applied Physics*, vol. 36, no. 12, pp. 3770–3778, 1965, doi:10.1063/1.1713945.

[47] B. E. Deal, “The current understanding of charges in the thermally oxidized silicon structure," *Journal of the Electrochemical Society*, vol. 121, no. 6, pp. 198C–205C, 1974, doi:10.1149/1.2402380.

[48] P. L. Castro and B. E. Deal, “Low-temperature reduction of fast surface states associated with thermally oxidized silicon," *Journal of the Electrochemical Society*, vol. 118, no. 2, pp. 280, 1971, doi:10.1149/1.2408016.

[49] L. Do Thanh and P. Balk, “Elimination and Generation of Si-SiO_2 Interface Traps by Low Temperature Hydrogen Annealing," *Journal of the Electrochemical Society*, vol. 135, no. 7, pp. 1797, 1988, doi:10.1149/1.2096133.

[50] M. l. Reed and J. D. Plummer, “Chemistry of Si-SiO_2 interface trap annealing," *Journal of Applied Physics*, vol. 63, no. 12, pp. 5776–5793, 1988, doi:10.1063/1.340317.

[51] A. W. Blakers, A. Wang, A. M. Milne, J. Zhao, and M. A. Martin, “22.8% efficient silicon solar cell" *Applied Physics Letters*, vol. 55, no. 13, pp. 1363–1365, 1989, doi:10.1063/1.101596.

[52] D. Kray, M. Hermle, and S. W. Glunz, “Theory and experiments on the back side reflectance of silicon wafer solar cells," *Progress in Photovoltaics: Research and Applications*, vol. 16, no. 1, pp. 1–15, 2008, doi:10.1002/pip.769.

[53] J. Zhao, A. Wang, and M. A. Green, “24.5% efficiency silicon PERT cells on MCZ substrates and 24.7% efficiency PERL cells on FZ substrates," *Progress in Photovoltaics: Research and Applications*, vol. 7, no. 6, pp. 471–474, 1999, doi:10.1002/(SICI)1099-159X(199911/12)7:6<471::AID-PIP298>3.0.CO;2-7

[54] G. Declerck, R. Van Overstraeten, and G. Broux, “Measurement of low densities of surface states at Si-SiO_2 interface," *Solid State Electronics*, vol. 16, no. 12, pp. 1451–1460, 1973, doi:10.1016/0038-1101(73)90062-2.

[55] A. G. Aberle, S. W. Glunz, A. W. Stephens, and M. A. Green, “High-efficiency silicon solar cells: Si/SiO_2, interface parameters and their impact on device performance," *Progress in Photovoltaics: Research and Applications*, vol. 2, no. 4, pp. 265-273, 1994, doi:10.1002/pip.4670020402.

[56] M. J. Kerr and A. Cuevas, “Very low bulk and surface recombination in oxidized silicon wafers," *Semiconductor Science and Technology*, vol. 17, no. 1, pp. 35, 2001, doi:10.1088/0268-1242/17/1/306.

[57] M. J. Kerr and A. Cuevas, “General parameterization of Auger recombination in crystalline silicon," *Journal of Applied Physics*, vol. 91, no. 4, pp. 2473–2480, 2002, doi:10.1063/1.1432476.

[58] S. W. Glunz, A. B. Sproul, W. Warta, and W. Wettling, “Injection-level-dependent recombination velocities at the Si-SiO_2 interface for various dopant concentrations," *Journal of Applied Physics*, vol. 75, no. 3, pp. 1611–1615, 1994, doi:10.1063/1.356399.

[59] S. Xiao and S. Xu, “High-efficiency silicon solar cells—materials and devices physics," *Critical Reviews in Solid State and Materials Sciences*, vol. 39, no. 4, pp. 277–317, 2014, doi:10.1080/10408436.2013.834245.

[60] L. Alt, S. W. Ing, and K. W. Laendle, “Low-temperature deposition of silicon oxide films," *Journal of the Electrochemical Society*, vol. 110, no. 5, pp. 465, 1963, doi:10.1149/1.2425789.

[61] J. Batey and E. Tierney, “Low-temperature deposition of high-quality silicon dioxide by plasma-enhanced chemical vapor deposition," *Journal of Applied Physics*, vol. 60, no. 9, pp. 3136–3145, 1986, doi:10.1063/1.337726.

[62] T. Mueller, S. Schwertheim, M. Scherff, and W. R. Fahrner, “High quality passivation for heterojunction solar cells by hydrogenated amorphous silicon suboxide films," *Applied Physics Letters*, vol. 92, no. 3, pp. 033504, 2008, doi:10.1063/1.2837192.

[63] A. Kobayashi, O. Maida, M. Inoue, M. Takahashi, Y. Todokoro, and H. Kobayashi, “Ultrathin silicon dioxide layers with a low leakage current density formed by chemical oxidation of Si," *Applied Physics Letters*, vol. 81, no. 18, pp. 3410–3412, 2002, doi:10.1063/1.1517723.

[64] A. Kobayashi, O. Maida, M. Takahashi, and H. Iwasa, “Nitric acid oxidation of Si to form ultrathin silicon dioxide layers with a low leakage current density," *Journal of Applied Physics*, vol. 94, no. 11, pp. 7328–7335, 2003, doi:10.1063/1.1621720.

[65] N. E. Grant and K. R. McIntosh, “Silicon surface passivation by anodic oxidation annealed at 400^{o}C," *ECS Journal of Solid State Science and Technology*, vol. 3, no. 2, pp. P13–P16, 2013, doi:10.1149/2.009402jss.

[66] F. Feldmann, M. Bivour, C. Reichel, H. Steinkemper, M. Hermle, and S. W. Glunz, “Tunnel oxide passivated contacts as an alternative to partial rear contacts," *Solar Energy Materials and Solar Cells*, vol. 131, pp. 46–50, 2014, doi:10.1016/j.solmat.2014.06.015.

[67] B. Stegemann, K. M. Gad, P. Balamou, and D. Sixtensson, D. Vössing, M. Kasemann, H. Angermann, “Ultra-thin silicon oxide layers on crystalline silicon wafers: Comparison of advanced oxidation techniques with respect to chemically abrupt SiO_2/Si interfaces with low defect densities," *Applied Surface Science*, vol. 395, pp. 78–85, 2017, doi:10.1016/j.apsusc.2016.06.090.

[68] G. Chen, “The applications of DI-O_3 water on wafer surface preparation," in *proceedings of International Conference on Wafer Rinsing, Water Reclamation and Environmental Technology for Semiconductor Manufacturing*, 1999, pp. 100–123, https://www.semanticscholar.org/paper/The-Application-of-DIO-3-Water-on-Wafer-Surface-Chen/267db4719de2136b13fcb0c041401c586005f053.

[69] H. Ali, A. Moldovan, S. Mack, M. Wilson, W. V. Schoenfeld, and K. O. Davis, “Influence of surface preparation and cleaning on the passivation of boron diffused silicon surfaces for high efficiency photovoltaics," *Thin Solid Films*, vol. 636, pp. 412–418, 2017, doi:10.1016/j.tsf.2017.06.043.

[70] S. Bakhshi, N. Zin, K. O. Davis, M. Wilson, I. Kashkoush, W. V. Schoenfeld, “Improving silicon surface passivation with a silicon oxide layer grown via ozonated deionized water," in *proceedings of IEEE 44th Photovoltaic Specialist Conference (PVSC)*, 2017, pp. 322–325, doi:10.1109/PVSC.2017.8366153.

[71] J. R. Vig, “UV/ozone cleaning of surfaces," *Journal of Vacuum Science & Technology A: Vacuum, Surfaces, and Films*, vol. 3, no. 3, pp. 1027–1034, 1985, doi:10.1116/1.573115.

[72] D. A. Bolon and C. O. Kunz, “Ultraviolet depolymerization of photoresist polymers," *Polymer Engineering & Science*, vol. 12, no. 2, pp. 109–111, 1972, doi:10.1002/pen.760120206.

[73] A. Moldovan, F. Feldmann, G. Krugel, M. Zimmer, J. Rentsch, M. Hermle, A. Roth-Fölsch, K. Kaufmann, and C. Hagendorf, "Simple cleaning and conditioning of silicon surfaces with UV/Ozone sources," *Energy Procedia*, vol. 55, pp. 834–844, 2014, doi:10.1016/j.egypro.2014.08.067.

[74] S. Bakhshi, N. Zin, H. Ali, M. Wilson, D. Chanda, K. O. Davis, and W. V. Schoenfeld, "Simple and versatile UV-ozone oxide for silicon solar cell applications," *Solar Energy Materials and Solar Cells*, vol. 185, pp. 505–510, 2018, doi:10.1016/j.solmat.2018.06.006.

[75] K. Srinivasan and A. Kottantharayil, "Aluminium oxide thin film deposited by spray coating for p-type silicon surface passivation," *Solar Energy Materials and Solar Cells*, vol. 197, pp. 93–98, 2019, doi:10.1016/j.solmat.2019.03.048.

[76] S. Park, C. Kim, W. Lee, S. Sung, and M. Yoon, "Sol-gel metal oxide dielectrics for all-solution-processed electronics," *Materials Science and Engineering: R: Reports*, vol. 114, pp. 1–22, 2017, doi:10.1016/j.mser.2017.01.003.

[77] M. S. Mozumder, A. I. Mourad, H. Pervez, and R. Surkatti, "Recent developments in multifunctional coatings for solar panel applications: A review," *Solar Energy Materials and Solar Cells*, vol. 189, pp. 75–102, 2019, doi:10.1016/j.solmat.2018.09.015.

[78] A. M. Siouffi, "Silica gel-based monoliths prepared by the sol–gel method: facts and figures," *Journal of Chromatography A*, vol. 1000, no. 1-2, pp. 801–818, 2003, doi:10.1016/S0021-9673(03)00510-7.

[79] M. Fardad, "Catalysts and the structure of SiO_2 sol-gel films," *Journal of Materials Science*, vol. 35, no. 7, pp. 1835–1841, 2000, doi:10.1023/A:1004749107134.

[80] C. J. Brinker, "Hydrolysis and condensation of silicates: effects on structure," *Journal of Non-crystalline Solids*, vol. 100, no. 1-3, pp. 31–50, 1988, doi:10.1016/0022-3093(88)90005-1.

[81] C. Milea, C. Bogatu, and A. Duta, "The influence of parameters in silica sol-gel process," *Bulletin of the Transilvania University of Brasov, Series I: Engineering Sciences*, vol. 4, no. 1, p. 59, 2011, https://www.proquest.com/openview/b8415807cdaf80f5131ce1582a531566/1?pq-origsite=gscholar&cbl=105974.

[82] M. Fardad, E. Yeatman, E. Dawnay, M. Green, and F. Horowitz, “Effects of H_2O on structure of acid-catalysed SiO_2 sol-gel films," *Journal of Non-Crystalline Solids*, vol. 183, no. 3, pp. 260–267, 1995, doi:10.1016/0022-3093(94)00661-X.

[83] M. Matos, A. M. Carvalho, R. M. Almeida, and L. M. Ilharco, “Influence of processing parameters on the thickness of sol-gel silica films," *Sol-Gel Optics II*, vol. 1758, pp. 77–82, 1992, doi:10.1117/12.132002.

[84] A. Vincent, S. Babu, E. Brinley, A. Karakoti, S. Deshpande, and S. Seal, “Role of catalyst on refractive index tunability of porous silica antireflective coatings by solgel technique," *The Journal of Physical Chemistry C*, vol. 111, no. 23, pp. 8291–8298, 2007, doi:10.1021/jp0700736.

[85] F. Jaehnike, D. V. Pham, R. Anselmann, C. Bock, and U. Kunze, “High-quality solution-processed silicon oxide gate dielectric applied on indium oxide based thin-film transistors," *ACS Applied Materials & Interfaces*, vol. 7, no. 25, pp. 14011–14017, 2015, doi:10.1021/acsami.5b03105.

[86] J. J. Richardson, M. Björnmalm, and F. Caruso, “Technology-driven layer-by-layer assembly of nanofilms," *Science*, vol. 348, no. 6233, pp. aaa2491, 2015, doi:10.1126/science.aaa2491.

[87] K. Krogman, R. Cohen, P. Hammond, M. Rubner, and B. Wang, “Industrialscale spray layer-by-layer assembly for production of biomimetic photonic systems," *Bioinspiration & Biomimetics*, vol. 8, no. 4, pp. 045005, 2013, doi:10.1088/1748-3182/8/4/045005.

[88] M. Dierendonck, S. De Koker, R. De Rycke, and B. G. De Geest, “Just spray it–LbL assembly enters a new age," *Soft Matter*, vol. 10. no. 6, pp. 804–807, 2014, doi:10.1039/C3SM52202D.

[89] M. Esro, O. Kolosov, P. J. Jones, W. I. Milne, and G. Adamopoulos, “Structural and electrical characterization of SiO_2 gate dielectrics deposited from solutions at moderate temperatures in air," *ACS Applied Materials & Interfaces*, vol. 9, no. 1, pp. 529–536, 2016, doi:10.1021/acsami.6b11214.

[90] A. G. Aberle, M. B. Boreland, B. Hoex, T. Mueller, “Industrial silicon wafer solar cells–status and trends," *Green*, vol. 2, no. 4, pp. 135–148, 2012, doi:10.1515/green-2012-0007.

[91] C. Battaglia, A. Cuevas, and S. De Wolf, “High-efficiency crystalline silicon solar cells: status and perspectives," *Energy & Environmental Science*, vol. 9, no. 5, pp. 1552–1576, 2016, doi:10.1039/C5EE03380B

[92] J. R. Elmiger and M. Kunst, “Investigation of charge carrier injection in silicon nitride/silicon junctions," *Applied Physics Letters*, vol. 69, no. 4, pp. 517–519, 1996, doi:10.1063/1.117772.

[93] S. Dauwe, J. Schmidt, A. Metz, and R. Hezel, “Fixed charge density in silicon nitride films on crystalline silicon surfaces under illumination," in *proceedings IEEE 29th Photovoltaic Specialist Conference (PVSC)*, 2002, pp. 162–165, doi:10.1109/PVSC.2002.1190481.

[94] J. F. Lelièvre, E. Fourmond, A. Kaminski, O. Palais, D. Ballutaud, and M. Lemiti, “Study of the composition of hydrogenated silicon nitride SiN_x:H for efficient surface and bulk passivation of silicon," *Solar Energy Materials and Solar Cells*, vol. 93, no. 8, pp. 1281–1289, 2009, doi:10.1016/j.solmat.2009.01.023.

[95] Y. Larionova, V. Mertens, N. Harder, and R. Brendel, “Surface passivation of ntype Czochralski silicon substrates by thermal-SiO_2/plasma-enhanced chemical vapor deposition SiN stacks," *Applied Physics Letters*, vol. 96, no. 3, pp. 032105, 2010, doi:10.1063/1.3291681.

[96] J. Schmidt, M. Kerr, and A. Cuevas, “Surface passivation of silicon solar cells using plasma-enhanced chemical-vapour-deposited SiN films and thin thermal SiO_2/plasma SiN stacks," *Semiconductor Science and Technology*, vol. 16, no. 3, pp. 164, 2001, doi:0.1088/0268-1242/16/3/308.

[97] N. E Grant and K. R. McIntosh, “A review on low temperature chemically formed silicon dioxide for solar cell applications," in *proceedings of 48th Australian Solar Energy Society*, 2010, doi:10.13140/2.1.3541.3443.

[98] J. Mandelkorn and J. Lamneck Jr , “A new electric field effect in silicon solar cells," *Journal of Applied Physics*, vol. 44, no. 10, pp. 4785–4787, 1973, doi:10.1063/1.1662040.

[99] R. Preu, E. Lohmüller, S. Lohmüller, P. Saint-Cast, and J. M. Greulich, “Passivated emitter and rear cell—Devices, technology, and modeling," *Applied Physics Reviews*, vol. 7, no. 4, pp. 041315, 2020, doi:10.1063/5.0005090.

[100] S. Gatz, H. Hannebauer, R. Hesse, F. Werner, A. Schmidt, T. Dullweber, J. Schmidt, K. Bothe, and R. Brendel, “19.4%-efficient large-area fully screen-printed silicon solar cells," *Physica Status Solidi (RRL)–Rapid Research Letters*, vol. 5, no. 4, pp. 147–149, 2011, doi:10.1002/pssr.201105045.

[101] J. Zhao and M. A. Green, “Optimized antireflection coatings for high-efficiency silicon solar cells," *IEEE Transactions on Electron Devices*, vol. 38, no. 8, pp. 1925–1934, 1991, doi:10.1109/16.119035.

[102] J. Schmidt, R. Peibst, and R. Brendel, “Surface passivation of crystalline silicon solar cells: Present and future," *Solar Energy Materials and Solar Cells*, vol. 187, pp. 39–54, 2018, doi:10.1016/j.solmat.2018.06.047.

[103] A. G. Aberle, “Surface passivation of crystalline silicon solar cells: a review," *Progress in Photovoltaics: Research and Applications*, vol. 8, no. 5, pp. 473–487, 2000, doi:10.1002/1099-159X(200009/10)8:5<473::AID-PIP337>3.0.CO;2-D.

[104] T. Dullweber and J. Schmidt, “Industrial silicon solar cells applying the passivated emitter and rear cell (PERC) concept—A review," *IEEE Journal of Photovoltaics*, vol. 6, no. 5, pp. 1366–1381, 2016, doi:10.1109/JPHOTOV.2016.2571627.

[105] T. Dullweber, H. Hannebauer, S. Dorn, S. Schimanke, A. Merkle, C. Hampe, and R. Brendel, “Emitter saturation current densities of 22 fA/cm^2 applied to industrial PERC solar cells approaching 22% conversion efficiency," *Progress in Photovoltaics: Research and Applications*, vol. 25, no. 7, pp. 509–514, 2017, doi:10.1002/pip.2806.

[106] S. Werner, E. Lohmüller, S. Maier, S. Mourad, and A. Wolf, “Challenges for lowly doped phosphorus emitters in silicon solar cells with screen-printed silver contacts," *Energy Procedia*, vol. 124, pp. 936–946, 2017, doi:10.1016/j.egypro.2017.09.274.

[107] E. Lohmüller, J. Greulich, P. Saint-Cast, S. Lohmüller, S. Schmidt, U. Belledin, T. Fellmeth, S. Mack, G. Emanuel, K. Krieg, M. Zimmer, R. Kunert, F. Zobel, M. Linse, J. Horsel, M. Meβmer, A. Wolf, and R. Preu, “Front side optimization on boron- and gallium-doped Cz-Si PERC solar cells exceeding 22% conversion efficiency," in *proceedings of 37th European PV Solar Energy Conference and Exhibition*, 2020, pp. p–11, doi:10.4229/EUPVSEC20202020-2DV.3.19.

[108] G. Hahn, “Status of selective emitter technology," in *proceedings of 5th World Conference on Photovoltaic Energy Conversion (WCPEC)*, 2010, pp. 1091–1096, doi:10.4229/25thEUPVSEC2010-2DP.2.2.

[109] Y. Lv, Y. F. Zhuang, W. J. Wang, W. W. Wei, J. Sheng, S. Zhang, and W. Z. Shen, “Towards high-efficiency industrial p-type mono-like Si PERC solar cells" *Solar Energy Materials and Solar Cells*, vol. 204, pp. 110202, 2020, doi:10.1016/j.solmat.2019.110202.

[110] Y. Zhang, L. Wang, D. Chen, M. Kim, and B. Hallam, “Pathway towards 24% efficiency for fully screen-printed passivated emitter and rear contact solar cells," *Journal of Physics D: Applied Physics*, vol. 54, no. 21, pp. 214003, 2021, doi:10.1088/1361-6463/abe900.

[111] A. Hübner, A. G. Aberle, and R. Hezel, “Novel cost-effective bifacial silicon solar cells with 19.4% front and 18.1% rear efficiency," *Applied Physics Letters*, vol. 70, no. 8, pp. 1008–1010, 1997, doi:10.1063/1.118466.

[112] S. Dauwe, L. Mittelstädt, A. Metz, and R. Hezel, “Experimental evidence of parasitic shunting in silicon nitride rear surface passivated solar cells," *Progress in Photovoltaics: Research and Applications*, vol. 10, no. 4, pp. 271–278, 2002, doi:10.1002/pip.420.

[113] S. Dauwe, L. Mittelstadt, A. Metz, J. Schmidt, and R. Hezel, “Low-temperature rear surface passivation schemes for > 20% efficient silicon solar cells," in *proceedings of 3rd World Conference on Photovoltaic Energy Conversion (WCPEC)*, 2003, pp. 1395–1398, https://ieeexplore.ieee.org/abstract/document/1306183.

[114] R. Hezel and K. Jaeger, “Low-temperature surface passivation of silicon for solar cells," *Journal of the Electrochemical Society*, vol. 136, no. 2, pp. 518, 1989, doi:10.1149/1.2096673.

[115] G. Agostinelli, A. Delabie, P. Vitanov, Z. Alexieva, H. Dekkers, S. De Wolf, and G. Beaucarne, “Very low surface recombination velocities on p-type silicon wafers passivated with a dielectric with fixed negative charge" *Solar Energy Materials and Solar Cells*, vol. 90, no. 18-19, pp. 3438–3443, 2006, doi:10.1016/j.solmat.2006.04.014.

[116] B. Hoex, J. Schmidt, P. Pohl, M. C. M. Van de Sanden, and W. M. M. Kessels, "Silicon surface passivation by atomic layer deposited Al_2O_3," *Journal of Applied Physics*, vol. 104, no. 4, pp. 044903, 2008, doi:10.1063/1.2963707.

[117] P. Saint-Cast, D. Kania, M. Hofmann, J. Benick, J. Rentsch, and R. Preu, "Very low surface recombination velocity on p-type c-Si by high-rate plasma-deposited aluminum oxide," *Applied Physics Letters*, vol. 95, no. 15, pp. 151502, 2009, doi:10.1063/1.3250157.

[118] J. Schmidt, A. Merkle, R. Brendel, B. Hoex, M. C. M van de Sanden, and W. M. M. Kessels, "Surface passivation of high-efficiency silicon solar cells by atomic-layer-deposited Al_2O_3," *Progress in Photovoltaics: Research and Applications*, vol. 16, no. 6, pp. 461–466, 2008, doi:10.1002/pip.823.

[119] J. Schmidt, B. Veith, and R. Brendel, "Effective surface passivation of crystalline silicon using ultrathin Al_2O_3 films and Al_2O_3/SiN_x stacks," *Physica Status Solidi (RRL)–Rapid Research Letters*, vol. 3, no. 9, pp. 287–289, 2009, doi:10.1002/pssr.200903272.

[120] B. Veith, F. Werner, D. Zielke, R. Brendel, and J. Schmidt, "Comparison of the thermal stability of single Al_2O_3 layers and Al_2O_3/SiN_x stacks for the surface passiviation of silicon," *Energy Procedia*, vol. 8, pp. 307–312, 2011, doi:10.1016/j.egypro.2011.06.141.

[121] S. Joonwichien, M. Moriya, S. Utsunomiya, Y. Kida, K. Shirasawa, and H. Takato, "Mechanism of metallization-induced losses in the rear-side of fully screen-printed p-type PERC solar cells," *IEEE Journal of Photovoltaics*, vol. 10, no. 2, pp. 407–416, 2020, doi:10.1109/JPHOTOV.2019.2962337.

[122] F. Feldmann, M. Bivour, C. Reichel, M. Hermle, and S. W. Glunz, "A passivated rear contact for high-efficiency n-type silicon solar cells enabling high Vocs and FF>82%," in *proceedings of 28th European Photovoltaic Solar Energy Conference and Exhibition (EU PVSEC)*, 2013, pp. 988–992, doi:10.4229/28thEUPVSEC2013-2CO.4.4.

[123] T. Sugiura, S. Matsumoto, and N. Nakano, "Numerical analysis of p-type and ntype based carrier-selective contact solar cells with tunneling oxide thickness and bulk properties," *Japanese Journal of Applied Physics*, vol. 59, no. SG, pp. SGGF03, 2020, doi:10.35848/1347-4065/ab6a2c.

[124] C. Liu, D. Chen, Y. Chen, Y. Ling, Y. Zou, Y. Wang, J. Gong, Z. Feng, P. P. Altermatt, and P. J. Verlinden, “Industrial TOPCon solar cells on n-type quasi-mono Si wafers with efficiencies above 23%," *Solar Energy Materials and Solar Cells*, vol. 215, pp. 110690, 2020, doi:10.1016/j.solmat.2020.110690.

[125] Y. Chen, D. Chen, C. Liu, Z. Wang, Y. Zou, Y. He, Y. Wang, L. Yuan, J. Gong, W. Lin, X. Zhang, Y. Yang, H. Shen, Z. Feng, P. P. Altermatt, and P. J. Verlinden, “Mass production of industrial tunnel oxide passivated contacts (i-TOPCon) silicon solar cells with average efficiency over 23% and modules over 345 W," *Progress in Photovoltaics: Research and Applications*, vol. 27, no. 10, pp. 827–834, 2019, doi:10.1002/pip.3180.

[126] M. K. Stodolny, M. Lenes, Y. Wu, G. J. M. Janssen, I. G. Romijn, J. R. M. Luchies, and L. J. Geerligs, “n-Type polysilicon passivating contact for industrial bifacial n-type solar cells," *Solar Energy Materials and Solar Cells*, vol. 158, pp. 24–28, 2016, doi:10.1016/j.solmat.2016.06.034.

[127] A. Richter, J. Benick, F. Feldmann, A. Fell, M. Hermle, and S. W. Glunz, “n-Type Si solar cells with passivating electron contact: identifying sources for efficiency limitations by wafer thickness and resistivity variation," *Solar Energy Materials and Solar Cells*, vol. 173, pp. 96–105, 2017, doi:10.1016/j.solmat.2017.05.042.

[128] LONGi Claims 3 New Cell Conversion Efficiency Records, https://taiyangnews.info/technology/longi-claims-3-new-cell-conversion-efficiency-records/, (accessed January 1, 2022) .

[129] D. Yan, A. Cuevas, S. P. Phang, Y. Wan, and D. Macdonald, “23% efficient ptype crystalline silicon solar cells with hole-selective passivating contacts based on physical vapor deposition of doped silicon films," *Applied Physics Letters*, vol. 113, no. 6, pp. 061603, 2018, doi:10.1063/1.5037610.

[130] T. Gao, Q. Yang, X. Guo, Y. Huang, Z. Zhang, Z. Wang, M. Liao, C. Shou, Y. Zeng, B. Yan, G. Hou, X. Zhang, Y. Zhao, and J. Ye, “An industrially viable TOPCon structure with both ultra-thin SiO_x and n^+-poly-Si processed by PECVD for p-type c-Si solar cells," *Solar Energy Materials and Solar Cells*, vol. 200, pp. 109926, 2019, doi:10.1016/j.solmat.2019.109926.

[131] A. Richter, J. Benick, R. Müller, F. Feldmann, C. Reichel, M. Hermle, and S. W. Glunz, “Tunnel oxide passivating electron contacts as full-area rear emitter of

high-efficiency p-type silicon solar cells," *Progress in Photovoltaics: Research and Applications*, vol. 26, no. 8, pp. 579–586, 2018, doi:10.1002/pip.2960.

[132] P. Park, S. Bae, S. Park, J. Hyun, C. Lee, D. Choi, D. Kang, H. Han, Y. Kang, H, Lee, and D. Kim, "Role of polysilicon in poly-Si/SiO_x passivating contacts for high-efficiency silicon solar cells," *RSC Advances*, vol. 9, no. 40, pp. 23261–23266, 2019, doi:10.1039/C9RA03560E.

[133] F. Feldmann, M. Simon, M. Bivour, C. Reichel, M. Hermle, and M. W. Glunz, "Efficient carrier-selective p-and n-contacts for Si solar cells," *Solar Energy Materials and Solar Cells*, vol. 131, pp. 100–104, 2014, doi:10.1016/j.solmat.2014.05.039.

[134] H. Steinkemper, F. Feldmann, M. Bivour, and M. Hermle, "Numerical simulation of carrier-selective electron contacts featuring tunnel oxides," *IEEE Journal of Photovoltaics*, vol. 5, no. 5, pp. 1348–1356, 2015, doi:10.1109/JPHOTOV.2015.2455346.

[135] D. K. Schroder, *Semiconductor material and device characterization*, Jhon Wiley & Sons, 2006, ISBN:9780471739067.

[136] L. M. Terman, "An investigation of surface states at a silicon/silicon oxide interface employing metal-oxide-silicon diodes," *Solid-State Electronics*, vol. 5, no. 5, pp. 285–299, 1962, doi:10.1016/0038-1101(62)90111-9.

[137] C. N. Berglund, "Surface states at steam-grown silicon-silicon dioxide interfaces," *IEEE Transactions on Electron Devices*, vol. 10, pp. 701–705, 1966, doi:10.1109/T-ED.1966.15827.

[138] M. Kuhn, "A quasi-static technique for MOS CV and surface state measurements," *Solid-State Electronics*, vol. 13, no. 6, pp. 873–885, 1970, doi:10.1016/0038-1101(70)90073-0.

[139] R. Castagne and A. Vapaille, "Description of the SiO_2-Si interface properties by means of very low frequency MOS capacitance measurements," *Surface Science*, vol. 28, no. 1, pp. 157–193, 1971, doi:10.1016/0039-6028(71)90092-6.

[140] E. H. Nicollian and A. Goetzberger, "The Si-SiO_2, interface–electrical properties as determined by the metal-insulator-silicon conductance technique," *The Bell System Technical Journal*, vol. 46, no. 6, pp. 1055–1033, 1967, doi:10.1002/j.1538-7305.1967.tb01727.x.

[141] W. Hill and C. Coleman, “A single-frequency approximation for interface-state density determination," *Solid State Electronics*, vol. 23, no. 9, pp. 987–993, 1980, doi:10.1016/0038-1101(80)90064-7.

[142] *IEEE guide for the statistical analysis of electrical insulation breakdown data*, IEEE Std. 930-2004, 2005, doi:10.1109/IEEESTD.2005.96286.

[143] M. P. Wilson, M. J. Given, I. V. Timoshkin, S. J. MacGregor, T. Wang, M. A. Sinclair, K. J. Thomas, and J. M. Lehr, “Impulse-driven surface breakdown data: A Weibull statistical analysis," *IEEE Transactions on Plasma Science*, vol. 40, no. 10, pp. 2449–2456, 2012, doi:10.1109/TPS.2011.2181172.

[144] R. Ross, “Graphical methods for plotting and evaluating weibull distributed data," in *proceedings of 4th International Conference on Properties and Applications of Dielectric Materials (ICPADM)* , 1994, pp. 250–253, doi:10.1109/ICPADM.1994.413986.

[145] R. J. Singh and R. S. Srivastava, “Distribution of surface states based on Hill and Coleman conductance technique," *Pramana*, vol. 18, no. 2, pp. 137–143, 1982, doi:10.1007/BF02847983.

[146] Measurement of solar cell efficiency, https://www.pveducation.org/pvcdrom/characterisation/measurement-of-solar-cell-efficiency (accessed Januray 7, 2022).

[147] S. Bowden and A. Rohatgi, “Rapid and accurate determination of series resistance and fill factor losses in industrial silicon solar cells," in *proceedings of 17th European Photovoltaic Solar Energy Conference and Exhibition (EU PVSEC)*, 2001, http://hdl.handle.net/1853/26165.

[148] A. Vilalta-Clemente, K. Gloystein, and N. Frangis, “Principles of atomic force microscopy (AFM)," in *proceedings of Physics of Advanced Materials Winter School*, 2008.

[149] R. E. Bank, D. J. Rose, and W. Fichtner, “Numerical methods for semiconductor device simulation," *SIAM Journal on Scientific and Statistical Computing*, vol. 4, no. 3, pp. 416–435, 1983, doi:10.1137/0904032.

[150] Synopsys TCAD, http://www.synopsys.com, (accessed January 10, 2021).

[151] Z. Chen, K. Yasutake, A. Doolittle, and A. Rohatgi, “Record low SiO_2/Si interface state density for low temperature oxides prepared by direct plasma-enhanced chemical vapor deposition," *Applied Physics Letters*, vol. 63, no. 15, pp. 2117–2119, 1993, doi:10.1063/1.110558.

[152] C. Milea, C. Bogatu, and A. Duta, “The influence of parameters in silica sol-gel process," *Bulletin of the Transilvania University of Brasov, Series I: Engineering Sciences*, vol. 4, no. 1, p. 59, 2011.

[153] K. Vorotilov, E. Orlova, and V. Petrovsky, “Sol-gel silicon dioxide films," *Thin Solid Films*, vol. 209, no. 2, pp. 188–194, 1992, doi:10.1016/0040-6090(92)90674-Z.

[154] C. McDonagh, F. Sheridan, T. Butler, and B. MacCraith, “Characterisation of solgel-derived silica films," *Journal of Non-Crystalline Solids*, vol. 194, no. 1-2, pp. 72–77, 1996, doi:10.1016/0022-3093(95)00488-2.

[155] W. Kern, “The evolution of silicon wafer cleaning technology," *Journal of the Electrochemical Society*, vol. 137. no. 6, pp. 1887–1892, 1990, doi:10.1149/1.2086825.

[156] J. Drelich, E. Chibowski, D. D. Meng, and K. Terpilowski, “Hydrophilic and superhydrophilic surfaces and materials," *Soft Matter*, vol. 7, no. 21, pp. 9804–9828, 2011, doi:10.1039/C1SM05849E.

[157] H. Wang, B. Yu, S. Jiang, L. Jiang, and L. Qian, “UV/ozone-assisted tribochemistry-induced nanofabrication on Si (100) surfaces," *RSC Advances*, vol. 7, no. 63, pp. 39651–39656, 2017, doi:10.1039/C7RA07198A.

[158] P. Mezza, E. Chibowski, J. Phalippou, and R. Sempere, “Sol–gel derived porous silica films," *Journal of Non-crystalline Solids*, vol. 243, no. 1, pp. 75–79, 1999, doi:10.1016/S0022-3093(98)00825-4.

[159] W. Warren, P. Lenahan, C. Brinker, C. Ashley, and S. Reed, “Deposition of high quality sol-gel oxides on silicon," *Journal of Electronic Materials*, vol. 19, no. 5, pp. 425–428, 1990, doi:10.1007/BF02658001.

[160] G. Dingemans and W. M. M. Kessels, “Status and prospects of Al_2O_3-based surface passivation schemes for silicon solar cells," *Journal of Vacuum Science & Technology A: Vacuum, Surfaces, and Films*, vol. 30, no. 4, pp. 040802, 2012, doi:10.1116/1.4728205.

[161] E. Vazsonyi, K. De Clercq, R. Einhaus, E. Van Kerschaver, K. Said, J. Poortmans, J. Szlufcik, and J. Nijs, “Improved anisotropic etching process for industrial texturing of silicon solar cells," *Solar Energy Materials and Solar Cells*, vol. 57, no. 2, pp. 179-188, 1999, doi:10.1016/S0927-0248(98)00180-9.

[162] P. K. Basu, D. Sarangi, K. P. Shetty, and M. B. Boreland, “Liquid silicate additive for alkaline texturing of mono-Si wafers to improve process bath lifetime and reduce IPA consumption," *Solar Energy Materials and Solar Cells*, vol. 113, pp. 37-43, 2013, doi:10.1016/j.solmat.2013.01.037.

[163] R. Weimer, P. Lenahan, T. Marchione, and C. Brinker, “Electronic properties of solgel-derived oxides on silicon," *Applied Physics Letters*, vol. 51, no. 15, pp. 1179–1181, 1987, doi:10.1063/1.98725.

[164] K. J. Kim, J. W. Kim, M. Yang, and J. H. Shin, “Oxidation of Si during the growth of SiO_x by ion-beam sputter deposition: in situ x-ray photoelectron spectroscopy as a function of oxygen partial pressure and deposition temperature," *Physical Review B*, vol. 74, no. 15, pp. 153305, 2006, doi:10.1103/PhysRevB.74.153305.

[165] Y. Park, X. Li, and S. Rhee, “Characterization of the Si/SiO_2 interface formed by remote plasma enhanced chemical vapor deposition from SiH_4/N_2O with or without chlorine addition," *Journal of Vacuum Science & Technology B: Microelectronics and Nanometer Structures Processing, Measurement, and Phenomena*, vol. 14, no. 4, pp. 2660–2666, 1996, doi:10.1116/1.589001.

[166] T. S. Yadav, A. K. Sharma, A. Kottantharayil,and P. K. Basu, “Comparative study of different silicon oxides used as interfacial passivation layer (SiN_y:H/SiO_x/n^+-Si) in industrial monocrystalline silicon solar cells," *Solar Energy Materials and Solar Cells*, vol. 201, pp. 110077, 2019, doi:10.1016/j.solmat.2019.110077.

[167] S. Silvestre and A. Chouder, “Effects of shadowing on photovoltaic module performance," *Progress in Photovoltaics: Research and Applications*, vol. 16, no. 2, pp. 141–149, 2008, doi:10.1002/pip.780.

[168] R. Müller, C. Reichel, X. Yang, A. Richter, J. Benick, and M. Hermle, “Impact of the homogeneous junction breakdown in IBC solar cells on the passivation quality of Al_2O_3 and SiO_2s: degradation and regeneration behavior," *Energy Procedia*, vol. 124, pp. 365–370, 2017, doi:10.1016/j.egypro.2017.09.311.

[169] K. A. Collett, R. S. Bonilla, P. Hamer, G. Bourret-Sicotte, R. Lobo, T. Kho, and P. R. Wilshaw, “An enhanced alneal process to produce SRV < 1 cm/s in 1 Ω cm n-type Si," *Solar Energy Materials and Solar Cells*, vol. 173, pp. 50–58, 2017, doi:10.1016/j.solmat.2017.06.022.

[170] R. Bonilla Osorio, P. Hamer, and P. R. Wilshaw, “Lowest surface recombination in n-type oxidised crystalline silicon by means of extrinsic field effect passivation," in *proceedings of 32nd European Photovoltaic Solar Energy Conference and Exhibition (EU PVSEC)*, 2007, doi:10.4229/EUPVSEC20162016-2AV.2.13.

[171] V. Meemongkolkiat, D. S. Kim, and A. Rohatgi, “SiO_2-based spin-on dielectrics for back surface passivation of p-type Si solar cells." in *proceedings of 22nd European Photovoltaic Solar Energy Conference (EU PVSEC)*, 2007.

[172] S. Mack, A. Wolf, C. Brosinsky, S. Schmeisser, A. Kimmerle, P. Saint-Cast, M. Hofmann, and D. Biro, “Silicon surface passivation by thin thermal oxide/PECVD layer stack systems," *IEEE Journal of Photovoltaics*, vol. 1, no. 2, pp. 135–145, 2011, doi:10.1109/JPHOTOV.2011.2173299.

[173] Y. Hou, E. Aydin, M. De Bastiani, C. Xiao, F. H. Isikgor, D. Xue, B. Chen, H. Chen, B. Bahrami, A. H. Chowdhury, and E. H. Sargent, “Efficient tandem solar cells with solution-processed perovskite on textured crystalline silicon," *Science*, vol. 367, no. 6482, pp. 1135–1140, 2020, doi:10.1126/science.aaz369.

[174] A. M. Petersson, P. Lindberg, and T. Boström, “Optical and passivating properties of sol-gel derived silica and titania coatings on textured monocrystalline silicon," in *proceedings of 37th IEEE Photovoltaic Specialists Conference (PVSC)*, 2011, pp. 002918–002923, doi:10.1109/PVSC.2011.6186556.

[175] P. K. Basu and A. Khanna, “A new single-component low-cost emitter etch-back process for silicon wafer solar cells," *Clean Technologies and Environmental Policy*, vol. 19, no. 6, pp. 1655–1665, 2017, doi:10.1007/s10098-017-1354-9.

[176] P. K. Basu, K. P. Sreejith, T. S. Yadav, A. Kottanthariyil, and A. K. Sharma, “Novel low-cost alkaline texturing process for diamond-wire-sawn industrial monocrystalline silicon wafers," *Solar Energy Materials and Solar Cells*, vol. 185, pp. 406–414, 2018, doi:10.1016/j.solmat.2018.05.047.

[177] B. S. Richards, “Single-material TiO_2 double-layer antireflection coatings," *Solar Energy Materials and Solar Cells*, vol. 79, no. 3, pp. 369–390, 2003, doi:10.1016/S0927-0248(02)00473-7.

[178] TCAD Sentaurus application note, “Three-dimensional Optical Simulation of Textured Surface Silicon Solar Cell," 2016.

[179] 2/3-Diode Fit, https://nanohub.org/resources/downloads (accessed December 22, 2021)

[180] D. C. Walter, B. Lim, and J. Schmidt, “Realistic efficiency potential of next generation industrial Czochralski-grown silicon solar cells after deactivation of the boron–oxygen-related defect center," *Progress in Photovoltaics: Research and Applications*, vol. 24, no. 7, pp. 920–928, 2016, doi:10.1002/pip.2731.

[181] S. Mack, D. Herrmann, M. Lenes, M. Renes, and A. Wolf, “Progress in p-type Tunnel Oxide-Passivated Contact Solar Cells with Screen-Printed Contacts," *Solar RRL*, vol. 5, no. 5, pp. 2100152, 2021, doi:10.1002/solr.202100152.

[182] K. R. McIntosh, T. G. Allen, S. C. Baker-Finch, an M. D. Abbott, “Light trapping in isotextured silicon wafers," *IEEE Journal of Photovoltaics*, vol. 7, no. 1, pp. 110–117, 2016, doi:10.1109/JPHOTOV.2016.2621347.

[183] S. Manzoor, M. Filipič, M. Topič, and Z. Holman, “Revisiting light trapping in silicon solar cells with random pyramids," in *proceedings of 43rd IEEE Photovoltaic Specialists Conference (PVSC)*, 2016, pp. 2952–2954, doi:10.1109/PVSC.2016.7750201.

[184] B. T, Phong, “Illumination for computer generated pictures," *Communications of the ACM*, vol. 18, no. 6, pp. 311–317, 1975, doi:10.1145/360825.360839.

[185] T. H. Fung, M. U. Khan, Y. Zhang, N. J. Western, D. Payne, K. R. Mclntosh, M. D. Abbott, “Improved ray tracing on random pyramid texture via application of Phong scattering," *IEEE Journal of Photovoltaics*, vol. 9, no. 3, pp. 591–600, 2019, doi:10.1109/JPHOTOV.2019.2894688.

[186] A. Schenk, “Finite-temperature full random-phase approximation model of band gap narrowing for silicon device simulation," *Journal of Applied Physics*, vol. 84, no. 7, pp. 3684–3695, 1998, doi:10.1063/1.368545.

[187] D. B. M. Klaassen, “A unified mobility model for device simulation—I. Model equations and concentration dependence," *Solid-State Electronics*, vol. 35, no. 7, pp. 953–959, 1992, doi:10.1016/0038-1101(92)90325-7.

[188] A. Gehring and S. Selberherr, “Modeling of tunneling current and gate dielectric reliability for nonvolatile memory devices," *Transactions on Device and Materials Reliability*, vol. 4, no. 3, pp. 306–319, 2004, doi:10.1109/TDMR.2004.836727.

[189] J. Shewchun, R. Singh, and M. A. Green, “Theory of metal-insulatorsemiconductor solar cells," *Journal of Applied Physics*, vol. 48, no. 2, pp. 765–770, 1977, doi:10.1063/1.323667.

[190] P. Procel, P. Löper, F. Crupi, C. Ballif, and A. Ingenito, “Numerical simulations of hole carrier selective contacts in p-type c-Si solar cells," *Solar Energy Materials and Solar Cells*, vol. 200, pp. 109937, 2019, doi:10.1016/j.solmat.2019.109937.

[191] T. Sugiura, S. Matsumoto, and N. Nakano, “Numerical analysis of p-type and ntype based carrier-selective contact solar cells with tunneling oxide thickness and bulk properties," *Japanese Journal of Applied Physics*, vol. 59, no. SG, pp. SGGF03, 2020, doi:10.35848/1347-4065/ab6a2c.

[192] Y. Zeng, Q. Yang, Y. Wan, Z. Yang, M. Liao, Y. Huang, Z. Zhang, X. Guo, Z. Wang, P. Gao, C. Wu, B. Yan, and J. Ye, “Numerical exploration for structure design and free-energy loss analysis of the high-efficiency polysilicon passivated-contact p-type silicon solar cell," *Solar Energy*, vol. 178, pp. 249–256, 2019, doi:10.1016/j.solener.2018.12.044.

[193] F. Book, A. Dastgheib-Shirazi, B. Raabe, H. Haverkamp, G. Hahn, and P. Grabitz, “Detailed analysis of high sheet resistance emitters for selectively doped silicon solar cells," in *proceedings of 24th European Photovoltaic Solar Energy Conference (EU PVSEC)*, 2009, pp. 1719–1722, doi:10.4229/24thEUPVSEC2009-2CV.5.3.

[194] S. W. Glunz, B. Steinhauser, J. I. Polzin, C. Luderer, B. Grübel, T. Niewelt, A. M. Okasha, M. Bories, H. Nagel, K. Krieg, and F. Feldmann, “Silicon-based passivating contacts: The TOPCon route," *Progress in Photovoltaics: Research and Applications*, pp. 1-19, 2021, doi:10.1002/pip.3522.

[195] M. Bivour, S. Schröer, M. Hermle, and S. W Glunz, “Silicon heterojunction rear emitter solar cells: Less restrictions on the optoelectrical properties of front side TCOs," *Solar Energy Materials and Solar Cells*, vol. 122, pp. 120–129, 2014, doi:10.1016/j.solmat.2013.11.029.

[196] H. Huang, J. Lv, Y. Bao, R. Xuan, S. Sun, S. Sneck, S. Li, C. Modanese, H. Savin, A. Wang, and J. Zhao, “20.8% industrial PERC solar cell: ALD Al_2O_3 rear surface

passivation, efficiency loss mechanisms analysis and roadmap to 24%," *Solar Energy Materials and Solar Cells*, vol. 161, pp. 14–30, 2017, doi:10.1016/j.solmat.2016.11.018.

[197] S. Maus, F. Maischner, S. Riepe, J. Greulich, E. Lohmüller, F. Schindler, P. Saint-Cast, P. Krenckel, A. Hess, S. Lohmüller, A. Wolf, and R. Preu, "SMART cast-monocrystalline p-Type silicon passivated emitter and rear cells: efficiency benchmark and bulk lifetime analysis," *Solar RRL*, vol. 5, no. 4, pp. 2000752, 2021, doi:10.1002/solr.202000752.

[198] Y. Li, F. Ye, Y. Liu, W. Cai, S. Wang, G. Cheng, N. Yuan, and J. Ding, "Research of annealing and boron doping on SiO_x/p^+-Poly-Si hole-selective passivated contact," *IEEE Journal of Photovoltaics*, vol. 10, no. 6, pp. 1552–1556, 2020, doi:10.1109/JPHOTOV.2020.3016631.

[199] J. I. Polzin, F. Feldmann, B. Steinhauser, M. Hermle, and S. Glunz, "Realization of TOPCon using industrial scale PECVD equipment," in *proceedings of AIP Conference*, 2018, pp. 040018, doi:10.1063/1.5049281.

[200] W. J. Choi, K. Madani, Y. Y. Huang, A. Jain, Y. W. Ok, V. D. Kang, S. Choi, and A. Rohatgi, "Optimization of in-situ and ex-situ doped p+ passivating contact for high efficiency p-TOPCon solar cell application," in *proceedings of 48th IEEE Photovoltaic Specialists Conference (PVSC)*, 2021, pp. 1907–1912, doi:10.1109/PVSC43889.2021.9518759

[201] W. J. Choi, A. Jain, Y. Y. Huang, Y.W. Ok, and A. Rohatgi, "Quantitative understanding and implementation of screen printed p^+ poly-Si/oxide passivated contact to enhance the efficiency of p-PERC cells," in *proceedings of 47th IEEE Photovoltaic Specialists Conference (PVSC)*, 2020, pp. 0821–0824, doi:10.1109/PVSC45281.2020.9300878.

[202] S. Werner, E. Lohmüller, A. Wolf, and F. Clement, "Extending the limits of screen-printed metallization of phosphorus-and boron-doped surfaces," *Solar Energy Materials and Solar Cells*, vol. 158, pp. 37–42, 2016, doi:10.1016/j.solmat.2016.05.064.

List of Publications and Awards

Journal Papers

- Jayshree Bhajipale, Anil Kottantharayil, and K. P. Sreejith, "TCAD based numerical exploration of industrially feasible tunnel oxide passivated contact on p-type silicon," *Solar Energy*, vol. 253, pp. 231–239, 2023, doi:10.1016/j.solener.2023.02.040.

- Jayshree Bhajipale and Anil Kottantharayil, "Passivation of n- and p-type Silicon Surfaces with Spray-coated Sol-gel Silicon Oxide Thin Film," *IEEE Transactions of Electron Devices*, vol. 67, no. 11, pp. 5045-5052, 2020, doi:10.1109/TED.2020.3025981.

- Jayshree Bhajipale, Suchismita Mitra, Hemanta Ghosh, K. P. Sreejith, and Anil Kottantharayil, "Spray-coated SiO_2/PECVD SiN_x stack for the passivation of n^+ emitter of p-type Si solar cell," *Solar Energy*, vol. 246, pp. 113–118, 2022, doi:10.1016/j.solener.2022.09.037.

Conference Papers

- Jayshree Bhajipale, Anil Kottantharayil, and K. P. Sreejith, "Advantages of TOPCon cell with rear full area hole selective contact on p-type Si with front n^+ emitter over PERC," in *proceedings of 8th World Conference on Photovoltaic Energy Conversion (WCPEC)*, 2022, pp. 184–186, doi:10.4229/WCPEC-82022-1DV.4.17.

- Jayshree Bhajipale and Anil Kottantharayil, "Effectiveness of UV-Ozone treatment and alneal process for Si surface passivation with sol-gel spray-coated SiO_2 film," in *proceedings of ECS Meeting Abstracts*, 2021, pp. 643, doi:10.1149/MA2021-0213643mtgabs.

- Jayshree Bhajipale and Anil Kottantharayil, "Spray-coated SiO_2 thin film for passivation of n-type Cz silicon surface with S_{eff} ~6 cm-sec^{-1}," in *proceedings of*

47th IEEE Photovoltaic Specialists Conference (PVSC), 2020, pp. 0280–0283, doi:10.1109/PVSC45281.2020.9300907.

- Jayshree Bhajipale and Anil Kottantharayil, "Post deposition annealing temperature pptimization for gol-gel spray-coated SiO_2 film for p-type Cz Si surface passivation," in *proceedings of 5th IEEE International Conference on Emerging Electronics (ICEE)*, 2020, pp. 1–4, doi:10.1109/ICEE50728.2020.9777056.

Awards

- Winner of the poster award in the thematic area of "Silicon Materials and Cell" at the *8th World Conference on Photovoltaic Energy Conversion* for the work titled "Advantages of TOPCon cell with rear full area hole selective contact on p-type Si with front n^+ emitter over PERC" authored by Jayshree Bhajipale, Anil Kottantharayil, and K. P. Sreejith.

Acknowledgements

I express my sincere gratitude to my thesis supervisor Prof. Anil Kottantharayil for trusting me and giving me an opportunity to work in an emerging and challenging research area. He always motivated me through inputs, suggestions, and discussions. His analytical skills and thorough technical knowledge were a great inspiration. His desire for innovation and perfection has driven my thesis work to a bit higher standard and helped shape me as a researcher. I appreciate the freedom he gave me in exploring my research work which helped me grow as an independent researcher.

I also thank Prof. Pradeep Nair and Prof. Narendra Shiradkar for examining my annual progress seminar. The insightful feedback and suggestions have contributed significantly to my research progress. I would also like to thank Prof. K. L. Narasimhan and Prof. B. M. Arora for their valuable time, guidance, and feedback.

I acknowledge the Ministry of New and Renewable Energy (MNRE) for funding my doctoral thesis through the National Centre for Photovoltaic Research and Education (NCPRE). Also, I thank the IIT Bombay Nanofabrication Facility (IITBNF) for providing the necessary resources for my thesis work. I would also like to acknowledge Sophisticated Analytical Instrumentation Facility (SAIF), IIT Bombay, for their assistance in carrying out HR-TEM measurements.

I am deeply indebted to the NCPRE staff, Sandeep K., Nilesh K., Guru B., Almouzzam K., Siddharth B., and Ajin R., of the crystalline Si solar cell group of NCPRE for their help in the fabrication and characterization of Si wafers and solar cells. It was really a joyful experience working with all of them. I would also like to thank the scientific staff Dr. Hemanta G., Dr. Suchismita M., Dr. Ashok S., Dr. Prabir B., and Dr. Soma R. for the fruitful technical discussions that gave me new insight into the design of experiments and in data analysis.

A special thanks to NCPRE lab manager Dr. Diksha M., and staff, Kailash W., Rupali C., Gaurav H., Harsha T., Ashwini B., Kiran K., and Bharat P. for the administrative assistance. Also, the support from IITBNF staff members was outstanding. A special

thanks to Anjum A., Pankaj G., Minita S., Shilpa K., Vinayak S., Bhimraj S., Pradeep N., and Sunita N., for their help and cooperation.

I acknowledge the support and cooperation of my group members, Poonam, Sreejith, Pankaj, Kalaivani, Durgaprasad, Premsai, Tarun, Resmi, Robin, Sanchar, Dibyendu, and Saima and NCPRE Si group students, Astha, Swasti, Anil, and Irfan. Especially, Poonam for being a sister-like figure, Sreejith for being a senior-cum mentor, and Pankaj whose guidance and discussions kept me motivated during the initial days of my Ph.D.

I cherish the time spent with my friends, Prajakta, Pooja, Nikhil, Abin, Rashmi, Nilotpal, Tarni, Dhiman, Varun, Yugandhara, Prachi, Chandan, and my hostel wingmates. They made my stay at IIT Bombay memorable. The quality time spent with all of them is irreplaceable. Also, I am thankful to Jyoti, Bhoomika, Swapnil, Nikita, Harshit, Bidhan, Chirag, Sumit, and Siddharth for being just a call away. I appreciate all for being there for me through all the ups and downs in my professional and personal life.

I am indebted to my parents, brother, and grandmother for their selfless support and constant encouragement for my higher studies.